MESO-SCALE FINITE ELEMENT SIMULATION OF DEFORMATION BANDING IN FLUID-SATURATED SANDS

A DISSERTATION
SUBMITTED TO THE DEPARTMENT OF CIVIL AND ENVIRONMENTAL ENGINEERING
AND THE COMMITTEE ON GRADUATE STUDIES
OF STANFORD UNIVERSITY
IN PARTIAL FULFILLMENT OF THE REQUIREMENTS
FOR THE DEGREE OF
DOCTOR OF PHILOSOPHY

José E. Andrade
June 2006

I certify that I have read this dissertation and that, in my opinion, it is fully adequate in scope and quality as a dissertation for the degree of Doctor of Philosophy.

Ronaldo I. Borja Principal Adviser

I certify that I have read this dissertation and that, in my opinion, it is fully adequate in scope and quality as a dissertation for the degree of Doctor of Philosophy.

Peter M. Pinsky

I certify that I have read this dissertation and that, in my opinion, it is fully adequate in scope and quality as a dissertation for the degree of Doctor of Philosophy.

Ruben Juanes

Approved for the University Committee on Graduate Studies.

Abstract

Deformation banding is a ubiquitous failure mode in geomaterials such as rocks, concrete, and soils. It is well known that these bands of intense localized deformation can significantly reduce the load-carrying capacity of structures. Furthermore, when dealing with fluids-saturated geomaterials, the interplay between the compaction/dilation of pores and development of pore fluid pressures is expected to control not only the strength of the solid matrix but also its ability to block or transport such fluids. Accurate and thorough simulation of these phenomena (i.e. deformation banding and fluid flow) is challenging, as it requires numerical models capable of capturing micro-mechanical processes such as mineral particle rolling and sliding in granular soils and the coupling between porosity and relative permeability, while still maintaining a continuum mechanics framework. Until recently, these processes could not even be observed in the laboratory. Numerical models could only interpret material behavior as a *macroscopic* process and were, therefore, unable to model the very complex behavior of saturated geomaterials accurately.

In this dissertation, we propose a numerical model capable of capturing some of the most intricate and important features of sand behavior. Development of the model is further motivated by new advances in laboratory experimentation that allow for the observation of key parameters associated with material strength at a scale finer than specimen scale. One such parameter is porosity, a relative measure of the amount of voids in a soil sample. A novel elastoplastic constitutive model based on a meso-scale description of the porosity is proposed to simulate the behavior of the underlying sand matrix and to accurately predict the development of deformation bands in saturated samples. 'Meso-scale' is defined here as a scale smaller than specimen size but larger than particle size. The effect of meso-scale inhomogeneities on the deformation-diffusion behavior of loose and dense sands is studied by casting the meso-scale constitutive model within a mixed nonlinear finite element

framework. The main findings of this work are that meso-scale imperfections (in macroscopically homogeneous samples) are responsible for triggering deformation bands, which tend to strongly influence the direction and volume of fluid flow. Numerical simulations clearly show that failure and flow modes in dense sands are sharply distinct from those in loose sands. It is concluded that meso-scale inhomogeneities, which are inevitably present in 'homogeneous' samples of sand, play a crucial role in the mechanical behavior of specimens under drained and undrained conditions at finite strains.

Acknowledgments

I would like to express my sincerest gratitude to my academic advisor, Ronaldo Borja. Ronnie has gradually guided me towards becoming a critical thinker and an independent researcher. This dissertation is the product of his guidance and encouragement.

The dissertation committee has also played an important role in the completion of this thesis. Peter Pinsky has been a member of the reading committee but also a great teacher and advisor. I am grateful to Ruben Juanes for his constructive criticism of this work and for his advice on academic matters. Adrian Lew has not only been part of the dissertation committee but has also been a friend who has always stimulated me intellectually with his insatiable inquisitive style. Finally, I am grateful to Keith Loague for serving as chair of the dissertation committee.

The Blume and Shah families provided for three academic years of financial support in the form of fellowships and made possible my post-graduate studies at Stanford. Without their financial support, I would not have been able to come to Stanford and this dissertation would not have been possible. Once again, I would like to express my deepest gratitude to these two families who have made it possible for many graduate students to achieve their dreams. The remainder of my post-graduate study was funded by research assistantships through grant numbers CMS-0201317 and CMS-0324674 from the National Science Foundation. This support is gratefully acknowledged.

At Stanford, I have been blessed with wonderful friends. The five years I spent here with my family have been the most wonderful years of my life. My co-workers and friends at the John A. Blume Earthquake Engineering Center, have been people who have not only inspired me intellectually, but also have made my stay here a more pleasant one by offering me their friendship.

Finally, I want to thank the most important people in my life: my family. My parents have been a constant source of encouragement ever since I was a child. My parents were

my first teachers; they taught me the most important things in life and it is to them that I owe who I am as a person (though the negative parts of my character are my own device). My wife Claudia has been my ideal companion for eight years. She is my dearest friend, confidant, partner and advisor. She believed in me even when I did not. Now as parents, we share the blessing of having a wonderful daughter. Milena was born two years ago and ever since she arrived she became the center of my universe. It is to Milena that I dedicate this dissertation.

To Milena

Contents

List of Tables

List of Figures

Chapter 1

Introduction

1.1 Objectives and statement of the problem

The main objective of this dissertation is to develop a realistic numerical model for the detection of deformation banding in saturated granular media. Because of the complexity of the deformation phenomenon and its interaction with the fluid flow, it is imperative to develop a model that realistically accounts for the effective behavior of the underlying granular material. In particular, a constitutive model capable of including inhomogeneities in key strength parameters at the meso-scale is needed to study the effect of such inhomogeneities in the stability of samples of sand. The meso-scale here refers to a scale that is smaller than specimen size (centimeter scale), but larger than a typical grain (micrometer scale). Thus, in a typical sample encountered in the laboratory, the meso-scale would be the millimeter scale.

Deformation banding is a phenomenon that is observed in many solids such as metals, concrete, rocks, and soils. It can be defined as the process by which a narrow zone of localized deformations appears in a solid sample. When dealing with fluid-saturated samples of soil, the process is even more complex as the deformation of the solid matrix is coupled with the fluid flow. It is our objective here to develop a framework in which this coupling is realistically accounted for and where the impact of the coupled mechanical behavior on the stability and flow characteristics of saturated specimens of loose and dense sands is adequately captured.

1.2 Motivation

Strain localization is a ubiquitous mode of failure in geomaterials (e.g. soils, rocks, concrete), resulting in the loss of load-carrying capacity of the solid matrix. Furthermore, instabilities play a crucial role in the flow characteristics of fluid-saturated porous media. It has been shown that shear band instabilities, leading to the appearance of rock fractures in the field, can serve as channels or barriers for hydrocarbon flow, depending on the boundary conditions [12].

In general, instabilities can be labeled as diffuse and localized. In the case of relatively loose sands under saturated conditions, a diffuse instability phenomenon termed 'liquefaction' is observed both in the laboratory [13] and in the field [14]. This type of instability is attributed to the fact that relatively loose sands tend to contract when subjected to shearing loads and when the fluid (typically water) cannot escape fast enough, pore fluid pressures build up and contribute to a decrease in the overall strength of the soil matrix. The effect of soil liquefaction can be easily grasped by looking at a classical example of its catastrophic nature. Figure 1.1 shows a picture of a group of apartment buildings that failed due to loss of bearing capacity. The soil beneath the foundations liquefied and produced excessive displacements at the base, ultimately leading to the collapse of otherwise structurally-intact buildings [3].

Similarly, deformation banding is a type of localized instability that occurs both in the laboratory and in the field as a result of a concentration of deviatoric strains in a narrow zone within samples of relatively dense sands and, to a lesser extent, in samples of relatively loose sands. The next chapter deals with evidence of the occurrence of deformation banding in soils both in the laboratory and in the field, motivating our work further.

Strain localization is intimately linked to the mechanical behavior of the underlying solid. It is well known that relative density is a state parameter that strongly influences the mechanical behavior of sands and in particular, governs the strength characteristics of granular materials. Porosity is directly correlated to relative density and specific volume. New advances in laboratory experimentation make it possible to obtain a clear picture of the porosity field across a sample of sand. These new developments have motivated our work, which is in fact a collaborative research effort in which the initial porosity field from the experimental side could be utilized as input for our models. X-Ray Computed Tomography (CT) techniques, for example, can provide accurate measurements of the initial porosity

Figure 1.1: Group of apartment buildings in Niigata, Japan after a magnitude 6.5 earthquake rocked the town in 1964. The buildings failed due to loss of bearing capacity when the soil beneath liquefied (after Kramer [3]).

in the sample (see works in [4, 15, 16] for applications of CT technology to geomaterials). Incidentally, because of the resolution of the X-Ray image, we can observe the fluctuations in relative density at the meso-scale. The meso-scale approach has been utilized very recently by other researchers to account for inhomogeneities in other geomaterials such as concrete (e.g. see the works of Wriggers and Moftah [17] and Häfner et al. [18]). Nübel and Huang [19] perturbed the void ratio field in samples of granular material within a framework of Cosserat continuum, utilizing a hypoplastic constitutive model, and showed how these perturbations affect the stability of drained samples of sand.

1.3 Methodology

To simulate strain localization phenomena in loose and dense saturated sands, we have developed a mathematical model utilizing nonlinear continuum mechanics, mixture theory, theoretical and computational plasticity, and the finite element method. Continuum mechanics furnishes a mathematical framework to describe the kinematics of bodies and develop balance laws governing the deformation of solids and fluids. We also obtain suitable stress and strain measures from this framework. On the other hand, a novel constitutive

model for sands capable of capturing the more salient features of this particulate material was developed based on plasticity theory. The model utilizes a three-invariant yield surface, which delimits the elastic behavior of the material while accounting for the difference in strength between compressive and tensile behavior. Models based on plasticity theory can capture permanent deformations typical of geomaterials (e.g. concrete, soils, rocks, etc). The end of Chapter 2 contains a detailed discussion on the mechanical behavior of granular media.

Inhomogeneities at the meso-scale are incorporated into the plasticity model via a state parameter ψ, which contains information on the relative density at a point in the specimen. If $\psi < 0$, the point is said to be denser than critical, whereas $\psi > 0$ implies a point looser than critical. In this fashion, the macroscopic model is able to incorporate information on relative densities that could be present in the sample at the meso-scale and that, as we will show in the next chapters, could trigger unstable behavior at the specimen level. Further, it is well known that the behavior of dense sands is very different from that of loose sands. For example, dense sands tend to behave in a more 'brittle' fashion, reaching a distinct peak strength, whereas loose sands do not show such a clear peak strength. Hence, any realistic model for sands should be able to capture this difference in behavior at different relative densities.

Finally, the aforementioned model is cast into a nonlinear finite element program to simulate the behavior of saturated sand specimens numerically. The balance laws, obtained from continuum mechanics and mixture theory principles, are solved in time and space using a mixed finite element procedure. The numerical scheme is utilized to detect the onset of strain localization in inhomogeneous samples of sand and to compare their macroscopic behavior against that of homogeneous specimens.

1.4 Structure of presentation

The dissertation is organized in an incremental fashion, starting with the ingredients for the elastoplastic model for sands (Chapters 3 and 4) and finishing with the problem of fluid saturated media at finite deformation (Chapter 5). Together, these chapters tell the story of modeling deformation banding in saturated sands utilizing a constitutive model that captures meso-scale inhomogeneities in the porosity field and the most salient features of sand behavior. It is our personal opinion that these ingredients make the model unique and

allow us to obtain results that have been observed experimentally, but not yet replicated numerically.

Chapter 2 summarizes some of the relevant background literature. The discussion revolves around two major topics: strain localization and the mechanical behavior of sands.

Chapter 3 presents a novel constitutive model for capturing the effective or drained behavior of granular media. This two stress-invariant plasticity model is based on the critical state theory (CST) and introduces the state parameter ψ, which provides information on the relative density of a specimen at the meso-scale. Finite element implementation of the constitutive model is presented and the framework is then used to predict the location and direction of strain localization bands on dense sand specimens exhibiting structured density at the meso-scale.

In **Chapter 4**, the constitutive model for granular media is extended to account for the third stress invariant, thereby reproducing the difference in the compressive and extensional yield strengths commonly observed in geomaterials. Numerical implementation of the constitutive model in principal strain space yields a spectral form for the consistent tangent operator and allows for the design and implementation of a very efficient algorithm to search for the onset of strain localization. The numerical model is used to predict the occurrence of deformation bands on prismatic and cylindrical specimens of dense sands exhibiting unstructured random density at the meso-scale.

Chapter 5 deals with the modeling of deformation banding in saturated loose and dense sands with inhomogeneous porosities at the meso-scale. The previously developed plasticity model is used to obtain the underlying drained or effective stress response in the solid matrix. Additionally, permeability is naturally coupled with porosity to allow for a more realistic representation of the flow phenomenon. The formulation, based on the mixture theory, results in a classical $\boldsymbol{u} - p$ finite element scheme, which is used to investigate the effects of meso-scale inhomogeneities in the porosity and drainage conditions on the stability of the specimens loaded quasi-statically. It is shown that strain localization greatly influences flow characteristics in a sample. Additionally, it is shown that the deformation behavior of relatively dense and loose sands is sharply distinct and that this affects the mode of deformation banding and the pattern of fluid flow.

In conclusion, **Chapter 6** will summarize the most salient contributions and findings of this dissertation. Future lines of research related to this work will be identified and some recommendations on how to improve the framework presented herein will be given.

It is important to note that the core chapters of this dissertation (i.e. Chapters 3–5) are self-contained because they have been or are in the process of being published as individual journal articles. As a result, there will be some repetition of fundamental concepts. Furthermore, notations were chosen to be simple and clear for each chapter rather than for the dissertation as a whole; consequently, the notations may not be identical from chapter to chapter. Similar to the idea of idealizing a granular medium, the reader is encouraged to look at this dissertation as a smeared version of a system composed of discrete elements rather than as a 'perfect' continuum.

Chapter 2

Background Literature

2.1 Strain localization in the lab and in the field

Deformation banding is a type of localized instability that occurs in the laboratory as a result of a concentration of deviatoric strains in a narrow zone within samples of relatively dense sands and, to a lesser extent, in samples of relatively loose sands. For example, Alshibli et al. [4] reported the occurrence of strain localization in samples of dense and loose sands under drained conditions but noted that softening became more severe as specimen density increased. Softening was observed in all specimens that bifurcated and was attributed to the slip mechanism developed by narrow zones of intense deformation. A typical failure mode is shown in Figure 2.1 for a sample of medium dense Ottawa sand tested under plane strain conditions; a well-developed planar zone with a characteristic normal vector $\mathbf{n}$ can be observed.

If planar bands of intense deformation form in samples of sand under drained conditions, can they form under undrained conditions? Can drainage impact the stability of samples of sand? These questions were posed by Mokni and Desrues [20] who studied the occurrence of strain localization in samples of sand under undrained conditions and subjected to plane strain compression. They concluded that the volumetric constraint imposed by the globally undrained conditions, compounded by the fact that water is effectively incompressible, tends to delay the occurrence of shear bands in dilative samples of sand. Localization in samples of loose sand occurred even under undrained conditions. On the other hand, Han and Vardoulakis [21] presented limited experimental results showing shear banding does

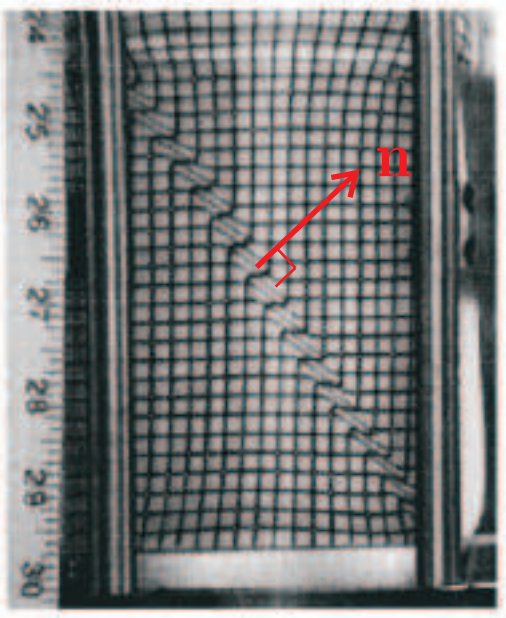

Figure 2.1: Typical failure mode for plane strain specimen (after Alshibli et al. [4]).

not occur in contractive sands during displacement-controlled undrained plane strain compression. Because of these apparent inconsistencies, Finno et al. [22] studied shear bands in plane strain compression of loose sands and concluded that shear banding consistently occurred in both drained and undrained tests on loose masonry sand.

In the field, zones of localized deformation can be directly linked to stability problems. For instance, Finno et al. [23, 24] showed the appearance of zones where deformation was highly localized during deep excavations in saturated Chicago clay. The largest incremental ground-surface settlements were associated with the development of distinct shear zones. Similarly, slope stability, which is clearly associated with modes of localized deformation, can occur because of static or dynamic loading causing very large human and economic losses. For example, the 7.6 magnitude Kashmir earthquake in October, 2005, triggered tens of miles of slope failures leaving many others in precariously unstable conditions. One such example of extensive slope instability is show in Figure 2.2, where the magnitude and scale of the landslide can be appreciated when one notes that the meandering structure parallel to the river in the center of the picture is actually a two-lane road.

Figure 2.2: Extensive landsliding in Neela Dandi Mountain, north of Muzaffarabad (after Durrani et al. [5]).

2.2 Strain localization analysis and simulation

The study of strain localization is by no means limited to experimental efforts. The first theoretical work dealing with discontinuities is usually attributed to Hadamard who, at the beginning of last century, came up with conditions for waves—propagating through elastic media—to become stationary [25]. Subsequently, Hill [26], Thomas [27], and Mandel [28], expanded Hadamard's compatibility conditions into the elasto-plastic regime. In the mid-seventies Rudnicki and Rice [29] published what has become one of the most influential papers in the literature dealing with strain localization in solids. They presented necessary conditions for the localization of deformation in pressure-sensitive dilatant materials. Rudnicki and Rice's approach consisted of investigating the necessary conditions for the so-called loss of strong ellipticity of the elasto-plastic tangent operator (see Marsden and Hughes [30] for a clear definition of strong ellipticity). This condition leads to the loss of positive definiteness of the acoustic tensor. All of the above-mentioned works follow what is now called the 'weak discontinuity' approach in which the solution is allowed to bifurcate into a solution involving discontinuous deformation gradients (see Reference [31] where this terminology is introduced).

More 'modern' analytical studies of strain localization in solids are directly applicable to soils, rocks, and concrete. In the late eighties, Ortiz looked at the analytical solution of localized failure in concrete [32]. The idea pursued by Ortiz was to look at damage

in concrete materials as an instability arising from the inelastic behavior of the material. Subsequent works investigating the properties of discontinuous bifurcation solutions in associative and nonassociative elastoplastic models for the case of linear and nonlinear kinematics are outlined in [33–39]. Extensive work has also taken place to understand a special case of bifurcation appearing in porous rocks termed 'compaction banding' [40–42]. Borja and Aydin [43] developed a consistent geological and and mathematical framework to characterize (and capture) the entire spectrum of localized deformation in tabular bands ranging from shear deformation bands (pure shear bands, compactive/dilative shear bands) to volumetric deformation bands (pure compaction/dilation bands).

Of particular relevance here are the works of Rudnicki [44], Larsson et al. [45], Borja [46], and Callari and Armero [47] who derived expressions for the acoustic tensor for partially saturated and saturated porous media. The expressions obtained are relevant for either locally drained or locally undrained conditions (see Chapter 4 for a thorough discussion). Rudnicki derived an expression for the undrained acoustic tensor at finite strain departing from the assumption that the first Piola-Kirchhoff stress can be decomposed into effective and pore pressure stress; a straight-forward generalization from the infinitesimal effective stress concept. Larsson et al. based their expression for the acoustic tensor, at small strains and under undrained conditions, on the concept of regularized strong discontinuity. Borja studied the kinematics of multi-phase bodies in the context of partially saturated soils at small strains and derived an expression for the undrained acoustic tensor for partially saturated conditions. Callari and Armero followed the strong discontinuity approach to obtain an expression for the undrained acoustic tensor at finite strains. Following a more physically-based approach, Vardoulakis analyzed experimental results from undrained plane-strain compression tests on water-saturated sands and looked at the influence of pore water flow and the occurrence of shear banding under undrained conditions [48, 49]. He concluded that no shear banding instabilities could occur in locally undrained (homogeneous) specimens.

The theoretical developments outlined above have spurred significant research efforts in the last couple of decades to try to capture strain localization in solids numerically. Examples of pioneering efforts in modeling strain localization using finite elements are the works by Prevost [50], Ortiz et al. [51], and Leroy and Ortiz [52]. Unfortunately, it was realized quite early that rate-independent plasticity models did not have a characteristic

length and hence introduced a pathologic mesh dependence when trying to model the propagation of deformation bands in elastoplastic solids. To remove this anomaly, different researchers opted for different approaches that allowed the introduction of a length scale emanating from the constitutive equations. Typical efforts involve the introduction of non-local constitutive models (e.g. Bažant et al. [53]), viscoplastic regularization (e.g. Loret and Prevost [54] and Prevost and Loret [55]), and Cosserat continuum constitutive models (e.g. the works by Muhlhaus and Vardoulakis [56], Nübel and Huang [19], and Li and Tang [57]). These approaches exploit the fact that granular media contain 'natural' length scales such as distance between particles and particle diameter, and the fact that individual particles are naturally amenable to micro-polar treatment.

Motivated by the lack of intrinsic length scale in rate-dependent inelastic constitutive models, Simo and co-workers developed what we now call the 'strong discontinuity' approach [31], which assumes a discontinuity in the displacement/velocity field (as opposed to the 'weak discontinuity' approach in which the displacement gradients are discontinuous, as discussed above). From its very inception, the strong discontinuity approach produced meaningful simulations of strain localization in elastoplastic solids without exhibiting mesh dependence. Armero and Garikipati [58] extended the approach to finite deformations within the context of the multiplicative decomposition of the deformation gradient. Larsson and Runesson [59] and Larsson et al. [45] developed the so-called 'regularized' strong discontinuity approach based on the work by Simo and co-workers. The work of Larsson et al. [45] is of particular relevance here as they simulated strain localization in locally undrained soils. Borja and Regueiro utilized the strong discontinuity approach to develop finite elements capable of capturing strain localization in frictional materials [60–63]. Borja [64] derived conditions for the onset of strain localization at finite strains and provided a link between the localization criteria for the regularized and unregularized strong discontinuity approaches.

2.3 Mechanical behavior and constitutive models for sands

One important aspect in the modeling of deformation response in drained and undrained soils is the ability to capture, in a realistic fashion, the most salient features of the underlying soil matrix. In the case of sands, there are several key features that have not been properly addressed in the literature and that this dissertation attempts to address in detail. In

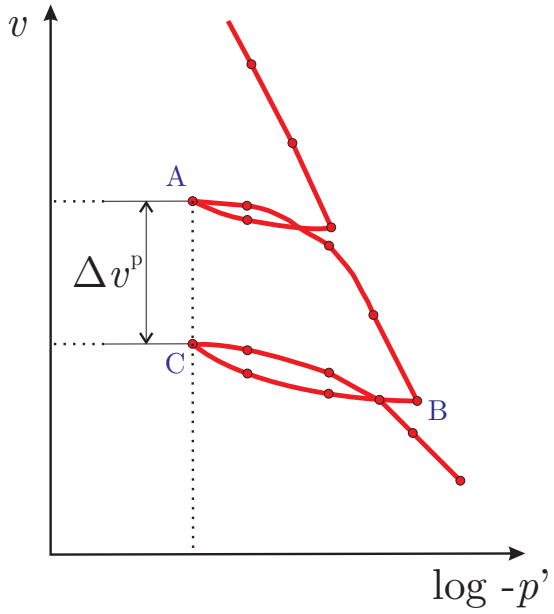

Figure 2.3: Compression plane for typical soil sample (after Schofield and Wroth [6]).

particular, every realistic model for sands should be able to capture the following signature phenomenological features:

- Nonlinear behavior and irreversible deformations
- Pressure dependence
- Different strength under triaxial extension and compression
- Relative density dependence
- Nonassociative plastic flow

Significant progress has been made in the formulation of phenomenological models for soils that can capture material nonlinearities as well as irreversible deformations. These features are clearly exposed in a one-dimensional consolidation tests such as the one depicted in Figure 2.3. Consider a soil sample at an initial state of specific volume v and effective pressure p', corresponding to point A in the figure. An increase in the effective pressure p' will compress the soil (reduce v) to point B. Now, suppose the pressure is decreased back to

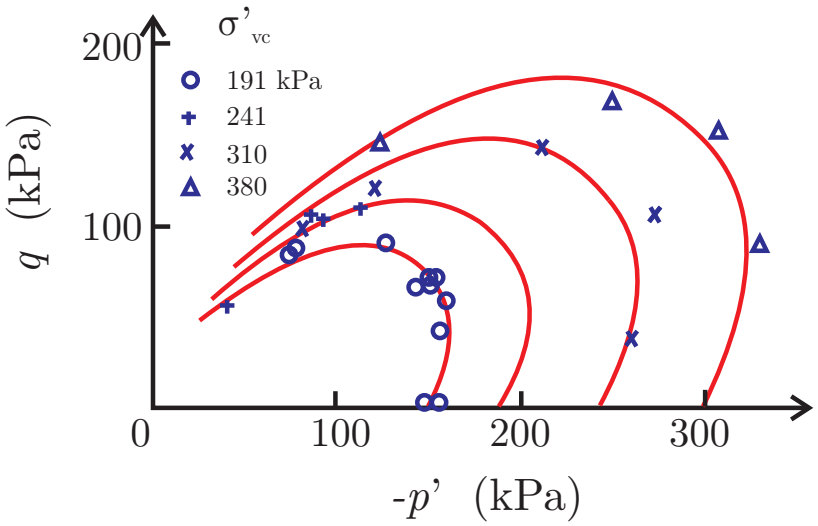

Figure 2.4: Data of yielding deduced from triaxial tests on undisturbed Winnipeg clay in effective stress plane (after Graham et al. [7]).

the original value at point A; the sample does not return to state point A, but rather goes to state point C, which is at the same pressure than A but at a different value of specific volume v. The sample has suffered an irreversible volumetric deformation Δv^{p}. At the same time, it is clear that the loading branch from point A to B is nonlinear, therefore the soil is said to deform in a materially nonlinear fashion. These types of phenomenological behavior in soils motivated the development of elastoplastic models aimed at capturing material nonlinearities and irrecoverable deformations. Classical elastoplastic models for soils include the Cam-Clay family of models originally proposed by Schofield and Wroth [6] and subsequently modified by Roscoe and Burland [65]. Borja and Tamagnini [66] extended the modified Cam-Clay model to account for the effect of geometric nonlinearities, which had been neglected in the original model.

Figure 2.4 shows a plot of failure/yield surfaces for different values of overburden stress for undisturbed samples of Winnipeg clay. The strength characteristics of the soil samples are clearly affected by the overburden stress and the effective pressure. Cam-Clay models are very effective in capturing pressure dependence in soils and the effect of the overburden pressure. Previous plasticity models were hopeless in trying to capture these features. For example, the von-Mises or J_2 model is pressure insensitive and the Drucker-Prager model

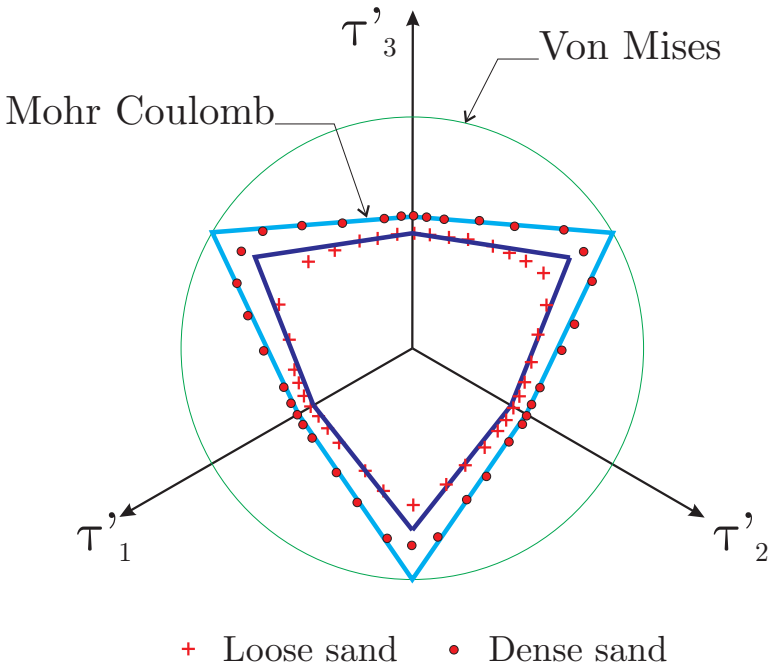

Figure 2.5: Yield surfaces and data obtained from Monterey sand in principal effective stress space (after Lade and Duncan [8]).

has no way of incorporating the effect of the overburden (and other important features such as plastic compaction). Other nonlinear plasticity models that take into account the pressure dependence are those of Lade and Duncan [8], Nova and Wood [67], Pastor at al [68], Pestana and Whittle [69]. The plastic potential proposed by Nova and Wood [67] is the predecessor of the of the plastic potential proposed in this work.

The different compressive/tensile strength is a characteristic of *all* geomaterials. Unfortunately, most people still model geomaterials using J_2-type models such as von-Mises and Drucker-Prager. In fact, even the Cam-Clay models presented above do not account for this important feature. The difference in tensile and compressive strength was demonstrated by Lade and Duncan who plotted different yield points on a deviatoric plane for samples of Monterey sand [8]. Figure 2.5 shows the difference in strength depending on whether the samples are in triaxial compression (e.g. negative τ_3') or triaxial extension (e.g. positive τ_3'). The figure also shows how the Mohr-Coulomb yield condition is able to capture this difference in strength. Any model with a circular projection on the deviatoric plane is hopeless in trying to capture this key feature. Efforts in trying to account for the

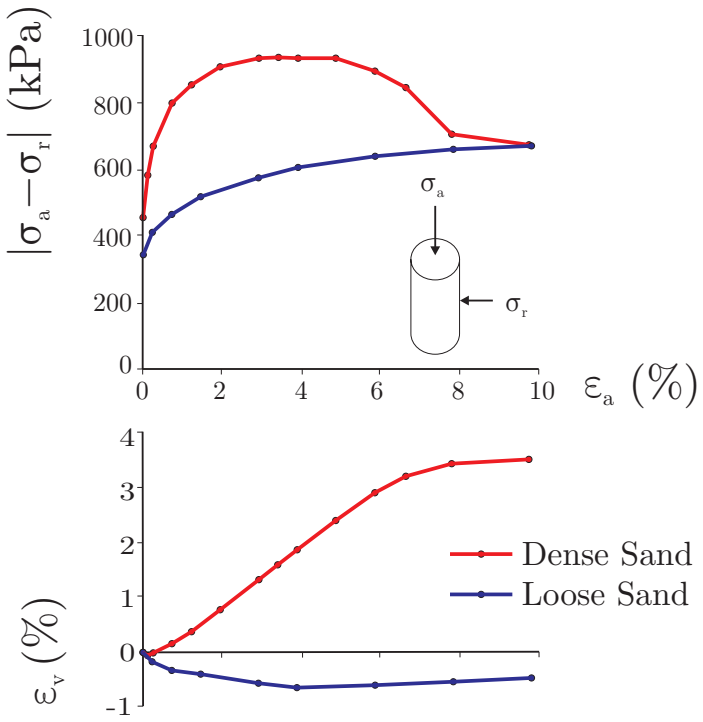

Figure 2.6: Macroscopic responses from triaxial compression in dense and loose sands. Top: Deviartoric stress versus axial strain. Bottom: Volumetric strain versus axial strain (after Cornforth [9]).

different behavior in triaxial extension/compression include the yield surfaces proposed by Matsuoka and Nakai [70] and Lade and Kim [71]. Other researchers opted for modifying the classical Cam-Clay models to account for all three stress invariants. Perić and Ayari [72, 73] introduced the effect of Lode's angle into the expression for the modified Cam-Clay yield surface and thereby obtained an enhanced expression that accounts for the difference in triaxial compression/extension for clays.

The behavior of sands is profoundly influenced by the relative density. It is well known that relatively loose sands behave very differently than relatively dense sands [74]. For instance, as illustrated in Figure 2.6 (top), if one plots the deviatoric response in dense and loose sands under otherwise identical triaxial compression, one finds that the dense sand tends to peak in a more distinct way than loose sands. Similarly, dense sands tend to dilate when sheared, whereas loose sands then to contract. This phenomenon is also observed in Figure 2.6 (bottom). The ability of a model to capture this feature is crucial when modeling

the different responses of sands at various densities, and it becomes even more important when sands are saturated and not allowed to drain. The Introduction sections in Chapters 2-4 shed more light on the importance of capturing relative density realistically. Very few models of sand account explicitly for relative density in the sense that they can capture the different compactive/dilative feature explained above. Some of the most notable examples of models that do account for relative density are those of Jefferies [2], Manzari and Dafalias [75], Pestana and Whittle [69], and Khalili et al. [76].

Finally, from a phenomenological stand point, it has been shown that sands (and many geomaterials in general) display nonassociativity of plastic flow. This means that the direction of plastic strain rate is not defined by the normal to the yield surface and hence suggests the existence of the so-called plastic potential surface, whose normal does define the direction of the plastic strain rates. This feature has been observed in the laboratory and reported by Poorooshasb et al. [10, 11], who, based on experimental evidence, proposed a model where the plastic potential surface differs from the yield surface. Figure 2.7 shows the model proposed based on test results for dense Ottawa sand. Also, from a theoretical stand point, Nova [77] showed that thermodynamic implications require geomaterials in general to display nonassociativity. However, experimental evidence in sands suggests that, whereas volumetric nonassociativity is clearly pronounced, deviatoric nonassociativity in sands is not as important. This was reported by Lade and Duncan [8] who showed that the direction of plastic flow rates on the deviatoric plane are roughly parallel to the normal to the yield surface on that plane.

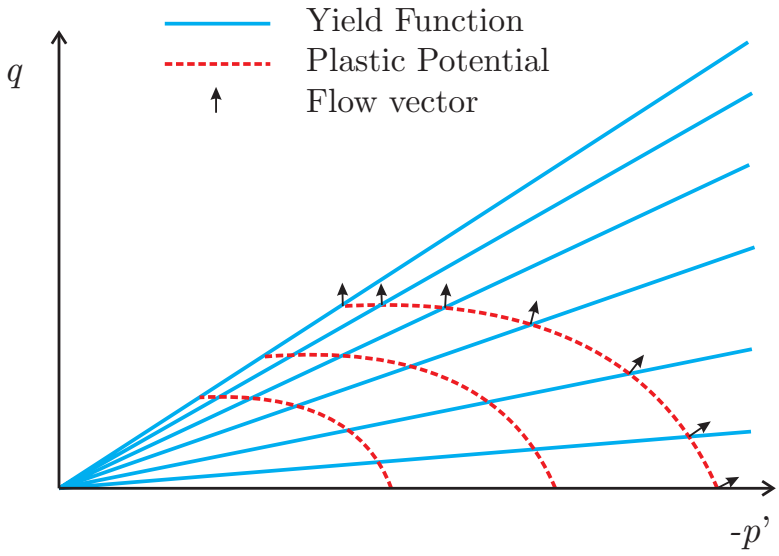

Figure 2.7: Yield loci and plastic potentials for dense Ottawa sand proposed by Poorooshasb et al. [10, 11].

Chapter 3

Critical state plasticity, Part VI: Meso-scale finite element simulation of strain localization in discrete granular materials

This Chapter is published in: R. I. Borja and J. E. Andrade. Critical state plasticity, Part VI: Meso-scale finite element simulation of strain localization in discrete granular materials. *Computer Methods in Applied Mechanics and Engineering*, 2006. In press for the John Argyris Memorial Special Issue.

Abstract

Development of accurate mathematical models of discrete granular material behavior requires a fundamental understanding of deformation and strain localization phenomena. This paper utilizes a meso-scale finite element modeling approach to obtain an accurate and thorough capture of deformation and strain localization processes in discrete granular materials such as sands. We employ critical state theory and implement an elastoplastic constitutive model for granular materials, a variant of a model called "Nor-Sand," allowing for non-associative plastic flow and formulating it in the finite deformation regime. Unlike the previous versions of critical state plasticity models presented in a series of "Cam-Clay"

papers, the present model contains an additional state parameter ψ that allows for a deviation or detachment of the yield surface from the critical state line. Depending on the sign of this state parameter, the model can reproduce plastic compaction as well as plastic dilation in either loose or dense granular materials. Through numerical examples we demonstrate how a structured spatial density variation affects the predicted strain localization patterns in dense sand specimens.

3.1 Introduction

Development of accurate mathematical models of discrete granular material behavior requires a fundamental understanding of the localization phenomena, such as the formation of shear bands in dense sands. For this reason, much experimental work has been conducted to gain a better understanding of the localization process in these materials [4, 15, 78–86]. The subject also has spurred considerable interest in the theoretical and computational modeling fields [19, 87–103]. It is important to recognize that the material response observed in the laboratory is a result of many different micro-mechanical processes, such as mineral particle rolling and sliding in granular soils, micro-cracking in brittle rocks, and mineral particle rotation and translation in the cement matrix of soft rocks. Ideally, any localization model for geomaterials must represent all of these processes. However, current limitations of experimental and mathematical modeling techniques in capturing the evolution in the micro-scale throughout testing have inhibited the use of a micro-mechanical description of the localized deformation behavior.

To circumvent the problems associated with the micro-mechanical modeling approach, a macro-mechanical approach is often used. For soils, this approach pertains to the specimen being considered as a macro-scale element from which the material response may be inferred. The underlying assumption is that the specimen is prepared uniformly and deformed homogeneously enough to allow extraction of the material response from the specimen response. However, it is well known that each specimen is unique, and that two identically prepared samples could exhibit different mechanical responses in the regime of instability even if they had been subjected to the same initially homogeneous deformation field. This implies that the size of a specimen is too large to accurately resolve the macro-scale field, and that it can only capture the strain localization phenomena in a very approximate way.

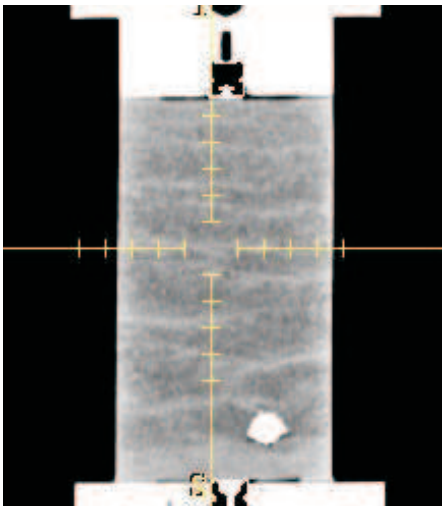

Figure 3.1: Cross-section through a biaxial specimen of silica sand analyzed by X-ray computed tomography; white spot is a piece of gravel.

In this paper, we adopt a more refined approach to investigating strain localization phenomena based on a meso-scale description of the granular material behavior. As a matter of terminology, the term "meso-scale" is used in this paper to refer to a scale larger than the grain scale (particle-scale) but smaller than the element, or specimen, scale (macro-scale). This approach is motivated primarily by the current advances in laboratory testing capabilities that allow accurate measurements of material imperfection in the specimens, such as X-ray Computed Tomography (CT) and Digital Image Processing (DIP) in granular soils [15, 78, 83, 84, 103]. For example, Figure 3.1 shows the result of a CT scan on a biaxial specimen of pure silica sand having a mean grain diameter of 0.5 mm and prepared via air pluviation. The gray level variations in the image indicate differences in the meso-scale local density, with lighter colors indicating regions of higher density (the large white spot in the lower level of the specimen is a piece of gravel). This advanced technology in laboratory testing, combined with DIP to quantitatively transfer the CT results as input into a numerical model, enhances an accurate meso-scale description of granular material behavior and motivates the development of robust meso-scale modeling approaches for replicating the shear banding processes in discrete granular materials.

The modeling approach pursued in this paper utilizes nonlinear continuum mechanics and the finite element method, in combination with a constitutive model based on critical state plasticity that captures both hardening and softening responses depending on the

state of the material at yield. The first plasticity model exhibiting such features that comes to mind is the classical modified Cam-Clay [6, 65, 66, 72, 73, 98, 104, 105]. However, this model may not be robust enough to reproduce the shear banding processes, particularly in sands, since it was originally developed to reproduce the hardening response of soils on the "wet" side of the critical state line, and not the dilative response on the "dry" side where this model poorly replicates the softening behavior necessary to trigger strain localization. To model the strain localization process more accurately, we use an alternative critical state formulation that contains an additional constitutive variable, namely, the state parameter ψ [2, 75, 106]. This parameter determines whether the state point lies below or above the critical state line, as well as enables a complete "detachment" of the yield surface from this line. By "detachment" we mean that the initial position of the critical state line and the state of stress alone do not determine the density of the material. Instead, one needs to specify the spatial variation of void ratio (or specific volume) *in addition* to the state parameters required by the classical Cam-Clay models. Through the state parameter ψ we can now prescribe quantitatively any measured specimen imperfection in the form of initial spatial density variation.

Specifically, we use classical plasticity theory along with a variant of "Nor-Sand" model proposed by Jefferies [2] to describe the constitutive law at the meso-scale level. The main difference between this and the classical Cam-Clay model lies in the description of the evolution of the plastic modulus. In classical Cam-Clay model the character of the plastic modulus depends on the sign of the plastic volumetric strain increment (determined from the flow rule), i.e., it is positive under compaction (hardening), negative under dilation (softening), and is zero at critical state (perfect plasticity). In sandy soils this may not be an accurate representation of hardening/softening responses since a dense sand could exhibit an initially contractive behavior, followed by a dilative behavior, when sheared. This important feature, called phase transformation in the literature [3, 107], cannot be reproduced by classical Cam-Clay models. In the present formulation the growth or collapse of the yield surface is determined by the deviatoric component of the plastic strain increment and by the position of the stress point relative to a so-called limit hardening dilatancy. Such description reproduces more accurately the softening response on the "dry" side of the critical state line.

The theoretical and computational aspects of this paper include the mathematical analyses of the thermodynamics of constitutive models characterized by elastoplastic coupling

[108, 109]. We also describe the numerical implementation of the finite deformation version of the model, the impact of B-bar integration near the critical state, and the localization of deformation on the "dry" side of the critical state line. We present two numerical examples demonstrating the localization of deformation in plane strain and full 3D loading conditions, highlighting in both cases the important role that the spatial density variation plays on the mechanical responses of dense granular materials.

Notations and symbols used in this paper are as follows: bold-faced letters denote tensors and vectors; the symbol '$\cdot$' denotes an inner product of two vectors (e.g. $\boldsymbol{a} \cdot \boldsymbol{b} = a_i b_i$), or a single contraction of adjacent indices of two tensors (e.g. $\boldsymbol{c} \cdot \boldsymbol{d} = c_{ij} d_{jk}$); the symbol ':' denotes an inner product of two second-order tensors (e.g. $\boldsymbol{c} : \boldsymbol{d} = c_{ij} d_{ij}$), or a double contraction of adjacent indices of tensors of rank two and higher (e.g. $\boldsymbol{C} : \boldsymbol{\epsilon}^{\mathrm{e}} = C_{ijkl} \epsilon^{\mathrm{e}}_{kl}$); the symbol '$\otimes$' denotes a juxtaposition, e.g., $(\boldsymbol{a} \otimes \boldsymbol{b})_{ij} = a_i b_j$. Finally, for any symmetric second order tensors $\boldsymbol{\alpha}$ and $\boldsymbol{\beta}$,$(\boldsymbol{\alpha} \otimes \boldsymbol{\beta})_{ijkl} = \alpha_{ij}\beta_{kl}$, $(\boldsymbol{\alpha} \oplus \boldsymbol{\beta})_{ijkl} = \alpha_{jl}\beta_{ik}$, and $(\boldsymbol{\alpha} \ominus \boldsymbol{\beta})_{ijkl} = \alpha_{il}\beta_{jk}$.

3.2 Formulation of the infinitesimal model

We begin by presenting the general features of the meso-scale constitutive model in the infinitesimal regime. Extension of the features to the finite deformation regime is then presented in the next section.

3.2.1 Hyperelastic response

We consider a stored energy density function $\Psi^{\mathrm{e}}(\boldsymbol{\epsilon}^{\mathrm{e}})$ in a granular assembly taken as a continuum; the macroscopic stress $\boldsymbol{\sigma}$ is given by

$$\boldsymbol{\sigma} = \frac{\partial \Psi^{\mathrm{e}}}{\partial \boldsymbol{\epsilon}^{\mathrm{e}}} \tag{3.2.1}$$

where

$$\Psi^{\mathrm{e}} = \widetilde{\Psi}^{\mathrm{e}}(\epsilon^{\mathrm{e}}_{\mathrm{v}}) + \frac{3}{2}\mu^{\mathrm{e}} \epsilon^{\mathrm{e}\,2}_{\mathrm{s}} \tag{3.2.2}$$

and

$$\widetilde{\Psi}(\epsilon^{\mathrm{e}}_{\mathrm{v}}) = -p_0 \widetilde{\kappa} \exp \omega\,, \qquad \omega = -\frac{\epsilon^{\mathrm{e}}_{\mathrm{v}} - \epsilon^{\mathrm{e}}_{\mathrm{v}0}}{\widetilde{\kappa}}\,, \qquad \mu^{\mathrm{e}} = \mu_0 + \frac{\alpha_0}{\widetilde{\kappa}} \widetilde{\Psi}(\epsilon^{\mathrm{e}}_{\mathrm{v}}). \tag{3.2.3}$$

The independent variables are the infinitesimal macroscopic volumetric and deviatoric strain invariants

$$\epsilon_{\mathrm{v}}^{\mathrm{e}} = \mathrm{tr}(\boldsymbol{\epsilon}^{\mathrm{e}})\,, \qquad \epsilon_{\mathrm{s}}^{\mathrm{e}} = \sqrt{\frac{2}{3}}\,\|\boldsymbol{e}^{\mathrm{e}}\|\,, \qquad \boldsymbol{e}^{\mathrm{e}} = \boldsymbol{\epsilon}^{\mathrm{e}} - \frac{1}{3}\epsilon_{\mathrm{v}}^{\mathrm{e}}\mathbf{1}, \tag{3.2.4}$$

where $\boldsymbol{\epsilon}^{\mathrm{e}}$ is the elastic component of the infinitesimal macroscopic strain tensor. The material parameters required for definition are the reference strain $\epsilon_{\mathrm{v0}}^{\mathrm{e}}$ and reference pressure p_0 of the elastic compression curve, as well as the elastic compressibility index $\widetilde{\kappa}$. The above model produces pressure-dependent elastic bulk and shear moduli, in accord with a well-known soil behavioral feature. Equation (3.2.3) results in a constant elastic shear modulus$\mu^{\mathrm{e}} = \mu_0$ when $\alpha_0 = 0$. This model is conservative in the sense that no energy is generated or lost in a closed elastic loading loop [1].

3.2.2 Yield surface, plastic potential function, and flow rule

We consider the first two stress invariants

$$p = \frac{1}{3}\,\mathrm{tr}\,\boldsymbol{\sigma}, \qquad q = \sqrt{\frac{3}{2}}\|\boldsymbol{s}\|, \qquad \boldsymbol{s} = \boldsymbol{\sigma} - p\mathbf{1}, \tag{3.2.5}$$

where $p \leq 0$ in general. We define a yield function F of the form

$$F = q + \eta p, \tag{3.2.6}$$

where

$$\eta = \begin{cases} M\left[1 + \ln\left(p_{\mathrm{i}}/p\right)\right] & \text{if} \quad N = 0; \\ M/N\left[1 - (1-N)\left(p/p_{\mathrm{i}}\right)^{N/(1-N)}\right] & \text{if} \quad N > 0. \end{cases} \tag{3.2.7}$$

Here, $p_{\mathrm{i}} < 0$ is called the "image stress" representing the size of the yield surface, defined such that the stress ratio $\eta = -q/p = M$ when $p = p_{\mathrm{i}}$. A closed-form expression for p_{i} is

$$\frac{p_{\mathrm{i}}}{p} = \begin{cases} \exp(\eta/M - 1) & \text{if} \quad N = 0; \\ [(1-N)/(1-\eta N/M)] & \text{if} \quad N > 0. \end{cases} \tag{3.2.8}$$

The parameter $N \geq 0$ determines the curvature of the yield surface on the hydrostatic axis and typically has a value less than 0.4 for sands [2]; as N increases, the curvature increases. Figure 3.2 shows yield surfaces for different values of N. For comparison, a plot of the conventional elliptical yield surface used in modified Cam-Clay plasticity theory is

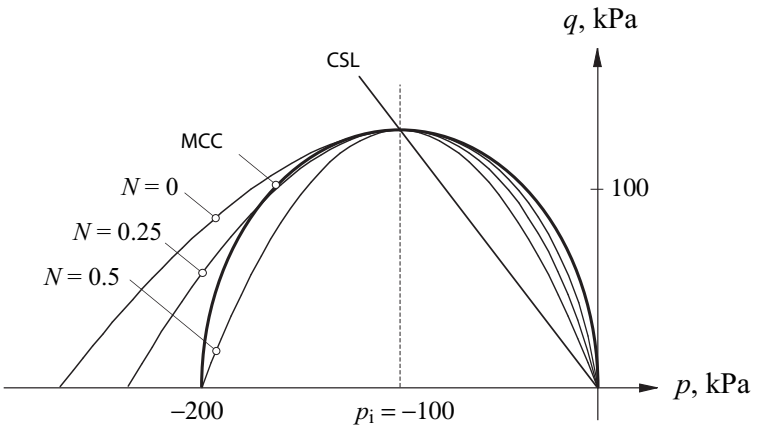

Figure 3.2: Comparison of shapes of critical state yield surfaces.

also shown [65].

Next we consider a plastic potential function of the form

$$Q = q + \overline{\eta} p, \tag{3.2.9}$$

where

$$\overline{\eta} = \begin{cases} M\left[1 + \ln(\overline{p}_{\mathrm{i}}/p)\right] & \text{if} \quad \overline{N} = 0; \\ (M/\overline{N})\left[1 - (1-\overline{N})(p/\overline{p}_{\mathrm{i}})^{\overline{N}/(1-\overline{N})}\right] & \text{if} \quad \overline{N} > 0. \end{cases} \tag{3.2.10}$$

The plastic flow is associative if $\overline{N} = N$ and $\overline{p}_{\mathrm{i}} = p_{\mathrm{i}}$, and non-associative otherwise. For the latter case, we assume that $\overline{N} \leq N$ resulting in a plastic potential function that is 'flatter' than the yield surface (if $\overline{N} < N$), as shown in Figure 3.3. This effectively yields a smaller dilatancy angle than is predicted by the assumption of associative normality, similar in idea to the thermodynamic restriction that the dilatancy angle must be at most equal to the friction angle in Mohr-Coulomb or Drucker-Prager materials, see [110, 111] for further elaboration.

The variable $\overline{p}_{\mathrm{i}}$ is a free parameter that determines the final size of the plastic potential function. If we set $Q = 0$ whenever the stress point (p, q) lies on the yield surface, then $\overline{p}_{\mathrm{i}}$ can be determined as

$$\frac{\overline{p}_{\mathrm{i}}}{p} = \begin{cases} \exp(\overline{\eta}/M - 1) & \text{if} \quad \overline{N} = 0; \\ \left[(1-\overline{N})/(1 - \overline{\eta}\,\overline{N}/M)\right]^{(1-\overline{N})/\overline{N}} & \text{if} \quad \overline{N} > 0. \end{cases} \tag{3.2.11}$$

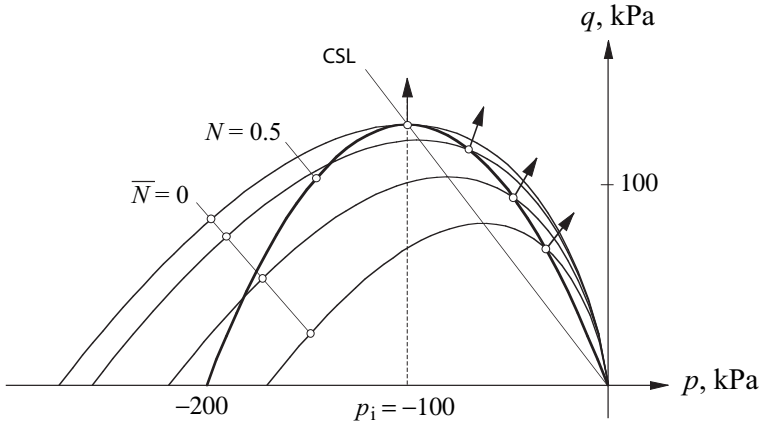

Figure 3.3: Yield function and family of plastic potential surfaces.

The flow rule then writes

$$\dot{\boldsymbol{\epsilon}}^{\mathrm{p}} = \dot{\lambda}\boldsymbol{q}, \qquad \boldsymbol{q} := \frac{\partial Q}{\partial \boldsymbol{\sigma}}, \tag{3.2.12}$$

where $\dot{\lambda} \geq 0$ is a nonegative plastic multiplier, and

$$\boldsymbol{q} = \frac{\partial q}{\partial \boldsymbol{\sigma}} + \overline{\eta}\frac{\partial p}{\partial \boldsymbol{\sigma}} + p\frac{\partial \overline{\eta}}{\partial \boldsymbol{\sigma}} = -\frac{1}{3}\left(\frac{M - \overline{\eta}}{1 - \overline{N}}\right)\mathbf{1} + \sqrt{\frac{3}{2}}\frac{\boldsymbol{s}}{\|\boldsymbol{s}\|}, \qquad \overline{N} \geq 0. \tag{3.2.13}$$

In this case, the variable $\overline{p}_{\mathrm{i}}$ does not have to enter into the formulation since $\overline{\eta}$ can be determined directly from the relation $\overline{\eta} = \eta$.

The first two invariants of $\dot{\boldsymbol{\epsilon}}^{\mathrm{p}}$ are

$$\dot{\epsilon}_{\mathrm{v}}^{\mathrm{p}} = \operatorname{tr}\dot{\boldsymbol{\epsilon}}^{\mathrm{p}} = -\dot{\lambda}\left(\frac{M - \eta}{1 - \overline{N}}\right), \qquad \dot{\epsilon}_{\mathrm{s}}^{\mathrm{p}} = \sqrt{\frac{2}{3}}\,\|\dot{\boldsymbol{e}}^{\mathrm{p}}\| = \dot{\lambda}, \qquad \dot{\boldsymbol{e}}^{\mathrm{p}} = \dot{\boldsymbol{\epsilon}}^{\mathrm{p}} - \frac{1}{3}\dot{\epsilon}_{\mathrm{v}}^{\mathrm{p}}\mathbf{1}. \tag{3.2.14}$$

where $\overline{N} \geq 0$. Note that $\dot{\epsilon}_{\mathrm{v}}^{\mathrm{p}} > 0$ (dilation) whenever $\eta > M$, and $\dot{\epsilon}_{\mathrm{v}}^{\mathrm{p}} < 0$ (compaction) whenever $\eta < M$. Plastic flow is purely isochoric when $\dot{\epsilon}_{\mathrm{v}}^{\mathrm{p}} = 0$, which occurs when $\eta = M$. Furthermore, note that

$$\boldsymbol{f} := \frac{\partial F}{\partial \boldsymbol{\sigma}} = \frac{\partial q}{\partial \boldsymbol{\sigma}} + \eta\frac{\partial p}{\partial \boldsymbol{\sigma}} + p\frac{\partial \eta}{\partial \boldsymbol{\sigma}} = -\frac{1}{3}\left(\frac{M - \eta}{1 - N}\right)\mathbf{1} + \sqrt{\frac{3}{2}}\frac{\boldsymbol{s}}{\|\boldsymbol{s}\|}, \qquad N \geq 0, \tag{3.2.15}$$

Since $\operatorname{tr}\boldsymbol{f} = 0$ whenever $\eta = M$, then plastic flow is always associative at this stress state regardless of the values of $\overline{N}$ and N. Non-associative plastic flow is possible only in the volumetric sense for this two-invariant model.

For perfect plasticity the reduced dissipation inequality requires the stresses to perform nonnegative plastic incremental work [112], i.e.,

$$\mathcal{D}^{\mathrm{p}} = \boldsymbol{\sigma} : \dot{\boldsymbol{\epsilon}}^{\mathrm{p}} = \dot{\lambda}\boldsymbol{\sigma} : \boldsymbol{q} \geq 0. \tag{3.2.16}$$

Using the stress tensor decomposition $\boldsymbol{\sigma} = \boldsymbol{s} + p\mathbf{1}$ and substituting relation (3.2.13) into (3.2.16), we obtain

$$\mathcal{D}^{\mathrm{p}} = -\dot{\lambda}\left(\eta + \frac{M - \overline{\eta}}{1 - \overline{N}}\right) p \geq 0 \qquad \Longrightarrow \qquad \eta + \frac{M - \overline{\eta}}{1 - \overline{N}} \geq 0 \tag{3.2.17}$$

since $p \leq 0$. Now, if the stress point is on the yield surface then (3.2.7) determines the stress ratio η, and (3.2.17) thus becomes

$$-\frac{M\overline{N}}{N}\left[1 - (1 - N)\left(\frac{p}{p_{\mathrm{i}}}\right)^{N/(1-N)}\right] + M \geq 0. \tag{3.2.18}$$

However, $M > 0$ since this is a physical parameter, and so we get

$$\overline{N} \leq N\left[1 - (1 - N)\left(\frac{p}{p_{\mathrm{i}}}\right)^{N/(1-N)}\right]^{-1}. \tag{3.2.19}$$

The expression inside the pair of brackets is equal to unity at the stress space origin when $p = 0$, reduces to N at the image stress point when $\eta = M$ and $p = p_{\mathrm{i}}$, and is zero on the hydrostatic axis when $\eta = 0$ and $p = p_{\mathrm{i}}/(1 - N)^{(1-N)/N}$. The corresponding inverses are equal to unity, $1/N > 1$, and positive infinity, respectively. Hence, for (3.2.19) to remain true at all times, we must have

$$\overline{N} \leq N, \tag{3.2.20}$$

as postulated earlier.

3.2.3 State parameter and plastic dilatancy

In classical Cam-Clay models the image stress p_{i} coincides with a point on the critical state line (CSL), a locus of points characterized by isochoric plastic flow in the space defined by the stress invariants p and q and by the specific volume v. The CSL is given by the pair of

equations

$$q_{\mathrm{c}} = -Mp_{\mathrm{c}}, \qquad v_{\mathrm{c}} = v_{\mathrm{c}0} - \widetilde{\lambda}\ln(-p_{\mathrm{c}}), \tag{3.2.21}$$

where subscript "c" denotes that the point $(v_{\mathrm{c}}, p_{\mathrm{c}}, q_{\mathrm{c}})$ is on the CSL. The parameters are the compressibility index $\widetilde{\lambda}$ and the reference specific volume $v_{\mathrm{c}0}$. Thus, any given point on the yield surface has an associated specific volume, and isochoric plastic flow can only take place on the CSL.

To apply the model to sands, which exhibit different types of volumetric yielding depending on initial density, the yield surface is detached from the critical state line along the v-axis. Thus, the state point (v, p, q) may now lie either above or below the critical specific volume v_{c} at the same stress p depending on whether the sand is looser or denser than critical. Following the notations of [2], a state parameter ψ is introduced to denote the relative distance along the v-axis of the current state point to a point v_{c} on the CSL at the same p,

$$\psi = v - v_{\mathrm{c}}. \tag{3.2.22}$$

Further, a state parameter ψ_{i} is introduced denoting the distance of the same current state point to $v_{\mathrm{c,i}}$ on the CSL at $p = p_{\mathrm{i}}$,

$$\psi_{\mathrm{i}} = v - v_{\mathrm{c,i}}, \qquad v_{\mathrm{c,i}} = v_{\mathrm{c}0} - \widetilde{\lambda}\ln(-p_{\mathrm{i}}), \tag{3.2.23}$$

where $v_{\mathrm{c,i}}$ is the value of v_{c} at the stress p_{i}, and $v_{\mathrm{c}0}$ is the reference value of v_{c} when $p_{\mathrm{i}} = 1$, see (3.2.21). The relation between ψ and ψ_{i} is (see Figure 3.4)

$$\psi_{\mathrm{i}} = \psi + \widetilde{\lambda}\ln\left(\frac{p_{\mathrm{i}}}{p}\right). \tag{3.2.24}$$

Hence, ψ is negative below the CSL and positive above it. An upshot of disconnecting the yield surface from the CSL is that it is no longer possible to locate a state point on the yield surface by prescribing p and q alone; one also needs to specify the state parameter ψ to completely describe the state of a point. Furthermore, isochoric plastic flow does not anymore occur only on the CSL but could also take place at the image stress point. Finally, the parameter ψ_{i} dictates the amount of plastic dilatancy in the case of dense sands.

Formally, plastic dilatancy is defined by the expression

$$D := \dot{\epsilon}^{\mathrm{p}}_{\mathrm{v}}/\dot{\epsilon}^{\mathrm{p}}_{\mathrm{s}} = \frac{\eta - M}{1 - \overline{N}}. \tag{3.2.25}$$

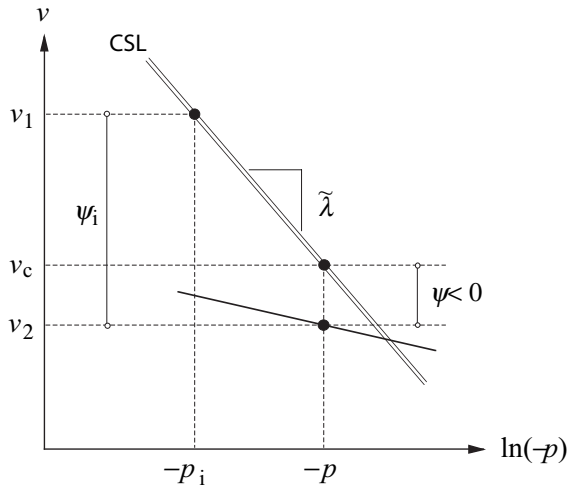

Figure 3.4: Geometric representation of state parameter ψ.

This definition is valid for all possible values of η, even for $\eta = 0$ where Q is not a smooth function. However, experimental evidence on a variety of sands suggests that there exists a maximum possible plastic dilatancy, D^*, which limits a plastic hardening response. The value of D^* depends on the state parameter ψ_i, increasing in value as the state point lies farther and farther away from the CSL on the dense side. An empirical correlation has been established experimentally in [2] between the plastic dilatancy D^* and the state parameter ψ_i, and takes the form

$$D^* = \alpha\psi_i, \tag{3.2.26}$$

where $\alpha \approx -3.5$ typically for most sands. The corresponding value of stress ratio at this limit hardening dilatancy is

$$\eta^* = M + D^*(1 - \overline{N}) = M + \alpha\psi_i(1 - \overline{N}) = M + \overline{\alpha}\psi_i(1 - N), \tag{3.2.27}$$

and the corresponding size of the yield surface is

$$\frac{p_i^*}{p} = \begin{cases} \exp(\overline{\alpha}\psi_i/M) & \text{if} \quad \overline{N} = N = 0; \\ (1 - \overline{\alpha}\psi_i N/M)^{(N-1)/N} & \text{if} \quad 0 \le \overline{N} \le N \ne 0, \end{cases} \tag{3.2.28}$$

where

$$\overline{\alpha}\beta = \alpha, \qquad \beta = \frac{1 - N}{1 - \overline{N}}. \tag{3.2.29}$$

In the above expression we have introduced a non-associativity parameter $\beta \leq 1$, where $\beta = 1$ in the associative case.

3.2.4 Consistency condition and hardening law

For elastoplastic response the standard consistency condition on the yield function F reads

$$\dot{F} = \boldsymbol{f} : \dot{\boldsymbol{\sigma}} - H\dot{\lambda} = 0\,, \qquad \dot{\lambda} > 0, \tag{3.2.30}$$

where H is the plastic modulus given by the equation

$$H = -\frac{1}{\dot{\lambda}}\frac{\partial F}{\partial p_{\mathrm{i}}}\dot{p}_{\mathrm{i}} = -\frac{1}{\dot{\lambda}}\left(\frac{p}{p_{\mathrm{i}}}\right)^{1/(1-N)} M\dot{p}_{\mathrm{i}}. \tag{3.2.31}$$

Since $p/p_{\mathrm{i}} > 0$, the sign of the plastic modulus depends on the sign of $\dot{p}_{\mathrm{i}}$: $H > 0$ if $\dot{p}_{\mathrm{i}} < 0$ (hardening), $H < 0$ if $\dot{p}_{\mathrm{i}} > 0$ (softening), and $H = 0$ if $\dot{p}_{\mathrm{i}} = 0$ (perfect plasticity).

In classical Cam-Clay theory the sign of H depends on the sign of $\dot{\epsilon}^{\mathrm{p}}_{\mathrm{v}}$, i.e., H is positive for compaction and negative for expansion. However, as noted above, this simple criterion does not adequately capture the hardening/softening responses of sands, which are shown to be dependent on the limit hardening plastic dilatancy D^*, i.e., H is positive if $D < D^*$ and negative if $D > D^*$. Thus, any postulated hardening law must satisfy the obvious relationship

$$\operatorname{sgn} H = \operatorname{sgn}(-\dot{p}_{\mathrm{i}}) = \operatorname{sgn}(D^* - D) = \operatorname{sgn}(\eta^* - \eta) = \operatorname{sgn}(p_{\mathrm{i}} - p^*_{\mathrm{i}}), \tag{3.2.32}$$

where 'sgn' is the sign operator. Furthermore, in terms of the cumulative plastic shear strain

$$\epsilon^{\mathrm{p}}_{\mathrm{s}} = \int_t \dot{\epsilon}^{\mathrm{p}}_{\mathrm{s}}\,\mathrm{d}t, \tag{3.2.33}$$

we require that

$$\lim_{\epsilon^{\mathrm{p}}_{\mathrm{s}}\to\infty} H = \lim_{\epsilon^{\mathrm{p}}_{\mathrm{s}}\to\infty} (-\dot{p}_{\mathrm{i}}) = \lim_{\epsilon^{\mathrm{p}}_{\mathrm{s}}\to\infty} (D^* - D) = \lim_{\epsilon^{\mathrm{p}}_{\mathrm{s}}\to\infty} (\eta^* - \eta) = \lim_{\epsilon^{\mathrm{p}}_{\mathrm{s}}\to\infty} (p_{\mathrm{i}} - p^*_{\mathrm{i}}) = 0. \tag{3.2.34}$$

Thus, any postulated hardening law must reflect a condition of perfect plasticity as the plastic shear strain becomes very large. Note that the above restriction is stronger, e.g.,

than the weaker condition $D^* - D = 0$, without the limit, which could occur even if the stress and image points do not coincide. The limiting condition $\epsilon_{\mathrm{s}}^{\mathrm{p}} \to \infty$ insures that the stress and image points approach the CSL, and that these two points coincide in the limit.

A general evolution for $-\dot{p}_{\mathrm{i}}$ satisfying the requirements stated above may be given by an equation of the form

$$-\dot{p}_{\mathrm{i}} = f(p_{\mathrm{i}} - p_{\mathrm{i}}^*)\dot{\epsilon}_{\mathrm{s}}^{\mathrm{p}} = f(p_{\mathrm{i}} - p_{\mathrm{i}}^*)\dot{\lambda}, \tag{3.2.35}$$

where f is a simple odd scalar function of its argument, i.e., $f(-x) = -f(x)$ and $\operatorname{sgn} f = \operatorname{sgn} x$. (Alternately, one can use either D or η in the argument for f). In this case, the expression for the plastic modulus becomes

$$H = M \left(\frac{p}{p_{\mathrm{i}}} \right)^{1/(1-N)} f(p_{\mathrm{i}} - p_{\mathrm{i}}^*). \tag{3.2.36}$$

Taking $f(x) = hx$, where h is a positive dimensionless constant, we arrive at a phenomenological expression of the form similar to that presented in [2],

$$f(p_{\mathrm{i}} - p_{\mathrm{i}}^*) = h(p_{\mathrm{i}} - p_{\mathrm{i}}^*). \tag{3.2.37}$$

This results in a plastic modulus given by the equation

$$H = Mh \left(\frac{p}{p_{\mathrm{i}}} \right)^{1/(1-N)} (p_{\mathrm{i}} - p_{\mathrm{i}}^*). \tag{3.2.38}$$

To summarize, the transition point between hardening and softening responses is represented by the limit hardening dilatancy D^*, which approaches zero on the CSL.

3.2.5 Implications to entropy production

Consider the Helmholtz free energy function $\Psi = \Psi(\boldsymbol{\epsilon}^{\mathrm{e}}, \epsilon_{\mathrm{s}}^{\mathrm{p}})$. For now, we avoid making the usual additive decomposition of the free energy into $\Psi = \Psi^{\mathrm{e}}(\boldsymbol{\epsilon}^{\mathrm{e}}) + \Psi^{\mathrm{p}}(\epsilon_{\mathrm{s}}^{\mathrm{p}})$; in fact, we shall demonstrate that such decomposition is not possible in the present model. Ignoring the non-mechanical powers, the local Clausius-Duhem inequality yields

$$\boldsymbol{\sigma} : \dot{\boldsymbol{\epsilon}} - \frac{\mathrm{d}\Psi}{\mathrm{d}t} \geq 0. \tag{3.2.39}$$

Applying the chain rule for $\mathrm{d}\Psi/\mathrm{d}t$ and invoking the standard Coleman relations results in the constitutive relation

$$\boldsymbol{\sigma} = \frac{\partial \Psi(\boldsymbol{\epsilon}^{\mathrm{e}}, \epsilon_{\mathrm{s}}^{\mathrm{p}})}{\partial \boldsymbol{\epsilon}^{\mathrm{e}}}, \tag{3.2.40}$$

plus the reduced dissipation inequality

$$\boldsymbol{\sigma} : \dot{\boldsymbol{\epsilon}}^{\mathrm{p}} - p_{\mathrm{i}} \dot{\epsilon}_{\mathrm{s}}^{\mathrm{p}} \geq 0\,, \qquad p_{\mathrm{i}} = \frac{\partial \Psi(\boldsymbol{\epsilon}^{\mathrm{e}}, \epsilon_{\mathrm{s}}^{\mathrm{p}})}{\partial \epsilon_{\mathrm{s}}^{\mathrm{p}}}. \tag{3.2.41}$$

Here, we have chosen p_{i} to be the stress-like plastic internal variable conjugate to $\epsilon_{\mathrm{s}}^{\mathrm{p}}$. With an appropriate set of material parameters we have ensured before that $\boldsymbol{\sigma} : \dot{\boldsymbol{\epsilon}}^{\mathrm{p}} \geq 0$ (see Sec. 3.2.2). Since $\dot{\epsilon}_{\mathrm{s}}^{\mathrm{p}} = \dot{\lambda} \geq 0$ and $p_{\mathrm{i}} < 0$, the reduced dissipation inequality as written above holds provided that

$$\frac{\partial \Psi(\boldsymbol{\epsilon}^{\mathrm{e}}, \epsilon_{\mathrm{s}}^{\mathrm{p}})}{\partial \epsilon_{\mathrm{s}}^{\mathrm{p}}} \leq 0. \tag{3.2.42}$$

Now, consider the evolution for p_{i} as postulated in (3.2.35). Integrating in time yields

$$\frac{\partial \Psi(\boldsymbol{\epsilon}^{\mathrm{e}}, \epsilon_{\mathrm{s}}^{\mathrm{p}})}{\partial \epsilon_{\mathrm{s}}^{\mathrm{p}}} \equiv p_{\mathrm{i}} = p_{\mathrm{i}0} - \int_{\epsilon_{\mathrm{s}0}^{\mathrm{p}}}^{\epsilon_{\mathrm{s}}^{\mathrm{p}}} f(p_{\mathrm{i}} - p_{\mathrm{i}}^{*})\, \mathrm{d}\epsilon_{\mathrm{s}}^{\mathrm{p}}, \tag{3.2.43}$$

where $p_{\mathrm{i}0}$ is the reference value of p_{i} when $\epsilon_{\mathrm{s}}^{\mathrm{p}} = \epsilon_{\mathrm{s}0}^{\mathrm{p}}$. Recalling that f is a simple odd function, the right-hand side of the above equation is negative provided that $\operatorname{sgn}(p_{\mathrm{i}} - p_{\mathrm{i}}^{*}) = \operatorname{sgn} H =$ positive. This implies that the reduced dissipation inequality is identically satisfied in the hardening regime.

Integrating once more gives a more definitive form of the Helmholtz free energy,

$$\Psi(\boldsymbol{\epsilon}^{\mathrm{e}}, \epsilon_{\mathrm{s}}^{\mathrm{p}}) = \int_{\epsilon_{\mathrm{s}0}^{\mathrm{p}}}^{\epsilon_{\mathrm{s}}^{\mathrm{p}}} p_{\mathrm{i}0}\, \mathrm{d}\epsilon_{\mathrm{s}}^{\mathrm{p}} - \int_{\epsilon_{\mathrm{s}0}^{\mathrm{p}}}^{\epsilon_{\mathrm{s}}^{\mathrm{p}}} \int_{\epsilon_{\mathrm{s}0}^{\mathrm{p}}}^{\epsilon_{\mathrm{s}}^{\mathrm{p}}} f(p_{\mathrm{i}} - p_{\mathrm{i}}^{*})\, \mathrm{d}\epsilon_{\mathrm{s}}^{\mathrm{p}} \mathrm{d}\epsilon_{\mathrm{s}}^{\mathrm{p}} + \Psi^{\mathrm{e}}(\boldsymbol{\epsilon}^{\mathrm{e}}) + \Psi_0, \tag{3.2.44}$$

where $\Psi^{\mathrm{e}}(\boldsymbol{\epsilon}^{\mathrm{e}})$ is the usual elastic stored energy function. The first two integrals represent the plastic component of the free energy,

$$\Psi^{\mathrm{p}} = \Psi^{\mathrm{p}}(\boldsymbol{\epsilon}^{\mathrm{e}}, \epsilon_{\mathrm{s}}^{\mathrm{p}}) = \int_{\epsilon_{\mathrm{s}0}^{\mathrm{p}}}^{\epsilon_{\mathrm{s}}^{\mathrm{p}}} p_{\mathrm{i}0}\, \mathrm{d}\epsilon_{\mathrm{s}}^{\mathrm{p}} - \int_{\epsilon_{\mathrm{s}0}^{\mathrm{p}}}^{\epsilon_{\mathrm{s}}^{\mathrm{p}}} \int_{\epsilon_{\mathrm{s}0}^{\mathrm{p}}}^{\epsilon_{\mathrm{s}}^{\mathrm{p}}} f(p_{\mathrm{i}} - p_{\mathrm{i}}^{*})\, \mathrm{d}\epsilon_{\mathrm{s}}^{\mathrm{p}} \mathrm{d}\epsilon_{\mathrm{s}}^{\mathrm{p}}. \tag{3.2.45}$$

Note in this case that Ψ^{p} depends not only on $\epsilon_{\mathrm{s}}^{\mathrm{p}}$ but also on $\boldsymbol{\epsilon}^{\mathrm{e}}$ through the variable p_{i}^{*}.

The Cauchy stress tensor then becomes

$$\boldsymbol{\sigma} = \frac{\partial \Psi^{\mathrm{e}}(\boldsymbol{\epsilon}^{\mathrm{e}})}{\partial \boldsymbol{\epsilon}^{\mathrm{e}}} + \underbrace{\int_{\epsilon_{\mathrm{s0}}^{\mathrm{p}}}^{\epsilon_{\mathrm{s}}^{\mathrm{p}}} \int_{\epsilon_{\mathrm{s0}}^{\mathrm{p}}}^{\epsilon_{\mathrm{s}}^{\mathrm{p}}} f'(p_{\mathrm{i}} - p_{\mathrm{i}}^*) \frac{\partial p_{\mathrm{i}}^*}{\partial \boldsymbol{\epsilon}^{\mathrm{e}}} \, \mathrm{d}\epsilon_{\mathrm{s}}^{\mathrm{p}} \mathrm{d}\epsilon_{\mathrm{s}}^{\mathrm{p}}}_{\mathrm{O}(\Delta \epsilon_{\mathrm{s}}^{\mathrm{p}\,2})} , \tag{3.2.46}$$

where $\Delta\epsilon_{\mathrm{s}}^{\mathrm{p}} = \epsilon_{\mathrm{s}}^{\mathrm{p}} - \epsilon_{\mathrm{s0}}^{\mathrm{p}}$, and

$$\frac{\partial p_{\mathrm{i}}^*}{\partial \boldsymbol{\epsilon}^{\mathrm{e}}} = (1 - N) \frac{\overline{\alpha} p_{\mathrm{i}}^* / M}{1 - \overline{\alpha} \psi_{\mathrm{i}} N / M} \frac{\partial \psi_{\mathrm{i}}}{\partial \boldsymbol{\epsilon}^{\mathrm{e}}} + \frac{p_{\mathrm{i}}^*}{p} \frac{\partial p}{\partial \boldsymbol{\epsilon}^{\mathrm{e}}}, \qquad N \geq 0. \tag{3.2.47}$$

Strictly, then, the Cauchy stress tensor depends not only on $\boldsymbol{\epsilon}^{\mathrm{e}}$ but also on $\epsilon_{\mathrm{s}}^{\mathrm{p}}$. Attempts have been made in the past to capture this dependence of $\boldsymbol{\sigma}$ on $\epsilon_{\mathrm{s}}^{\mathrm{p}}$; for example, a nonlinear elasticity model in which the elastic shear modulus varies with a stress-like plastic internal variable similar to p_{i} has been proposed in [109, 113]. However, these developments have not gained much acceptance in the literature due, primarily, to the lack of experimental data and to the difficulty with obtaining such test data.

It must be noted that the observed dependence of Ψ^{p} on the elastic strain $\boldsymbol{\epsilon}^{\mathrm{e}}$ occurs only prior to reaching the critical state where $\Delta\epsilon_{\mathrm{s}}^{\mathrm{p}}$ remains "relatively small," and thus, the second-order term in (3.2.46) may be ignored (such as done in Sec. 3.2.1). Most of the intense shearing (i.e., large $\Delta\epsilon_{\mathrm{s}}^{\mathrm{p}}$) in fact occurs at the critical state where $f(p_{\mathrm{i}} - p_{\mathrm{i}}^*) = 0$, at which condition the additive decomposition of the free energy into $\Psi^{\mathrm{e}}(\boldsymbol{\epsilon}^{\mathrm{e}})$ and $\Psi^{\mathrm{p}}(\epsilon_{\mathrm{s}}^{\mathrm{p}})$ holds, see (3.2.44).

3.2.6 Numerical implementation

Even though the plastic internal variable p_{i} depends on the state parameter ψ_{i}, and that this variable is deeply embedded in the plastic modulus H, the model is still amenable to fully implicit numerical integration. Table 3.1 summarizes the relevant rate equations used in the constitutive theory. Table 3.2 summarizes the algorithmic counterpart utilizing the classical return mapping scheme. For improved efficiency, the return mapping algorithm in Table 3.2 is performed in the strain invariant space, as demonstrated below, leading to a system of nonlinear equations with three unknowns. As usual, it is assumed that $\Delta\boldsymbol{\epsilon}$ is given, which implies that both the elastic trial strain $\boldsymbol{\epsilon}^{\mathrm{e\,tr}}$ and the total strain $\boldsymbol{\epsilon}$ are known. Note that v_0 is the initial value of the specific volume at the beginning of the calculations when $\boldsymbol{\epsilon} = \mathbf{0}$, and should not be confused with v_{c0}. As usual, the main goal is to find the

Table 3.1: Summary of rate equations for plasticity model for sands, infinitesimal deformation version.

1. Strain rates: $\dot{\boldsymbol{\epsilon}} = \dot{\boldsymbol{\epsilon}}^{\mathrm{e}} + \dot{\boldsymbol{\epsilon}}^{\mathrm{p}}$
2. Hyperelastic rate equations: $\dot{\boldsymbol{\sigma}} = \mathbf{c}^{\mathrm{e}} : \dot{\boldsymbol{\epsilon}}^{\mathrm{e}}; \quad \mathbf{c}^{\mathrm{e}} = \partial^2 \Psi^{\mathrm{e}} / \partial \boldsymbol{\epsilon}^{\mathrm{e}} \partial \boldsymbol{\epsilon}^{\mathrm{e}}$
3. Flow rule: $\dot{\boldsymbol{\epsilon}}^{\mathrm{p}} = \dot{\lambda} \boldsymbol{q}$
4. State parameter: $\dot{\psi}_{\mathrm{i}} = \dot{v} + \widetilde{\lambda} \dot{p}_{\mathrm{i}} / p_{\mathrm{i}}$ from (3.2.23)
5. Hardening law: $-\dot{p}_{\mathrm{i}} = f(p_{\mathrm{i}} - p_{\mathrm{i}}^*)\dot{\lambda}$ from (3.2.35)
6. Consistency condition: $\boldsymbol{f} : \dot{\boldsymbol{\sigma}} - H\dot{\lambda} = 0$
7. Kuhn-Tucker conditions: $\dot{\lambda} \geq 0, \quad F \leq 0, \quad \dot{\lambda} F = 0$

final stresses $\boldsymbol{\sigma}$ and the discrete plastic multiplier $\Delta\lambda$ for a given strain increment $\Delta\boldsymbol{\epsilon}$. Following [66, 111], consider the following local residual equations generated by the applied strain increment $\Delta\boldsymbol{\epsilon}$

$$\boldsymbol{r} = \boldsymbol{r}(\boldsymbol{x}) = \left\{ \begin{array}{c} \epsilon_{\mathrm{v}}^{\mathrm{e}} - \epsilon_{\mathrm{v}}^{\mathrm{e\,tr}} + \Delta\lambda\beta\partial_p F \\ \epsilon_{\mathrm{s}}^{\mathrm{e}} - \epsilon_{\mathrm{s}}^{\mathrm{e\,tr}} + \Delta\lambda\partial_q F \\ F \end{array} \right\}; \qquad \boldsymbol{x} = \left\{ \begin{array}{c} \epsilon_{\mathrm{v}}^{\mathrm{e}} \\ \epsilon_{\mathrm{s}}^{\mathrm{e}} \\ \Delta\lambda \end{array} \right\} \tag{3.2.48}$$

where β is the non-associativity parameter defined in (3.2.29). The goal is to dissipate the residual vector $\boldsymbol{r}$ by finding the solution vector $\boldsymbol{x}^*$ using a local Newton iteration.

In developing the local Jacobian matrix $\boldsymbol{r}'(\boldsymbol{x})$ used for Newton iteration, it is convenient to define the following mapping induced by the numerical algorithm

$$\boldsymbol{y} = \left\{ \begin{array}{c} p \\ q \\ p_{\mathrm{i}} \end{array} \right\} = \left\{ \begin{array}{c} p(\epsilon_{\mathrm{v}}^{\mathrm{e}}, \epsilon_{\mathrm{s}}^{\mathrm{e}}) \\ q(\epsilon_{\mathrm{v}}^{\mathrm{e}}, \epsilon_{\mathrm{s}}^{\mathrm{e}}) \\ p_{\mathrm{i}}(\epsilon_{\mathrm{v}}^{\mathrm{e}}, \epsilon_{\mathrm{s}}^{\mathrm{e}}, \Delta\lambda) \end{array} \right\} \qquad \Longrightarrow \qquad \boldsymbol{y} = \boldsymbol{y}(\boldsymbol{x}) \tag{3.2.49}$$

The tangent $\boldsymbol{y}'(\boldsymbol{x}) = \boldsymbol{D}$ defines the slope, given by

$$\boldsymbol{D} = \left[\begin{array}{ccc} D_{11} & D_{12} & D_{13} \\ D_{21} & D_{22} & D_{23} \\ D_{31} & D_{32} & D_{33} \end{array} \right] = \left[\begin{array}{ccc} \partial_{\epsilon_{\mathrm{v}}^{\mathrm{e}}} p & \partial_{\epsilon_{\mathrm{s}}^{\mathrm{e}}} p & 0 \\ \partial_{\epsilon_{\mathrm{v}}^{\mathrm{e}}} q & \partial_{\epsilon_{\mathrm{s}}^{\mathrm{e}}} q & 0 \\ \partial_{\epsilon_{\mathrm{v}}^{\mathrm{e}}} p_{\mathrm{i}} & \partial_{\epsilon_{\mathrm{s}}^{\mathrm{e}}} p_{\mathrm{i}} & \partial_{\Delta\lambda} p_{\mathrm{i}} \end{array} \right]. \tag{3.2.50}$$

Table 3.2: Return mapping algorithm for plasticity model for sands, infinitesimal deformation version.

1. Elastic strain predictor: $\boldsymbol{\epsilon}^{\mathrm{e\,tr}} = \boldsymbol{\epsilon}^{\mathrm{e}}_n + \Delta\boldsymbol{\epsilon}$
2. Elastic stress predictor: $\boldsymbol{\sigma}^{\mathrm{tr}} = \partial\Psi^{\mathrm{e}}/\partial\boldsymbol{\epsilon}^{\mathrm{e\,tr}}$; $\quad p_{\mathrm{i}}^{\mathrm{tr}} = p_{\mathrm{i},n}$
3. Check if yielding: $F\left(\boldsymbol{\sigma}^{\mathrm{tr}}, p_{\mathrm{i}}^{\mathrm{tr}}\right) \geq 0$?
   No, set $\boldsymbol{\epsilon}^{\mathrm{e}} = \boldsymbol{\epsilon}^{\mathrm{e\,tr}}$; $\quad \boldsymbol{\sigma} = \boldsymbol{\sigma}^{\mathrm{tr}}$; $\quad p_{\mathrm{i}} = p_{\mathrm{i}}^{\mathrm{tr}}$ and exit
4. Yes, initialize $\Delta\lambda = 0$ and iterate for $\Delta\lambda$ (steps 5–7)
5. Plastic corrector: $\boldsymbol{\epsilon}^{\mathrm{e}} = \boldsymbol{\epsilon}^{\mathrm{e\,tr}} - \Delta\lambda\boldsymbol{q}$, $\quad \boldsymbol{\sigma} = \partial\Psi^{\mathrm{e}}/\partial\boldsymbol{\epsilon}^{\mathrm{e}}$
6. Update plastic internal variable p_{i}:
   (a) Cumulative strain: $\boldsymbol{\epsilon} = \boldsymbol{\epsilon}_n + \Delta\boldsymbol{\epsilon}$
   (b) Specific volume: $v = v_0(1 + \operatorname{tr}\boldsymbol{\epsilon})$
   (c) Initialize $p_{\mathrm{i}} = p_{\mathrm{i},n}$ and iterate for p_{i} (steps 6d-f)
      (d) State parameter: $\psi_{\mathrm{i}} = v - v_{\mathrm{c}0} + \widetilde{\lambda}\ln(-p_{\mathrm{i}})$
      (e) Limit hardening plastic variable:
$$p_{\mathrm{i}}^{*} = p \times \begin{cases} \exp\left(\overline{\alpha}\psi_{\mathrm{i}}/M\right) & \text{if} \quad \overline{N} = N = 0, \\ \left(1 - \overline{\alpha}\psi_{\mathrm{i}}N/M\right)^{(N-1)/N} & \text{if} \quad 0 \leq \overline{N} \leq N \neq 0. \end{cases}$$
      (f) Plastic internal variable: $p_{\mathrm{i}} = p_{\mathrm{i},n} - f(p_{\mathrm{i}} - p_{\mathrm{i}}^{*})\Delta\lambda$
7. Discrete consistency condition: $F\left(p, q, p_{\mathrm{i}}\right) = 0$

The hyperelastic equations take the following form independent of the discrete plastic multiplier $\Delta\lambda$ (and hence, $D_{13} = D_{23} = 0$)

$$p = p_0 \exp\,\omega \left[1 + \frac{3\alpha_0}{2\widetilde{\kappa}} \epsilon_{\rm s}^{\rm e\,2}\right], \qquad q = 3(\mu_0 - \alpha_0 p_0 \exp\omega)\epsilon_{\rm s}^{\rm e}. \tag{3.2.51}$$

Thus,

$$\begin{aligned} D_{11} &= -\frac{p_0}{\widetilde{\kappa}} \exp\,\omega \left[1 + \frac{3\alpha_0}{2\widetilde{\kappa}}\,\epsilon_{\rm s}^{\rm e\,2}\right], \\ D_{22} &= 3\mu_0 - 3\alpha_0 p_0 \exp\,\omega, \\ D_{12} &= D_{21} = \frac{3p_0\alpha_0\epsilon_{\rm s}^{\rm e}}{\widetilde{\kappa}} \exp\,\omega. \end{aligned} \tag{3.2.52}$$

We recall that $D_{21} = D_{12}$ from the postulated existence of an elastic stored energy function $\Psi^{\rm e}$.

The plastic internal variable $p_{\rm i}$ is deeply embedded in the evolution equations and is best calculated iteratively, as shown in Table 3.2. First, from Step No. 6(f), we construct a scalar residual equation

$$r(p_{\rm i}) = p_{\rm i} - p_{{\rm i},n} + f(p_{\rm i} - p_{\rm i}^*)\Delta\lambda, \tag{3.2.53}$$

where $p_{\rm i}^*$ is calculated in succession from Step No. 6(e,d) of Table 3.2 using the current estimate for $p_{\rm i}$. Using a sub-local Newton iteration, we determine the root that dissipates this residual iteratively. The sub-local scalar tangent operator takes the simple form

$$r'(p_{\rm i}) = 1 + f'(p_{\rm i} - p_{\rm i}^*)\Delta\lambda \left[1 - \frac{\widetilde{\lambda}\overline{\alpha}(1-N)}{M - \overline{\alpha}\psi_{\rm i} N}\left(\frac{p_{\rm i}^*}{p_{\rm i}}\right)\right], \qquad N \geq 0. \tag{3.2.54}$$

Having determined the converged value of $p_{\rm i}$, we can then calculate the corresponding values of $\psi_{\rm i}$ and $p_{\rm i}^*$ and proceed with the following differentiation.

From Table 3.2, Step No. 6(f), we obtain the variation

$$\frac{\partial p_{\rm i}}{\partial \epsilon_{\rm v}^{\rm e}} = -f'(p_{\rm i} - p_{\rm i}^*)\Delta\lambda \left(\frac{\partial p_{\rm i}}{\partial \epsilon_{\rm v}^{\rm e}} - \frac{\partial p_{\rm i}^*}{\partial \epsilon_{\rm v}^{\rm e}}\right). \tag{3.2.55}$$

From Step No. 6(e), we get

$$\frac{\partial p_{\rm i}^*}{\partial \epsilon_{\rm v}^{\rm e}} = \left(\overline{\alpha} p_{\rm i}^* \frac{1-N}{M - \overline{\alpha}\psi_{\rm i} N}\right)\frac{\partial \psi_{\rm i}}{\partial \epsilon_{\rm v}^{\rm e}} + \frac{p_{\rm i}^*}{p} D_{11}, \qquad N \geq 0. \tag{3.2.56}$$

From Step No. 6(d), we obtain

$$\frac{\partial \psi_{\rm i}}{\partial \epsilon_{\rm v}^{\rm e}} = \frac{\widetilde{\lambda}}{p_{\rm i}} \frac{\partial p_{\rm i}}{\partial \epsilon_{\rm v}^{\rm e}}. \tag{3.2.57}$$

Combining these last three equations gives

$$\begin{aligned} D_{31} &= \frac{\partial p_{\rm i}}{\partial \epsilon_{\rm v}^{\rm e}} = c^{-1} f'(p_{\rm i} - p_{\rm i}^*) \Delta\lambda \left(\frac{p_{\rm i}^*}{p}\right) D_{11}; \\ c &= 1 + f'(p_{\rm i} - p_{\rm i}^*) \Delta\lambda \left[1 - \frac{\widetilde{\lambda}\overline{\alpha}(1-N)}{M - \overline{\alpha}\psi_{\rm i} N} \left(\frac{p_{\rm i}^*}{p_{\rm i}}\right)\right]. \end{aligned} \tag{3.2.58}$$

Note that c is the converged value of $r'(p_{\rm i})$ when $r = 0$, cf. (3.2.54). Following a similar procedure, we obtain

$$D_{32} = \frac{\partial p_{\rm i}}{\partial \epsilon_{\rm s}^{\rm e}} = c^{-1} f'(p_{\rm i} - p_{\rm i}^*) \Delta\lambda \left(\frac{p_{\rm i}^*}{p}\right) D_{12}. \tag{3.2.59}$$

Again, using the same implicit differentiation, we get

$$D_{33} = \frac{\partial p_{\rm i}}{\partial \Delta\lambda} = -c^{-1} f(p_{\rm i} - p_{\rm i}^*). \tag{3.2.60}$$

For the hardening law adopted in [2], $f'(p_{\rm i} - p_{\rm i}^*)$ reduces to the constant h.

It is also convenient to define the following vector operator

$$\boldsymbol{H} = \left[\begin{array}{ccc} H_1 & H_2 & H_3 \end{array}\right] = \left[\begin{array}{ccc} \partial^2_{pp} & \partial^2_{pq} & \partial^2_{pp_{\rm i}} \end{array}\right] F. \tag{3.2.61}$$

For the yield function at hand, the elements of $\boldsymbol{H}$ are as follows. First, we obtain the first derivatives

$$\begin{aligned} \frac{\partial F}{\partial p} &= \begin{cases} M \ln(p_{\rm i}/p) & \text{if} \quad N = 0, \\ (M/N)[1 - (p/p_{\rm i})^{N/(1-N)}] & \text{if} \quad N > 0, \end{cases} \\ \frac{\partial F}{\partial q} &= 1, \qquad \frac{\partial F}{\partial p_{\rm i}} = M \left(\frac{p}{p_{\rm i}}\right)^{1/(1-N)}, \qquad N \geq 0. \end{aligned} \tag{3.2.62}$$

Then, for $N \geq 0$, we have

$$H_1 = -\frac{1}{1-N} \frac{M}{p} \left(\frac{p}{p_{\rm i}}\right)^{N/(1-N)}, \qquad H_2 = 0, \qquad H_3 = \frac{1}{1-N} \frac{M}{p} \left(\frac{p}{p_{\rm i}}\right)^{1/(1-N)}. \tag{3.2.63}$$

Finally, from the product formula induced by the chain rule, we define the vector operator $\boldsymbol{G}$,

$$\boldsymbol{G} = \boldsymbol{H}\boldsymbol{D} = \left[\begin{array}{ccc} G_1 & G_2 & G_3 \end{array} \right]. \tag{3.2.64}$$

The algorithmic local tangent operator for Newton iteration is then given by

$$\begin{aligned} \boldsymbol{r}'(\boldsymbol{x}) \quad &= \\ &\left[\begin{array}{ccc} 1 + \Delta\lambda\beta G_1 & \Delta\lambda\beta G_2 & \beta(\partial_p F + \Delta\lambda G_3) \\ 0 & 1 & \partial_q F \\ (D_{11}\partial_p + D_{21}\partial_q + D_{31}\partial_{p_\mathrm{i}})F & (D_{12}\partial_p + D_{22}\partial_q + D_{32}\partial_{p_\mathrm{i}})F & D_{33}\partial_{p_\mathrm{i}} F \end{array} \right]. \end{aligned} \tag{3.2.65}$$

Remark 1. The numerical algorithm described above entails two levels of nested Newton iterations to determine the local unknowns. An alternative approach would be to consider p_i as a fourth local unknown, along with $\epsilon_\mathrm{v}^\mathrm{e}$, $\epsilon_\mathrm{s}^\mathrm{e}$ and $\Delta\lambda$, and solve them all iteratively in one single Newton loop. We have found that either approach works well for the problem at hand, and that either one demonstrates about the same computational efficiency.

3.2.7 Algorithmic tangent operator

The algorithmic tangent operator $\mathbf{c} = \partial\boldsymbol{\sigma}/\partial\boldsymbol{\epsilon}^{\mathrm{e\,tr}} \equiv \partial\boldsymbol{\sigma}/\partial\boldsymbol{\epsilon}$ is used for the global Newton iteration of the finite element problem. It has been shown in [43, 114] that it can also be used in lieu of the theoretically correct elastoplastic constitutive operator $\mathbf{c}^{\mathrm{ep}}$ for detecting the onset of material instability, provided the step size is 'small.' To derive the algorithmic tangent operator, consider the following expression for the Cauchy stress tensor

$$\boldsymbol{\sigma} = p\mathbf{1} + \sqrt{\frac{2}{3}} q\widehat{\boldsymbol{n}}, \tag{3.2.66}$$

where $\widehat{\boldsymbol{n}} = \boldsymbol{s}/\|\boldsymbol{s}\| = \boldsymbol{e}^\mathrm{e}/\|\boldsymbol{e}^\mathrm{e}\| = \boldsymbol{e}^{\mathrm{e\,tr}}/\|\boldsymbol{e}^{\mathrm{e\,tr}}\|$ from the co-axiality of the principal directions. The chain rule then yields (see [66])

$$\begin{aligned} \mathbf{c} = \frac{\partial\boldsymbol{\sigma}}{\partial\boldsymbol{\epsilon}} \quad &= \quad \mathbf{1} \otimes \left(D_{11}\frac{\partial\epsilon_\mathrm{v}^\mathrm{e}}{\partial\boldsymbol{\epsilon}} + D_{12}\frac{\partial\epsilon_\mathrm{s}^\mathrm{e}}{\partial\boldsymbol{\epsilon}} \right) + \sqrt{\frac{2}{3}}\widehat{\boldsymbol{n}} \otimes \left(D_{21}\frac{\partial\epsilon_\mathrm{v}^\mathrm{e}}{\partial\boldsymbol{\epsilon}} + D_{22}\frac{\partial\epsilon_\mathrm{s}^\mathrm{e}}{\partial\boldsymbol{\epsilon}} \right) \\ &+ \quad \frac{2q}{3\epsilon_\mathrm{s}^{\mathrm{e\,tr}}} \left(\boldsymbol{I} - \frac{1}{3}\mathbf{1} \otimes \mathbf{1} - \widehat{\boldsymbol{n}} \otimes \widehat{\boldsymbol{n}} \right), \end{aligned} \tag{3.2.67}$$

where $\boldsymbol{I}$ is the fourth-rank identity tensor with components $I_{ijkl} = (\delta_{ik}\delta_{jl} + \delta_{il}\delta_{jk})/2$. Our goal is to obtain closed-form expressions for the derivatives $\partial\epsilon_{\mathrm{v}}^{\mathrm{e}}/\partial\boldsymbol{\epsilon}$ and $\partial\epsilon_{\mathrm{s}}^{\mathrm{e}}/\partial\boldsymbol{\epsilon}$.

Using the same strain invariant formulation of the previous section, we now write the same local residual vector as $\boldsymbol{r} = \boldsymbol{r}(\epsilon_{\mathrm{v}}^{\mathrm{e\,tr}}, \epsilon_{\mathrm{s}}^{\mathrm{e\,tr}}, \boldsymbol{x})$, where $\boldsymbol{x}$ is the vector of local unknowns. We recall that the trial elastic strains were held fixed at the local level; however, at the global level they themselves are now the iterates. Consequently, at the converged state where $\boldsymbol{r} = \boldsymbol{0}$, we now write the strain derivatives of the residual vector as

$$\frac{\partial \boldsymbol{r}}{\partial \boldsymbol{\epsilon}} = \left.\frac{\partial \boldsymbol{r}}{\partial \boldsymbol{\epsilon}}\right|_x + \left(\left.\frac{\partial \boldsymbol{r}}{\partial \boldsymbol{x}}\right|_{\epsilon_{\mathrm{v}}^{\mathrm{e\,tr}}, \epsilon_{\mathrm{s}}^{\mathrm{e\,tr}}} \right) \cdot \frac{\partial \boldsymbol{x}}{\partial \boldsymbol{\epsilon}} = \boldsymbol{0}, \tag{3.2.68}$$

which gives

$$\boldsymbol{a} \cdot \frac{\partial \boldsymbol{x}}{\partial \boldsymbol{\epsilon}} = -\left.\frac{\partial \boldsymbol{r}}{\partial \boldsymbol{\epsilon}}\right|_x \qquad \Longrightarrow \qquad \frac{\partial \boldsymbol{x}}{\partial \boldsymbol{\epsilon}} = -\boldsymbol{b} \cdot \left.\frac{\partial \boldsymbol{r}}{\partial \boldsymbol{\epsilon}}\right|_x . \tag{3.2.69}$$

We recognize $\boldsymbol{a}$ as the same 3×3 tangent matrix $\boldsymbol{r}'(\boldsymbol{x})$ in (3.2.65) evaluated *at the locally converged state*, and $\boldsymbol{b} = \boldsymbol{a}^{-1}$. In component form, we have

$$\left\{ \begin{array}{c} \partial\epsilon_{\mathrm{v}}^{\mathrm{e}}/\partial\boldsymbol{\epsilon} \\ \partial\epsilon_{\mathrm{s}}^{\mathrm{e}}/\partial\boldsymbol{\epsilon} \\ \partial\Delta\lambda/\partial\boldsymbol{\epsilon} \end{array} \right\} = \left[\begin{array}{ccc} b_{11} & b_{12} & b_{13} \\ b_{21} & b_{22} & b_{23} \\ b_{31} & b_{32} & b_{33} \end{array} \right] = \left\{ \begin{array}{c} (1 - \Delta\lambda\beta\theta H_3)\boldsymbol{1} \\ \sqrt{2/3}\widehat{\boldsymbol{n}} \\ -\theta\partial_{p_{\mathrm{i}}} F \boldsymbol{1} \end{array} \right\}, \tag{3.2.70}$$

in which $\partial p_{\mathrm{i}}/\partial\boldsymbol{\epsilon} = \theta\boldsymbol{1}$, and

$$\theta = c^{-1}\Delta\lambda f'(p_{\mathrm{i}} - p_{\mathrm{i}}^*) v_0 p_{\mathrm{i}}^* \frac{\overline{\alpha}(1-N)}{M - \overline{\alpha}\psi_{\mathrm{i}} N}, \tag{3.2.71}$$

is the linearization of the term associated with the state parameter ψ_{i}. This facilitates the solution of the desired strain derivatives,

$$\frac{\partial \epsilon_{\mathrm{v}}^{\mathrm{e}}}{\partial \boldsymbol{\epsilon}} = \widetilde{b}_{11}\boldsymbol{1} + \sqrt{\frac{2}{3}}\, b_{12}\widehat{\boldsymbol{n}}, \qquad \frac{\partial \epsilon_{\mathrm{s}}^{\mathrm{e}}}{\partial \boldsymbol{\epsilon}} = \widetilde{b}_{21}\boldsymbol{1} + \sqrt{\frac{2}{3}}\, b_{22}\widehat{\boldsymbol{n}}, \tag{3.2.72}$$

where

$$\begin{aligned} \widetilde{b}_{11} &= (1 - \Delta\lambda\beta\theta H_3) b_{11} - (\theta\partial_{p_{\mathrm{i}}} F) b_{13}, \\ \widetilde{b}_{21} &= (1 - \Delta\lambda\beta\theta H_3) b_{21} - (\theta\partial_{p_{\mathrm{i}}} F) b_{23}. \end{aligned} \tag{3.2.73}$$

Defining the matrix product

$$\begin{bmatrix} \overline{D}_{11} & \overline{D}_{12} \\ \overline{D}_{21} & \overline{D}_{22} \end{bmatrix} = \begin{bmatrix} D_{11} & D_{12} \\ D_{21} & D_{22} \end{bmatrix} \begin{bmatrix} \widetilde{b}_{11} & b_{12} \\ \widetilde{b}_{21} & b_{22} \end{bmatrix}, \tag{3.2.74}$$

the consistent tangent operator then becomes

$$\begin{aligned} \mathbf{c} &= \left(\overline{D}_{11} - \frac{2q}{9\epsilon_{\mathrm{s}}^{\mathrm{e}\,\mathrm{tr}}}\right)\mathbf{1}\otimes\mathbf{1} + \sqrt{\frac{2}{3}}\left(\overline{D}_{12}\mathbf{1}\otimes\widehat{\boldsymbol{n}} + \overline{D}_{21}\widehat{\boldsymbol{n}}\otimes\mathbf{1}\right) \\ &+ \frac{2q}{3\epsilon_{\mathrm{s}}^{\mathrm{e}\,\mathrm{tr}}}(\boldsymbol{I} - \widehat{\boldsymbol{n}}\otimes\widehat{\boldsymbol{n}}) + \frac{2}{3}\overline{D}_{22}\widehat{\boldsymbol{n}}\otimes\widehat{\boldsymbol{n}}. \end{aligned} \tag{3.2.75}$$

In the elastic regime the submatrix $[\,b_{ij}\,]$ becomes an identity matrix, and hence $\overline{D}_{ij} = D_{ij}$ for $i, j = 1, 2$. In this case, $\mathbf{c}$ reduces to the hyperelastic tangent operator $\mathbf{c}^{\mathrm{e}}$.

Remark 2. As shown in Figure 3.3, the proposed yield and plastic potential functions create corners on the compaction side of the hydrostatic axis. While the model is primarily developed to accurately capture dilative plastic flow, and therefore is not expected to perform well in stress states dominated by hydrostatic compaction, numerical problems could still arise in general boundary-value problem simulations when the stress ratio η as defined by (3.2.7) goes to zero or even becomes negative. In order to avoid a negative η, we introduce a 'cap' on the plastic potential function such that

$$Q = \begin{cases} q + \overline{\eta}p & \text{if} \quad \overline{\eta} = \eta \geq \chi M, \\ -p & \text{if} \quad \overline{\eta} = \eta < \chi M, \end{cases} \tag{3.2.76}$$

where χ is a user-specified parameter controlling the position of the plastic potential function cap, e.g., $\chi = 0.10$. For the case where $\overline{\eta} < \chi M$, the local residual vector simplifies to

$$\boldsymbol{r}(\boldsymbol{x}) = \begin{Bmatrix} \epsilon_{\mathrm{v}}^{\mathrm{e}} - \epsilon_{\mathrm{v}}^{\mathrm{e}\,\mathrm{tr}} - \Delta\lambda \\ \epsilon_{\mathrm{s}}^{\mathrm{e}} - \epsilon_{\mathrm{s}}^{\mathrm{e}\,\mathrm{tr}} \\ F \end{Bmatrix}. \tag{3.2.77}$$

The local tangent operator is given by

$$\boldsymbol{r}'(\boldsymbol{x}) = \begin{bmatrix} 1 & 0 & -1 \\ 0 & 1 & 0 \\ (D_{11}\partial_p + D_{21}\partial_q)F & (D_{12}\partial_p + D_{22}\partial_q)F & 0 \end{bmatrix}. \tag{3.2.78}$$

Finally, the strain derivative of $\boldsymbol{r}$ holding $\boldsymbol{x}$ fixed reduces to

$$\left.\frac{\partial \boldsymbol{r}}{\partial \boldsymbol{\epsilon}}\right|_x = \left\{ \begin{array}{c} \mathbf{1} \\ \sqrt{2/3}\widehat{\boldsymbol{n}} \\ \mathbf{0} \end{array} \right\}. \tag{3.2.79}$$

Of course, one can also insert a smooth cap near the nose of the plastic potential function as an alternative to the planar cap.

3.3 Finite deformation plasticity; localization of deformation

In the preceding section we have reformulated an infinitesimal rigid-plastic constitutive model for sands to accommodate non-associated plasticity and hyperelasticity. In this section we further generalize the model to accommodate finite deformation plasticity. The final model is then used to capture deformation and failure initiation in dense sands, focusing on the effects of uneven void distribution on the local and global responses.

3.3.1 Entropy inequality

Consider the multiplicative decomposition of deformation gradient for a local material point X [30, 115, 116]

$$\boldsymbol{F}(X,t) = \boldsymbol{F}^{\mathrm{e}}(X,t) \cdot \boldsymbol{F}^{\mathrm{p}}(X,t). \tag{3.3.1}$$

In the following we shall use as a measure of elastic deformation the contravariant tensor field $\boldsymbol{b}^{\mathrm{e}}$ reckoned with respect to the current placement, called the left Cauchy-Green deformation tensor,

$$\boldsymbol{b}^{\mathrm{e}} = \boldsymbol{F}^{\mathrm{e}} \cdot \boldsymbol{F}^{\mathrm{e}\,\mathrm{t}}. \tag{3.3.2}$$

Assume then that the free energy is given by

$$\Psi = \Psi(X, \boldsymbol{b}^{\mathrm{e}}, \varepsilon_{\mathrm{s}}^{\mathrm{p}}). \tag{3.3.3}$$

As in the infinitesimal model, we investigate conditions under which we could isolate an elastic stored energy function from the above free energy function.

For the purely mechanical theory the local dissipation function takes the form

$$\mathcal{D} = \boldsymbol{\tau} : \boldsymbol{d} - \frac{\mathrm{d}\Psi(X, \boldsymbol{b}^{\mathrm{e}}, \varepsilon_{\mathrm{s}}^{\mathrm{p}})}{\mathrm{d}t} \geq 0, \tag{3.3.4}$$

where $\boldsymbol{\tau} = J\boldsymbol{\sigma}$ is the symmetric Kirchhoff stress tensor, $J = \det(\boldsymbol{F})$, $\boldsymbol{d} = \mathrm{sym}(\boldsymbol{l})$ is the rate of deformation tensor, and $\boldsymbol{l}$ is the spatial velocity gradient. Using the chain rule and invoking the standard Coleman relations yields the constitutive equation [117]

$$\boldsymbol{\tau} = 2\frac{\partial\Psi(X, \boldsymbol{b}^{\mathrm{e}}, \varepsilon_{\mathrm{s}}^{\mathrm{p}})}{\partial \boldsymbol{b}^{\mathrm{e}}} \cdot \boldsymbol{b}^{\mathrm{e}}, \tag{3.3.5}$$

along with the reduced dissipation inequality

$$\mathcal{D} = \boldsymbol{\tau} : \boldsymbol{d}^{\mathrm{p}} - \pi_{\mathrm{i}}\dot{\varepsilon}_{\mathrm{s}}^{\mathrm{p}} \geq 0, \tag{3.3.6}$$

where $\boldsymbol{d}^{\mathrm{p}}$ is the plastic component of the rate of deformation,

$$\boldsymbol{d}^{\mathrm{p}} = \mathrm{sym}(\boldsymbol{l}^{\mathrm{p}}), \qquad \boldsymbol{l}^{\mathrm{p}} := \boldsymbol{F}^{\mathrm{e}} \cdot \boldsymbol{L}^{\mathrm{p}} \cdot \boldsymbol{F}^{\mathrm{e}-1}, \qquad \boldsymbol{L}^{\mathrm{p}} := \dot{\boldsymbol{F}}^{\mathrm{p}} \cdot \boldsymbol{F}^{\mathrm{p}-1}, \tag{3.3.7}$$

and

$$\pi_{\mathrm{i}} = \frac{\partial\Psi(X, \boldsymbol{b}^{\mathrm{e}}, \varepsilon_{\mathrm{s}}^{\mathrm{p}})}{\partial\varepsilon_{\mathrm{s}}^{\mathrm{p}}}, \tag{3.3.8}$$

is a stress-like plastic internal variable equivalent to p_{i} of the infinitesimal theory.

We assume that π_{i} evolves in the same way as p_{i}, i.e.,

$$-\dot{\pi}_{\mathrm{i}} = \phi(\pi_{\mathrm{i}} - \pi_{\mathrm{i}}^{*})\dot{\varepsilon}_{\mathrm{s}}^{\mathrm{p}}, \tag{3.3.9}$$

where π_{i}^{*} depends not only on π_{i} but also on $\boldsymbol{b}^{\mathrm{e}}$. Integrating (3.3.9) gives

$$\pi_{\mathrm{i}} = \pi_{\mathrm{i}0} - \int_{\varepsilon_{\mathrm{s}0}^{\mathrm{p}}}^{\varepsilon_{\mathrm{s}}^{\mathrm{p}}} \phi(\pi_{\mathrm{i}} - \pi_{\mathrm{i}}^{*})\,\mathrm{d}\varepsilon_{\mathrm{s}}^{\mathrm{p}}. \tag{3.3.10}$$

Integrating once more, we get

$$\Psi(X, \boldsymbol{b}^{\mathrm{e}}, \varepsilon_{\mathrm{s}}^{\mathrm{p}}) = \int_{\varepsilon_{\mathrm{s}0}^{\mathrm{p}}}^{\varepsilon_{\mathrm{s}}^{\mathrm{p}}} \pi_{\mathrm{i}0}\,\mathrm{d}\varepsilon_{\mathrm{s}}^{\mathrm{p}} - \int_{\varepsilon_{\mathrm{s}0}^{\mathrm{p}}}^{\varepsilon_{\mathrm{s}}^{\mathrm{p}}}\int_{\varepsilon_{\mathrm{s}0}^{\mathrm{p}}}^{\varepsilon_{\mathrm{s}}^{\mathrm{p}}} \phi(\pi_{\mathrm{i}} - \pi_{\mathrm{i}}^{*})\,\mathrm{d}\varepsilon_{\mathrm{s}}^{\mathrm{p}}\mathrm{d}\varepsilon_{\mathrm{s}}^{\mathrm{p}} + \Psi^{\mathrm{e}}(X, \boldsymbol{b}^{\mathrm{e}}) + \Psi_0, \tag{3.3.11}$$

where $\Psi^{\mathrm{e}}(X, \boldsymbol{b}^{\mathrm{e}})$ is the elastic stored energy function. Finally, using the constitutive equation

(3.3.5) once again, we get

$$\boldsymbol{\tau} = 2\left[\frac{\partial \Psi^{\mathrm{e}}(X, \boldsymbol{b}^{\mathrm{e}})}{\partial \boldsymbol{b}^{\mathrm{e}}} + \underbrace{\int_{\varepsilon^{\mathrm{p}}_{\mathrm{s}0}}^{\varepsilon^{\mathrm{p}}_{\mathrm{s}}} \int_{\varepsilon^{\mathrm{p}}_{\mathrm{s}0}}^{\varepsilon^{\mathrm{p}}_{\mathrm{s}}} \phi'(\pi_{\mathrm{i}} - \pi^{*}_{\mathrm{i}}) \frac{\partial \pi^{*}_{\mathrm{i}}}{\partial \boldsymbol{b}^{\mathrm{e}}} \, \mathrm{d}\varepsilon^{\mathrm{p}}_{\mathrm{s}} \mathrm{d}\varepsilon^{\mathrm{p}}_{\mathrm{s}}}_{\mathrm{O}(\Delta \varepsilon^{\mathrm{p}2}_{\mathrm{s}})}\right] \cdot \boldsymbol{b}^{\mathrm{e}}. \tag{3.3.12}$$

The second-order terms in (3.3.12) can be ignored at the initial stage of loading when $\Delta\varepsilon^{\mathrm{p}}_{\mathrm{s}}$ is small, thus leaving the Kirchhoff stress varying with the elastic stored energy function alone. When $\Delta\varepsilon^{\mathrm{p}}_{\mathrm{s}}$ is large, $\phi(\pi_{\mathrm{i}} - \pi^{*}_{\mathrm{i}})$ vanishes at critical state, and so the elastic and plastic parts of the free energy uncouple. In both cases the stresses can be expressed in terms of the elastic stored energy function alone, i.e.,

$$\boldsymbol{\tau} = 2\frac{\partial \Psi^{\mathrm{e}}(X, \boldsymbol{b}^{\mathrm{e}})}{\partial \boldsymbol{b}^{\mathrm{e}}} \cdot \boldsymbol{b}^{\mathrm{e}}. \tag{3.3.13}$$

Once again, the perfectly plastic behavior at critical state is a key feature of the model that allows for the uncoupling of the free energy.

3.3.2 Finite deformation plasticity model

Consider the stress invariants

$$p = \frac{1}{3}\operatorname{tr}\boldsymbol{\tau}, \qquad q = \sqrt{\frac{3}{2}}\|\boldsymbol{\xi}\|, \qquad \boldsymbol{\xi} = \boldsymbol{\tau} - p\mathbf{1}. \tag{3.3.14}$$

Then, as in the infinitesimal theory the yield function can be defined as

$$F = q + \eta p \leq 0, \tag{3.3.15}$$

where

$$\eta = \begin{cases} M\left[1 + \ln(\pi_{\mathrm{i}}/p)\right] & \text{if} \quad N = 0; \\ (M/N)\left[1 - (1-N)(p/\pi_{\mathrm{i}})^{N/(1-N)}\right] & \text{if} \quad N > 0. \end{cases} \tag{3.3.16}$$

The material parameters M and N are similar in meaning to those of the infinitesimal theory, although their values should now be calibrated in the finite deformation regime.

The flow rule may be written as before,

$$\boldsymbol{d}^{\mathrm{p}} = \dot{\lambda}\boldsymbol{q}, \qquad \boldsymbol{q} = \frac{\beta}{3}\frac{\partial F}{\partial p}\mathbf{1} + \sqrt{\frac{3}{2}}\frac{\partial F}{\partial q}\widehat{\boldsymbol{n}}, \qquad \widehat{\boldsymbol{n}} = \boldsymbol{\xi}/\|\boldsymbol{\xi}\|, \tag{3.3.17}$$

where $\beta \leq 1$ is the non-associativity parameter. We postulate a similar hardening law in Kirchhoff stress space given by (3.3.9), with

$$\operatorname{sgn}\left[\phi\left(\pi_{\mathrm{i}} - \pi_{\mathrm{i}}^{*}\right)\right] = \operatorname{sgn} H, \tag{3.3.18}$$

to capture either a hardening or softening response depending on the position of the state point relative to the limit hardening dilatancy. Table 3.3 then summarizes the rate equations for the finite deformation plasticity model.

Table 3.3: Summary of rate equations for plasticity model for sands, finite deformation version.

1. Velocity gradient: $\boldsymbol{l} = \boldsymbol{l}^{\mathrm{e}} + \boldsymbol{l}^{\mathrm{p}}$
2. Hyperelastic rate equation: $\dot{\boldsymbol{\tau}} = \boldsymbol{\alpha}^{\mathrm{e}} : \boldsymbol{l}^{\mathrm{e}}$
3. Flow rule: $\boldsymbol{d}^{\mathrm{p}} = \operatorname{sym}(\boldsymbol{l}^{\mathrm{p}}) = \dot{\lambda}\boldsymbol{q}, \qquad \boldsymbol{\omega}^{\mathrm{p}} = \operatorname{skw}(\boldsymbol{l}^{\mathrm{p}}) = \mathbf{0}$
4. State parameter: $\dot{\psi}_{\mathrm{i}} = \dot{v} + \widetilde{\lambda}\dot{\pi}_{\mathrm{i}}/\pi_{\mathrm{i}}$
5. Hardening law: $-\dot{\pi}_{\mathrm{i}} = \phi(\pi_{\mathrm{i}} - \pi_{\mathrm{i}}^{*})\dot{\lambda}$
6. Consistency condition: $\boldsymbol{f} : \dot{\boldsymbol{\tau}} - H\dot{\lambda} = 0, \quad \boldsymbol{f} = \partial F/\partial\boldsymbol{\tau}$
7. Kuhn-Tucker conditions: $\dot{\lambda} \geq 0, \quad F \leq 0, \quad \dot{\lambda}F = 0$

The model summarized in Table 3.3 has some noteworthy features. First, the formulation assumes that the plastic spin $\boldsymbol{\omega}^{\mathrm{p}}$ is zero (see [118] for some discussions on the significance of the plastic spin). Second, the fourth-order spatial elastic tangent operator $\boldsymbol{\alpha}^{\mathrm{e}}$ can be determined from the expression

$$\boldsymbol{\alpha}^{\mathrm{e}} = \mathbf{c}^{\mathrm{e}} + \boldsymbol{\tau} \oplus \mathbf{1} + \boldsymbol{\tau} \ominus \mathbf{1}, \tag{3.3.19}$$

where $(\boldsymbol{\tau} \oplus \mathbf{1})_{ijkl} = \tau_{jl}\delta_{ik}$, $(\boldsymbol{\tau} \ominus \mathbf{1})_{ijkl} = \tau_{il}\delta_{jk}$, and $\mathbf{c}^{\mathrm{e}}$ is a spatial tangential elasticity tensor obtained from the push-forward of all the indices of the second tangential elasticity tensor

defined in [30]. Finally, the specific volume varies according to the kinematical relation

$$v = Jv_0 \qquad \Longrightarrow \qquad \dot{v} = \dot{J}v_0 = Jv_0\,\mathrm{tr}(\boldsymbol{l}) = v\,\mathrm{tr}(\boldsymbol{l}). \tag{3.3.20}$$

Thus, just as in the infinitesimal theory where the rate equations may be viewed as driven by the strain rate $\dot{\boldsymbol{\epsilon}}$, the rate equations shown in Table 3.3 may be viewed as driven by the spatial velocity gradient $\boldsymbol{l}$.

3.3.3 Numerical implementation

For the problem at hand we employ a standard elastic predictor-plastic corrector algorithm based on the product formula for $\boldsymbol{b}^{\mathrm{e}}$, as summarized in Table 3.4. Let

$$\boldsymbol{b}^{\mathrm{e}}_n = \boldsymbol{F}^{\mathrm{e}}_n \cdot \boldsymbol{F}^{\mathrm{e}\,\mathrm{t}}_n. \tag{3.3.21}$$

Suppressing plastic flow, the trial elastic predictor for $\boldsymbol{b}^{\mathrm{e}}$ is

$$\boldsymbol{b}^{\mathrm{e}\,\mathrm{tr}} \equiv \boldsymbol{b}^{\mathrm{e}\,\mathrm{tr}}_{n+1} = \boldsymbol{f}_{n+1} \cdot \boldsymbol{b}^{\mathrm{e}}_n \cdot \boldsymbol{f}^{\mathrm{t}}_{n+1}\,, \qquad \boldsymbol{f}_{n+1} = \frac{\partial \boldsymbol{x}_{n+1}}{\partial \boldsymbol{x}_n}. \tag{3.3.22}$$

The plastic corrector emanates from the exponential approximation

$$\boldsymbol{b}^{\mathrm{e}} = \exp(-2\Delta\lambda \boldsymbol{q}) \cdot \boldsymbol{b}^{\mathrm{e}\,\mathrm{tr}}\,, \qquad \boldsymbol{q} \equiv \boldsymbol{q}_{n+1} = \frac{\partial Q}{\partial \boldsymbol{\tau}}. \tag{3.3.23}$$

From the co-axiality of plastic flow, the principal directions of $\boldsymbol{q}$ and $\boldsymbol{\tau}$ coincide.

Next we obtain a spectral decomposition of $\boldsymbol{b}^{\mathrm{e}}$,

$$\boldsymbol{b}^{\mathrm{e}} = \sum_{A=1}^{3} (\lambda^{\mathrm{e}}_A)^2 \boldsymbol{m}^{(A)}\,, \qquad \boldsymbol{m}^{(A)} = \boldsymbol{n}^{(A)} \otimes \boldsymbol{n}^{(A)}, \tag{3.3.24}$$

where λ^{e}_A are the elastic principal stretches, $\boldsymbol{n}^{(A)}$ are the unit principal directions, and $\boldsymbol{m}^{(A)}$ are the spectral directions. The corresponding elastic logarithmic stretches are

$$\varepsilon^{\mathrm{e}}_A = \ln(\lambda^{\mathrm{e}}_A)\,, \qquad A = 1, 2, 3. \tag{3.3.25}$$

From material frame indifference $\Psi^{\mathrm{e}}(X, \boldsymbol{b}^{\mathrm{e}})$ only varies with $\varepsilon^{\mathrm{e}}_A$, and so we can write $\overline{\Psi}^{\mathrm{e}} =$

Table 3.4: Return mapping algorithm for plasticity model for sands, finite deformation version.

1. Elastic deformation predictor: $\boldsymbol{b}^{\mathrm{e}\,\mathrm{tr}} = \boldsymbol{f}_{n+1} \cdot \boldsymbol{b}^{\mathrm{e}}_{n} \cdot \boldsymbol{f}^{\mathrm{t}}_{n+1}$
2. Elastic stress predictor: $\boldsymbol{\tau}^{\mathrm{tr}} = 2(\partial \Psi^{\mathrm{e}}/\partial \boldsymbol{b}^{\mathrm{e}\,\mathrm{tr}}) \cdot \boldsymbol{b}^{\mathrm{e}\,\mathrm{tr}}; \quad \pi_{\mathrm{i}}^{\mathrm{tr}} = \pi_{\mathrm{i},n}$
3. Check if yielding: $F(p^{\mathrm{tr}}, q^{\mathrm{tr}}, \pi_{\mathrm{i}}^{\mathrm{tr}}) \geq 0$?
   No, set $\boldsymbol{b}^{\mathrm{e}} = \boldsymbol{b}^{\mathrm{e}\,\mathrm{tr}}; \quad \boldsymbol{\tau} = \boldsymbol{\tau}^{\mathrm{tr}}; \quad \pi_{\mathrm{i}} = \pi_{\mathrm{i}}^{\mathrm{tr}}$ and exit
4. Yes, initialize $\Delta\lambda = 0$ and iterate for $\Delta\lambda$ (steps 5-8)
5. Spectral decomposition: $\boldsymbol{b}^{\mathrm{e}\,\mathrm{tr}} = \sum_{A=1}^{3} (\lambda_A^{\mathrm{e}\,\mathrm{tr}})^2 \boldsymbol{m}^{\mathrm{tr}(A)}$
6. Plastic corrector in principal logarithmic stretches: $\varepsilon_A^{\mathrm{e}} = \ln(\lambda_A^{\mathrm{e}})$,
   $\varepsilon_A^{\mathrm{e}\,\mathrm{tr}} = \ln(\lambda_A^{\mathrm{e}\,\mathrm{tr}}), \quad \varepsilon_A^{\mathrm{e}} = \varepsilon_A^{\mathrm{e}\,\mathrm{tr}} - \Delta\lambda q_A, \quad \tau_A = \partial \overline{\Psi}^{\mathrm{e}}/\partial \varepsilon_A^{\mathrm{e}}\,, \; A = 1, 2, 3.$
7. Update plastic internal variable π_{i}:
   (a) Total deformation gradient: $\boldsymbol{F} = \boldsymbol{f}_{n+1} \cdot \boldsymbol{F}_n$
   (b) Specific volume: $v = v_0 \det \boldsymbol{F} = v_0 J$
   (c) Initialize $\pi_{\mathrm{i}} = \pi_{\mathrm{i},n}$ and iterate for π_{i} (steps 7d-f)
      (d) State parameter: $\psi_{\mathrm{i}} = v - v_{c0} + \widetilde{\lambda} \ln(-\pi_{\mathrm{i}})$
      (e) Limit hardening plastic variable:

$$\pi_{\mathrm{i}}^{*} = p \times \begin{cases} \exp(\overline{\alpha}\psi_{\mathrm{i}}/M) & \text{if} \quad \overline{N} = N = 0, \\ (1 - \overline{\alpha}\psi_{\mathrm{i}} N/M)^{(N-1)/N} & \text{if} \quad 0 \leq \overline{N} \leq N \neq 0. \end{cases}$$

      (f) Plastic internal variable: $\pi_{\mathrm{i}} = \pi_{\mathrm{i},n} - \phi(\pi_{\mathrm{i}} - \pi_{\mathrm{i}}^{*})\Delta\lambda$
8. Discrete consistency condition: $F(p, q, \pi_{\mathrm{i}}) = 0$
9. Spectral resolution: $\boldsymbol{b}^{\mathrm{e}} = \sum_{A=1}^{3} (\lambda_A^{\mathrm{e}})^2 \boldsymbol{m}^{\mathrm{tr}(A)}$

$\overline{\Psi}^{\mathrm{e}}(X, \varepsilon_1^{\mathrm{e}}, \varepsilon_2^{\mathrm{e}}, \varepsilon_2^{\mathrm{e}})$, which gives

$$\frac{\partial \Psi^{\mathrm{e}}}{\partial \boldsymbol{b}^{\mathrm{e}}} = \frac{1}{2} \sum_{A=1}^{3} \frac{1}{(\lambda_A^{\mathrm{e}})^2} \frac{\partial \overline{\Psi}^{\mathrm{e}}}{\partial \varepsilon_A^{\mathrm{e}}} \boldsymbol{m}^{(A)}. \tag{3.3.26}$$

The elastic constitutive equation then writes

$$\boldsymbol{\tau} = 2 \frac{\partial \Psi^{\mathrm{e}}}{\partial \boldsymbol{b}^{\mathrm{e}}} \cdot \boldsymbol{b}^{\mathrm{e}} = \sum_{A=1}^{3} \tau_A \boldsymbol{m}^{(A)}, \qquad \tau_A = \frac{\partial \overline{\Psi}^{\mathrm{e}}}{\partial \varepsilon_A^{\mathrm{e}}}, \tag{3.3.27}$$

implying that the spectral directions of $\boldsymbol{\tau}$ and $\boldsymbol{b}^{\mathrm{e}}$ also coincide. Thus, $\boldsymbol{b}^{\mathrm{e}}$ and $\boldsymbol{q}$ are also co-axial, and for (3.3.23) to hold, $\boldsymbol{b}^{\mathrm{e}}$ and $\boldsymbol{b}^{\mathrm{e}\,\mathrm{tr}}$ must also be co-axial, i.e.,

$$\boldsymbol{m}^{(A)} = \boldsymbol{m}^{\mathrm{tr}\,(A)}. \tag{3.3.28}$$

This allows the plastic corrector phase to take place along the principal axes, as shown in Table 3.4.

Alternatively, we can utilize the algorithm developed for the infinitesimal theory by working on the invariant space of the logarithmic elastic stretch tensor. Let

$$\varepsilon_{\mathrm{v}}^{\mathrm{e}} = \varepsilon_1^{\mathrm{e}} + \varepsilon_2^{\mathrm{e}} + \varepsilon_3^{\mathrm{e}}, \qquad \varepsilon_{\mathrm{s}}^{\mathrm{e}} = \frac{1}{3} \sqrt{2[(\varepsilon_1^{\mathrm{e}} - \varepsilon_2^{\mathrm{e}})^2 + (\varepsilon_1^{\mathrm{e}} - \varepsilon_3^{\mathrm{e}})^2 + (\varepsilon_2^{\mathrm{e}} - \varepsilon_3^{\mathrm{e}})^2]}, \tag{3.3.29}$$

denote the first two invariants of the logarithmic elastic stretch tensor (similar definitions may be made for $\varepsilon_{\mathrm{v}}^{\mathrm{e}\,\mathrm{tr}}$ and $\varepsilon_{\mathrm{s}}^{\mathrm{e}\,\mathrm{tr}}$), and

$$p = \frac{1}{3}(\tau_1 + \tau_2 + \tau_3), \qquad q = \sqrt{[(\tau_1 - \tau_2)^2 + (\tau_1 - \tau_3)^2 + (\tau_2 - \tau_3)^2]/2}, \tag{3.3.30}$$

denote the first two invariants of the Kirchhoff stress tensor. If we take the functional relationships $p = p(\varepsilon_{\mathrm{v}}^{\mathrm{e}}, \varepsilon_{\mathrm{s}}^{\mathrm{e}})$, $q = q(\varepsilon_{\mathrm{v}}^{\mathrm{e}}, \varepsilon_{\mathrm{s}}^{\mathrm{e}})$, and $\pi_{\mathrm{i}} = \pi_{\mathrm{i}}(\varepsilon_{\mathrm{v}}^{\mathrm{e}}, \varepsilon_{\mathrm{s}}^{\mathrm{e}}, \Delta\lambda)$ as before, using the same elastic stored energy function but now expressed in terms of the logarithmic principal elastic stretches, then the local residual vector writes

$$\boldsymbol{r} = \boldsymbol{r}(\boldsymbol{x}) = \left\{ \begin{array}{c} \varepsilon_{\mathrm{v}}^{\mathrm{e}} - \varepsilon_{\mathrm{v}}^{\mathrm{e}\,\mathrm{tr}} + \Delta\lambda\beta\partial_p F \\ \varepsilon_{\mathrm{s}}^{\mathrm{e}} - \varepsilon_{\mathrm{s}}^{\mathrm{e}\,\mathrm{tr}} + \Delta\lambda\partial_q F \\ F \end{array} \right\}; \qquad \boldsymbol{x} = \left\{ \begin{array}{c} \varepsilon_{\mathrm{v}}^{\mathrm{e}} \\ \varepsilon_{\mathrm{s}}^{\mathrm{e}} \\ \Delta\lambda \end{array} \right\}. \tag{3.3.31}$$

In this case, the local Jacobian $\boldsymbol{r}'(\boldsymbol{x})$ takes a form *identical* to that developed for the infinitesimal theory, see (3.2.65).

Comparing Tables 3.2 and 3.4, we see that the algorithm for finite deformation plasticity differs from the infinitesimal version only through a few additional steps entailed for the spectral decomposition and resolution of the deformation and stress tensors. Construction of $\boldsymbol{b}^{\mathrm{e}}$ from the spectral values requires two steps. The first involves resolution of the principal elastic logarithmic stretches from the first two invariants calculated from return mapping,

$$\varepsilon^{\mathrm{e}}_A = \frac{1}{3}\,\varepsilon^{\mathrm{e}}_{\mathrm{v}}\delta_A + \sqrt{\frac{3}{2}}\,\varepsilon^{\mathrm{e}}_{\mathrm{s}}\widehat{n}_A\,, \qquad \widehat{n}_A = \sqrt{\frac{2}{3}}\,\frac{\varepsilon^{\mathrm{e}\,\mathrm{tr}}_A - (\varepsilon^{\mathrm{e}\,\mathrm{tr}}_{\mathrm{v}}/3)\delta_A}{\varepsilon^{\mathrm{e}\,\mathrm{tr}}_{\mathrm{s}}}, \tag{3.3.32}$$

where $\delta_A = 1$ for $A = 1, 2, 3$.The above transformation entails scaling the deviatoric component of the predictor tensor by the factor $\varepsilon^{\mathrm{e}}_{\mathrm{s}}/\varepsilon^{\mathrm{e}\,\mathrm{tr}}_{\mathrm{s}}$ and adding the volumetric component. The second step involves a spectral resolution from the principal elastic logarithmic strains (cf. (3.3.24))

$$\boldsymbol{b}^{\mathrm{e}} = \sum_{A=1}^{3} \exp(2\varepsilon^{\mathrm{e}}_A)\boldsymbol{m}^{\mathrm{tr}\,(A)}. \tag{3.3.33}$$

The next section demonstrates that a closed-form consistent tangent operator is available for the above algorithm.

3.3.4 Algorithmic tangent operator

For simplicity, we restrict to a quasi-static problem whose weak form of the linear momentum balance over an initial volume $\mathcal{B}$ with surface $\partial\mathcal{B}$ reads

$$\int_{\mathcal{B}} (\mathrm{GRAD}\,\boldsymbol{\eta} : \boldsymbol{P} - \rho_0\boldsymbol{\eta}\cdot\boldsymbol{G})\,\mathrm{d}V - \int_{\partial\mathcal{B}^t} \boldsymbol{\eta}\cdot\boldsymbol{t}\,\mathrm{d}A = 0, \tag{3.3.34}$$

where $\rho_0\boldsymbol{G}$ is the reference body force vector, $\boldsymbol{t} = \boldsymbol{P}\cdot\boldsymbol{n}$ is the nominal traction vector on $\partial\mathcal{B}^t \subset \partial\mathcal{B}$, $\boldsymbol{n}$ is the unit vector on $\partial\mathcal{B}^t$, $\boldsymbol{\eta}$ is the weighting function,

$$\boldsymbol{P} = \boldsymbol{\tau}\cdot\boldsymbol{F}^{-\mathrm{t}} \tag{3.3.35}$$

is the nonsymmetric first Piola-Kirchhoff stress tensor, and GRAD is the gradient operator evaluated with respect to the reference configuration. We recall the internal virtual work

$$W^{\mathrm{e}}_{\mathrm{INT}} = \int_{\mathcal{B}^{\mathrm{e}}} \mathrm{GRAD}\,\boldsymbol{\eta} : \boldsymbol{P}\,\mathrm{d}V = \int_{\mathcal{B}^{\mathrm{e}}} \mathrm{grad}\,\boldsymbol{\eta} : \boldsymbol{\tau}\,\mathrm{d}V \tag{3.3.36}$$

for any $\mathcal{B}^{\mathrm{e}} \subset \mathcal{B}$, where grad is the gradient operator evaluated with respect to the current configuration. The first variation gives [64]

$$\delta W^{\mathrm{e}}_{\mathrm{INT}} = \int_{\mathcal{B}^{\mathrm{e}}} \mathrm{grad}\,\boldsymbol{\eta} : \mathbf{a} : \mathrm{grad}\,\delta\boldsymbol{u}\,\mathrm{d}V, \tag{3.3.37}$$

where $\boldsymbol{u}$ is the displacement field, and

$$\mathbf{a} = \boldsymbol{\alpha} - \boldsymbol{\tau} \ominus \mathbf{1}, \qquad \delta\boldsymbol{\tau} = \boldsymbol{\alpha} : \mathrm{grad}\,\delta\boldsymbol{u}. \tag{3.3.38}$$

Evaluation of $\mathbf{a}$ thus requires determination of the algorithmic tangent operator $\boldsymbol{\alpha}$.

We also recall the following spectral representation of the algorithmic tangent operator $\boldsymbol{\alpha}$ [64]

$$\begin{aligned} \boldsymbol{\alpha} &= \sum_{A=1}^{3}\sum_{B=1}^{3} a_{AB}\boldsymbol{m}^{(A)} \otimes \boldsymbol{m}^{(B)} \\ &+ \sum_{A=1}^{3}\sum_{B\neq A} \frac{\tau_B - \tau_A}{\lambda_B^{\mathrm{e\,tr}\,2} - \lambda_A^{\mathrm{e\,tr}\,2}} \left(\lambda_B^{\mathrm{e\,tr}\,2}\boldsymbol{m}^{(AB)} \otimes \boldsymbol{m}^{(AB)} + \lambda_A^{\mathrm{e\,tr}\,2}\boldsymbol{m}^{(AB)} \otimes \boldsymbol{m}^{(BA)}\right), \end{aligned} \tag{3.3.39}$$

where $\boldsymbol{m}^{(AB)} = \boldsymbol{n}^{(A)} \otimes \boldsymbol{n}^{(B)}$, $A \neq B$. The coefficients a_{AB} are elements of the consistent tangent operator obtained from a return mapping in principal axes, and is formally defined as

$$a_{AB} = \frac{\partial\tau_A}{\partial\varepsilon_B^{\mathrm{e\,tr}}} \equiv \frac{\partial\tau_A}{\partial\varepsilon_B}, \qquad A, B = 1, 2, 3. \tag{3.3.40}$$

The values of these coefficients are specific to the constitutive model in question, as well as dependent on the numerical integration algorithm utilized for the model. For the present critical state plasticity theory a_{AB} is evaluated as follows.

The expression for a principal Kirchhoff stress is

$$\tau_A = p\delta_A + \sqrt{\frac{2}{3}}q\,\widehat{n}_A\,, \qquad A = 1, 2, 3. \tag{3.3.41}$$

Differentiating with respect to a principal logarithmic strain gives

$$\begin{aligned} a_{AB} = \frac{\partial \tau_A}{\partial \varepsilon_B} &= \delta_A \left(D_{11} \frac{\partial \varepsilon_{\mathrm{v}}^{\mathrm{e}}}{\partial \varepsilon_B} + D_{12} \frac{\partial \varepsilon_{\mathrm{s}}^{\mathrm{e}}}{\partial \varepsilon_B} \right) + \sqrt{\frac{2}{3}} \widehat{n}_A \left(D_{21} \frac{\partial \varepsilon_{\mathrm{v}}^{\mathrm{e}}}{\partial \varepsilon_B} + D_{22} \frac{\partial \varepsilon_{\mathrm{s}}^{\mathrm{e}}}{\partial \varepsilon_B} \right) \\ &+ \frac{2q}{3\varepsilon_{\mathrm{s}}^{\mathrm{e\,tr}}} \left(\delta_{AB} - \frac{1}{3} \delta_A \delta_B - \widehat{n}_A \widehat{n}_B \right), \qquad A, B = 1, 2, 3, \end{aligned} \tag{3.3.42}$$

where δ_{AB} is the Kronecker delta. The coefficients D_{11}, D_{22}, and D_{21} are identical in form to those shown in (3.2.52) except that the strain invariants now take on logarithmic definitions. As in the infinitesimal theory, we obtain the unknown strain derivatives above from the local residual vector, whose own derivatives write

$$\frac{\partial r_A}{\partial \varepsilon_B} = \left. \frac{\partial r_A}{\partial \varepsilon_B} \right|_x + \sum_{C=1}^{3} \underbrace{\left. \frac{\partial r_A}{\partial x_C} \right|_{\varepsilon_{\mathrm{v}}^{\mathrm{e\,tr}}, \varepsilon_{\mathrm{s}}^{\mathrm{e\,tr}}}}_{\overline{a}_{AC}} \frac{\partial x_C}{\partial \varepsilon_B} = 0, \qquad A, B = 1, 2, 3, \tag{3.3.43}$$

where the matrix $[\overline{a}_{AB}]$ corresponds to the same algorithmic local tangent operator given in (3.2.65). Letting $[b_{AB}]$ denote the inverse of $[\overline{a}_{AB}]$, we can then solve

$$\frac{\partial x_A}{\partial \varepsilon_B} = - \sum_{C=1}^{3} b_{AC} \left. \frac{\partial r_C}{\partial \varepsilon_B} \right|_x, \qquad A, B = 1, 2, 3. \tag{3.3.44}$$

This latter equation provides the desired strain derivatives,

$$\left\{ \begin{array}{c} \partial \varepsilon_{\mathrm{v}}^{\mathrm{e}} / \partial \varepsilon_A \\ \partial \varepsilon_{\mathrm{s}}^{\mathrm{e}} / \partial \varepsilon_A \\ \partial \Delta\lambda / \partial \varepsilon_A \end{array} \right\} = \left[\begin{array}{ccc} b_{11} & b_{12} & b_{13} \\ b_{21} & b_{22} & b_{23} \\ b_{31} & b_{32} & b_{33} \end{array} \right] \left\{ \begin{array}{c} (1 - \Delta\lambda \beta \theta H_3) \delta_A \\ \sqrt{2/3} \widehat{n}_A \\ -\theta \partial_{\pi_{\mathrm{i}}} F \delta_A \end{array} \right\}, \quad A = 1, 2, 3, \tag{3.3.45}$$

where

$$\begin{aligned} \theta &= c^{-1} \Delta\lambda \phi'(\pi_{\mathrm{i}} - \pi_{\mathrm{i}}^*) v \pi_{\mathrm{i}}^* \frac{\overline{\alpha}(1 - N)}{M - \overline{\alpha} \psi_{\mathrm{i}} N}, \\ c &= 1 + \phi'(\pi_{\mathrm{i}} - \pi_{\mathrm{i}}^*) \Delta\lambda \left[1 - \frac{\widetilde{\lambda} \overline{\alpha}(1 - N)}{M - \overline{\alpha} \psi_{\mathrm{i}} N} \left(\frac{\pi_{\mathrm{i}}^*}{\pi_{\mathrm{i}}} \right) \right]. \end{aligned} \tag{3.3.46}$$

Note that the finite deformation expression for θ utilizes the current value of the specific volume v whereas the infinitesimal version uses the initial value v_0 (cf. (3.2.71)). Inserting the expressions for $\partial \varepsilon_{\mathrm{v}}^{\mathrm{e}} / \partial \varepsilon_A$ and $\partial \varepsilon_{\mathrm{s}}^{\mathrm{e}} / \partial \varepsilon_A$ back in (3.3.42) yields the closed-form solution

for a_{AB}, which takes an identical form to (3.2.75):

$$\begin{aligned} a_{AB} &= \left(\overline{D}_{11} - \frac{2q}{9\varepsilon_{\rm s}^{\rm e\,tr}}\right)\delta_A\delta_B + \sqrt{\frac{2}{3}}\left(\overline{D}_{12}\delta_A\widehat{n}_B + \overline{D}_{21}\widehat{n}_A\delta_B\right) \\ &+ \frac{2q}{3\varepsilon_{\rm s}^{\rm e\,tr}}(\delta_{AB} - \widehat{n}_A\widehat{n}_B) + \frac{2}{3}\overline{D}_{22}\widehat{n}_A\widehat{n}_B, \qquad A,B = 1,2,3. \end{aligned} \tag{3.3.47}$$

See (3.2.72)–(3.2.74) for specific expressions for the coefficients $\overline{D}_{ij}$.

3.3.5 Localization condition

Following [29, 64], we summarize the following alternative (and equivalent) expressions for the localization condition into planar bands. We denote the continuum elastoplastic counterpart of the algorithmic tensor $\boldsymbol{\alpha}$ by

$$\begin{aligned} \boldsymbol{\alpha}^{\rm ep} &= \sum_{A=1}^{3}\sum_{B=1}^{3} a_{AB}^{\rm ep}\boldsymbol{m}^{(A)}\otimes\boldsymbol{m}^{(B)} \\ &+ \sum_{A=1}^{3}\sum_{B\neq A}\frac{\tau_B-\tau_A}{\lambda_B^{\rm e\,2}-\lambda_A^{\rm e\,2}}\left(\lambda_B^{\rm e\,2}\boldsymbol{m}^{(AB)}\otimes\boldsymbol{m}^{(AB)} + \lambda_A^{\rm e\,2}\boldsymbol{m}^{(AB)}\otimes\boldsymbol{m}^{(BA)}\right), \end{aligned} \tag{3.3.48}$$

where $a_{AB}^{\rm ep}$ is the continuum elastoplastic tangent stiffness matrix in principal axes. (Note, this formula appears in [43, 111, 114] with a factor "1/2" before the spin-term summations, a typographical error). Then,

$$\mathbf{a}^{\rm ep} = \boldsymbol{\alpha}^{\rm ep} - \boldsymbol{\tau}\ominus\mathbf{1} \tag{3.3.49}$$

defines the continuum counterpart of the fourth-order tensor $\mathbf{a}$ in (3.3.38).

Alternatively, we denote the constitutive elastoplastic material tensor $\mathbf{c}^{\rm ep}$ by the expression [117]

$$\mathbf{c}^{\rm ep} = \sum_{A=1}^{3}\sum_{B=1}^{3} a_{AB}^{\rm ep}\boldsymbol{m}^{(A)}\otimes\boldsymbol{m}^{(B)} + \sum_{A=1}^{3}\tau_A\boldsymbol{\omega}^{(A)}, \tag{3.3.50}$$

in which

$$\begin{aligned} \boldsymbol{\omega}^{(A)} &= 2\Big[\boldsymbol{I}_b - \boldsymbol{b}^{\rm e}\otimes\boldsymbol{b}^{\rm e} + I_3 b_A^{-1}(\mathbf{1}\otimes\mathbf{1} - \boldsymbol{I}) + b_A(\boldsymbol{b}^{\rm e}\otimes\boldsymbol{m}^{(A)} + \boldsymbol{m}^{(A)}\otimes\boldsymbol{b}^{\rm e}) \\ &- I_3 b_A^{-1}(\mathbf{1}\otimes\boldsymbol{m}^{(A)} + \boldsymbol{m}^{(A)}\otimes\mathbf{1}) + \psi\boldsymbol{m}^{(A)}\otimes\boldsymbol{m}^{(A)}\Big]/D_A, \end{aligned} \tag{3.3.51}$$

where b_A is the Ath principal value of $\boldsymbol{b}^{\mathrm{e}}$, I_1 and I_3 are the first and third invariants of $\boldsymbol{b}^{\mathrm{e}}$,

$$\boldsymbol{I}_b = (\boldsymbol{b}^{\mathrm{e}} \oplus \boldsymbol{b}^{\mathrm{e}} + \boldsymbol{b}^{\mathrm{e}} \ominus \boldsymbol{b}^{\mathrm{e}})/2, \qquad \psi = I_1 b_A + I_3 b_A^{-1} - 4b_A^2, \tag{3.3.52}$$

and

$$D_A := 2b_A^2 - I_1 b_A + I_3 b_A^{-1}. \tag{3.3.53}$$

Note that $\mathrm{c}^{\mathrm{ep}}_{ijkl} = 2F_{iA}F_{jB}F_{kC}F_{lD}\mathrm{C}^{\mathrm{ep}}_{ABCD}$ is the spatial push-forward of the first tangential elastoplastic tensor $\mathbf{C}^{\mathrm{ep}}$ [30]. Then,

$$\mathbf{a}^{\mathrm{ep}} = \mathbf{c}^{\mathrm{ep}} + \boldsymbol{\tau} \oplus \mathbf{1} \tag{3.3.54}$$

defines an alternative expression to (3.3.49).

Using $\mathbf{a}^{\mathrm{ep}}$ from either (3.3.49) or (3.3.54), we can evaluate the elements of the Eulerian elastoplastic acoustic tensor $\boldsymbol{a}$ as

$$a_{ij} = n_k \mathrm{a}^{\mathrm{ep}}_{ikjl} n_l, \tag{3.3.55}$$

where n_k and n_l are elements of the unit normal vector $\boldsymbol{n}$ to a potential deformation band reckoned with respect to the current configuration. Defining the localization function as

$$\mathcal{F} = \inf\big|_n(\det \boldsymbol{a}), \tag{3.3.56}$$

we can then infer the inception of a deformation band from the initial vanishing of $\mathcal{F}$. Though theoretically one needs to use the constitutive operators $\boldsymbol{\alpha}^{\mathrm{ep}}$ or $\mathbf{c}^{\mathrm{ep}}$ to obtain the acoustic tensor $\boldsymbol{a}$, the algorithmic tangent tensors are equally acceptable for bifurcation analyses for small step sizes [114].

3.4 Numerical simulations

We present two numerical examples demonstrating the meso-scale modeling technique. To highlight the triggering of strain localization via imposed material inhomogeneity, we only considered regular specimens (either rectangular or cubical) along with boundary conditions favoring the development of homogeneous deformation (a pin to arrest rigid body modes and vertical rollers at the top and bottom ends of the specimen). A common technique of perturbing the initial condition is to prescribe a weak element; however, this is unrealistic

and arbitrary. In the following simulations we have perturbed the initial condition by prescribing a spatially varying specific volume (or void ratio) consisting of horizontal layers of relatively homogeneous density but with some variation in the vertical direction. This resulted in vein-like soil structures in the density field closely resembling that shown in the photograph of Figure 3.1 and mimicked the placement of sand with a common laboratory technique called pluviation. The specific volume fields were assumed to range from 1.60 to 1.70, with a mean value of 1.63. These values were chosen such that all points remained on the dense side of the CSL ($\psi_{\mathrm{i}} < 0$).

3.4.1 Plane strain simulation

As a first example we considered a finite element mesh 1 m wide and 2 m tall and consisting of 4,096 constant strain triangular elements shown in Figure 3.5. The mesh is completely symmetric to avoid any bias introduced by the triangles. The vertical sides were subjected to pressure loads (natural boundary condition), whereas the top end was compressed by moving roller supports (essential boundary condition). The load-time functions are shown in Figure 3.6 with scaling factors $\gamma = 100$ kPa and $\beta = 0.40$ m for pressure load $G_1(t)$ and vertical compression $G_2(t)$, respectively. The material parameters are summarized in Tables 3.5 and 3.6 and roughly represent those of dense Erksak sand, see [2]. The preconsolidation stress was set to $p_{\mathrm{c}} = -130$ kPa and the reference specific volume was assumed to have a value $v_{\mathrm{c0}} = 1.915$ (uniform for all elements). The distribution of initial specific volume is shown in Figure 3.7.

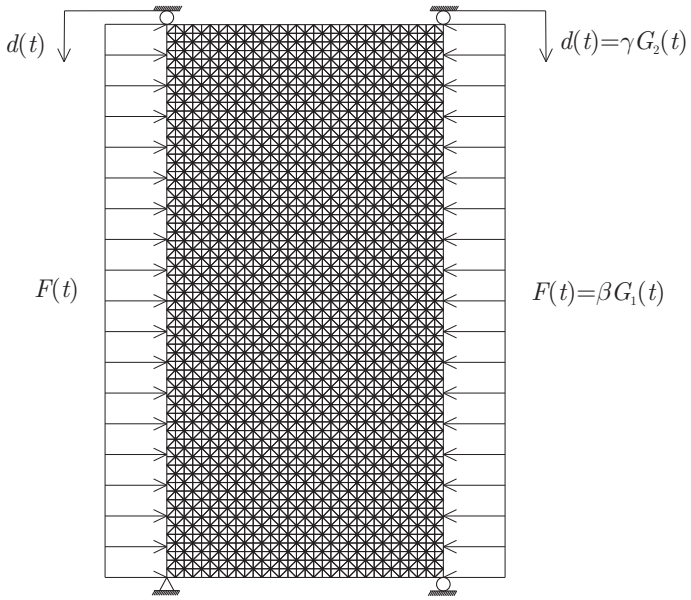

Figure 3.5: Finite element mesh for plane strain compression problem.

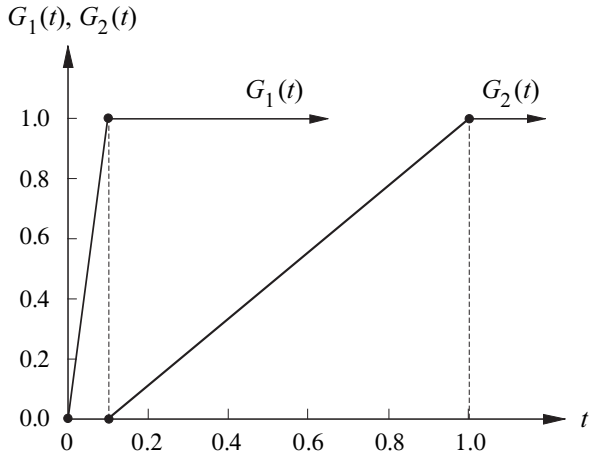

Figure 3.6: Load-time functions.

Symbol	Value	Parameter
$\widetilde{\kappa}$	0.03	compressibility
α_0	0	coupling coefficient
μ_0	2000 kPa	shear modulus
p_0	-100 kPa	reference pressure
$\epsilon^{\mathrm{e}}_{\mathrm{v}0}$	0	reference strain

Table 3.5: Summary of hyperelastic material parameters (see [1] for laboratory testing procedure).

Symbol	Value	Parameter
$\widetilde{\lambda}$	0.04	compressibility
N	0.4	for yield function
$\overline{N}$	0.2	for plastic potential
h	280	hardening coefficient

Table 3.6: Summary of plastic material parameters (see [2] for laboratory testing procedure).

Figure 3.8 shows contours of the determinant function and the logarithmic deviatoric strains at the onset of localization for the case of finite deformations, which occurred at a nominal axial strain of 12.26%. Localization for the infinitesimal model was slightly delayed at 12.34%. The figure shows a clear correlation between regions in the specimen where the determinant function vanished for the first time and where the deviatoric strains were most intense. Furthermore, the figure reveals an X-pattern of shear band formation captured by both shear deformation and determinant function contours, reproducing those observed in laboratory experiments [4, 80].

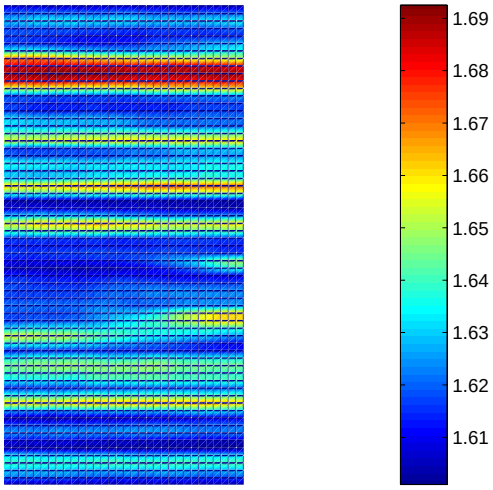

Figure 3.7: Initial specific volume for plane strain compression problem.

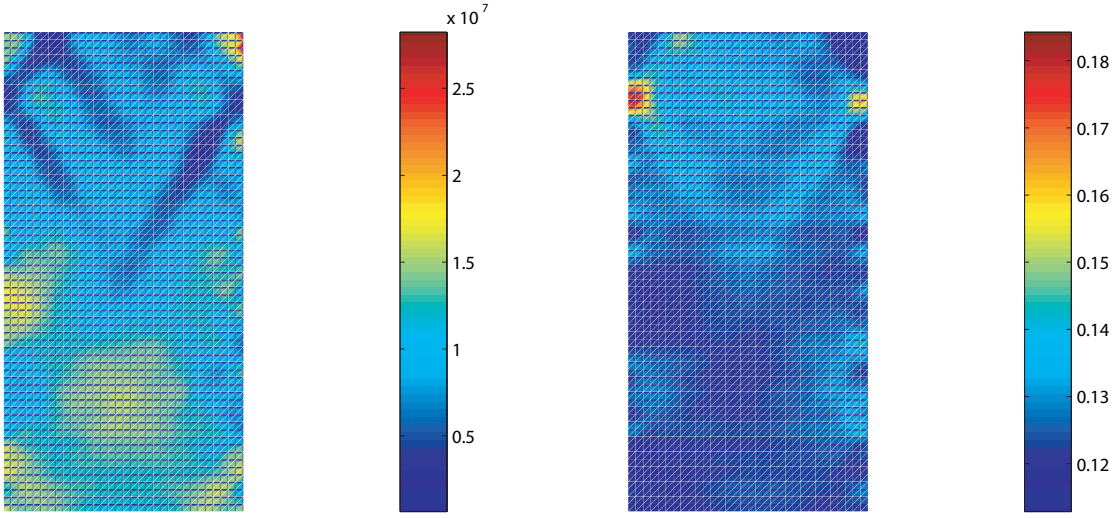

(a) (b)

Figure 3.8: Contours of: (a) determinant function; and (b) deviatoric invariant of logarithmic stretches at onset of localization.

Figure 3.9 displays contours of the plastic modulus and the logarithmic volumetric

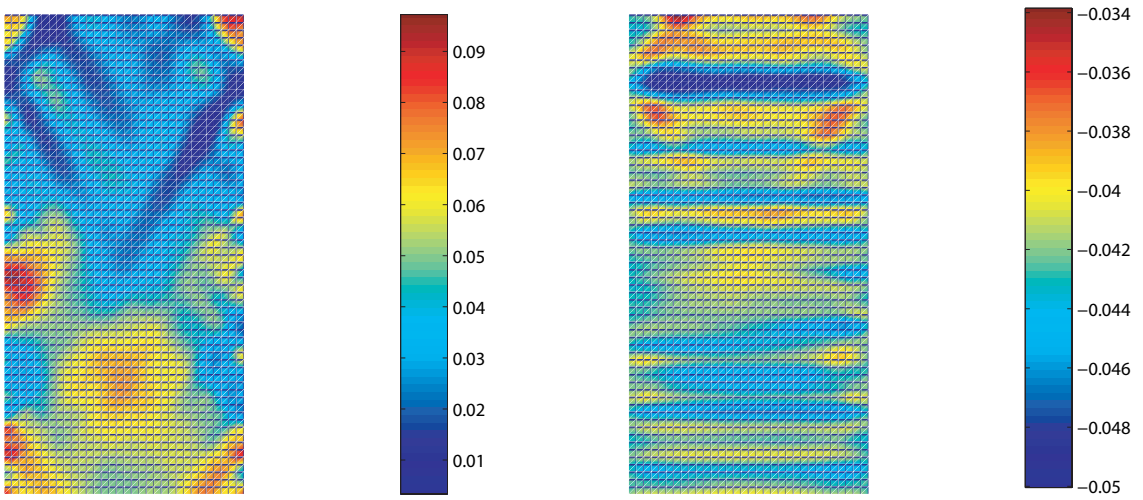

(a) (b)

Figure 3.9: Contours of: (a) plastic hardening modulus; and (b) volumetric invariant of logarithmic stretches at onset of strain localization.

strains at the onset of localization. We recall that for this plasticity model the plastic modulus is a function of the state of stress, and in this figure low values of hardening modulus correlate with areas of highly localized shear strains shown in Figure 3.8. On the other hand, volumetric strains at localization appear to resemble the initial distribution of specific volume shown in Figure 3.7. In fact the blue pocket of high compression extending horizontally at the top of the sample (Figure 3.9b) is representative of that experienced by the red horizontal layer of relatively low density shown in Figure 3.7. The calculated shear bands were predominantly dilative.

3.4.2 Three-dimensional simulation

For the 3D simulation we considered a cubical finite element mesh shown in Figure 3.10. The mesh is 1 m wide by 1 m deep by 2 m tall and consists of 2000 eight-node brick elements. All four vertical faces of the mesh were subjected to pressure loads of 100 kPa (natural boundary condition). The top face at $z = 2$ m was compressed vertically by moving roller supports according to the same load-time function shown in Figure 3.6 (essential boundary condition), effectively replicating a laboratory testing protocol for 'triaxial' compression on a specimen with a square cross-section. The initial distribution of specific volume is also

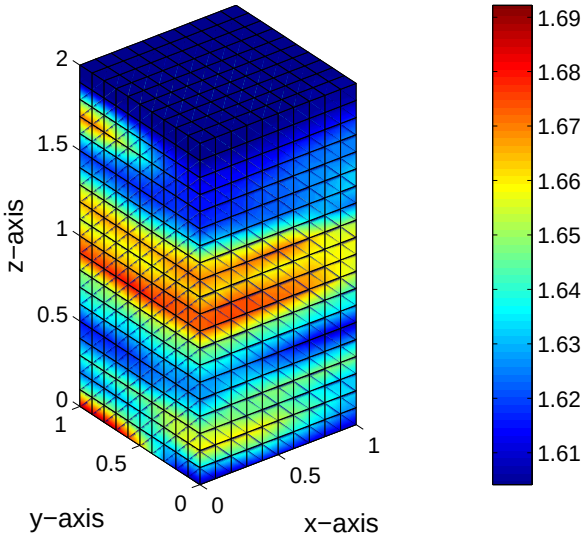

Figure 3.10: Finite element mesh and initial specific volume for 3D compression problem.

shown in Figure 3.10 and roughly mimicked the profile for plane strain shown in Figure 3.7.

Figures 3.11 and 3.12 compare the nominal axial stress and volume change behaviors, respectively, of specimens with and without imposed heterogeneities. The homogeneous specimen was created to have a uniform specific volume equal to the volume average of the specific volume for the equivalent heterogeneous specimen, or 1.63 in this case. We used both the standard numerical integration and B-bar method for the calculations [119–121], but there was not much difference in the predicted responses. However, softening within the range of deformation shown in these figures was detected by all solutions except by the homogeneous specimen simulation. Furthermore, an earlier overall dilation from an initially contractive behavior was detected by the heterogeneous specimen simulation (Figure 3.12). This reversal in volume change behavior from contractive to dilative is usually termed 'phase transformation' in the geotechnical literature, a feature that is not replicated by classical Cam-Clay models. Figure 3.13 shows that this phase transition was captured by the constitutive model by first yielding on the compression side of the yield surface, and later by yielding on the dilation side.

Figure 3.14 shows contours of the determinant function $\mathcal{F}$ at a nominal axial strain of 8.78%, where the determinant vanished for the first time at a Gauss point located in the interior of the heterogeneous specimen. Unlike the plane strain solution, the potential shear

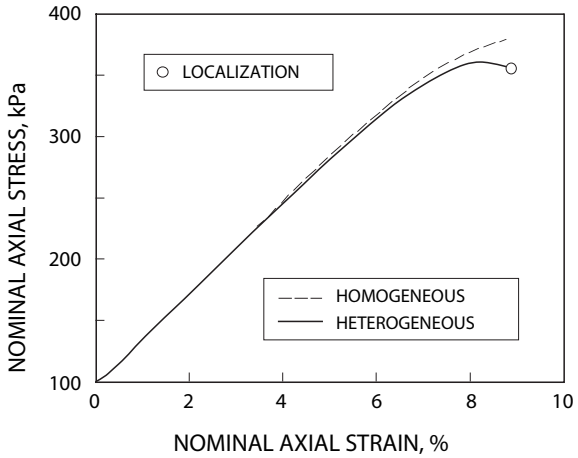

Figure 3.11: Nominal axial stress-axial strain responses for 3D compression problem.

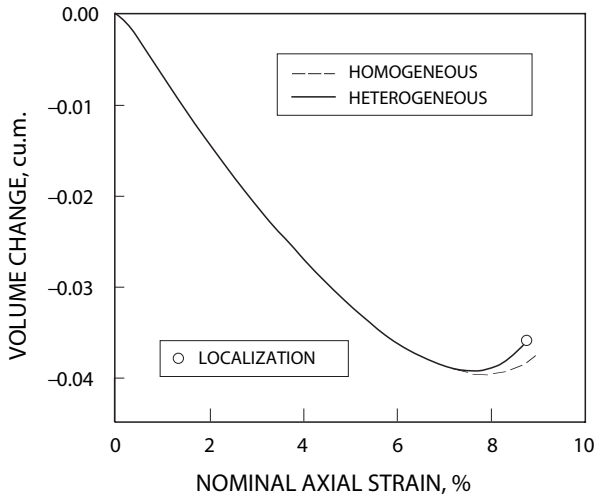

Figure 3.12: Volume change-nominal axial strain responses for 3D compression problem.

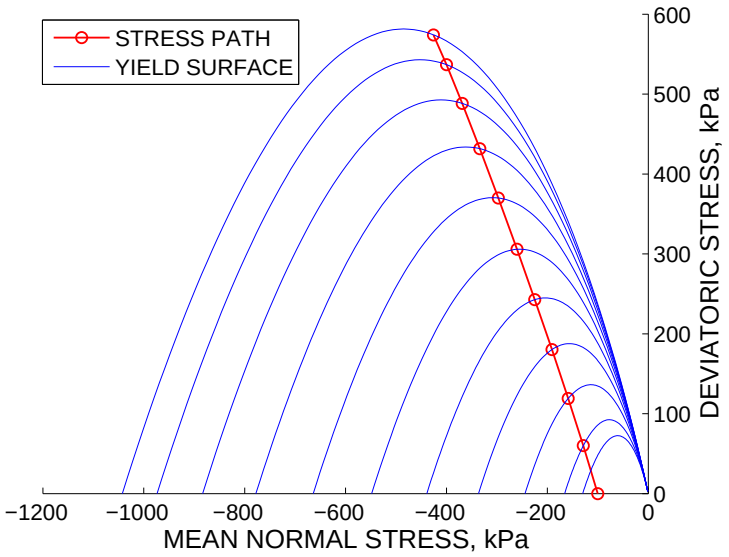

Figure 3.13: Stress path for homogeneous specimen simulation with finite deformation.

band did not exhibit an X-pattern in this case. Instead, the solution predicted a well-defined band extending across the specimen. Note that the horizontal slices shown in Figure 3.14b have been rotated by 90 degrees on the horizontal plane relative to the orientation of the solid volume shown in Figure 3.14a for optimal 3D visualization (red regions in Figure 3.14a must be matched with red regions in Figure 3.14b, etc.). As for the homogeneous specimen, the computation was carried out up to 15% nominal axial strain but the sample did not localize.

Figure 3.15 shows contours of the deviatoric invariant of logarithmic stretches at the point of initial localization. Again, the horizontal slices (Figure 3.15b) are 90 degrees rotated relative to the solid volume (Figure 3.15a) for better visualization. Comparing Figures 3.14 and 3.15, the solutions clearly correlated regions in the specimen where the determinant function vanished for the first time with regions where the deviatoric strains were most intense (a 'blue' determinant region correlates with a 'red' deviatoric strain region, etc.). In contrast, Figure 3.16 shows contours of the volumetric invariant of logarithmic stretches resembling the initial specific volume profile of Figure 3.10. In general, these observations are similar to those observed for the plane strain example. For completeness, Figure 3.17 shows the deformed FE mesh for the heterogeneous sample at the instant of initial localization, suggesting that the specimen moved laterally as well as twisted torsionally. Note once again

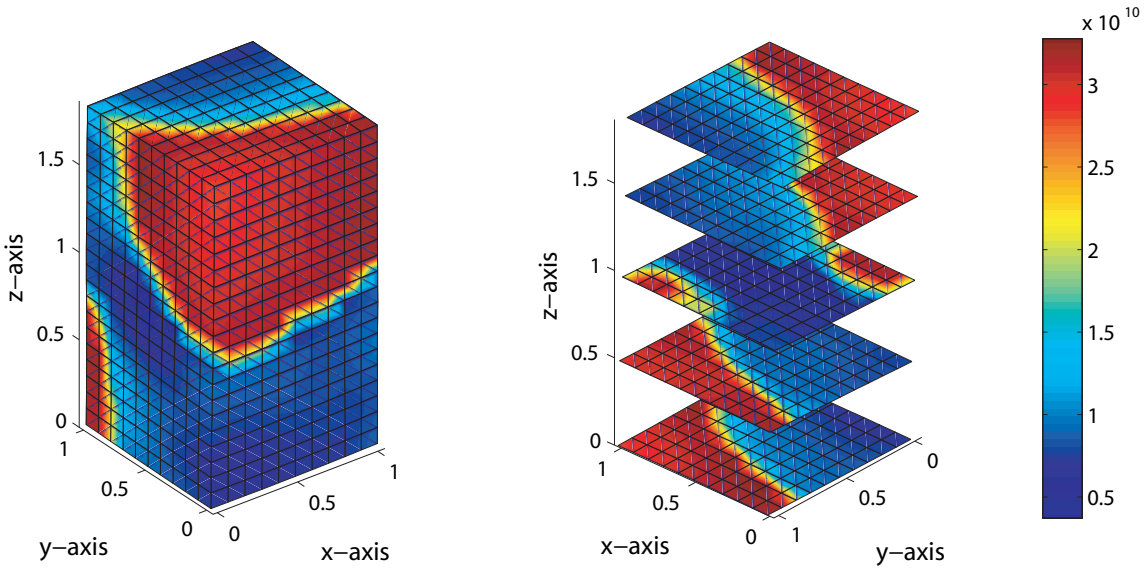

(a) (b)

Figure 3.14: Determinant function at onset of localization.

that this non-uniform deformation was triggered by the imposed initial density variation alone.

Finally, Figure 3.18 shows the convergence profiles of global Newton iterations for the full 3D finite deformation simulation of a heterogeneous specimen with B-bar integration. The iterations converged quadratically in all cases, suggesting optimal performance. We emphasize that all of the results presented above only pertain to the prediction of when and where a potential shear band will emerge. We have not pursued the simulations beyond the point of bifurcation due to mesh sensitivity issues inherent in rate-independent classical plasticity models in the post-localized regime. A host of regularization techniques either in the constitutive description or finite element solution are available and should be used to advance the solution to this regime.

3.5 Closure

We have presented a meso-scale finite element modeling approach for capturing deformation and strain localization in dense granular materials using critical state plasticity theory and nonlinear finite element analysis. This approach has been motivated in large part by

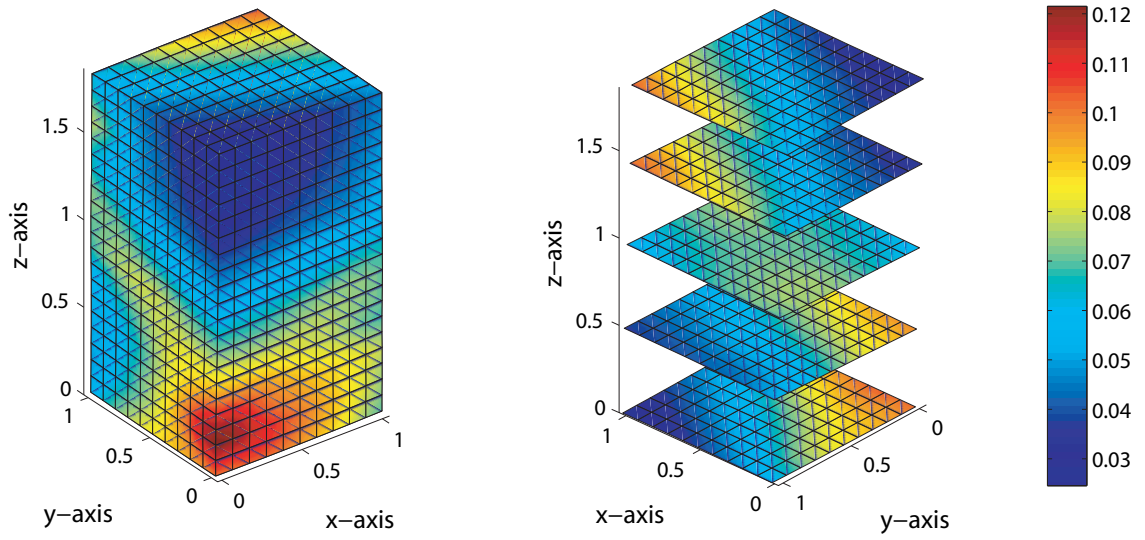

(a) (b)

Figure 3.15: Deviatoric invariant of logarithmic stretches at onset of strain localization.

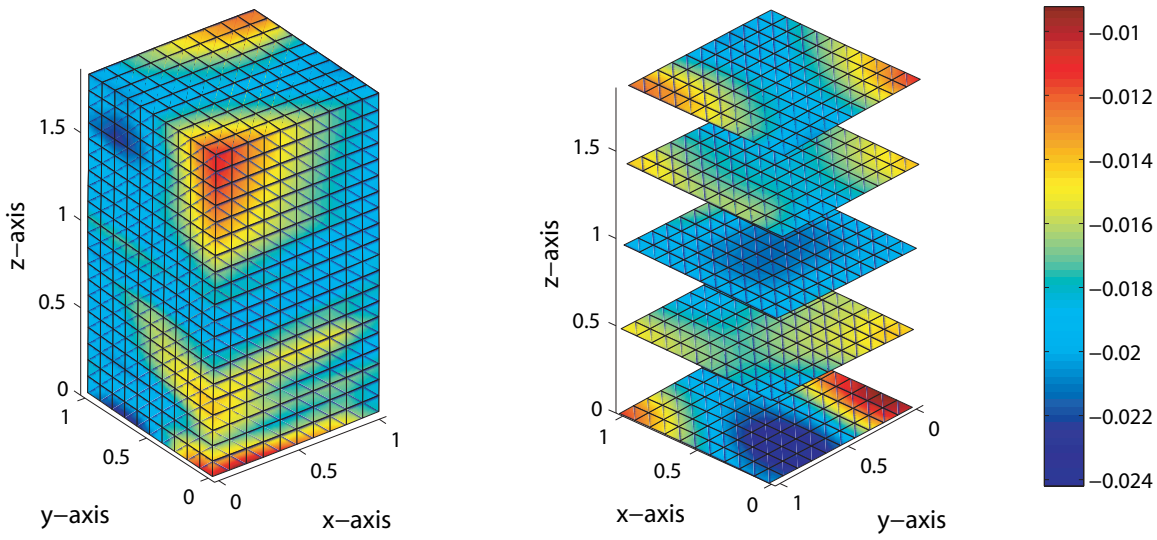

(a) (b)

Figure 3.16: Volumetric invariant of logarithmic stretches at onset of strain localization.

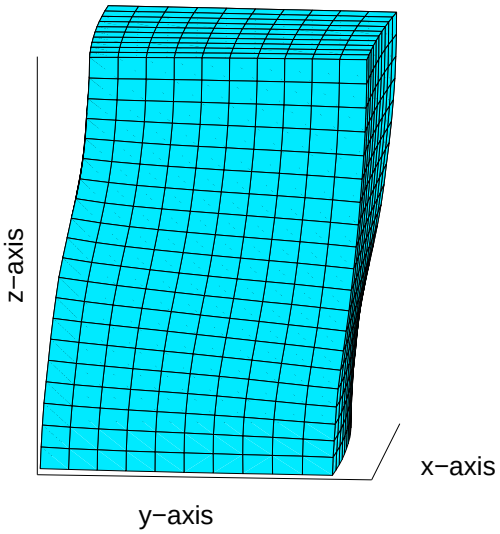

Figure 3.17: Deformed finite element mesh at onset of localization (deformation magnified by a factor of 3).

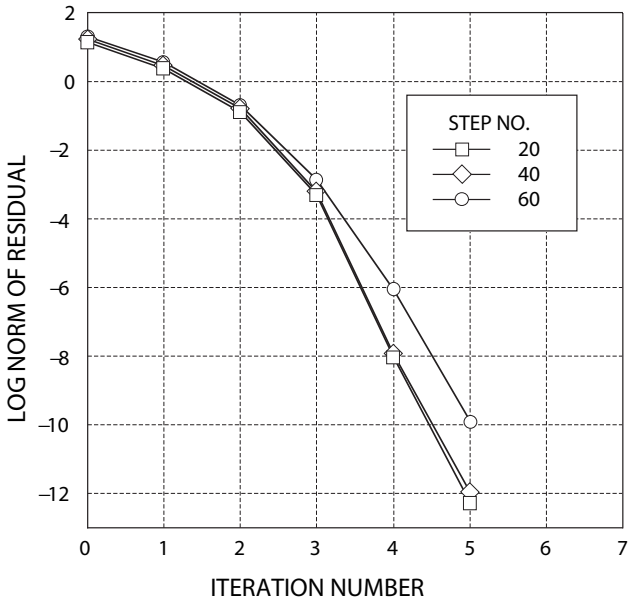

Figure 3.18: Convergence profiles of global Newton iterations: finite deformation simulation of heterogeneous specimen with B-bar.

recent trends in geotechnical laboratory testing allowing accurate quantitative measurement of the spatial density variation in discrete granular materials. The meso-scale approach provides a more realistic mathematical representation of imperfection; hence, it is expected to provide a more thorough capture of the deformation and strain localization processes in these materials. Potential extensions of the studies include a three-invariant enhancement of the plasticity model and application of the model to unstructured random density fields (in contrast to the structured density fields simulated in this paper). These aspects will be reported upon in a future publication.

Acknowledgments

This work has been supported by National Science Foundation under Grant Nos. CMS-0201317 and CMS-0324674 to Stanford University. We thank Professor Jack Baker of Stanford University for his assistance in generating the initial specific volume profiles used in the numerical examples, and Professor Amy Rechenmacher of USC for providing the X-Ray CT image shown in Figure 3.1. We also thank the two anonymous reviewers for their constructive reviews.

Chapter 4

Capturing strain localization in dense sands with random density

This Chapter is published in: J.E. Andrade and R. I. Borja. Capturing strain localization in dense sands with random density. *International Journal for Numerical Methods in Engineering*, 2006. In press.

Abstract

This paper presents a three-invariant constitutive framework suitable for the numerical analyses of localization instabilities in granular materials exhibiting unstructured random density. A recently proposed elastoplastic model for sands based on critical state plasticity is enhanced with the third stress invariant to capture the difference in the compressive and extensional yield strengths commonly observed in geomaterials undergoing plastic deformation. The new three-invariant constitutive model, similar to its two-invariant predecessor, is capable of accounting for meso-scale inhomogeneities as well as material and geometric nonlinearities. Details regarding the numerical implementation of the model into a fully nonlinear finite element framework are presented and a closed-form expression for the consistent tangent operator, whose spectral form is used in the strain localization analyses, is derived. An algorithm based on the spectral form of the so-called acoustic tensor is proposed to search for the necessary conditions for deformation bands to develop. The aforementioned framework is utilized in a series of boundary-value problems on dense sand

specimens whose density fields are modeled as exponentially distributed unstructured random fields to account for the effect of inhomogeneities at the meso-scale and the intrinsic uncertainty associated with them.

4.1 Introduction

Shear bands in granular materials, characterized by thin zones of intense shearing, have been a subject of considerable research interest since they impact many problems in the fields of geoengineering and geoscience. In geoengineering, shear bands control the deformation behavior and stability of earth structures such as dams, tunnels, excavations and foundations. In geoscience, they are commonly associated with grain fracturing and grain size reduction (termed "cataclasis" in the literature [43]) that are known to alter the strength and transport properties of geological systems. Various experimental and theoretical studies have thus attempted to analyze and describe the occurrence and patterns of shear bands in granular materials such as soils and rocks.

In sand bodies, shear band formations are now investigated in the laboratory using advanced testing techniques such as gamma-rays, stereophotogrammetry, and X-Ray Computed Tomography (CT), see [80]. Along with the more traditional laboratory testing procedures such as triaxial and simple shear testing, high-end testing provides an opportunity to view the specimen as an imperfect structure. For example, it is now possible to measure quantitatively the density and displacement fields within the specimen with a high degree of precision. Instead of viewing the entire specimen as a homogeneous element, which has been traditionally done in the past, it is now possible to digitally measure and quantify the properties and mechanical responses of an imperfect specimen on a finer scale.

Ironically, whereas development of very sophisticated constitutive models for element testing has previously outpaced the development of laboratory testing capabilities supporting the demands of these complex models, the reverse is now true with the advent of high-end precision laboratory testing. There is now a shortage of mathematical models that can adequately capture the quantified heterogeneities in the properties and mechanical responses of imperfect soil samples. This is because many of these sophisticated models are simply too complex to be implemented efficiently into multi-purpose finite element codes, and so only a handful of these models have been successful in finding their way into general-purpose computer codes. Since heterogeneous samples require that their responses be analyzed as

a boundary-value problem and not as an elemental point, many of these complex models have to be reformulated first before they can be used for general-purpose boundary-value problem simulations.

A promising approach to simulating material heterogeneity in specimens of discrete granular materials such as sand bodies is through meso-scale modeling. By "meso-scale" we mean a scale larger than a particle size but smaller than the specimen dimensions. We do not wish to go to particle level at this point since there is currently a lack of testing capabilities to capture all the particle information such as shapes, dimensions, and motion of the individual particles throughout testing. In contrast, some of the high-end testing techniques mentioned above, specifically the CT digital imaging technique, can very well be combined with existing computer tools that permit an accurate quantification of material heterogeneity in soil samples. Examples of such techniques include Digital Image Processing (DIP) for quantifying the spatial density variation and Digital Image Correlation (DIC) for tracking the motion of a group of particles contained in a "meso-element" having the size of a pixel [83, 84].

From a modeling standpoint, a key variable that quantitatively describes material heterogeneity on a meso-scale level is density. Whereas it may be argued that other constitutive variables such as strength and stiffness could also vary spatially within a soil sample, and therefore they should also be considered as meso-variables, it is generally difficult if not impossible to measure their spatial variation in a heterogeneous soil sample. In contrast, DIP can be used to analyze pixel patterns provided by CT images to correlate the gray level with density pattern in the individual pixels. Furthermore, strength and stiffness are known to correlate strongly with density in soils, so it seems plausible to claim that density is indeed a key measure of material heterogeneity.

Having chosen density as a key measure of material heterogeneity, we now consider a constitutive model based on critical state plasticity theory that permits the specification of spatial density variation within a soil sample. One such model, derived from the "Nor-Sand" of Jefferies [2] and presented by Borja and Andrade [122], utilizes a variable called "state parameter" ψ to describe the density of a meso-element relative to that at the critical state line for the same effective mean normal stress [2, 75, 106]. Where the point lies below the critical state line, ψ is negative (denser than critical), and where it lies above, ψ is positive (looser than critical). Traditional Cam-Clay type models [65, 66, 72, 73, 104, 105],

do not have the capability to independently prescribe the density (or void ratio) of a meso-element, since, by prescribing the degree of overconsolidation [65] and the current state of stress, one is bound to calculate a unique void ratio. By introducing the state parameter in the constitutive description, the density (or other equivalent measures thereof, such as the void ratio and specific volume) is effectively "detached" from the critical state line.

This paper moves one step further in refinement to the two-invariant model presented by Borja and Andrade [122] in that we now also quantify the influence of the third stress invariant in the constitutive description of meso-element behavior. Granular materials such as soils are known to exhibit yield stresses in compression that are higher than those in extension, so it only makes sense to include the third stress invariant in the constitutive formulation. Furthermore, it has been shown that the third stress invariant does enhance the onset of strain localization [111, 114], thus further motivating the present effort. For the present paper we introduce the third stress invariant through Lode's angle [123] and employ a return mapping algorithm in principal elastic logarithmic stretches (within the framework of multiplicative plasticity) to carry out the numerical integration in discrete load steps.

Apart from the inclusion of the third stress invariant, the present paper also models the effect of unstructured random density fields in the mathematical characterization of nearly homogeneous soil samples at meso-scale. Borja and Andrade [122] have shown that a well defined density structure, generated deterministically, could greatly impact the position of the resulting shear band. However, in reality most laboratory testing procedures attempt to generate as nearly uniform soil samples as possible. Thus the numerical simulations presented in this paper focus on nearly homogeneous density fields, generated randomly and without any preferred structure, to better capture reality. We show with extensive numerical simulations that even with such minute perturbations in the density field a shear band would still form even in cases where it would not form in perfectly homogeneous specimens. Further, we show that different shear bands could form in each randomly generated specimen, even with a very tight density distribution, affirming the common notion that each physical specimen is unique.

Evaluation of the consistent tangent operator (CTO) is critical for the success of a nonlinear iterative algorithm based on Newton's method, and in this paper we derive such tangent operator in spectral form based on Lie derivatives. Quite recently, Borja [114] has shown that such operator can also be used in lieu of the constitutive tangent operator

for strain localization analysis, so the CTO serves a dual role in the present numerical simulations. All simulations presented in this paper have been conducted in the 3D finite deformation regime, including the calculation of the minimum values of the localization function for shear band analysis [64]. For the latter analysis we also present an algorithm for a 3D search in spectral directions.

As for notations and symbols used in this paper, bold-faced letters denote tensors and vectors; the symbol '$\cdot$' denotes an inner product of two vectors (e.g. $\boldsymbol{a}\cdot\boldsymbol{b} = a_i b_i$), or a single contraction of adjacent indices of two tensors (e.g. $\boldsymbol{c}\cdot\boldsymbol{d} = c_{ij}d_{jk}$); the symbol ':' denotes an inner product of two second-order tensors (e.g. $\boldsymbol{c} : \boldsymbol{d} = c_{ij}d_{ij}$), or a double contraction of adjacent indices of tensors of rank two and higher (e.g. $\boldsymbol{C} : \boldsymbol{\epsilon}^{\mathrm{e}} = C_{ijkl}\epsilon^{\mathrm{e}}_{kl}$); the symbol '$\otimes$' denotes a juxtaposition, e.g., $(\boldsymbol{a}\otimes\boldsymbol{b})_{ij} = a_i b_j$. Finally, for any symmetric second order tensors $\boldsymbol{\alpha}$ and $\boldsymbol{\beta}$, $(\boldsymbol{\alpha}\otimes\boldsymbol{\beta})_{ijkl} = \alpha_{ij}\beta_{kl}$, $(\boldsymbol{\alpha}\oplus\boldsymbol{\beta})_{ijkl} = \beta_{ik}\alpha_{jl}$, and $(\boldsymbol{\alpha}\ominus\boldsymbol{\beta})_{ijkl} = \alpha_{il}\beta_{jk}$.

4.2 Constitutive assumptions

In this section we present a three-invariant enhancement of the critical state plasticity model by Borja and Andrade [122]. As mentioned in the Introduction, geomaterials exhibit a higher yield strength in compression than in extension, so the addition of the third stress invariant is critical for modeling the behavior of geomaterials more realistically. Further, the hyperelastoplastic model hinges on the well established assumption that the deformation gradient tensor can be decomposed multiplicatively into elastic and plastic parts [115],

$$\boldsymbol{F} = \boldsymbol{F}^{\mathrm{e}}\cdot\boldsymbol{F}^{\mathrm{p}}, \tag{4.2.1}$$

where $\boldsymbol{F}^{\mathrm{e}}$ and $\boldsymbol{F}^{\mathrm{p}}$ are defined as the elastic and plastic deformation gradient, respectively.

4.2.1 The hyperelastic model

Consider an isotropic hyperelastic response entailing a strain energy that is a function of either the elastic right Cauchy-Green deformation tensor $\boldsymbol{C}^{\mathrm{e}}$ or the left Cauchy-Green tensor $\boldsymbol{b}^{\mathrm{e}}$ i.e., $\Psi = \Psi(\boldsymbol{C}^{\mathrm{e}}) = \Psi(\boldsymbol{b}^{\mathrm{e}})$ [30, 124], where

$$\boldsymbol{C}^{\mathrm{e}} := \boldsymbol{F}^{\mathrm{e}\,\mathrm{t}}\cdot\boldsymbol{F}^{\mathrm{e}} \qquad \text{and} \qquad \boldsymbol{b}^{\mathrm{e}} := \boldsymbol{F}^{\mathrm{e}}\cdot\boldsymbol{F}^{\mathrm{e}\,\mathrm{t}}. \tag{4.2.2}$$

The principal elastic stretches emanate from $\boldsymbol{F}^{\mathrm{e}} \cdot \boldsymbol{N}^a = \lambda_a^{\mathrm{e}} \boldsymbol{n}^a$ (no sum), where λ_a^{e} for $a = 1, 2, 3$ are the principal elastic stretches in the corresponding principal directions $\boldsymbol{N}^a$ and $\boldsymbol{n}^a$ in the intermediate and current configuration, respectively. We recall the well known spectral decomposition,

$$\boldsymbol{b}^{\mathrm{e}} = \sum_{a=1}^{3} \lambda_a^{\mathrm{e}\,2} \boldsymbol{n}^a \otimes \boldsymbol{n}^a. \tag{4.2.3}$$

The elastic region is assumed to be governed by the isotropic strain energy function proposed in [1] and utilized in modeling of granular bodies in [66, 125]

$$\Psi\left(\varepsilon_{\mathrm{v}}^{\mathrm{e}}, \varepsilon_{\mathrm{s}}^{\mathrm{e}}\right) = \tilde{\Psi}\left(\varepsilon_{\mathrm{v}}^{\mathrm{e}}\right) + \frac{3}{2}\mu^{\mathrm{e}} \varepsilon_{\mathrm{s}}^{\mathrm{e}\,2}, \tag{4.2.4}$$

where

$$\tilde{\Psi}\left(\varepsilon_{\mathrm{v}}^{\mathrm{e}}\right) = -p_0 \hat{\kappa} \exp \omega, \qquad \omega = -\frac{\varepsilon_{\mathrm{v}}^{\mathrm{e}} - \varepsilon_{\mathrm{v}\,0}^{\mathrm{e}}}{\hat{\kappa}}, \qquad \mu^{\mathrm{e}} = \mu_0 + \frac{\alpha_0}{\hat{\kappa}} \tilde{\Psi}\left(\varepsilon_{\mathrm{v}}^{\mathrm{e}}\right). \tag{4.2.5}$$

The independent variables are the volumetric and deviatoric invariants of the elastic logarithmic stretch tensor, respectively,

$$\varepsilon_{\mathrm{v}}^{\mathrm{e}} = \varepsilon_1^{\mathrm{e}} + \varepsilon_2^{\mathrm{e}} + \varepsilon_3^{\mathrm{e}} \qquad \text{and} \qquad \varepsilon_{\mathrm{s}}^{\mathrm{e}} = \frac{1}{3}\sqrt{2\left[\left(\varepsilon_1^{\mathrm{e}} - \varepsilon_2^{\mathrm{e}}\right)^2 + \left(\varepsilon_2^{\mathrm{e}} - \varepsilon_3^{\mathrm{e}}\right)^2 + \left(\varepsilon_3^{\mathrm{e}} - \varepsilon_1^{\mathrm{e}}\right)^2\right]}, \tag{4.2.6}$$

where $\varepsilon_a^{\mathrm{e}} \equiv \ln \lambda_a^{\mathrm{e}}$. Hence, the strain energy function is an invariant function of the elastic deformations. The Kirchhoff stress tensor $\boldsymbol{\tau}$ is coaxial with the deformation tensor $\boldsymbol{b}^{\mathrm{e}}$ and defined such that

$$\boldsymbol{\tau} = 2\frac{\partial \Psi}{\partial \boldsymbol{b}^{\mathrm{e}}} \cdot \boldsymbol{b}^{\mathrm{e}}. \tag{4.2.7}$$

The above hyperelastic model produces pressure-dependent elastic bulk and shear moduli, a feature commonly observed in the laboratory. The elastic constants necessary for a full description of the elasticity are the reference strain $\varepsilon_{\mathrm{v}\,0}^{\mathrm{e}}$ and the reference pressure p_0 of the elastic compression curve, as well as the compressibility index $\hat{\kappa}$. The model produces coupled volumetric and deviatoric responses in the case $\alpha_0 \neq 0$ for which μ^{e} is a nonlinear function of the volumetric deformations. Otherwise, for $\alpha_0 = 0$ the responses are decoupled and the shear modulus $\mu^{\mathrm{e}} \equiv \mu_0$ is constant.

4.2.2 Yield surface, plastic potential, their derivatives and the flow rule

We define the three invariants of the Kirchhoff stress tensor as

$$p = \frac{1}{3}\operatorname{tr}\boldsymbol{\tau}, \qquad q = \sqrt{\frac{3}{2}}\|\boldsymbol{\xi}\|, \qquad \frac{1}{\sqrt{6}}\cos 3\theta = \frac{\operatorname{tr}\boldsymbol{\xi}^3}{\chi^3} \equiv y, \tag{4.2.8}$$

where $\boldsymbol{\xi} = \boldsymbol{\tau} - p\mathbf{1}$ is the deviatoric component of the stress tensor $\boldsymbol{\tau}$, and $\chi = \sqrt{\operatorname{tr}\boldsymbol{\xi}^2}$. The quantity p is called the mean normal stress and is assumed negative throughout. Further, θ is the Lode's angle whose values range from $0 \leq \theta \leq \pi/3$; it defines an angle on a deviatoric plane emanating from a tension corner.

From these three stress invariants we construct a yield surface of the form

$$F(\boldsymbol{\tau}, \pi_{\mathrm{i}}) = F(p, q, \theta, \pi_{\mathrm{i}}) = \zeta(\theta)\, q + p\eta(p, \pi_{\mathrm{i}}) \tag{4.2.9}$$

where

$$\eta = \begin{cases} M\left[1 + \ln\left(\pi_{\mathrm{i}}/p\right)\right] & \text{if} \quad N = 0 \\ M/N\left[1 - (1-N)\left(p/\pi_{\mathrm{i}}\right)^{N/(1-N)}\right] & \text{if} \quad N > 0. \end{cases} \tag{4.2.10}$$

The image stress $\pi_{\mathrm{i}} < 0$ controls the size of the yield surface; it is defined such that the stress ratio $\eta = -\zeta q/p = M$ when $p = \pi_{\mathrm{i}}$. Note the subscript 'i' stands for image and should not be confused with index notation. The parameter $N \geq 0$ determines the curvature of the yield surface on a meridian plane and it typically has a value less than or equal to 0.4 for sands [2]. Lode's angle θ plays the role of the third stress invariant modifying the shape of the yield surface on a deviatoric plane through the function $\zeta = \zeta(\theta)$. Many forms for the function $\zeta(\theta)$ have been proposed in the literature (see [126] for a historical survey). Here we adopt the form proposed by Gudehus in [127] and Argyris et al. in [128], namely,

$$\zeta(\theta, \rho) = \frac{(1+\rho) + (1-\rho)\cos 3\theta}{2\rho} \tag{4.2.11}$$

where ρ is a constant parameter called ellipticity. The above function is only convex for $7/9 \leq \rho \leq 1$ [129] and satisfies the boundary conditions: (a) $\zeta = 1/\rho$ when $\theta = 0$ i.e., tension corner; and (b) $\zeta = 1$ when $\theta = \pi/3$ i.e., compression corner. A typical three-invariant yield surface of the form presented above for $\rho = 0.78$ is shown in Figure 1. It can be seen from this figure that the yield surface exhibits a greater yield strength under compression than under extension.

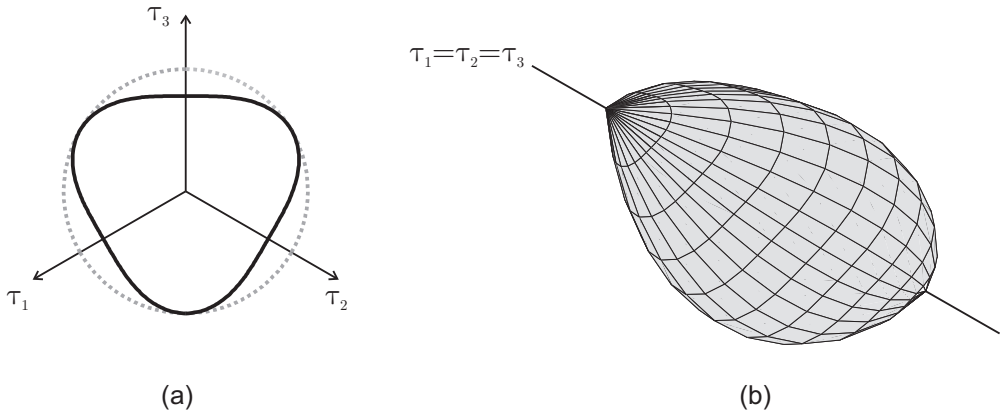

Figure 4.1: Three-invariant yield surface in Kirchhoff stress space for $\rho = 0.78$. (a) Cross-section on deviatoric plane, dashed line represents two-invariant counterpart for comparison and (b) three-dimensinal view.

Additionally, to underscore the fact that the formulation presented herein is general and independent of the choice of the shape function $\zeta(\theta, \rho)$, in some of our numerical examples, we will also utilize the form proposed by Willam and Warnke [130] i.e.,

$$\zeta(\theta,\rho) = \frac{4\left(1-\rho^2\right)\cos^2\theta + (2\rho-1)^2}{2\left(1-\rho^2\right)\cos\theta + (2\rho-1)\left[4\left(1-\rho^2\right)\cos^2\theta + 5\rho^2 - 4\rho\right]^{1/2}}. \tag{4.2.12}$$

This function is smooth and convex in the range $1/2 \leq \rho \leq 1$, and has the same boundary conditions than the shape function in (4.2.11).

Similar to the yield surface, we can postulate a plastic potential function of the form

$$Q(\boldsymbol{\tau}, \overline{\pi}_{\mathrm{i}}) = Q(p, q, \theta, \overline{\pi}_{\mathrm{i}}) = \overline{\zeta}(\theta)\, q + p\overline{\eta}(p, \overline{\pi}_{\mathrm{i}}) \tag{4.2.13}$$

with

$$\overline{\eta} = \begin{cases} M\left[1 + \ln\left(\overline{\pi}_{\mathrm{i}}/p\right)\right] & \text{if} \quad \overline{N} = 0 \\ M/\overline{N}\left[1 - \left(1-\overline{N}\right)\left(p/\overline{\pi}_{\mathrm{i}}\right)^{\overline{N}/\left(1-\overline{N}\right)}\right] & \text{if} \quad \overline{N} > 0. \end{cases} \tag{4.2.14}$$

When $\overline{\pi}_{\mathrm{i}} = \pi_{\mathrm{i}}$, $\overline{N} = N$ and $\overline{\zeta} = \zeta$, plastic flow is associative; otherwise, it is nonassociative in both the volumetric and deviatoric sense. The material parameter $\overline{N}$ controls the amount of *volumetric* nonassociativity, whereas the shape function $\overline{\zeta} = \zeta(\theta, \overline{\rho})$ plays a similar role than that used in the yield surface, but the ellipticity $\overline{\rho}$ can be different from ρ, hence

introducing *deviatoric* nonassociativity. We note in passing that the plastic potential in (4.2.13) is essentially that proposed by Jefferies in [2] for $\overline{\zeta} = 1$.

Recall the multiplicative decomposition of the deformation gradient tensor in (4.2.1), which leads to an additive decomposition of the velocity gradient $\boldsymbol{l}$,

$$\boldsymbol{l} = \boldsymbol{l}^{\mathrm{e}} + \boldsymbol{l}^{\mathrm{p}} \qquad \Rightarrow \qquad \boldsymbol{d} = \boldsymbol{d}^{\mathrm{e}} + \boldsymbol{d}^{\mathrm{p}}, \tag{4.2.15}$$

where $\boldsymbol{d} \equiv \operatorname{sym} \boldsymbol{l}$, $\boldsymbol{d}^{\mathrm{e}} \equiv \operatorname{sym} \boldsymbol{l}^{\mathrm{e}}$, and $\boldsymbol{d}^{\mathrm{p}} \equiv \operatorname{sym} \boldsymbol{l}^{\mathrm{p}}$. Neglecting the plastic spin $\boldsymbol{\omega}^{\mathrm{p}}$ (see [118] for significance and consequences), we write the flow rule as

$$\boldsymbol{d}^{\mathrm{p}} = \dot{\lambda} \boldsymbol{q}, \tag{4.2.16}$$

where $\dot{\lambda}$ is the so-called consistency parameter, and $\boldsymbol{q} := \partial Q / \partial \boldsymbol{\tau}$. Adopting the spectral approach [111], we recast the above gradient as

$$\boldsymbol{q} = \frac{\partial Q}{\partial \boldsymbol{\tau}} = \sum_{a=1}^{3} \frac{\partial Q}{\partial \tau_a} \boldsymbol{m}^a = \sum_{a=1}^{3} q_a \boldsymbol{m}^a \tag{4.2.17}$$

where $\boldsymbol{m}^a := \boldsymbol{n}^a \otimes \boldsymbol{n}^a$, and the vectors $\boldsymbol{n}^a$ for $a = 1, 2, 3$, are the principal directions of the stress tensor $\boldsymbol{\tau}$, i.e., $\boldsymbol{\tau} \cdot \boldsymbol{n}^a = \tau_a \boldsymbol{n}^a$, with principal stresses τ_a for $a = 1, 2, 3$. Note that the stress tensor $\boldsymbol{\tau}$ and the elastic left Cauchy-Green deformation tensor $\boldsymbol{b}^{\mathrm{e}}$ are coaxial due to the isotropy assumption made in Section 4.2.1 above. The spectral decomposition of the flow rule is consequently a by-product of the coaxiality of the tensors $\boldsymbol{\tau}$ and $\boldsymbol{b}^{\mathrm{e}}$ as well as the fact that Q is an isotropic function of the stress tensor and hence its gradient and the stress tensor are also coaxial. It is then useful to expand q_a such that

$$q_a = \frac{\partial Q}{\partial p} \frac{\partial p}{\partial \tau_a} + \frac{\partial Q}{\partial q} \frac{\partial q}{\partial \tau_a} + \frac{\partial Q}{\partial \theta} \frac{\partial \theta}{\partial \tau_a} \tag{4.2.18}$$

where we can easily show that

$$\frac{\partial p}{\partial \tau_a} = \frac{1}{3} \delta_a, \qquad \frac{\partial q}{\partial \tau_a} = \sqrt{\frac{3}{2}} \frac{\xi_a}{\chi} \equiv \sqrt{\frac{3}{2}} \hat{n}_a, \qquad \frac{\partial \theta}{\partial \tau_a} \equiv \theta_a = -\left(\frac{2}{\sqrt{6}} \csc 3\theta \right) y_a, \tag{4.2.19}$$

where $\delta_a = 1$, and ξ_a for $a = 1, 2, 3$ are the eigenvalues of the deviatoric stress tensor $\boldsymbol{\xi}$. Additionally,

$$y_a = \frac{\partial y}{\partial \tau_a} = 3 \frac{\xi_a^2}{\chi^3} - 3 \frac{\operatorname{tr}\left(\boldsymbol{\xi}^3\right) \xi_a}{\chi^5} - \frac{\delta_a}{\chi}, \tag{4.2.20}$$

which we use to write q_a in more compact form

$$q_a = \frac{1}{3}\partial_p Q \delta_a + \sqrt{\frac{3}{2}}\partial_q Q \hat{n}_a + \partial_\theta Q \theta_a. \tag{4.2.21}$$

From equations (4.2.9) and (4.2.13), we obtain

$$\frac{\partial Q}{\partial p} = \beta \frac{\partial F}{\partial p}, \qquad \frac{\partial Q}{\partial q} = \overline{\zeta}, \qquad \frac{\partial Q}{\partial \theta} = \overline{\zeta}' q, \tag{4.2.22}$$

where we have used the volumetric nonassociativity parameter
$\beta := (1-N) \,/\, \left(1-\overline{N}\right)$. Thus,

$$q_a = \frac{1}{3}\beta\partial_p F \delta_a + \sqrt{\frac{3}{2}}\partial_q Q \hat{n}_a + \partial_\theta Q \theta_a, \tag{4.2.23}$$

from where we clearly see the volumetric and deviatoric nonassociativity in the plastic flow. Using the above expression for the yield surface, we calculate the derivatives

$$\frac{\partial F}{\partial p} = \frac{\eta - M}{1-N}, \qquad \frac{\partial F}{\partial q} = \zeta, \qquad \frac{\partial F}{\partial \theta} = \zeta' q. \tag{4.2.24}$$

It is now convenient to evaluate the second derivative of the plastic potential with respect to the stress tensor, as it will be used in the numerical implementation of the model. Here, we exploit the uncoupling between the volumetric and deviatoric terms in F and write

$$\begin{aligned} q_{ab} &= \frac{1}{9}\beta\partial^2_{pp} F \delta_a \delta_b + \sqrt{\frac{3}{2}}\partial_q Q \hat{n}_{ab} + \partial_\theta Q \theta_{ab} + \partial^2_{\theta\theta} Q \theta_a \theta_b \\ &+ \sqrt{\frac{3}{2}}\partial^2_{q\theta} Q \left(\hat{n}_a \theta_b + \theta_a \hat{n}_b\right), \end{aligned} \tag{4.2.25}$$

where, from equations (4.2.24) and (4.2.22), we get

$$\partial^2_{pp} F = -\frac{M}{1-N}\frac{1}{p}\left(\frac{p}{p_\mathrm{i}}\right)^{N/(1-N)}, \qquad \partial^2_{\theta\theta} Q = \overline{\zeta}'' q, \qquad \partial^2_{q\theta} Q = \overline{\zeta}'. \tag{4.2.26}$$

Furthermore, from equations $(4.2.19)_{2,3}$ we get, respectively,

$$\hat{n}_{ab} = \frac{1}{\chi}\left(\delta_{ab} - \frac{1}{3}\delta_a\delta_b - \hat{n}_a\hat{n}_b\right) \qquad \text{and} \qquad \theta_{ab} = -\left(\frac{2}{\sqrt{6}}\csc 3\theta\right) y_{ab} - (3\cot 3\theta)\,\theta_a\theta_b, \tag{4.2.27}$$

with

$$y_{ab} = 6\frac{\xi_a\delta_{ab}}{\chi^3} - 3\frac{\operatorname{tr}\boldsymbol{\xi}^3}{\chi^5}\left(\delta_{ab} - \frac{1}{3}\delta_a\delta_b - 5\frac{\xi_a\xi_b}{\chi^2}\right) + \frac{1}{\chi^3}\left(\delta_a\xi_b + \xi_a\delta_b\right) - \frac{9}{\chi^5}\left(\xi_a\xi_b^2 + \xi_a^2\xi_b\right) \qquad \text{(no sum)}. \tag{4.2.28}$$

Reduced dissipation inequality: the second law of thermodynamics

For perfect plasticity, the reduced dissipation inequality requires the stresses to perform nonnegative plastic incremental work [112], i.e.,

$$\mathcal{D}^{\mathrm{p}} \equiv \boldsymbol{\tau} : \boldsymbol{d}^{\mathrm{p}} = \dot{\lambda}\boldsymbol{\tau} : \boldsymbol{q} = \dot{\lambda}\sum_{a=1}^{3}\tau_a q_a \geq 0. \tag{4.2.29}$$

Realizing that $\sum_{a=1}^{3}\tau_a\theta_a = 0$, we can write

$$\mathcal{D}^{\mathrm{p}} = \dot{\lambda}\left(p\partial_p Q + q\partial_q Q\right) = -\dot{\lambda}p\left(\frac{M-\overline{\eta}}{1-\overline{N}} + \overline{\eta}\right) \geq 0, \tag{4.2.30}$$

where we have exploited the fact that at yield $F = Q = 0$. Since $-\dot{\lambda}p \geq 0$ and $1 - \overline{N} > 0$, we require $-\overline{N}\overline{\eta} + M \geq 0$. Now, for a stress point on the yield surface, the relationship $\overline{\eta}/\overline{\zeta} = \eta/\zeta$ holds, hence,

$$\mathcal{D}^{\mathrm{p}} \geq 0 \qquad \Rightarrow \qquad -M\frac{\overline{N}}{N}\frac{\overline{\zeta}}{\zeta}\left[1 - (1-N)\left(\frac{p}{\pi_{\mathrm{i}}}\right)^{N/(1-N)}\right] + M \geq 0. \tag{4.2.31}$$

It can be seen that the function inside the square brackets is a monotonically decreasing function and always less than unity for $p \in [\pi_{\mathrm{c}}, 0]$, where $\pi_{\mathrm{c}} = \pi_{\mathrm{i}}/\left(1-N\right)^{(1-N)/N}$ is the preconsolidation pressure. Therefore, since $M > 0$ as it is a physical parameter, we get the condition $\left(\overline{N}\,\overline{\zeta}\right)/\left(N\zeta\right) \leq 1$, which is satisfied at all times if

$$\overline{N} \leq N \qquad \text{and} \qquad \overline{\zeta} \leq \zeta. \tag{4.2.32}$$

The first condition was already derived by the authors in [122] in the context of two-invariant plasticity, whereas the second condition is a by-product of the third invariant. Both restrictions derived above can be linked to the angle of friction and angle of dilation as $\overline{N} \leq N$ implies lower dilatancy than that achieved from a volumetric associative flow

rule. On the other hand, it is easy to show that the second condition requires $\rho \leq \overline{\rho}$, and since

$$\rho \equiv \frac{3 - \sin\phi_c}{3 + \sin\phi_c} \qquad \text{and} \qquad \overline{\rho} \equiv \frac{3 - \sin\psi_c}{3 + \sin\psi_c}, \tag{4.2.33}$$

where ϕ_c is the angle of internal friction at critical and ψ_c is the dilatancy angle at critical, it follows that

$$\psi_c \leq \phi_c, \tag{4.2.34}$$

which is very much consistent with thermodynamic conditions found for Mohr-Coulomb or Drucker-Prager materials and experimental observations in geomaterials, see [110, 111] for further elaboration.

Remark 3. Experimental evidence in granular materials seems to suggest deviatoric nonassociativity in these materials is not pronounced. Lade and Duncan [8] have shown that, for dense sands, the plastic strain rates are perpendicular to the yield surface on a deviatoric plane. Nevertheless, the formulation presented above is general and allows for deviatoric and volumetric nonassociativity.

4.2.3 Maximum plastic dilatancy, hardening law and the consistency condition

We recall the definitions for the volumetric and deviatoric plastic strain rate invariants, respectively,

$$\dot{\varepsilon}^{\mathrm{p}}_{\mathrm{v}} = \operatorname{tr} \boldsymbol{d}^{\mathrm{p}} \qquad \text{and} \qquad \dot{\varepsilon}^{\mathrm{p}}_{\mathrm{s}} = \sqrt{\frac{2}{3}} \left\| \boldsymbol{d}^{\mathrm{p}} - 1/3\dot{\varepsilon}^{\mathrm{p}}_{\mathrm{v}}\mathbf{1} \right\|. \tag{4.2.35}$$

Using the definitions above and equations (4.2.16)-(4.2.17), and (4.2.21) we get

$$\dot{\varepsilon}^{\mathrm{p}}_{\mathrm{v}} = \dot{\lambda} \sum_{a=1}^{3} q_a \qquad \text{and} \qquad \dot{\varepsilon}^{\mathrm{p}}_{\mathrm{s}} = \dot{\lambda} \sqrt{\frac{2}{3} \sum_{a=1}^{3} \tilde{q}_a^2}, \tag{4.2.36}$$

where we have $\sum_{a=1}^{3} q_a = \partial_p Q$, and $\tilde{q}_a = q_a - 1/3\partial_p Q \delta_a$. Hence,

$$\dot{\varepsilon}^{\mathrm{p}}_{\mathrm{v}} = \dot{\lambda}\beta\partial_p F \qquad \text{and} \qquad \dot{\varepsilon}^{\mathrm{p}}_{\mathrm{s}} = \dot{\lambda}\sqrt{\frac{2}{3}}\Omega\left(q, \theta\right), \tag{4.2.37}$$

with

$$\Omega\left(\boldsymbol{\tau}\right) = \Omega\left(q, \theta\right) = \sqrt{\frac{3}{2}(\partial_q Q)^2 + (\partial_\theta Q)^2 \left[\theta_1^2 + \theta_2^2 + \theta_3^2\right]}. \tag{4.2.38}$$

Now, we recall the definition of plastic dilatancy

$$D := \frac{\dot{\varepsilon}_{\mathrm{v}}^{\mathrm{p}}}{\dot{\varepsilon}_{\mathrm{s}}^{\mathrm{p}}} = \sqrt{\frac{3}{2}}\beta\frac{\partial_p F}{\Omega}, \tag{4.2.39}$$

which we can use to obtain the maximum dilatancy and thereby maximum stress ratio η^* such that

$$D^* = \alpha\psi_{\mathrm{i}} = \sqrt{\frac{3}{2}}\beta\frac{\eta^* - M}{(1-N)\,\Omega}. \tag{4.2.40}$$

After rearranging, we get $\eta^* = \sqrt{2/3}\overline{\alpha}\psi_{\mathrm{i}}(1-N)\Omega + M$, with $\alpha = \beta\overline{\alpha}$ and $\alpha \approx -3.5$ for sands. Recall the maximum plastic dilatancy is used to limit the amount of dilation in a sand specimen on the 'wet' side of the critical state line. As in the original model proposed by Been and Jefferies in [106] and Jefferies in [2], the maximum dilatancy is obtained through an empirical relation with the state parameter ψ_{i}, which is a distance between the specific volume of the sample and the specific volume at critical at the image pressure i.e.,

$$\psi_{\mathrm{i}} = v - v_{c0} + \hat{\lambda}\ln\left(-\pi_{\mathrm{i}}\right), \tag{4.2.41}$$

where v is the specific volume, v_{c0} is the reference specific volume at unit pressure, and $\hat{\lambda}$ is the plastic compressibility index. All of these parameters emanate from the so-called critical state theory which postulates the existence of the critical state line. Inserting the above result into equation (4.2.10) and solving for the corresponding limiting image pressure we get, cf. [122],

$$\frac{\pi_{\mathrm{i}}^*}{p} = \begin{cases} \exp\left(\sqrt{2/3}\overline{\alpha}/M\psi_{\mathrm{i}}\Omega\right) & \text{if} \quad \overline{N} = N = 0, \\ \left(1 - \sqrt{2/3}\overline{\alpha}\psi_{\mathrm{i}}\Omega N/M\right)^{(N-1)/N} & \text{if} \quad 0 \leq \overline{N} \leq N \neq 0. \end{cases} \tag{4.2.42}$$

Recall the hardening law, which relates the image pressure with the state of stress, the state parameter ψ_{i}, and the *deviatoric* component of plastic flow, i.e.,

$$\dot{\pi}_{\mathrm{i}} = h\left(\pi_{\mathrm{i}}^* - \pi_{\mathrm{i}}\right)\dot{\varepsilon}_{\mathrm{s}}^{\mathrm{p}} = \sqrt{\frac{2}{3}}h\dot{\lambda}\left(\pi_{\mathrm{i}}^* - \pi_{\mathrm{i}}\right)\Omega, \tag{4.2.43}$$

where h is a constant material property, to be calibrated in the finite deformation regime.

Finally, for elastoplasticity the consistency condition necessitates

$$\dot{F} = \boldsymbol{f} : \dot{\boldsymbol{\tau}} - H\dot{\lambda} = 0, \qquad \dot{\lambda} > 0, \tag{4.2.44}$$

where $\boldsymbol{f} := \partial F/\partial \boldsymbol{\tau}$ and H is the so-called hardening modulus defined as

$$H = -\frac{1}{\dot{\lambda}}\frac{\partial F}{\partial \pi_{\mathrm{i}}}\dot{\pi}_{\mathrm{i}} = -\frac{1}{\dot{\lambda}}\left(\frac{p}{\pi_{\mathrm{i}}}\right)^{1/(1-N)} M\dot{\pi}_{\mathrm{i}}. \tag{4.2.45}$$

Since $p/\pi_{\mathrm{i}} > 0$, the sign of the hardening modulus is governed by the sign of the image pressure rate: $H > 0$ if $\dot{\pi}_{\mathrm{i}} < 0$ (expansion of the yield surface, hardening), $H < 0$ if $\dot{\pi}_{\mathrm{i}} > 0$ (contraction of the yield surface, softening), and $H = 0$ if $\dot{\pi}_{\mathrm{i}} = 0$ (perfect plasticity).

Remark 4. The continuum formulation presented above is a generalization of that presented in [122]. In fact, when $\zeta = \overline{\zeta} = 1 \; \forall\, \theta \in [0, \pi/3]$, all derivatives of Q with respect to θ drop out, and with $\Omega = \sqrt{3/2}$ we recover the original two-invariant version of the model.

4.3 Numerical implementation

We perform a numerical stress point integration based on the product formula algorithm similar to that proposed by Simo in [117]. However, here we perform the return mapping in the elastic principal stretch directions to accommodate for nonlinear elasticity. Note that the algorithm provides a closed-form expression for the consistent tangent operator (CTO). The numerical implementation developed below is summarized in Tables 4.1 and 4.2. Table 4.1 presents a summary of the evolution equations used in the local return mapping, whose recipe is presented in turn in Table 4.2.

4.3.1 Local return mapping algorithm

Recall the definition of the elastic left Cauchy-Green deformation tensor given in equation $(4.2.2)_2$. From this expression we obtain the trial elastic left Cauchy-Green deformation tensor at time station t_{n+1} by freezing plastic flow i.e.,

$$\boldsymbol{b}^{\mathrm{e\,tr}} \equiv \tilde{\boldsymbol{b}} = \boldsymbol{f}_{n+1} \cdot \boldsymbol{b}^{\mathrm{e}}_{n} \cdot \boldsymbol{f}^{\mathrm{t}}_{n+1}, \qquad \boldsymbol{f}_{n+1} = \frac{\partial \boldsymbol{x}_{n+1}}{\partial \boldsymbol{x}_{n}}. \tag{4.3.1}$$

Table 4.1: Summary of rate equations in three-invariant elastoplastic model for sands.

1. Additive velocity gradient: $\boldsymbol{l} = \boldsymbol{l}^{\mathrm{e}} + \boldsymbol{l}^{\mathrm{p}} \quad \Longrightarrow \quad \boldsymbol{d} = \boldsymbol{d}^{\mathrm{e}} + \boldsymbol{d}^{\mathrm{p}}$
2. Hyperelastic rate equations: $\mathcal{L}_{\boldsymbol{v}}(\boldsymbol{\tau}) = \boldsymbol{c}^{\mathrm{e}} : \boldsymbol{d}^{\mathrm{e}}$;
   $\boldsymbol{c}^{\mathrm{e}} = 4\boldsymbol{b}^{\mathrm{e}} \cdot \partial\Psi / (\partial\boldsymbol{b}^{\mathrm{e}} \otimes \partial\boldsymbol{b}^{\mathrm{e}}) \cdot \boldsymbol{b}^{\mathrm{e}}$
3. Nonassociative flow rule: $\boldsymbol{d}^{\mathrm{p}} = \operatorname{sym} \boldsymbol{l}^{\mathrm{p}} = \dot{\lambda}\boldsymbol{q}$;
   $\boldsymbol{\omega}^{\mathrm{p}} = \operatorname{skw} \boldsymbol{l}^{\mathrm{p}} = \boldsymbol{0}$
4. State parameter: $\dot{\psi}_{\mathrm{i}} = \dot{v} + \hat{\lambda}\dot{\pi}_{\mathrm{i}}/\pi_{\mathrm{i}}$
5. Hardening law: $\dot{\pi}_{\mathrm{i}} = \sqrt{2/3} h \dot{\lambda} (\pi_{\mathrm{i}}^{*} - \pi_{\mathrm{i}}) \Omega$
6. Consistency condition: $\boldsymbol{f} : \dot{\boldsymbol{\tau}} - H\dot{\lambda} = 0$
7. Kuhn-Tucker optimality conditions: $\dot{\lambda} \geq 0, \quad F \leq 0, \quad \dot{\lambda}F = 0$

Using the results presented in [117], the trial elastic deformation tensor can be related to the elastic deformation tensor via the exponential approximation

$$\boldsymbol{b}^{\mathrm{e}} = \exp(-2\Delta\lambda\boldsymbol{q}) \cdot \tilde{\boldsymbol{b}}, \tag{4.3.2}$$

hence, $\varepsilon_a^{\mathrm{e}} = \varepsilon_a^{\mathrm{e\,tr}} - \Delta\lambda q_a$ and where $\varepsilon_a^{\mathrm{e\,tr}} \equiv \tilde{\varepsilon}_a$ for $a = 1, 2, 3$. From these results in principal logarithmic stretches and utilizing the yield criterion, we formulate the residual vector [111, 122, 131],

$$\boldsymbol{r}(\boldsymbol{x}) = \begin{Bmatrix} \varepsilon_1^{\mathrm{e}} - \varepsilon_1^{\mathrm{e\,tr}} + \Delta\lambda q_1 \\ \varepsilon_2^{\mathrm{e}} - \varepsilon_2^{\mathrm{e\,tr}} + \Delta\lambda q_2 \\ \varepsilon_3^{\mathrm{e}} - \varepsilon_3^{\mathrm{e\,tr}} + \Delta\lambda q_3 \\ F \end{Bmatrix} \qquad \text{with} \qquad \boldsymbol{x} = \begin{Bmatrix} \varepsilon_1^{\mathrm{e}} \\ \varepsilon_2^{\mathrm{e}} \\ \varepsilon_3^{\mathrm{e}} \\ \Delta\lambda \end{Bmatrix} \tag{4.3.3}$$

Table 4.2: Return mapping algorithm for three-invariant elastoplastic model for sands.

1. Elastic deformation predictor: $\tilde{\boldsymbol{b}} = \boldsymbol{f}_{n+1} \cdot \boldsymbol{b}_n^{\mathrm{e}} \cdot \boldsymbol{f}_{n+1}^{\mathrm{t}}$
2. Elastic stress predictor: $\boldsymbol{\tau}^{\mathrm{tr}} = 2\partial\Psi/\partial\tilde{\boldsymbol{b}} \cdot \tilde{\boldsymbol{b}}$; $\quad \pi_{\mathrm{i}}^{\mathrm{tr}} = \pi_{\mathrm{i},n}$
3. Check if yielding: $F\left(\boldsymbol{\tau}^{\mathrm{tr}}, \pi_{\mathrm{i}}^{\mathrm{tr}}\right) \geq 0$?
   No, set $\boldsymbol{b}^{\mathrm{e}} = \boldsymbol{b}^{\mathrm{e}\,\mathrm{tr}} \equiv \tilde{\boldsymbol{b}}$; $\quad \boldsymbol{\tau} = \boldsymbol{\tau}^{\mathrm{tr}}$; $\quad \pi_{\mathrm{i}} = \pi_{\mathrm{i}}^{\mathrm{tr}}$ and exit
4. Yes, initialize $\Delta\lambda = 0$, build residual $\boldsymbol{r}(\boldsymbol{x})$ and iterate for $\boldsymbol{x}$ (steps 5-8)
5. Spectral decomposition: $\tilde{\boldsymbol{b}} = \sum_{a=1}^{3} \tilde{\lambda}_a^2 \boldsymbol{m}^a$
6. Plastic corrector in principal logarithmic stretches: $\varepsilon_a^{\mathrm{e}} = \ln \lambda_a^{\mathrm{e}}$;
   $\tilde{\varepsilon}_a \equiv \varepsilon_a^{\mathrm{e}\,\mathrm{tr}} = \ln \tilde{\lambda}_a$; $\quad \varepsilon_a^{\mathrm{e}} = \varepsilon_a^{\mathrm{e}\,\mathrm{tr}} - \Delta\lambda q_a$; $\quad \tau_a = \partial\overline{\Psi}/\partial\varepsilon_a^{\mathrm{e}}$ $\quad$ for $a = 1, 2, 3$
7. Update plastic internal variable π_{i}:
   (a) Total deformation gradient: $\boldsymbol{F} = \boldsymbol{f}_{n+1} \cdot \boldsymbol{F}_n$
   (b) Specific volume: $v = v_0 \det \boldsymbol{F} = v_0 J$
   (c) Initialize $\pi_{\mathrm{i}} = \pi_{\mathrm{i},n}$ and iterate for π_{i} (steps 7d-f)
      (d) State parameter: $\psi_{\mathrm{i}} = v - v_{c0} + \hat{\lambda} \ln(-\pi_{\mathrm{i}})$
      (e) Limit hardening plastic variable:

$$\pi_{\mathrm{i}}^* = p \times \begin{cases} \exp\left(\sqrt{2/3}\overline{\alpha}/M\psi_{\mathrm{i}}\Omega\right) & \text{if} \quad \overline{N} = N = 0, \\ \left(1 - \sqrt{2/3}\overline{\alpha}\psi_{\mathrm{i}}\Omega N/M\right)^{(N-1)/N} & \text{if} \quad 0 \leq \overline{N} \leq N \neq 0. \end{cases}$$

      (f) Plastic internal variable: $\pi_{\mathrm{i}} = \pi_{\mathrm{i},n} + \sqrt{\frac{2}{3}} h \Delta\lambda \left(\pi_{\mathrm{i}}^* - \pi_{\mathrm{i}}\right) \Omega$
8. Discrete consistency condition: $F(p, q, \theta, \pi_{\mathrm{i}}) = 0$
9. Spectral resolution: $\boldsymbol{b}^{\mathrm{e}} = \sum_{a=1}^{3} \lambda_a^{\mathrm{e}\,2} \boldsymbol{m}^a$

as the vector of local unknowns. The Newton-Raphson scheme necessitates the Jacobian

$$\boldsymbol{r}'(\boldsymbol{x}) = \begin{bmatrix} 1+\Delta\lambda\partial q_1/\partial\varepsilon_1^{\mathrm{e}} & \Delta\lambda\partial q_1/\partial\varepsilon_2^{\mathrm{e}} & \Delta\lambda\partial q_1/\partial\varepsilon_3^{\mathrm{e}} & q_1+\Delta\lambda\partial q_1/\partial\Delta\lambda \\ \Delta\lambda\partial q_2/\partial\varepsilon_1^{\mathrm{e}} & 1+\Delta\lambda\partial q_2/\partial\varepsilon_2^{\mathrm{e}} & \Delta\lambda\partial q_2/\partial\varepsilon_3^{\mathrm{e}} & q_2+\Delta\lambda\partial q_2/\partial\Delta\lambda \\ \Delta\lambda\partial q_3/\partial\varepsilon_1^{\mathrm{e}} & \Delta\lambda\partial q_3/\partial\varepsilon_2^{\mathrm{e}} & 1+\Delta\lambda\partial q_3/\partial\varepsilon_3^{\mathrm{e}} & q_3+\Delta\lambda\partial q_3/\partial\Delta\lambda \\ \partial F/\partial\varepsilon_1^{\mathrm{e}} & \partial F/\partial\varepsilon_2^{\mathrm{e}} & \partial F/\partial\varepsilon_3^{\mathrm{e}} & \partial F/\partial\Delta\lambda \end{bmatrix}. \tag{4.3.4}$$

The local tangent operator is fully defined once the quantities $\partial q_a/\partial\varepsilon_b^{\mathrm{e}}$, $\partial q_a/\partial\Delta\lambda$, $\partial F/\partial\varepsilon_a^{\mathrm{e}}$ for $a,b=1,2,3$, and $\partial F/\partial\Delta\lambda$ are thoroughly computed. We compute these essential derivatives in what follows.

Let us start by calculating the gradient

$$\frac{\partial q_a}{\partial\varepsilon_b^{\mathrm{e}}} = q_{ac}a_{cb}^{\mathrm{e}} + \frac{\partial q_a}{\partial\pi_{\mathrm{i}}}\frac{\partial\pi_{\mathrm{i}}}{\partial\varepsilon_b^{\mathrm{e}}}, \tag{4.3.5}$$

where $a_{ab}^{\mathrm{e}} := \partial\tau_a/\partial\varepsilon_a^{\mathrm{e}}$ is the elastic continuum tangent operator in principal directions. Also, we have

$$\frac{\partial q_a}{\partial\pi_{\mathrm{i}}} = \frac{1}{3}\beta\frac{\partial^2 F}{\partial p\partial\pi_{\mathrm{i}}}\delta_a, \qquad \frac{\partial^2 F}{\partial p\partial\pi_{\mathrm{i}}} = \frac{1}{1-N}\frac{M}{p}\left(\frac{p}{\pi_{\mathrm{i}}}\right)^{\frac{1}{1-N}}. \tag{4.3.6}$$

The last term of equation (4.3.5) is furnished by the hardening law, which we recall from equation (4.2.43) and then integrate with a Backward Euler scheme to get

$$\pi_{\mathrm{i}} = \pi_{\mathrm{i},n} + \sqrt{\frac{2}{3}}h\Delta\lambda\left(\pi_{\mathrm{i}}^* - \pi_{\mathrm{i}}\right)\Omega, \tag{4.3.7}$$

where $\pi_{\mathrm{i},n}$ is the converged value of the image pressure at the previous time step t_n. Therefore,

$$\left(1+\sqrt{\frac{2}{3}}h\Delta\lambda\Omega\right)\frac{\partial\pi_{\mathrm{i}}}{\partial\varepsilon_b^{\mathrm{e}}} = \sqrt{\frac{2}{3}}h\Delta\lambda\left[\left(\frac{\partial\pi_{\mathrm{i}}^*}{\partial\tau_a}a_{ab}^{\mathrm{e}} + \frac{\partial\pi_{\mathrm{i}}^*}{\partial\psi_{\mathrm{i}}}\frac{\partial\psi_{\mathrm{i}}}{\partial\varepsilon_b^{\mathrm{e}}}\right)\Omega + \left(\pi_{\mathrm{i}}^* - \pi_{\mathrm{i}}\right)\Omega_a a_{ab}^{\mathrm{e}}\right], \tag{4.3.8}$$

where we have

$$\frac{\partial\pi_{\mathrm{i}}^*}{\partial\tau_a} = \frac{1}{3}\frac{\pi_{\mathrm{i}}^*}{p}\delta_a + (1-N)\frac{\pi_{\mathrm{i}}^*}{M-\sqrt{2/3}\overline{\alpha}\psi_{\mathrm{i}}\Omega N}\sqrt{\frac{2}{3}}\overline{\alpha}\psi_{\mathrm{i}}\Omega_a \tag{4.3.9}$$

and

$$\Omega_a = \frac{1}{\Omega}\left[\frac{3}{2}\overline{\zeta}\,\overline{\zeta}'\theta_a + \overline{\zeta}'q\left(\overline{\zeta}''\theta_a q + \overline{\zeta}'\sqrt{3/2}\hat{n}_a\right)\theta_c^2\delta_c + \left(\overline{\zeta}'q\right)^2\theta_c\theta_{ca}\right]. \tag{4.3.10}$$

Finally, recalling the definition of ψ_{i} we get

$$\frac{\partial \pi_{\mathrm{i}}^*}{\partial \psi_{\mathrm{i}}} = \sqrt{\frac{2}{3}}\overline{\alpha}\Omega\left(1-N\right)\frac{\pi_{\mathrm{i}}^*}{M-\sqrt{2/3}\overline{\alpha}\psi_{\mathrm{i}}\Omega N} \qquad \text{and} \qquad \frac{\partial \psi_{\mathrm{i}}}{\partial \varepsilon_b^{\mathrm{e}}} = \frac{\hat{\lambda}}{\pi_{\mathrm{i}}}\frac{\partial \pi_{\mathrm{i}}}{\partial \varepsilon_b^{\mathrm{e}}}. \tag{4.3.11}$$

Therefore,

$$\frac{\partial \pi_{\mathrm{i}}}{\partial \varepsilon_b^{\mathrm{e}}} = c^{-1}\sqrt{\frac{2}{3}}h\Delta\lambda\left[\Omega\frac{\partial \pi_{\mathrm{i}}^*}{\partial \tau_a} + \left(\pi_{\mathrm{i}}^* - \pi_{\mathrm{i}}\right)\Omega_a\right]a_{ab}^{\mathrm{e}}, \tag{4.3.12}$$

where $c = 1 + \sqrt{2/3}h\Delta\lambda\Omega(1-\hat{\lambda}/\pi_{\mathrm{i}}\partial\pi_{\mathrm{i}}^*/\partial\psi_{\mathrm{i}})$.

It is only left for us to evaluate the derivatives $\partial q_a/\partial\Delta\lambda$, $\partial F/\partial\varepsilon_b^{\mathrm{e}}$, and $\partial F/\partial\Delta\lambda$. By the chain rule, we have

$$\frac{\partial q_a}{\partial \Delta\lambda} = \frac{\partial q_a}{\partial \pi_{\mathrm{i}}}\underbrace{c^{-1}\sqrt{\frac{2}{3}}h\Omega\left(\pi_{\mathrm{i}}^* - \pi_{\mathrm{i}}\right)}_{\partial\pi_{\mathrm{i}}/\partial\Delta\lambda}. \tag{4.3.13}$$

Finally, we compute

$$\frac{\partial F}{\partial \varepsilon_b^{\mathrm{e}}} = f_a a_{ab}^{\mathrm{e}} + \frac{\partial F}{\partial \pi_{\mathrm{i}}}\frac{\partial \pi_{\mathrm{i}}}{\partial \varepsilon_b^{\mathrm{e}}} \qquad \text{and} \qquad \frac{\partial F}{\partial \Delta\lambda} = \frac{\partial F}{\partial \pi_{\mathrm{i}}}\frac{\partial \pi_{\mathrm{i}}}{\partial \Delta\lambda}, \tag{4.3.14}$$

where

$$f_a \equiv \frac{\partial F}{\partial \tau_a} = \frac{1}{3}\partial_p F\delta_a + \sqrt{\frac{3}{2}}\partial_q F\hat{n}_a + \partial_\theta F\theta_a \qquad \text{and} \qquad \frac{\partial F}{\partial \pi_{\mathrm{i}}} = M\left(\frac{p}{\pi_{\mathrm{i}}}\right)^{1/(1-N)}. \tag{4.3.15}$$

In addition to the above local iterative scheme, one sub-local scheme is necessary to solve for π_{i} as it is a nonlinear function of the state of stress, and the state parameter ψ_{i}. This is easily accomplished by introducing the scalar residual

$$r\left(\pi_{\mathrm{i}}\right) = \pi_{\mathrm{i}} - \pi_{\mathrm{i},n} - \sqrt{\frac{2}{3}}h\Delta\lambda\left(\pi_{\mathrm{i}}^* - \pi_{\mathrm{i}}\right)\Omega, \tag{4.3.16}$$

with the scalar tangent operator

$$r'\left(\pi_{\mathrm{i}}\right) = 1 + \sqrt{\frac{2}{3}}h\Delta\lambda\Omega\left(1 - \frac{\hat{\lambda}}{\pi_{\mathrm{i}}}\frac{\partial \pi_{\mathrm{i}}^*}{\partial \psi_{\mathrm{i}}}\right). \tag{4.3.17}$$

Once the sub-local loop is finished and a value for π_{i} is obtained, then ψ_{i} and π_{i}^* can be evaluated and the solution algorithm can proceed to the local Newton-Raphson scheme presented above.

4.3.2 Consistent tangent in principal directions

Let us start by deriving the elastic tangent in principal directions a^{e}_{ab}. Recall the hyperelastic formulation presented in subsection 4.2.1. We have the strain energy function $\Psi\left(\varepsilon^{\mathrm{e}}_{\mathrm{v}}, \varepsilon^{\mathrm{e}}_{\mathrm{s}}\right)$ from which the Kirchhoff stress tensor is obtained such that

$$\tau_a = 2\frac{\partial \Psi}{\partial \lambda^{\mathrm{e}\,2}_a}\lambda^{\mathrm{e}\,2}_a = \frac{\partial \overline{\Psi}}{\partial \varepsilon^{\mathrm{e}}_a} = \frac{1}{3}p\delta_a + \sqrt{\frac{2}{3}}q\hat{n}_a \qquad \text{(no sum)}, \tag{4.3.18}$$

where we have used the definitions $p = \partial\Psi/\partial\varepsilon^{\mathrm{e}}_{\mathrm{v}}$ and $q = \partial\Psi/\partial\varepsilon^{\mathrm{e}}_{\mathrm{s}}$. Hence,

$$a^{\mathrm{e}}_{ab} = K^{\mathrm{e}}\delta_a\delta_b + 2\mu^{\mathrm{e}}\left(\delta_{ab} - \frac{1}{3}\delta_a\delta_b\right) + \sqrt{\frac{2}{3}}d^{\mathrm{e}}\left(\delta_a\hat{n}_b + \hat{n}_a\delta_b\right), \tag{4.3.19}$$

where $K^{\mathrm{e}} := \partial p/\partial\varepsilon^{\mathrm{e}}_{\mathrm{v}}$ is the elastic bulk modulus, $3\mu^{\mathrm{e}} := \partial q/\partial\varepsilon^{\mathrm{e}}_{\mathrm{s}}$ where μ^{e} is the elastic shear modulus, and $d^{\mathrm{e}} := \partial^2\Psi/(\partial\varepsilon^{\mathrm{e}}_{\mathrm{v}}\partial\varepsilon^{\mathrm{e}}_{\mathrm{s}})$.

Now, let us define $\tilde{a}^{\mathrm{ep}}_{ab} := \partial\tau_a/\partial\tilde{\varepsilon}_b$ as the *consistent* tangent in principal directions, which we can evaluate with the help of the converged local residual vector via the chain rule. Specifically,

$$\tilde{a}^{\mathrm{ep}}_{ab} = a^{\mathrm{e}}_{ac}a^{\mathrm{p}}_{cb} \qquad \text{with} \qquad a^{\mathrm{p}}_{cb} \equiv \frac{\partial\varepsilon^{\mathrm{e}}_c}{\partial\tilde{\varepsilon}_b}. \tag{4.3.20}$$

We can then recall the converged local residual vector $\boldsymbol{r}(\boldsymbol{x}) = \boldsymbol{0}$ and by the chain rule obtain

$$\frac{\partial x_i}{\partial\tilde{\varepsilon}_a} = -b_{ij}\left.\frac{\partial r_j}{\partial\tilde{\varepsilon}_a}\right|_{\boldsymbol{x}}, \tag{4.3.21}$$

where $\boldsymbol{b} := [\boldsymbol{r}']^{-1}$ and therefore

$$a^{\mathrm{p}}_{ab} = b_{ac}\left(\delta_{cb} - \Delta\lambda\left.\frac{\partial q_c}{\partial\tilde{\varepsilon}_b}\right|_{\boldsymbol{x}}\right) - b_{a4}\left.\frac{\partial F}{\partial\tilde{\varepsilon}_b}\right|_{\boldsymbol{x}} \qquad \text{for} \qquad a, b, c = 1, 2, 3. \tag{4.3.22}$$

We also have

$$\left.\frac{\partial q_a}{\partial\tilde{\varepsilon}_b}\right|_{\boldsymbol{x}} = \frac{\partial q_a}{\partial\pi_{\mathrm{i}}}\left.\frac{\partial\pi_{\mathrm{i}}}{\partial\tilde{\varepsilon}_b}\right|_{\boldsymbol{x}} \qquad \text{and} \qquad \left.\frac{\partial F}{\partial\tilde{\varepsilon}_b}\right|_{\boldsymbol{x}} = \frac{\partial F}{\partial\pi_{\mathrm{i}}}\left.\frac{\partial\pi_{\mathrm{i}}}{\partial\tilde{\varepsilon}_b}\right|_{\boldsymbol{x}}, \tag{4.3.23}$$

where

$$\left.\frac{\partial\pi_{\mathrm{i}}}{\partial\tilde{\varepsilon}_a}\right|_{\boldsymbol{x}} = c^{-1}\sqrt{\frac{2}{3}}h\Delta\lambda\Omega v\frac{\partial\pi^*_{\mathrm{i}}}{\partial\psi_{\mathrm{i}}}\delta_a. \tag{4.3.24}$$

We note that in the special case of pure elasticity, the tangent $a^{\mathrm{p}}_{ab} \equiv \delta_{ab}$ and thus, $\tilde{a}^{\mathrm{ep}}_{ab} \equiv a^{\mathrm{e}}_{ab}$. It will be shown in the next section, that the consistent tangent in principal directions contributes to the global consistent tangent operator, which for this particular class of

return mapping algorithm can be obtained in closed-form.

4.4 Consistent tangent operators in spectral form based on Lie derivatives

It is generally recognized that a consistent linearization of the so-called weak form of balance of linear momentum is critical for optimal performance of an iterative algorithm [124, 132, 133]. In particular, in the presence of nonlinear kinematics the concept of directional derivatives plays a key role in the linearization process. We proceed to developing the CTO for the case of elastoplasticity. For the elastoplastic formulation, isotropy (i.e., $\Psi = \Psi\left(\lambda_1^{\mathrm{e}}, \lambda_2^{\mathrm{e}}, \lambda_3^{\mathrm{e}}\right)$) furnishes a connection between the elastic and trial kinematical quantities and consequently, it is a crucial component in our developments. The result hinges on two main results.

Proposition 1. *The Kirchhoff stress tensor can be obtained using the trial elastic left Cauchy-Green deformation tensor* $\boldsymbol{b}^{\mathrm{e\,tr}} \equiv \tilde{\boldsymbol{b}} := \tilde{\boldsymbol{F}} \cdot \tilde{\boldsymbol{F}}^{\mathrm{t}}$*, i.e.,*

$$\boldsymbol{\tau} = 2\frac{\partial \tilde{\Psi}}{\partial \tilde{\boldsymbol{b}}} \cdot \tilde{\boldsymbol{b}}, \tag{4.4.1}$$

where $\boldsymbol{F}^{\mathrm{e\,tr}} \equiv \tilde{\boldsymbol{F}} = \sum_{a=1}^{3} \tilde{\lambda}_a \boldsymbol{n}^a \otimes \boldsymbol{N}^a$ *is the trial elastic deformation gradient.*

Proof. By definition,

$$\boldsymbol{\tau} = 2\frac{\partial \Psi\left(\boldsymbol{b}^{\mathrm{e}}\right)}{\partial \boldsymbol{b}^{\mathrm{e}}} \cdot \boldsymbol{b}^{\mathrm{e}}. \tag{4.4.2}$$

We also know that we can decompose $\tilde{\boldsymbol{b}}$ and $\boldsymbol{b}^{\mathrm{e}}$ spectrally and get, respectively

$$\tilde{\boldsymbol{b}} = \sum_{a=1}^{3} \tilde{\lambda}_a^2 \boldsymbol{m}^a \quad \text{and} \quad \boldsymbol{b}^{\mathrm{e}} = \sum_{a=1}^{3} \lambda_a^{\mathrm{e}\,2} \boldsymbol{m}^a, \tag{4.4.3}$$

where we note the fact that the tensors $\tilde{\boldsymbol{b}}$ and $\boldsymbol{b}^{\mathrm{e}}$ have the same eigenvectors, a by-product of the return mapping algorithm. Then we use equations (4.4.2) and (4.4.3) along with the chain rule and write

$$\boldsymbol{\tau} = 2\sum_{a=1}^{3} \frac{\partial \tilde{\Psi}}{\partial \tilde{\lambda}_a^2} \frac{\partial \tilde{\lambda}_a^2}{\partial \lambda_a^{\mathrm{e}\,2}} \lambda_a^{\mathrm{e}\,2} \boldsymbol{m}^a = 2\sum_{a=1}^{3} \frac{\partial \tilde{\Psi}}{\partial \tilde{\lambda}_a^2} \frac{\tilde{\lambda}_a^2}{\lambda_a^{\mathrm{e}\,2}} \lambda_a^{\mathrm{e}\,2} \boldsymbol{m}^a = 2\frac{\partial \tilde{\Psi}}{\partial \tilde{\boldsymbol{b}}} \cdot \tilde{\boldsymbol{b}}, \tag{4.4.4}$$

where we have exploited the algorithmic relationship between λ_a^{e} and $\tilde{\lambda}_a$ (cf. equation (4.5,b) in [117]) and the isotropy of the strain-energy function. □

Proposition 2. *Define the trial elastic right Cauchy-Green deformation tensor* $\tilde{\boldsymbol{C}} := \tilde{\boldsymbol{F}}^{\mathrm{t}} \cdot \tilde{\boldsymbol{F}} = \sum_{a=1}^{3} \tilde{\lambda}_a^2 \boldsymbol{M}^a$*, then*

$$\boldsymbol{\tau} = 2\frac{\partial \tilde{\Psi}}{\partial \tilde{\boldsymbol{b}}} \cdot \tilde{\boldsymbol{b}} = 2\tilde{\boldsymbol{F}} \cdot \underbrace{\frac{\partial \tilde{\Psi}}{\partial \tilde{\boldsymbol{C}}}}_{:=1/2\tilde{\boldsymbol{S}}} \cdot \tilde{\boldsymbol{F}}^{\mathrm{t}} = \tilde{\boldsymbol{F}} \cdot \tilde{\boldsymbol{S}} \cdot \tilde{\boldsymbol{F}}^{\mathrm{t}}. \tag{4.4.5}$$

Proof. This is a standard result in continuum mechanics, but we will prove it here for completeness. We start by taking the time derivative of the strain-energy function

$$\begin{aligned} \dot{\tilde{\Psi}} &= \frac{\partial \tilde{\Psi}}{\partial \tilde{\boldsymbol{b}}} : \dot{\tilde{\boldsymbol{b}}} = \frac{\partial \tilde{\Psi}}{\partial \tilde{\boldsymbol{C}}} : \dot{\tilde{\boldsymbol{C}}} \\ &= 2\left[\frac{\partial \tilde{\Psi}}{\partial \tilde{\boldsymbol{b}}} \cdot \tilde{\boldsymbol{F}}\right] : \dot{\tilde{\boldsymbol{F}}} = 2\left[\tilde{\boldsymbol{F}} \cdot \frac{\partial \tilde{\Psi}}{\partial \tilde{\boldsymbol{C}}}\right] : \dot{\tilde{\boldsymbol{F}}}, \end{aligned} \tag{4.4.6}$$

where we have exploited the symmetries of $\tilde{\boldsymbol{b}}$ and $\tilde{\boldsymbol{C}}$, the isotropy of $\tilde{\Psi}$, and the chain rule. Consequently, since the expression above must hold for *all* $\tilde{\boldsymbol{F}}$, we conclude $\partial \tilde{\Psi}/\partial \tilde{\boldsymbol{b}} = \tilde{\boldsymbol{F}} \cdot \partial \tilde{\Psi}/\partial \tilde{\boldsymbol{C}} \cdot \tilde{\boldsymbol{F}}^{-1}$, from where equation (4.4.5) follows. □

With equations (4.4.1) and (4.4.5), it is then easy to obtain a closed form expression for the CTO by utilizing the spectral decomposition approach along with the relationship between the material time derivative and the Lie derivative of the Kirchhoff stress tensor. We start by taking the material time derivative of the Kirchhoff stress tensor

$$\begin{aligned} \dot{\boldsymbol{\tau}} &= \frac{d}{dt}\left(\tilde{\boldsymbol{F}} \cdot \tilde{\boldsymbol{S}} \cdot \tilde{\boldsymbol{F}}^{\mathrm{t}}\right) \\ \dot{\boldsymbol{\tau}} &= \dot{\tilde{\boldsymbol{F}}} \cdot \tilde{\boldsymbol{S}} \cdot \tilde{\boldsymbol{F}}^{\mathrm{t}} + \tilde{\boldsymbol{F}} \cdot \tilde{\boldsymbol{S}} \cdot \dot{\tilde{\boldsymbol{F}}}^{\mathrm{t}} + \tilde{\boldsymbol{F}} \cdot \underbrace{\frac{\partial \tilde{\boldsymbol{S}}}{\partial \tilde{\boldsymbol{C}}}}_{:=\tilde{\boldsymbol{A}}} : \dot{\tilde{\boldsymbol{C}}} \cdot \tilde{\boldsymbol{F}}^{\mathrm{t}}. \end{aligned} \tag{4.4.7}$$

It is then necessary to explicate all three terms above. We recall $\tilde{\boldsymbol{F}} = \boldsymbol{F} \cdot \boldsymbol{F}_n^{\mathrm{p}\,-1}$ and thus $\dot{\tilde{\boldsymbol{F}}} = \dot{\boldsymbol{F}} \cdot \boldsymbol{F}_n^{\mathrm{p}\,-1} = \boldsymbol{l} \cdot \tilde{\boldsymbol{F}}$, where $\boldsymbol{F}_n^{\mathrm{p}}$ is the plastic deformation gradient at time t_n. Using this result, we can calculate

$$\dot{\tilde{\boldsymbol{C}}} = \tilde{\boldsymbol{F}}^{\mathrm{t}} \cdot \boldsymbol{l} \cdot \tilde{\boldsymbol{F}} + \tilde{\boldsymbol{F}}^{\mathrm{t}} \cdot \boldsymbol{l}^{\mathrm{t}} \cdot \tilde{\boldsymbol{F}} = 2\tilde{\boldsymbol{F}}^{\mathrm{t}} \cdot \boldsymbol{d} \cdot \tilde{\boldsymbol{F}}. \tag{4.4.8}$$

It is now possible to rewrite equation (4.4.7) as

$$\dot{\boldsymbol{\tau}} = \boldsymbol{l}\cdot\boldsymbol{\tau} + \boldsymbol{\tau}\cdot\boldsymbol{l}^{\mathrm{t}} + \tilde{\boldsymbol{c}} : \boldsymbol{d} \tag{4.4.9}$$

where we identify $\mathcal{L}_{\boldsymbol{v}}(\boldsymbol{\tau}) = \tilde{\boldsymbol{c}} : \boldsymbol{d}$ and

$$\tilde{c}_{ijkl} = 2\tilde{F}_{iI}\tilde{F}_{jJ}\tilde{F}_{kK}\tilde{F}_{lL}\tilde{A}_{IJKL}. \tag{4.4.10}$$

It is clear that since $\tilde{\Psi} = \tilde{\Psi}\left(\tilde{\lambda}_1, \tilde{\lambda}_2, \tilde{\lambda}_3\right)$, then it follows that $\tilde{\boldsymbol{S}} = \sum_{a=1}^{3} \tilde{S}_a \boldsymbol{M}^a$ and $\tilde{\boldsymbol{C}} = \sum_{a=1}^{3} \tilde{\lambda}_a^2 \boldsymbol{M}^a$ are coaxial and consequently

$$\tilde{\boldsymbol{A}} = \sum_{a=1}^{3}\sum_{b=1}^{3} \frac{\partial \tilde{S}_a}{\partial \tilde{\lambda}_b^2} \boldsymbol{M}^a \otimes \boldsymbol{M}^b + \frac{1}{2}\sum_{a=1}^{3}\sum_{b\neq a} \frac{\tilde{S}_b - \tilde{S}_a}{\tilde{\lambda}_b^2 - \tilde{\lambda}_a^2}\left(\boldsymbol{M}^{ab}\otimes\boldsymbol{M}^{ab} + \boldsymbol{M}^{ab}\otimes\boldsymbol{M}^{ba}\right) \tag{4.4.11}$$

and therefore, by pushing $\tilde{\boldsymbol{A}}$ forward with equation (4.4.10) and using the fact that $\tilde{\lambda}_a^2\tilde{S}_a = \tau_a$ we obtain

$$\tilde{\boldsymbol{c}} = \sum_{a=1}^{3}\sum_{b=1}^{3} \underbrace{\left(\tilde{a}_{ab}^{\mathrm{ep}} - 2\tau_a\delta_{ab}\right)}_{:=\tilde{c}_{ab}} \boldsymbol{m}^a\otimes\boldsymbol{m}^b + \sum_{a=1}^{3}\sum_{b\neq a} \underbrace{\frac{\tau_b\tilde{\lambda}_a^2 - \tau_a\tilde{\lambda}_b^2}{\tilde{\lambda}_b^2 - \tilde{\lambda}_a^2}}_{:=\tilde{\gamma}_{ab}} \left(\boldsymbol{m}^{ab}\otimes\boldsymbol{m}^{ab} + \boldsymbol{m}^{ab}\otimes\boldsymbol{m}^{ba}\right) \tag{4.4.12}$$

where $\tilde{a}_{ab}^{\mathrm{ep}} := \partial\tau_a/\partial\tilde{\varepsilon}_b$, $\tilde{\varepsilon}_b := \ln\tilde{\lambda}_b$, and where $\boldsymbol{M}^a := \boldsymbol{N}^a\otimes\boldsymbol{N}^a$, $\boldsymbol{M}^{ab} := \boldsymbol{N}^a\otimes\boldsymbol{N}^b$ and $\boldsymbol{m}^{ab} := \boldsymbol{n}^a\otimes\boldsymbol{n}^b$. We observe from equation (4.4.12) that the CTO possesses minor symmetries but lacks major symmetry if $\tilde{a}_{ab}^{\mathrm{ep}} \neq \tilde{a}_{ba}^{\mathrm{ep}}$, which is certainly the case for non-associative plasticity or when the integration algorithm destroys the symmetry of the tangent operator [66, 134].

4.5 Search algorithm in principal stress space

Consider the expression for the total tangent operator i.e., $\boldsymbol{a}^{\mathrm{ep}} = \boldsymbol{c}^{\mathrm{ep}} + \boldsymbol{\tau}\oplus\boldsymbol{1}$, where the elastoplastic tangent operator is form-identical to the CTO derived above, namely,

$$\boldsymbol{c}^{\mathrm{ep}} = \sum_{a=1}^{3}\sum_{b=1}^{3} c_{ab}^{\mathrm{ep}}\boldsymbol{m}^a\otimes\boldsymbol{m}^b + \sum_{a=1}^{3}\sum_{b\neq a}\gamma_{ab}\left(\boldsymbol{m}^{ab}\otimes\boldsymbol{m}^{ab} + \boldsymbol{m}^{ab}\otimes\boldsymbol{m}^{ba}\right). \tag{4.5.1}$$

We use this operator in defining the Eulerian acoustic tensor for nonlinear kinematics [64]

$$A_{ik} \equiv n_j a^{\text{ep}}_{ijkl} n_l, \tag{4.5.2}$$

where n_i for $i = 1, 2, 3$ are the components of the unit vector $\boldsymbol{n}$ normal to an impending shear band in the current configuration. Since the principal directions of the stress tensor $\boldsymbol{\tau}$ span $\mathbb{R}^3$, we can construct *any* vector as a linear combination of these eigenvectors. Specifically,

$$\boldsymbol{n} = \sum_{a=1}^{3} \alpha_a \boldsymbol{n}^a \tag{4.5.3}$$

which we can then combine with (4.5.2) and (4.5.1) to get the spectral components of the acoustic tensor

$$\hat{A}_{ab} = \begin{cases} \alpha_a^2 c^{\text{ep}}_{aa} + \sigma + \sum_{c \neq a} \alpha_c^2 \gamma_{ca} & \text{if} \quad a = b \\ \alpha_a \left(c^{\text{ep}}_{ab} + \gamma_{ab} \right) \alpha_b & \text{if} \quad a \neq b \end{cases} \qquad \text{(no sum)} \tag{4.5.4}$$

where $\sigma := \boldsymbol{n} \cdot \boldsymbol{\tau} \cdot \boldsymbol{n}$ is the component of the stress tensor normal to the shear band and $\hat{A}_{ab} := \boldsymbol{n}^a \cdot \boldsymbol{A} \cdot \boldsymbol{n}^b$ are the components of the acoustic tensor in principal direction basis.

We recall that a necessary condition for localization is [29, 64, 122],

$$\mathcal{F}(\boldsymbol{A}) = \inf |_{\boldsymbol{n}} \det(\boldsymbol{A}) = 0. \tag{4.5.5}$$

Note that the determinant of a second order tensor is an invariant quantity under rotations i.e., $\det(\boldsymbol{A}) = \det(\hat{\boldsymbol{A}})$, so this allows us to use the spectral form of the acoustic tensor only. Defining $f = \det(\hat{\boldsymbol{A}})$, the localization condition can be rewritten in the equivalent form

$$\frac{\partial f}{\partial \alpha_a} = 0, \qquad a = 1, 2, 3 \tag{4.5.6}$$

which provides three optimality conditions that need to be satisfied in order to obtain a local minimum. We can further reduce the number of unknowns by introducing the spherical coordinates (θ,ϕ,$\|\boldsymbol{n}\|_2$) in principal space (see Figure 4.2). We require $\|\boldsymbol{n}\|_2 \equiv 1$, which introduces a trivial constraint on the system. Some algorithms use this constraint in the framework of Lagrange multipliers to solve for $\mathcal{F}$ (e.g. see Ortiz et al. [51]).

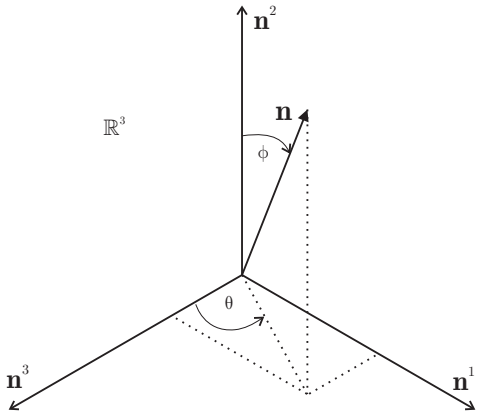

Figure 4.2: Reference frame in principal directions basis.

From Figure 4.2, we have the coordinate relations

$$\alpha_1 = \sin\theta \sin\phi, \qquad \alpha_2 = \cos\phi, \qquad \alpha_3 = \cos\theta \sin\phi. \tag{4.5.7}$$

We can then use these relations to rewrite the localization condition by defining the vector $\boldsymbol{\beta} = \{\theta, \phi\}^{\mathrm{t}}$, and by the chain rule,

$$\frac{\partial f}{\partial \beta_i} = \sum_{a=1}^{3} \frac{\partial f}{\partial \alpha_a} \frac{\partial \alpha_a}{\partial \beta_i} = 0, \qquad i = 1, 2. \tag{4.5.8}$$

Due to the highly nonlinear nature of the optimality conditions in equation (4.5.8), we resort to a Newton-Raphson iterative procedure by expanding the residual around a previous iteration and equating it to zero i.e.,

$$\left.\frac{\partial f}{\partial \boldsymbol{\beta}}\right|_{k+1} \approx \left.\frac{\partial f}{\partial \boldsymbol{\beta}}\right|_{k} + \left.\frac{\partial^2 f}{\partial \boldsymbol{\beta} \partial \boldsymbol{\beta}}\right|_{k} \cdot \underbrace{\left(\boldsymbol{\beta}_{k+1} - \boldsymbol{\beta}_k\right)}_{:=\Delta\boldsymbol{\beta}} = 0 \tag{4.5.9}$$

and hence

$$\Delta\boldsymbol{\beta} = -\left(\frac{\partial^2 f}{\partial \boldsymbol{\beta} \partial \boldsymbol{\beta}}\right)_{k}^{-1} \cdot \left.\frac{\partial f}{\partial \boldsymbol{\beta}}\right|_{k}. \tag{4.5.10}$$

The first approximation $\boldsymbol{\beta_0}$ is furnished by a coarse sweep over half a unit ball i.e., $[0, \pi] \times$

$[0, \pi]$, where the global minimum of the function f is attained.

Now, it remains to explicate the right hand side of equation (4.5.10). Using the fact that $\partial \det(\hat{\boldsymbol{A}})/\partial \hat{\boldsymbol{A}} = \det(\hat{\boldsymbol{A}})\hat{\boldsymbol{A}}^{-\mathrm{t}}$, along with the chain rule, we get

$$\frac{\partial f}{\partial \boldsymbol{\beta}} = f\,\hat{\boldsymbol{A}}^{-\mathrm{t}} : \frac{\partial \hat{\boldsymbol{A}}}{\partial \boldsymbol{\alpha}} \cdot \frac{\partial \boldsymbol{\alpha}}{\partial \boldsymbol{\beta}} \tag{4.5.11}$$

where $\partial \hat{\boldsymbol{A}}/\partial \boldsymbol{\alpha}$ is a third-order tensor with components (cf. equation (4.5.4))

$$\frac{\partial \hat{A}_{ab}}{\partial \alpha_c} = \begin{cases} 2\alpha_a \delta_{ac} c^{\mathrm{ep}}_{aa} + 2\alpha_c \tau_c + \underbrace{2\alpha_c \gamma_{ca}}_{c \neq a} & \text{if} \quad a = b \\ \delta_{ac}\left(c^{\mathrm{ep}}_{ab} + \gamma_{ab}\right)\alpha_b + \alpha_a\left(c^{\mathrm{ep}}_{ab} + \gamma_{ab}\right)\delta_{bc} & \text{if} \quad a \neq b \end{cases} \quad \text{(no sum)}, \tag{4.5.12}$$

with δ_{ab} being the Kronecker delta. Further, the components of the matrix $\partial \boldsymbol{\alpha}/\partial \boldsymbol{\beta}$ can be easily computed to yield

$$\frac{\partial \boldsymbol{\alpha}}{\partial \boldsymbol{\beta}} = \begin{bmatrix} \partial_\theta \alpha_1 & \partial_\phi \alpha_1 \\ \partial_\theta \alpha_2 & \partial_\phi \alpha_2 \\ \partial_\theta \alpha_3 & \partial_\phi \alpha_3 \end{bmatrix}. \tag{4.5.13}$$

The Jacobian matrix can be calculated with the aid of the chain rule as

$$\frac{\partial^2 f}{\partial \boldsymbol{\beta} \partial \boldsymbol{\beta}} = \frac{\partial \boldsymbol{\alpha}}{\partial \boldsymbol{\beta}} \cdot \boldsymbol{J} \cdot \frac{\partial \boldsymbol{\alpha}}{\partial \boldsymbol{\beta}} + \frac{\partial f}{\partial \boldsymbol{\alpha}} \cdot \frac{\partial^2 \alpha}{\partial \boldsymbol{\beta} \partial \boldsymbol{\beta}}, \tag{4.5.14}$$

where

$$\boldsymbol{J} = f\left[\left(\hat{\boldsymbol{A}}^{-\mathrm{t}} : \frac{\partial \hat{\boldsymbol{A}}}{\partial \boldsymbol{\alpha}}\right) \otimes \left(\hat{\boldsymbol{A}}^{-\mathrm{t}} : \frac{\partial \hat{\boldsymbol{A}}}{\partial \boldsymbol{\alpha}}\right) - \frac{\partial \hat{\boldsymbol{A}}}{\partial \boldsymbol{\alpha}} : \hat{\boldsymbol{A}}^{-\mathrm{t}} \ominus \hat{\boldsymbol{A}}^{-1} : \frac{\partial \hat{\boldsymbol{A}}}{\partial \boldsymbol{\alpha}} + \hat{\boldsymbol{A}}^{-\mathrm{t}} : \frac{\partial^2 \hat{\boldsymbol{A}}}{\partial \boldsymbol{\alpha} \partial \boldsymbol{\alpha}}\right]. \tag{4.5.15}$$

Finally, the fourth order tensor $\partial^2 \hat{\boldsymbol{A}}/(\partial \boldsymbol{\alpha} \partial \boldsymbol{\alpha})$ can be written in component form as

$$\frac{1}{2}\frac{\partial \hat{A}_{ab}}{\partial \alpha_c \partial \alpha_d} = \begin{cases} \delta_{ac}\delta_{bd} c^{\mathrm{ep}}_{aa} + \delta_{cd}\tau_c + \underbrace{\delta_{cd}\gamma_{ca}}_{c \neq a} & \text{if} \quad a = b \\ \left(c^{\mathrm{ep}}_{ab} + \gamma_{ab}\right)\mathcal{I}_{abcd} & \text{if} \quad a \neq b \end{cases} \quad \text{(no sum)}, \tag{4.5.16}$$

where $\mathcal{I}_{abcd} = 1/2\left(\delta_{ac}\delta_{bd} + \delta_{ad}\delta_{bc}\right)$ is the fourth-order identity tensor.

Note that the tensors presented in equations (4.5.12,4.5.16) are very sparse, thus making the assembly of the residual vector and the Jacobian matrix very straightforward. Also, the Hessian matrix in (4.5.16) is only calculated once in the algorithm as it is not a function

of the α_a's. At this point, it is easy to recognize the importance of the fact that since the algorithm is based on Newton-Raphson scheme, asymptotic quadratic rate of convergence is achieved and as a result the algorithm only needs to iterate a few times to find the global minimum, provided, of course, that the first guess is close enough to the solution.

It has been shown by several researchers that for a wide class of elastoplastic models, at least one of the α_a's is zero and therefore the search only needs to take place on the principal planes [29, 35, 135, 136]. For example, classical models such as von-Misses, Drucker-Prager, and Mohr-Coulomb can all be shown to localize within one of the principal planes, even for the case of finite strains, provided a suitable form of the elastic continuum tangent is utilized (isotropic). Also, the infinitesimal version of the elastoplastic model presented herein can be shown to belong to the class of constitutive models described above. Due to the spectral nature of the algorithm presented here, the on-plane feature is easily activated, thus making the search very efficient. This feature is not present in some of the previously proposed search algorithms available in the literature, see for example the works by Ortiz et al. [51] and Mosler [137], which always perform fully three-dimensional searches. Simulations underscoring the main features of the algorithm such as asymptotic quadratic rate and the on-plane feature are included in the Numerical examples section.

Remark 5. Note that the formulation presented above is general and applicable to models with linear and nonlinear kinematics. The same algorithm can be easily utilized for the case of infinitesimal deformations provided that the stress terms are set identically equal to zero, for example.

Remark 6. As pointed out first in [114], the *consistent* tangent operator can be used in lieu of its continuum counterpart to search for the necessary condition for localization, provided a small enough load step is taken. This can be accomplished, in light of the above described search algorithm, by replacing c_{ab}^{ep} with $\tilde{c}_{ab}$ and γ_{ab} with $\tilde{\gamma}_{ab}$. It is very convenient to use the algorithmic operator as it is already available from the material subroutine and therefore the continuum tangent is not to be used explicitly.

4.6 Numerical examples

In this section we conduct local stress-point simulations to illustrate the main features of the three-invariant constitutive formulation developed in this work. Localization analyses are conducted at this level and the convergence profile of the search algorithm for the minimum

determinant is reported. Then, a series of boundary-value problems at the finite element level are performed with the objective of studying the behavior of granular bodies exhibiting unstructured random density fields. The simulations focus on *detecting* bifurcation and no effort is made to try to capture post-bifurcation behavior. Hence all simulations are stopped once bifurcation is detected.

4.6.1 Stress-point simulations

At the stress-point level, we performed two strain-driven simulations to highlight the difference in the responses resulting from the inclusion of the third stress invariant and to test the performance of the search algorithm for the minimum value of the localization function. Two material points with identical properties, except for the ellipticity parameters ρ and $\overline{\rho}$, were strained until they reached localization. The hyperelastic parameters are as follows: compressibility coefficient $\hat{\kappa} = 0.01$; reference elastic volumetric strain $\varepsilon^{\mathrm{e}}_{\mathrm{v}\,0} = 0$ at a reference pressure $p_0 = -100$ kPa; initial shear modulus $\mu_0 = 5400$ kPa; and coupling constant $\alpha_0 = 0$ (see section 4.2.1 for notation). The plasticity parameters are: plastic compressibility coefficient $\hat{\lambda} = 0.0135$; critical state parameter $M = 1.2$; shape parameters $N = 0.4$ and $\overline{N} = 0.2$ (nonassociative volumetric plastic flow); and hardening constant $h = 280$ (see section 4.2.2 for notation). Both material points were initially denser than critical with an initial specific volume $v = 1.59$ and a reference specific volume $v_{c0} \approx 1.81$. The only difference in material properties is the ellipticity: one material point had $\rho = \overline{\rho} = 1$ (two-invariant formulation, circular cross-section and associative flow on the deviatoric plane) and the other had $\rho = 0.7$ and $\overline{\rho} = 0.8$ (non-circular, convex cross-section, nonassociative flow on deviatoric plane). Both material points were modeled using the Willam-Warnke shape function in equation (4.2.12).

The loading protocol is as follows. We prescribed two equal sets of relative deformation gradient $\boldsymbol{f}_{n+1} = \partial \boldsymbol{x}_{n+1}/\partial \boldsymbol{x}_n$: the first set was prescribed over n_1 steps, followed by the second for n_2 steps until localization was reached. The two relative deformation gradients are

$$\boldsymbol{f}_1 = \begin{bmatrix} 1+\lambda_2 & 0 & 0 \\ 0 & 1-\lambda_1 & 0 \\ 0 & 0 & 1 \end{bmatrix} \qquad \text{and} \qquad \boldsymbol{f}_2 = \begin{bmatrix} 1 & 0 & 0 \\ 0 & 1-\lambda_2 & 0 \\ 0 & 0 & 1+\lambda_1 \end{bmatrix}, \tag{4.6.1}$$

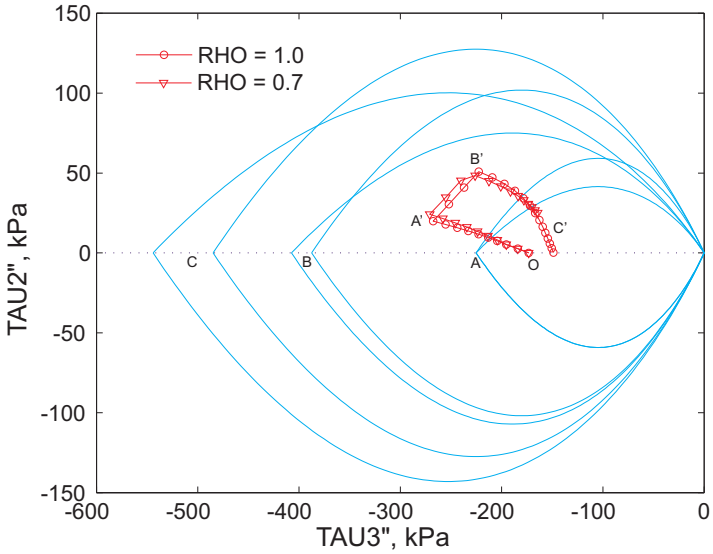

Figure 4.3: Stress paths on meridian plane. Yield surfaces expand from A to B and to C whereas stress paths follow O–A'–B'–C' trajectory.

hence, the total deformation gradient is

$$\boldsymbol{F} = \boldsymbol{f}_2^{n_2} \cdot \boldsymbol{f}_1^{n_1}, \tag{4.6.2}$$

where $\lambda_1 = 1 \times 10^{-3}$ and $\lambda_2 = 4 \times 10^{-4}$. The material points were mostly compressed in the first $n_1 = 10$ steps, and then mostly stretched in the subsequent n_2 steps, hence the total number of steps is given by $n = n_1 + n_2$. The stress paths followed by the two material points are shown in Figures 4.3 and 4.4, with Figure 4.3 showing the stress paths on a meridian plane and Figure 4.4 showing them on a deviatoric plane. The paths are plotted using rotated principal stress axis as described in [111]. The trajectories followed by the two stress points are similar. The stress paths started at point O and then were loaded to point A' after the first n_1 steps, and subsequently deformed to points B' and C', where they localized. Similarly, the yield surfaces expanded from A to B to C, without softening.

The sample with $\rho = 0.7$ localized first at $n = 22$, whereas the sample with $\rho = 1$ localized at $n = 26$. The function $\mathcal{F}(\boldsymbol{A})$ for both stress points is plotted in Figure 4.5 where we see minor differences in the trajectories, yet the stress point with $\rho = 0.7$ localized sooner. Hence, the third invariant enhances strain localization. The values for the function

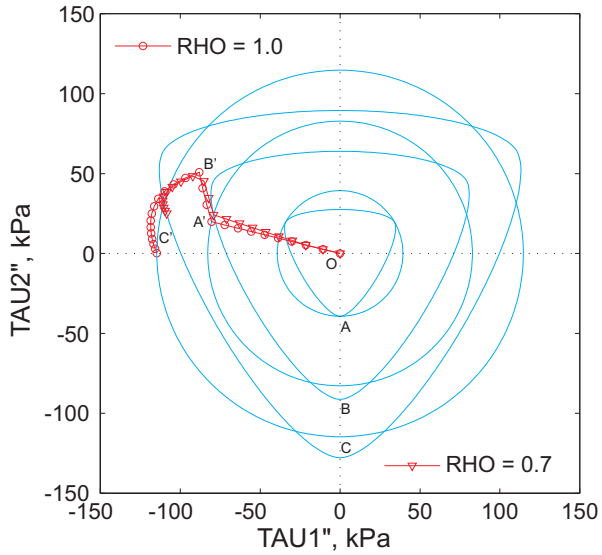

Figure 4.4: Stress paths on deviatoric plane. Yield surfaces expand from A to B and to C whereas stress paths follow O–A'–B'–C' trajectory.

$\mathcal{F}(\boldsymbol{A})$ are obtained by the search algorithm outlined in Section 4.5 by sweeping the $\mathbb{R}^3$ space via the angles θ and ϕ. One such a profile swept by the search algorithm is shown in Figure 4.6, where the determinant of the acoustic tensor is plotted as a function of θ and ϕ at the onset of localization for the material point with $\rho = 0.7$. One such profile is swept at each time step where the search algorithm finds one of usually two wells and then returns a solution. One interesting note from Figure 4.6 is that localization was achieved at $\phi = \pi/2$ (see end of section 4.5 for discussion). Finally, the convergence profile for the search algorithm at various load steps is reported in Figure 4.7 where optimal quadratic convergence is observed.

4.6.2 Simulations with cubical specimens

Randomization of the density field in a specimen is achieved through the void ratio e, defined as the ratio between the volume occupied by empty voids and the intrinsic volume of the solid phase, i.e., $e := V_v/V_s$. The main issue concerns finding a plausible probability density function describing the natural dispersion of voids in a sample of granular materials. Shahinpoor [138] used statistical mechanical theory on a collection of Voronoi cells to obtain an exact expression for the probability density function for the distributions of void ratio

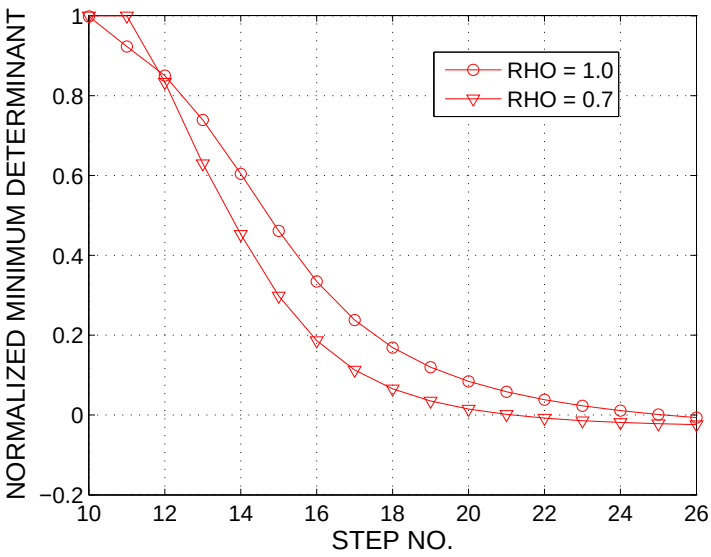

Figure 4.5: Minimum determinant of the acoustic tensor at various load steps.

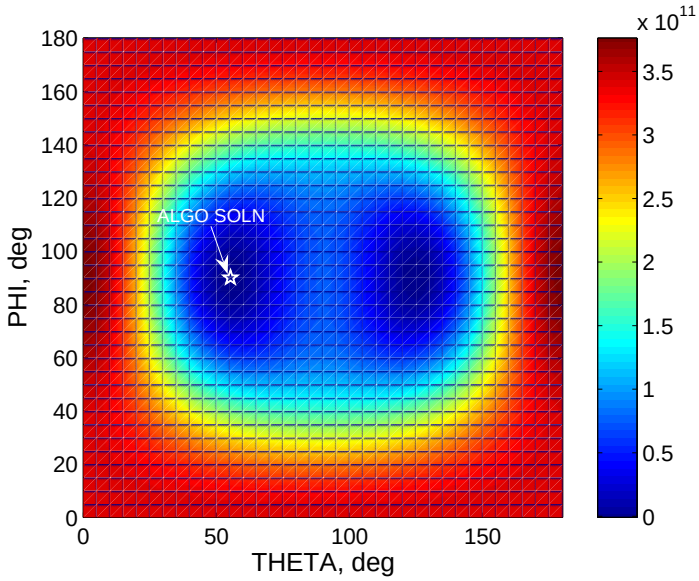

Figure 4.6: Profile of the determinant of the acoustic tensor for three-invariant model with $\rho = 0.7$ at onset of localization.

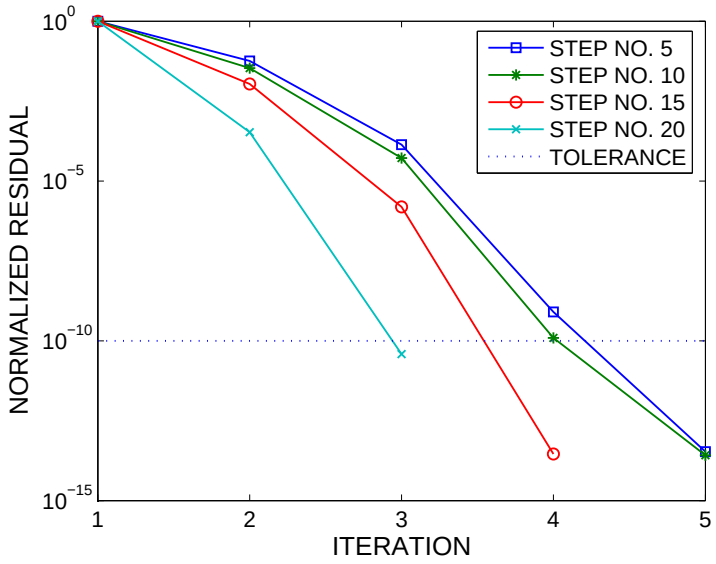

Figure 4.7: Convergence profile for search algorithm at various load steps.

in a random aggregate of granular material. The probability distribution function for e was established to be a truncated exponential distribution. It also has been used by Nübel and Huang [19] to study localized deformation patterns in granular media.

Here, we adopted a truncated exponential density function for e of the form

$$f_e(e) = \frac{\gamma \exp(-\gamma e)}{\exp(-\gamma e_d) - \exp(-\gamma e_l)}, \tag{4.6.3}$$

where e_d is the lower bound of the distribution corresponding to the densest state, e_l is the upper bound of the distribution corresponding to the loosest state, and γ plays the role of a fitting parameter. We used these bounds to restrict the amount of dispersion in the density of the sample, thus controlling the amount of inhomogeneities. The expected value of the distribution is given by [139]

$$\overline{e} = \int_{e_d}^{e_l} e f_e(e)\, \mathrm{d}e, \tag{4.6.4}$$

where

$$\overline{e} = \frac{1}{\gamma} + \frac{e_d \exp(-\gamma e_d) - e_l \exp(-\gamma e_l)}{\exp(-\gamma e_d) - \exp(-\gamma e_l)}, \tag{4.6.5}$$

Hence, we can *prescribe* the expected value or mean void ratio $\overline{e}$ subject to the upper and lower bounds e_d and e_l, respectively, provided we solve for the fitting coefficient γ. This is

easily accomplished by a Newton-Raphson scheme on the residual

$$r(\gamma) = \overline{e} - \frac{1}{\gamma} - \frac{e_d \exp(-\gamma e_d) - e_l \exp(-\gamma e_l)}{\exp(-\gamma e_d) - \exp(-\gamma e_l)}. \tag{4.6.6}$$

The random density field was then generated on the assumption that the values of void ratio in space are mutually independent. For this reason, these random fields are called "unstructured" due to the lack of correlation in the density field between points A and B in the same sample.

We then sheared in compression two rectangular specimens with dimensions $1 \times 1 \times 2$ m and assumed to behave according to the constitutive framework presented above, up to the onset of localization. The material properties for both specimens were identical to those of the stress-point with $\rho = \overline{\rho} = 0.78$ and $v_{c0} \approx 1.85$ discussed in the previous section. The Argyris-Gudehus shape function given in equation (4.2.11) was utilized in the simulations. At the structural level the density field was generated using the exponential distribution described above with a mean void ratio $\overline{e} = 0.63$ and lower and upper bounds $e_d = 0.54$ and $e_l = 0.64$, respectively. Hence, the two specimens, which we will call 'INHOMOGENEOUS 1' and 'INHOMOGENEOUS 2' for identification purposes, represent two different realizations of the same distribution function for the void ratio field, with otherwise identical mechanical properties. Figure 4.8 shows the discretized specimens with their respective initial specific volume field $v := 1 + e$. The rectangular domains were discretized using 2000 trilinear hexahedral elements equipped with the B-bar method for nonlinear kinematics using the so-called mean dilation technique [120, 121] (see [119] for a survey on the B-bar method).

The boundary conditions applied to the specimens were as follows. All four lateral faces were initially subjected to a constant confining pressure of 100 kPa (Newman BCs). The bottom and top faces of the specimens ($z = 0, 1$ m) were supported by rollers with a pin at the $(0, 0, 0)$m point for stability (Dirichlet BCs). The bottom face was constrained from displacement in the z-direction, whereas the top face was subjected to a vertical displacement responsible for shearing the samples in compression. The samples were loaded in two phases. Phase one, an all-around confining pressure was applied to consolidate the sample followed by phase two, where the top face was displaced vertically. The objective of this loading protocol, favoring homogeneous deformations in perfectly homogeneous samples, is twofold: to observe if any significant differences are introduced by perturbing the density

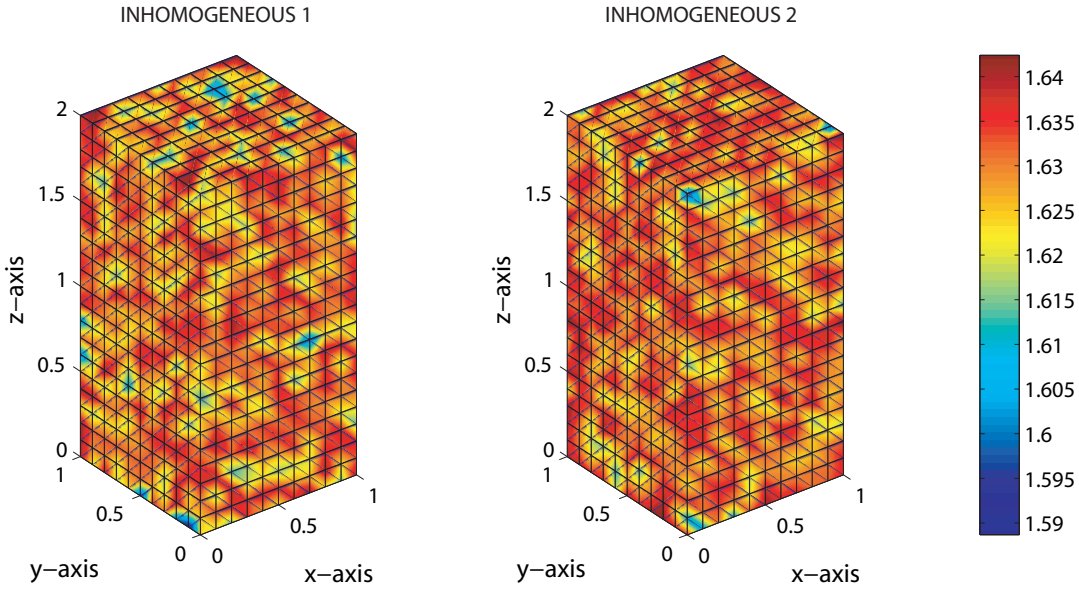

Figure 4.8: Initial specific volume field and finite element discretization for inhomogeneous rectangular specimens.

field by comparing the homogeneous response against perturbed responses from the samples shown in Figure 4.8, and to compare the responses of two inhomogeneous samples from two realizations of the density field. To this end, a homogeneous sample with constant void ratio $v = 1.63$ was subjected to the same BCs described above, and its response compared against its inhomogeneous counterparts.

Figure 4.9 shows the contours of the function $\mathcal{F}(\boldsymbol{A})$, for both inhomogeneous samples, superimposed on the deformed mesh at the onset of localization. Here, we define localization when one or more Gauss points have detected the first negative incursion of the function $\mathcal{F}(\boldsymbol{A})$ (even though contours appear as positive due to averaging necessary for plotting). Both inhomogeneous samples localized at a nominal axial strain of around 5.8%, yet, from Figure 4.9, we observe that the deformation patterns and the inclinations of the impending shear bands are conjugate to each other, almost looking as mirror images. This same trend is observed in Figure 4.10 which compares the contours of the total deviatoric strain invariant on both inhomogeneous samples. Comparing Figures 4.9 and 4.10, note a strong correlation between the vanishing of the determinant of the acoustic tensor and the localized values of the deviatoric component of deformation (shear strains).

Figure 4.11 shows the nominal axial stress as a function of the nominal axial strain for

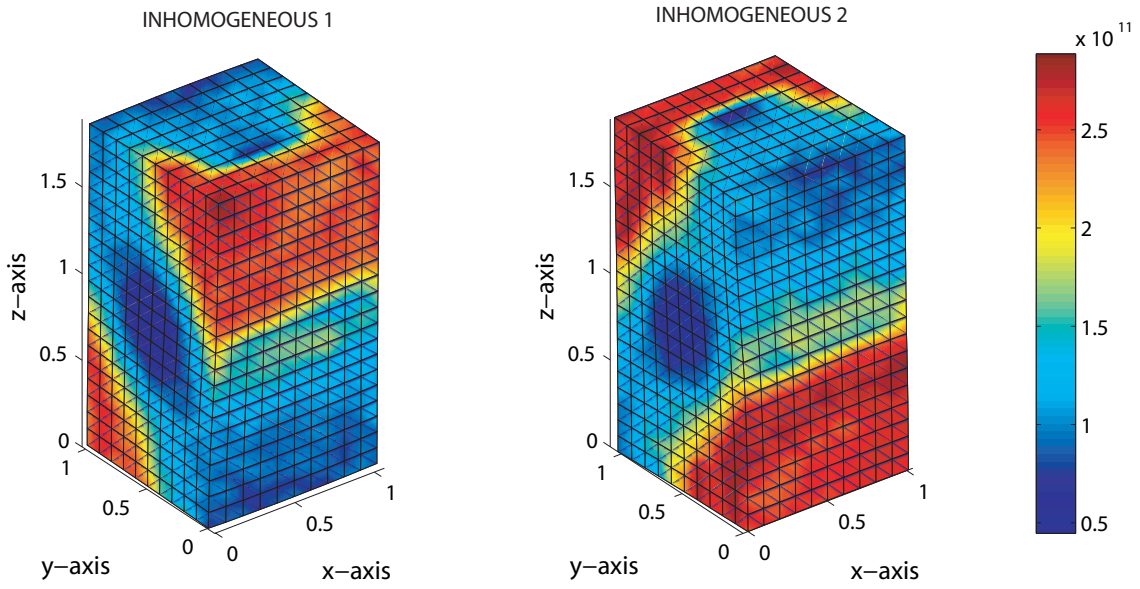

Figure 4.9: Contour of function $\mathcal{F}(\boldsymbol{A})$ at onset of localization for inhomogeneous rectangular specimens.

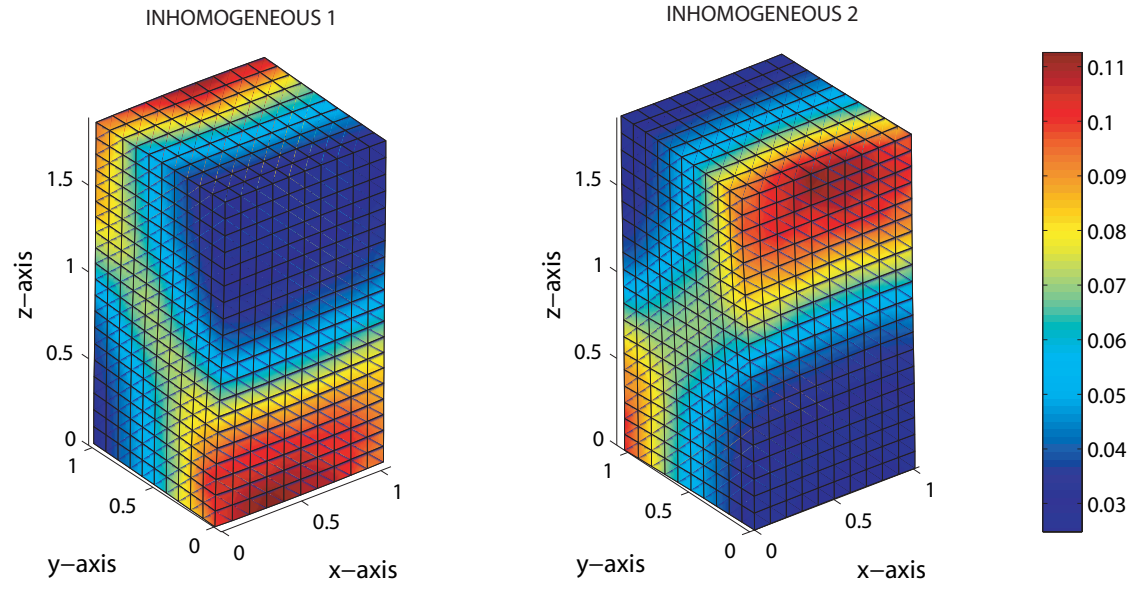

Figure 4.10: Deviatoric strain invariant field at onset of localization for inhomogeneous rectangular specimens.

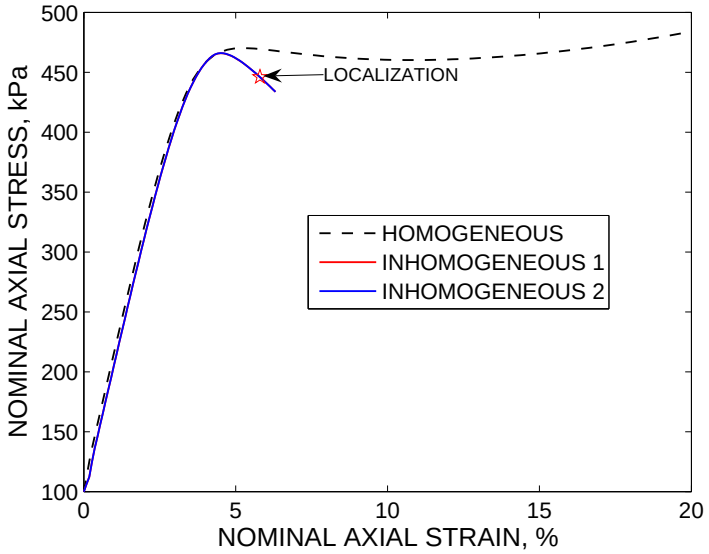

Figure 4.11: Nominal axial stress response for rectangular specimens.

both inhomogeneous specimens and their homogeneous counterpart. We see a close agreement in the global responses up to about 4% nominal axial strain, where the inhomogeneous responses softened and eventually localized at 5.8% strain. The homogeneous sample, however, underwent very little softening and in fact continued to harden. The change in volume experienced by the heterogeneous and homogeneous samples are compared in Figure 4.12. Unlike Figure 4.11, the responses seem identical throughout the duration of the simulations. Note that the samples compacted first, and then dilated. This trend is very common in dense sands.

From these simulations we conclude that perturbations in the density field via inhomogeneities at the meso-scale tend to trigger the onset of localization. Also, as we compare the responses of two nearly identical inhomogeneous samples, we observe localization patterns that are conjugate of each another. The mechanical responses of the heterogeneous samples in the early stages of deformation are very similar to those of their homogeneous counterpart, suggesting that we can calibrate the meso-scale model parameters from global specimen responses during the early stages of loading.

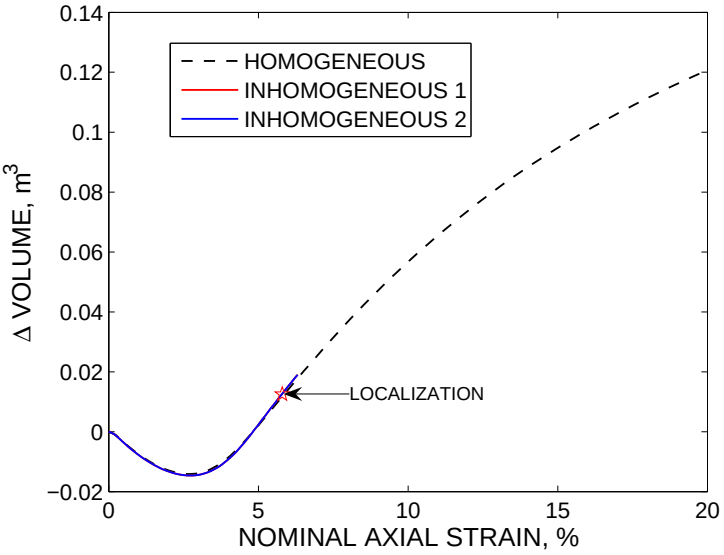

Figure 4.12: Volume change response for rectangular specimens.

4.6.3 Simulations with cylindrical specimens

Next, two inhomogeneous cylindrical specimens exhibiting random unstructured density fields were loaded in biaxial compression with BCs (and geometry) that emulated 'triaxial' testing in the laboratory. Both specimens are 2 m in diameter and 4 m tall. The elastoplastic properties of these specimens are identical to those in the simulations with cubical specimens described above. However, here we used two different density fields to simulate the effects of increasing the spread in the random field on the localization properties of dense sand samples. To this end, the first inhomogeneous sample, which we call 'INHOMO 1.58-1.61', has a density field such that $\overline{e} = 0.59$, with lower and upper bounds $e_d = 0.58$ and $e_l = 0.61$, representing a relatively narrow distribution of void ratio. As for the second sample, we increased the spread in the void ratio field while keeping the mean constant, i.e., $\overline{e} = 0.59$, with lower and upper bounds $e_d = 0.56$ and $e_l = 0.68$. We will call this specimen 'INHOMO 1.56-1.68'. Figure 4.13 displays the initial specific volume field superimposed on the original configuration for both inhomogeneous samples. The cylindrical domains were discretized using 1280 eight-node brick elements equipped with the B-bar method.

As for the BCs, the specimens were biaxially loaded with a confining pressure applied on the sleeve of the cylinders (Neumann BC) while the top and bottom faces were supported

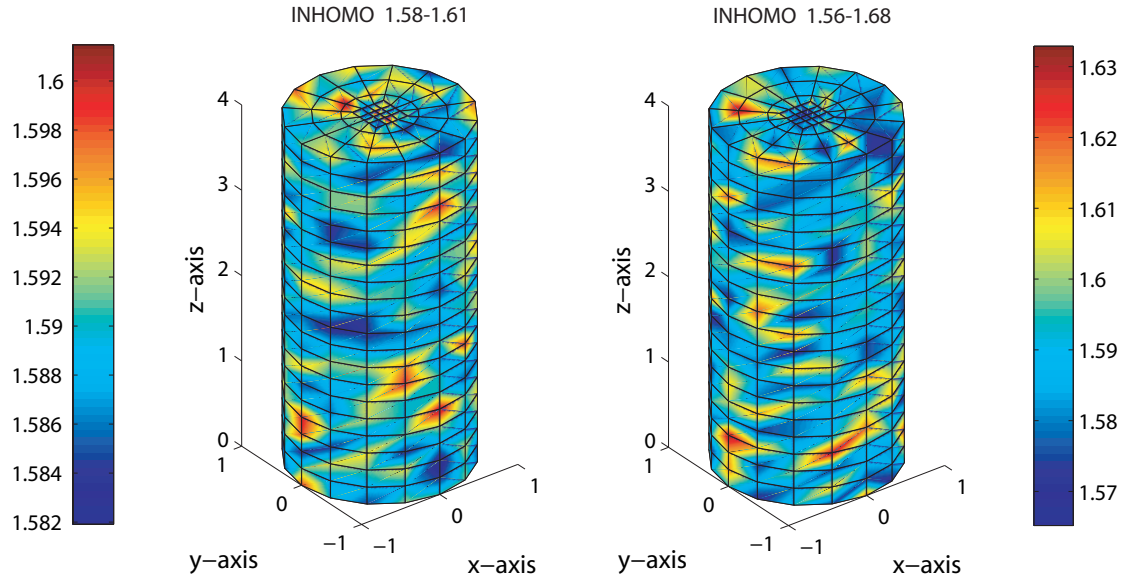

Figure 4.13: Initial specific volume field and finite element discretization for inhomogeneous cylindrical specimens.

on rollers (Dirichlet BC). The point $(0, 0, 0)$m in the specimens was supported by a pin for stability. As in the rectangular specimen simulations, the bottom face was constrained to move vertically while the top face was compressed to mimic a homogeneous deformation. The samples were then loaded as before, with an initial confining pressure of 100 kPa followed by axial compression from the top face until localization was detected.

Figures 4.14 and 4.15 show an 'X-ray' rendering of the deviatoric strain invariant and the function $\mathcal{F}(\boldsymbol{A})$, respectively, superimposed on different cut-planes in the deformed configuration for the 'INHOMO 1.58-1.61' sample. The sub-figures on the right show longitudinal panels while the sub-figures on the left show axial planes. Note a localized area of intense shearing going from the top-right to the bottom-left corner, compared with the rest of the sample that experienced lower values of shear strains. Similar trends were observed on the 'INHOMO 1.56-1.68' sample.

Figures 4.16 and 4.17 show nearly identical plots of the overall axial stress-axial strain and volumetric strain-axial strain for both inhomogeneous samples and their homogeneous counterpart with $e = 1.59$. The inhomogeneous samples localized at different instants whereas the homogeneous sample did not localize at all. Sample 'INHOMO 1.56-1.68' localized at 4.38% whereas 'INHOMO 1.58-1.61' localized at 4.76%. The global convergence

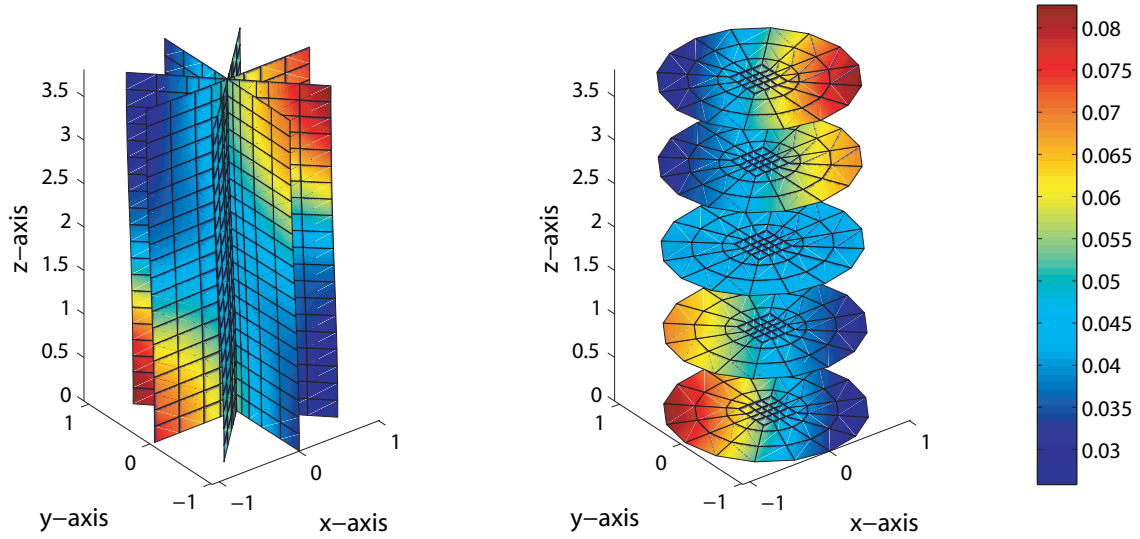

Figure 4.14: Total deviatoric strain invariant on various cut-planes at the onset of localization for sample 'INHOMO 1.58-1.61'.

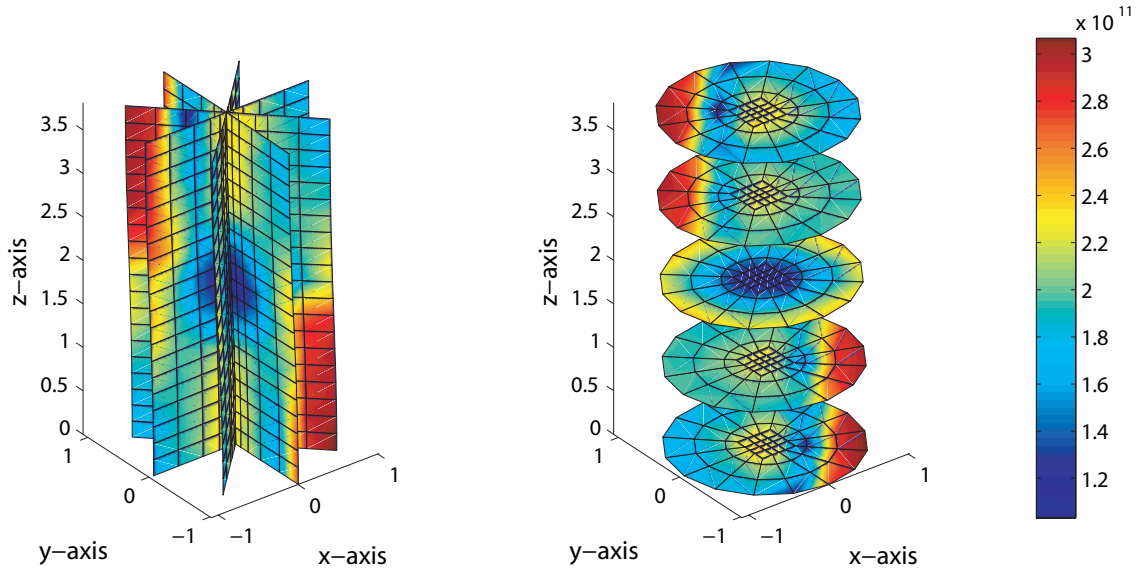

Figure 4.15: Determinant of acoustic tensor on various cut-planes at the onset of localization for sample 'INHOMO 1.58-1.61'.

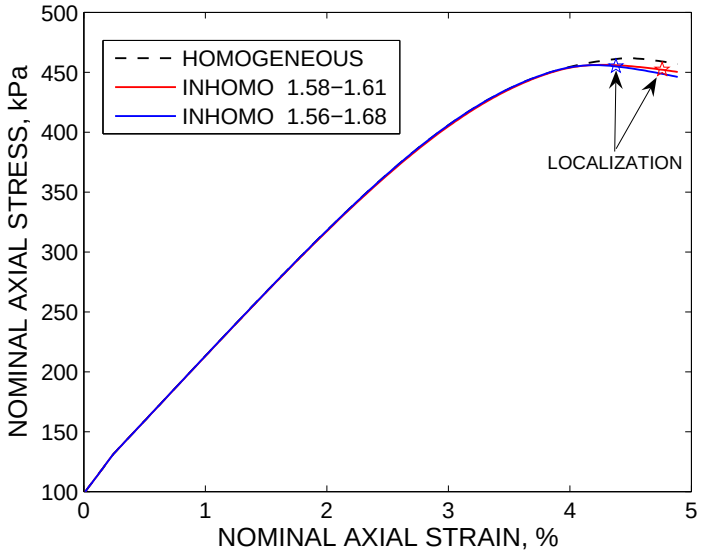

Figure 4.16: Nominal axial stress response for cylindrical specimens.

profile for the sample 'INHOMO 1.56-1.68' is reported in Figure 4.18, showing optimal rate of convergence.

4.7 Closure

We have presented a critical state plasticity model that utilizes all three invariants of the stress tensor for deformation and strain localization analyses of granular materials with random unstructured density at the meso-scale. For the implementation we have used the classical return mapping algorithm in the direction of the elastic logarithmic principal stretches. An iterative algorithm based on Newton's method was shown to deliver optimal performance. We also have presented a search algorithm for the minimum determinant of the acoustic tensor on the elastic principal stretch planes. Boundary-value problems mimicking soil samples have been analyzed using a truncated exponential distribution to generate random and unstructured density fields. Results of numerical simulations suggest that inhomogeneities tend to trigger strain localization, with heterogeneous samples localizing when their equivalent homogeneous counterparts would not. Results of the studies also suggest that heterogeneity in the density field tends to enhance and accelerate the onset of strain localization, even if the initial global deformation responses of a homogeneous sample

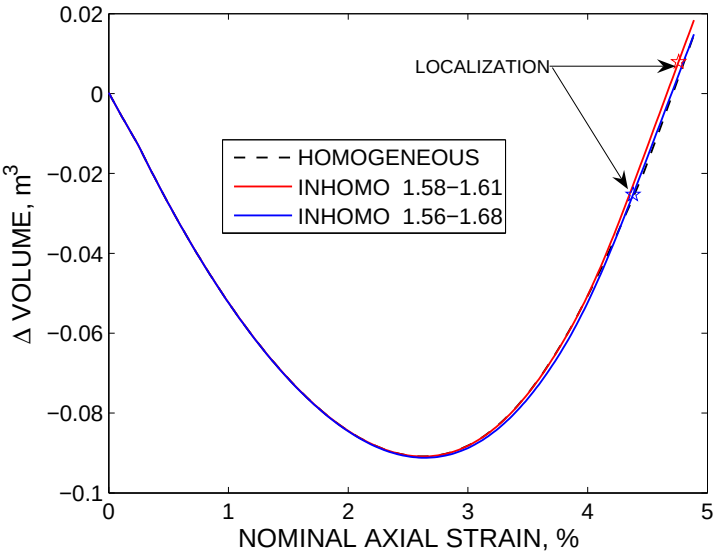

Figure 4.17: Volume change response for cylindrical specimens.

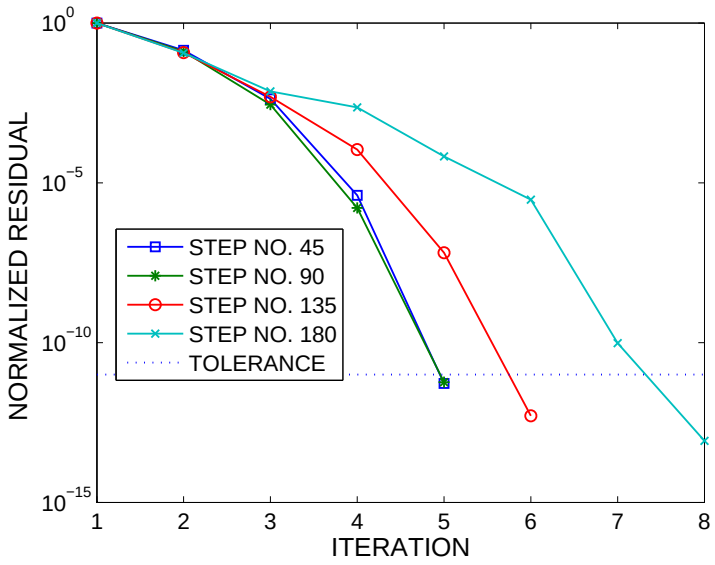

Figure 4.18: Convergence profile for finite element solution at various load steps.

and its heterogeneous counterpart appear to be the same. The framework presented in this paper is useful for investigating strain localization phenomena in heterogeneous granular materials at a finer scale.

Acknowledgments

This work has been supported by National Science Foundation under Grant Nos. CMS-0201317 and CMS-0324674 to Stanford University. The first author is grateful to Professor Adrian Lew of Stanford University for enlightening discussions regarding constitutive theory and Lie derivatives. We also thank the two anonymous reviewers for their constructive reviews.

Chapter 5

Modeling deformation banding in dense and loose fluid-saturated sands

This Chapter will be published in: J. E. Andrade and R. I. Borja. Modeling deformation banding in dense and loose fluid-saturated sands. *Finite Elements in Analysis and Design*, 2006. In review for the 18th Annual Melosh Competition Special Issue.

Abstract

Balance of mass and linear momentum of a solid-fluid mixture furnish a complete set of equations from which the displacements of the solid matrix and the pore pressures can be resolved for the case of quasi-static loading, resulting in the so-called $\boldsymbol{u} - p$ Galerkin formulation. In this work, a recently proposed model for dense sands is utilized to model the effective stress response of the solid matrix appearing in the balance of linear momentum equation. In contrast with other more traditional models, inherent inhomogeneities in the porosity field at the meso-scale are thoroughly incorporated and coupled with the macroscopic laws of mixture theory. Also, the hydraulic conductivity is naturally treated as a function of the porosity in the solid matrix, allowing for a more realistic representation of the physical phenomenon. The aforementioned balance laws are cast into a fully nonlinear finite element program utilizing isoparametric elements satisfying the Babuška-Brezzi

stability condition. Criteria for the onset of localization under locally drained and locally undrained conditions are derived and utilized to detect instabilities. Numerical simulations on dense and loose sand specimens are performed to study the effects of inhomogeneities on the stability of saturated porous media at the structural level.

5.1 Introduction

Deformation banding is one of the most common failure modes in geomaterials such as rock, concrete, and soil. It is well known that appearance of bands of intense localized deformation significantly reduces the load-carrying capacity of any structure that develops them [20, 140]. Furthermore, when dealing with fluid-saturated geomaterials, the interplay between the contraction/dilation of pores and development of pore fluid pressures is expected to influence not only the strength of the solid matrix but also its ability to block or transport such fluids [12]. Accurate and thorough simulation of these phenomena (i.e., deformation banding and fluid flow) requires numerical models capable of capturing fine-scale mechanical processes such as mineral particle rolling and sliding in granular soils and the coupling between porosity and relative permeability. Until recently, these processes could not even be observed in the laboratory. Numerical models could only interpret material behavior as a macroscopic process and were, therefore, unable to model the very complex behavior of saturated geomaterials accurately.

In this paper, we study the deformation-diffusion behavior of a two-phase system of soil and fluid. It is well known that the coupling between the mechanical behavior of the underlying drained solid and the fluid flow can lead to sharply distinct behavior of the overall mixed system. For instance, dilative saturated rock masses can lead to a phenomenon called 'dilatant hardening', which, as the name implies, tends to delay the onset of strain localization because effective pressures tend to increase and hence strengthen the sample in general [44, 141, 142]. On the other hand, relatively loose sands tend to compact when sheared. Therefore, when pores compact faster than the rate at which fluids can escape, pore fluid pressure increases and the effective pressure decreases, leading to a phenomenon known in the geotechnical community as 'liquefaction' [3, 13, 14]. Consequently, it is important to study the deformation-diffusion behavior in saturated granular media taking into account the effect of pore contraction/dilation and its influence on the relative density and permeability of the solid matrix. This is accomplished in this study.

Even though the interplay between fluid flow and solid deformation using finite elements has been studied before, the focus of models dealing with fully saturated and partially saturated soils has been on 'homogeneous' material response [45, 55, 143–150]. This has been a natural approach given the fact that the technology to infer material inhomogeneities in the laboratory has only been recently developed. Therefore, numerical models dealing with the simulation of strain localization have either imposed inhomogeneous deformation fields (e.g., [55, 143, 144]) or introduced arbitrary weaknesses in the otherwise pristine specimens (e.g., [50–52, 62]).

New advances in laboratory experimentation, such as X-Ray Computed Tomography (CT) and Digital Image Correlation (DIC) techniques, allow accurate observation of key parameters associated with material strength and provide the motivation for the development of more realistic models that incorporate information at a scale finer than specimen scale (see works in [4, 15, 16] for applications of X-Ray CT and [83, 151] for applications of DIC). In this paper, we adopt a refined constitutive model based on a meso-scale description of the porosity to simulate the development (location and direction) of deformation bands on saturated samples of sand. The effective stress behavior of the granular material is assumed to be governed by an elastoplastic model for sands developed by the authors in [122, 152]. The ability of the model to incorporate data depicting the inherent inhomogeneities in samples of sand at the meso-scale provides a natural and realistic source of inhomogeneity that, as we shall demonstrate subsequently, affects the stability and flow characteristics of sand specimens. As a matter of terminology the 'meso-scale' here refers to a scale smaller than specimen size but larger than particle size. In a typical sample encountered in the laboratory, the meso-scale refers to the millimeter scale.

The constitutive model for the effective stresses is a member of the critical state plasticity family of models. It is based on an original model proposed by Jefferies in [2] and extended by the authors in [122, 152]. Two main features distinguish this model from its critical state predecessors. First, the yield surface is allowed to 'detach' from the critical state line by introducing a state parameter ψ [106], allowing a state point to lie either above or below the critical state line (CSL). Through the state parameter ψ we are able to prescribe spatial values of porosity across the sample, which constitutes the connection to the meso-scale. Second, the model features a nonassociative flow rule and a three stress-invariant formulation, for capturing important features of sand behavior [153].

The model for the two-phase system is based on the theory of mixtures [154, 155], which

serves as the underlying theoretical block to develop balance laws for multi-phase bodies. Saturated granular media is modeled as a two-phase system composed of a solid phase and a fluid phase. This study extends the work of Li et al. [156] who considered *elastic* expulsion of fluids at finite strain and also extends the work by Armero [143] who looked at the strain localization behavior of *homogeneous* saturated samples of soil—obeying a generalized Drucker-Prager constitutive model—under boundary conditions favoring inhomogeneous deformations. Furthermore, here the fluid content is not decomposed into elastic and plastic parts as the porosity field is naturally coupled to the elastoplastic formulation emanating from the constitutive law for the porous matrix. The numerical implementation also differs from that of Armero [143] as it does not rely on the operator split technique, but rather solves the coupled system of nonlinear equations directly. It is worthwhile noting that Armero and Callari [157] and Callari and Armero [47] expanded the work by Armero [143] by developing a strong discontinuity model to model deformation banding in homogeneous saturated media at finite strains.

In this work, fluid-saturated porous media is modeled using nonlinear continuum mechanics and a novel constitutive model for sands. Furthermore, the effect of porosity is also accounted for by utilizing the Kozeny-Carman equation which relates the intrinsic permeability to the porosity [158]. The objective of this paper is to study the effect of fluctuations in porosity at the meso-scale on the stability and transport properties of samples of dense and loose sand analyzed as boundary-value problems.

Using the balance laws for the system, along with the concept of effective stresses, the strong form of the deformation-diffusion problem at finite deformations is developed. The variational form is obtained as a two-field mixed formulation where the displacements in the solid matrix $\boldsymbol{u}$ and the Cauchy fluid pressures p serve as basic unknowns. Thus, a classical $\boldsymbol{u} - p$ formulation is obtained and discretized in space using elements satisfying the Babuška-Brezzi stability condition [119, 159]. The linearization of the variational equations serve as the building block to develop expressions for the acoustic tensor for two extreme cases: the case of locally drained behavior and the case of locally undrained behavior. These expressions for the acoustic tensor are then utilized in the analysis of localization of strain for a fully saturated medium.

The structure of the paper is as follows. In Section 5.2 the conservation of mass and linear momentum equations for a two-phase mixture are derived. Section 5.3 describes

the constitutive framework utilized in the formulation. In particular, the concept of effective stress is introduced and the model governing the effective stresses is briefly described. Darcy's law is presented as the fundamental constitutive equation for fluid flow. In Section 5.4, the finite element solution procedure is presented and the linearization of the variational equations is addressed in detail. Section 5.5 addresses the extreme criteria for localization in fluid-saturated media. The framework described above is then utilized in a series of numerical examples presented in Section 5.6, where it is shown that the stability and flow properties of samples of sand is profoundly influenced by meso-scale inhomogeneities in the initial porosity field.

As for notations and symbols used in this paper, bold-faced letters denote tensors and vectors; the symbol '$\cdot$' denotes an inner product of two vectors (e.g. $\boldsymbol{a}\cdot\boldsymbol{b} = a_i b_i$), or a single contraction of adjacent indices of two tensors (e.g. $\boldsymbol{c}\cdot\boldsymbol{d} = c_{ij}d_{jk}$); the symbol ':' denotes an inner product of two second-order tensors (e.g. $\boldsymbol{c} : \boldsymbol{d} = c_{ij}d_{ij}$), or a double contraction of adjacent indices of tensors of rank two and higher (e.g. $\boldsymbol{C} : \boldsymbol{\epsilon}^{\mathrm{e}} = C_{ijkl}\epsilon^{\mathrm{e}}_{kl}$); the symbol '$\otimes$' denotes a juxtaposition, e.g., $(\boldsymbol{a}\otimes\boldsymbol{b})_{ij} = a_i b_j$. Finally, for any symmetric second order tensors $\boldsymbol{\alpha}$ and $\boldsymbol{\beta}$, $(\boldsymbol{\alpha}\otimes\boldsymbol{\beta})_{ijkl} = \alpha_{ij}\beta_{kl}$, $(\boldsymbol{\alpha}\oplus\boldsymbol{\beta})_{ijkl} = \beta_{ik}\alpha_{jl}$, and $(\boldsymbol{\alpha}\ominus\boldsymbol{\beta})_{ijkl} = \alpha_{il}\beta_{jk}$.

5.2 Balance laws: conservation of mass and linear momentum

Consider a two-phase mixture of solids and fluid. The balance equations are obtained by invoking the classical mixture theory (see for example the works in [154, 155]). Within this context, each α-phase (α = s, f, for solid and fluid, respectively) or constituent occupies a volume fraction, $\phi^\alpha := V_\alpha/V$, where V_α is the volume occupied by the α-phase and $V = V_{\mathrm{s}} + V_{\mathrm{f}}$ is the total volume of the mixture. Naturally,

$$\phi^{\mathrm{s}} + \phi^{\mathrm{f}} = 1. \tag{5.2.1}$$

The total mass of the mixture is defined by the mass contribution from each phase i.e., $M = M_{\mathrm{s}} + M_{\mathrm{f}}$. The inherent or true mass density for the α-phase is defined as $\rho_\alpha := M_\alpha/V_\alpha$. Also, the apparent or partial mass density is given by $\rho^\alpha = \phi^\alpha\rho_\alpha$. Therefore, the total mass density is given by

$$\rho = \rho^{\mathrm{s}} + \rho^{\mathrm{f}}. \tag{5.2.2}$$

Furthermore, both phases are assumed to be superimposed on top of each other and hence, a point $\boldsymbol{x}$ in the mixture is occupied by both solid and fluid simultaneously.

From this point forward, all inherent or true quantities pertaining to the α-phase are designated with a subscript, whereas apparent or partial quantities are designated with a superscript as a general notation.

5.2.1 Balance of mass

In deriving the balance laws, it is relevant to pose all time derivatives following a particular phase. From Figure 5.1, we note that the current configuration of the mixture in a region Ω is defined by the mapping of the solid-phase $\boldsymbol{\varphi}_{\mathrm{s}}\left(\boldsymbol{X}_{\mathrm{s}}, t\right)$, where $\boldsymbol{X}_{\mathrm{s}} \equiv \boldsymbol{X}$ is the position vector in the reference configuration $\Omega_0^{\mathrm{s}} \equiv \Omega_0$, and the mapping of the fluid-phase $\boldsymbol{\varphi}_{\mathrm{f}}\left(\boldsymbol{X}_{\mathrm{f}}, t\right)$, where $\boldsymbol{X}_{\mathrm{f}}$ is the position vector in the reference configuration Ω_0^{f}. Hence, it is convenient to define the total time-derivative following the α-phase such that

$$\frac{\mathrm{d}^{\alpha}\left(\square\right)}{\mathrm{d}t} = \frac{\partial\left(\square\right)}{\partial t} + \nabla^{\boldsymbol{x}}\left(\square\right) \cdot \boldsymbol{v}_{\alpha}, \tag{5.2.3}$$

where $\nabla^{\boldsymbol{x}}\left(\square\right) \equiv \partial\square/\partial\boldsymbol{x}$ is the gradient operator with respect to the current configuration Ω and $\boldsymbol{v}_{\alpha} \equiv \partial\boldsymbol{\varphi}_{\alpha}/\partial t$ is the velocity vector of the α-phase. For simplicity of notation and where there is no room for ambiguity, we drop the subscripts and superscripts for all quantities pertaining to the solid-phase, as we will write all balance laws following this phase. It is thus straight-forward to check the identity

$$\frac{\mathrm{d}^{\mathrm{f}}\left(\square\right)}{\mathrm{d}t} = \frac{\mathrm{d}\left(\square\right)}{\mathrm{d}t} + \nabla^{\boldsymbol{x}}\left(\square\right) \cdot \tilde{\boldsymbol{v}}, \tag{5.2.4}$$

where $\tilde{\boldsymbol{v}} := \boldsymbol{v}_{\mathrm{f}} - \boldsymbol{v}$ is the relative velocity vector and $\mathrm{d}/\mathrm{d}t\left(\square\right) \equiv \dot{\overline{\left(\square\right)}}$ is the total material time derivative following the solid-phase.

Consider the expression for the total mass of α-phase in the current configuration i.e.,

$$m^{\alpha} \equiv \int_{\Omega} \phi^{\alpha}\rho_{\alpha}\,\mathrm{d}\Omega = \int_{\Omega_0^{\alpha}} \phi^{\alpha}\rho_{\alpha}J_{\alpha}\,\mathrm{d}\Omega_0^{\alpha}, \qquad \alpha = \mathrm{s}, \mathrm{f}, \tag{5.2.5}$$

which has been pulled back to the reference configuration of the α-phase via the mapping $\boldsymbol{\varphi}_{\alpha}^{-1}$ and where $J_{\alpha} = \det \boldsymbol{F}_{\alpha}$ is the Jacobian of the deformation gradient tensor $\boldsymbol{F}_{\alpha} \equiv \partial\boldsymbol{\varphi}_{\alpha}/\partial\boldsymbol{X}_{\alpha}$. If there is no production of α-phase mass and there are no mass exchanges

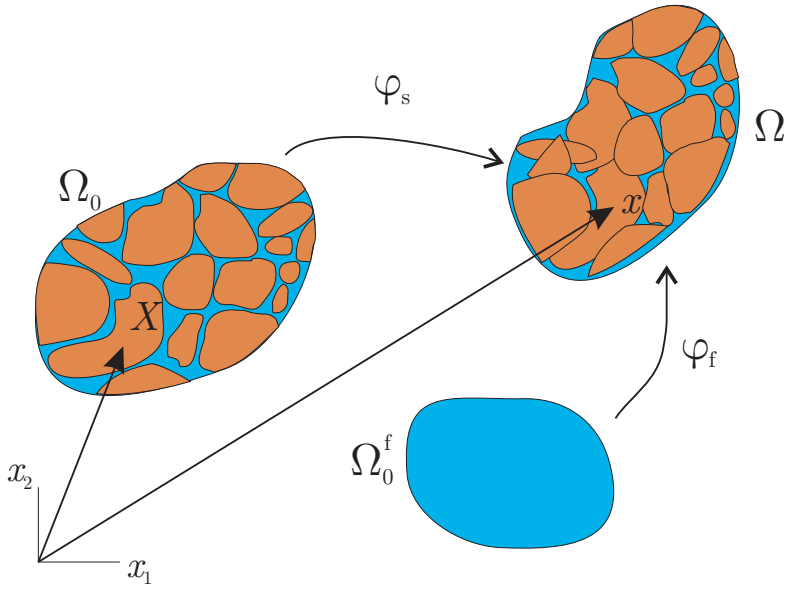

Figure 5.1: Current configuration Ω mapped from respective solid and fluid reference configurations.

amongst phases, conservation of mass implies

$$\frac{\mathrm{d}^\alpha}{\mathrm{d}t} m^\alpha = \int_{\Omega_0^\alpha} \frac{\mathrm{d}^\alpha}{\mathrm{d}t} \left(\phi^\alpha \rho_\alpha J_\alpha\right) \mathrm{d}\Omega_0^\alpha = 0, \qquad \alpha = \mathrm{s}, \mathrm{f}, \tag{5.2.6}$$

which after classical continuity arguments yields the localized form of the conservation of mass for the α-phase

$$\frac{\mathrm{d}^\alpha}{\mathrm{d}t} \rho^\alpha + \rho^\alpha \, \nabla^{\boldsymbol{x}} \cdot \boldsymbol{v}_\alpha = 0, \tag{5.2.7}$$

where $\nabla^{\boldsymbol{x}} \cdot (\square)$ is the divergence operator with respect to the current configuration. Making use of equation (5.2.7) and identity (5.2.4) the conservation of mass equation for the solid and fluid phases are, respectively,

$$\dot{\rho}^{\mathrm{s}} + \rho^{\mathrm{s}} \, \nabla^{\boldsymbol{x}} \cdot \boldsymbol{v} = 0 \tag{5.2.8a}$$

$$\dot{\rho}^{\mathrm{f}} + \rho^{\mathrm{f}} \, \nabla^{\boldsymbol{x}} \cdot \boldsymbol{v} = -\nabla^{\boldsymbol{x}} \cdot \boldsymbol{q}, \tag{5.2.8b}$$

where $\boldsymbol{q} \equiv \rho^{\mathrm{f}} \tilde{\boldsymbol{v}}$ is the Eulerian relative flow vector of the fluid phase with respect to the solid matrix. Adding equations (5.2.8a) and (5.2.8b), we get the basic conservation of mass

equation for the system, i.e.,

$$\boxed{\dot{\rho}_0 = -J\,\nabla^{\boldsymbol{x}}\cdot\boldsymbol{q},} \tag{5.2.9}$$

where $\rho_0 \equiv J\rho$ is the pull-back mass density of the mixture in the reference configuration. It is clear from the above equation that in the case of locally undrained deformations (i.e., when both phases of the mixture move as one) $\boldsymbol{q} \approx 0$ and thus the relative mass flux term in the right-hand side drops out and the classical conservation of mass for a mono-phase body is captured.

Equations (5.2.8a) and (5.2.8b) are typically simplified by recalling the definition of the partial densities and introducing the bulk modulus. For barotropic flows, there exists a functional relationship of the form $f_\alpha\left(p_\alpha, \rho_\alpha\right) = 0$, where p_α is the intrinsic Cauchy pressure in the α-phase or the force acting on this phase per unit area of the same phase [116, 156]. Thus, it is meaningful to define the bulk modulus of the alpha phase such that

$$K_\alpha = \rho_\alpha \frac{\mathrm{d}p_\alpha}{\mathrm{d}\rho_\alpha}, \qquad \alpha = \mathrm{s}, \mathrm{f}, \tag{5.2.10}$$

and therefore equations (5.2.8a) and (5.2.8b) can then be rewritten, respectively, as

$$\dot{\phi}^{\mathrm{s}} + \phi^{\mathrm{s}}\left(\frac{\dot{p}_{\mathrm{s}}}{K_{\mathrm{s}}} + \nabla^{\boldsymbol{x}}\cdot\boldsymbol{v}\right) = 0 \tag{5.2.11a}$$

$$\dot{\phi}^{\mathrm{f}} + \phi^{\mathrm{f}}\left(\frac{\dot{p}_{\mathrm{f}}}{K_{\mathrm{f}}} + \nabla^{\boldsymbol{x}}\cdot\boldsymbol{v}\right) = -\frac{1}{\rho_{\mathrm{f}}}\nabla^{\boldsymbol{x}}\cdot\boldsymbol{q}. \tag{5.2.11b}$$

Adding the last two equations and recalling equation (5.2.1), we get

$$\phi^{\mathrm{s}}\frac{\dot{p}_{\mathrm{s}}}{K_{\mathrm{s}}} + \phi^{\mathrm{f}}\frac{\dot{p}_{\mathrm{f}}}{K_{\mathrm{f}}} + \nabla^{\boldsymbol{x}}\cdot\boldsymbol{v} = -\frac{1}{\rho_{\mathrm{f}}}\nabla^{\boldsymbol{x}}\cdot\boldsymbol{q}. \tag{5.2.12}$$

The above equation can be expressed in terms of the Kirchhoff intrinsic pressures by recalling the relationship between the Kirchhoff and Cauchy stress tensors, i.e., $\boldsymbol{\tau}_\alpha \equiv J\boldsymbol{\sigma}_\alpha$ and as a result the Kirchhoff pressure for the α-phase is defined as $\vartheta_\alpha = Jp_\alpha$. Using the identity $\dot{J} = J\,\nabla^{\boldsymbol{x}}\cdot\boldsymbol{v}$ [30] we express equation (5.2.12) as

$$\phi^{\mathrm{s}}\frac{\dot{\vartheta}_{\mathrm{s}}}{K_{\mathrm{s}}} + \phi^{\mathrm{f}}\frac{\dot{\vartheta}_{\mathrm{f}}}{K_{\mathrm{f}}} + \dot{J}\left[1 - \frac{\phi^{\mathrm{s}}}{J}\frac{\vartheta_{\mathrm{s}}}{K_{\mathrm{s}}} - \frac{\phi^{\mathrm{f}}}{J}\frac{\vartheta_{\mathrm{f}}}{K_{\mathrm{f}}}\right] = -\frac{J}{\rho_{\mathrm{f}}}\nabla^{\boldsymbol{x}}\cdot\boldsymbol{q}. \tag{5.2.13}$$

Equation (5.2.13) is complete in the sense that neither constitutive nor kinematic assumptions have been introduced. In geomechanical applications, a typical and plausible assumption is to treat the solid phase as incompressible, and consequently $K_{\mathrm{s}} \to \infty$. Then, the *reduced* balance of mass equation for the mixture can be written as

$$\phi^{\mathrm{f}} \frac{\dot{\vartheta}_{\mathrm{f}}}{K_{\mathrm{f}}} + \dot{J} \left[1 - \frac{\phi^{\mathrm{f}}}{J} \frac{\vartheta_{\mathrm{f}}}{K_{\mathrm{f}}} \right] = -\frac{J}{\rho_{\mathrm{f}}} \nabla^{\boldsymbol{x}} \cdot \boldsymbol{q}. \tag{5.2.14}$$

Finally, we can write the Lagrangian balance of mass equation by making use of the Piola identity, i.e. $\nabla^{\boldsymbol{X}} \cdot \left(J \boldsymbol{F}^{-t} \right) = 0$ where $\nabla^{\boldsymbol{X}} \cdot (\square)$ is the divergence operator with respect to the reference configuration of the solid phase and the superscript 't' is the transpose operator. Thus,

$$J \nabla^{\boldsymbol{x}} \cdot \boldsymbol{q} = \nabla^{\boldsymbol{X}} \cdot \boldsymbol{Q}, \tag{5.2.15}$$

where $\boldsymbol{Q} \equiv J \boldsymbol{F}^{-1} \cdot \boldsymbol{q}$ is the Piola transform of the Eulerian vector $\boldsymbol{q}$. Therefore, the Lagrangian balance of mass equation takes the form, cf. equation (5.2.9),

$$\boxed{\dot{\rho}_0 = - \nabla^{\boldsymbol{X}} \cdot \boldsymbol{Q}.} \tag{5.2.16}$$

5.2.2 Balance of linear momentum

At this point, it is necessary to introduce the concept of partial stresses in a more rigorous way. Let $\boldsymbol{\sigma}^{\alpha}$ denote the Cauchy partial stress tensor for the α-phase. The total Cauchy stress tensor is obtained from the sum [46, 155, 160]

$$\boldsymbol{\sigma} = \boldsymbol{\sigma}^{\mathrm{s}} + \boldsymbol{\sigma}^{\mathrm{f}}. \tag{5.2.17}$$

From the above definition, an expression for the partial Cauchy pressure or mean normal stress for the α-phase can be readily obtained, i.e. $p^{\alpha} \equiv -1/3 \operatorname{tr} \boldsymbol{\sigma}^{\alpha}$ and hence, the intrinsic Cauchy pressures can be defined such that

$$p_{\mathrm{s}} = -\frac{1}{3\phi^{\mathrm{s}}} \operatorname{tr} \boldsymbol{\sigma}^{\mathrm{s}} \qquad \text{and} \qquad p_{\mathrm{f}} = -\frac{1}{3\phi^{\mathrm{f}}} \operatorname{tr} \boldsymbol{\sigma}^{\mathrm{f}}. \tag{5.2.18}$$

Also, the associated first Piola-Kirchhoff partial stress tensor can be defined as $\boldsymbol{P}^{\alpha} = J \boldsymbol{\sigma}^{\alpha} \cdot \boldsymbol{F}^{-t}$, the total first Piola-Kirchhoff stress tensor is given by

$$\boldsymbol{P} = \boldsymbol{P}^{\mathrm{s}} + \boldsymbol{P}^{\mathrm{f}}. \tag{5.2.19}$$

The linear momentum acting on the α-phase is given by [154, 155, 161]

$$\boldsymbol{l}^{\alpha} = \int_{\Omega} \rho^{\alpha} \boldsymbol{v}_{\alpha} \, \mathrm{d}\Omega, \tag{5.2.20}$$

whereas the resulting forces acting on the phase are [46]

$$\boldsymbol{r}^{\alpha} = \int_{\Omega} (\phi^{\alpha} \rho_{\alpha} \boldsymbol{g} + \phi^{\alpha} \boldsymbol{h}_{\alpha}) \, \mathrm{d}\Omega + \int_{\Gamma} \phi^{\alpha} \boldsymbol{t}_{\alpha} \, \mathrm{d}\Gamma, \tag{5.2.21}$$

where $\boldsymbol{g}$ is the gravity vector. The first term in (5.2.21) results from the body forces acting on the α-phase, the second term comes from the forces exerted on the α-phase from other phases in the mixture, and the third term emanates from the tractions imposed on the phase at the boundary Γ. Note that the partial traction is related to the partial Cauchy stress on the α-phase via the tetrahedron theorem i.e., $\boldsymbol{t}^{\alpha} \equiv \phi^{\alpha} \boldsymbol{t}_{\alpha} = \boldsymbol{\sigma}^{\alpha} \cdot \boldsymbol{n}$, where $\boldsymbol{n}$ is a unit vector normal to the surface Γ.

Balance of linear momentum on the α-phase necessitates

$$\frac{\mathrm{d}^{\alpha}}{\mathrm{d}t} \boldsymbol{l}^{\alpha} = \boldsymbol{r}^{\alpha}, \tag{5.2.22}$$

and after pull-back and push-forward operations and enforcing balance of mass, see equation (5.2.7), we get

$$\int_{\Omega} \rho^{\alpha} \boldsymbol{a}_{\alpha} \, \mathrm{d}\Omega = \boldsymbol{r}^{\alpha}, \tag{5.2.23}$$

where $\boldsymbol{a}_{\alpha} \equiv \mathrm{d}^{\alpha} \boldsymbol{v}^{\alpha} / \mathrm{d}t$ is the absolute acceleration vector for the α-phase. Once again, we can invoke localization arguments to get the point-wise version for the balance of linear momentum for the α-phase

$$\nabla^{\boldsymbol{x}} \cdot \boldsymbol{\sigma}^{\alpha} + \rho^{\alpha} \boldsymbol{g} + \phi^{\alpha} \boldsymbol{h}_{\alpha} = \rho^{\alpha} \boldsymbol{a}_{\alpha}, \tag{5.2.24}$$

which leads to the overall balance of linear momentum equation for the mixture i.e.,

$$\nabla^{\boldsymbol{x}} \cdot \boldsymbol{\sigma} + \rho \boldsymbol{g} = \rho \boldsymbol{a}_{\mathrm{s}} + \rho^{\mathrm{f}} \tilde{\boldsymbol{a}}, \tag{5.2.25}$$

where $\tilde{\boldsymbol{a}} \equiv\!= \boldsymbol{a}_{\mathrm{f}} - \boldsymbol{a}_{\mathrm{s}}$ is the relative acceleration. In obtaining the above equation, the balance of linear momentum equations for both phases have been added and the fact that $\phi^{\mathrm{s}} \boldsymbol{h}_{\mathrm{s}} + \phi^{\mathrm{f}} \boldsymbol{h}_{\mathrm{f}} = \boldsymbol{0}$, since these are mutually-equilibrating internal forces, has been exploited.

For the important case of quasi-static loading, all inertial forces are neglected and the equation of balance of linear momentum for the mixture reduces to the classical form

$$\boxed{\nabla^{\boldsymbol{x}}\cdot\boldsymbol{\sigma}+\rho\boldsymbol{g}=\boldsymbol{0}.} \tag{5.2.26}$$

In this work, only quasi-static loading conditions will be considered.

Finally, the Lagrangian form of the balance of linear momentum is easily obtained from its Eularian counterpart, namely,

$$\nabla^{\boldsymbol{X}}\cdot\boldsymbol{P}+\rho_0\boldsymbol{g}=\rho\boldsymbol{a}_{\mathrm{s}}+\rho^{\mathrm{f}}\tilde{\boldsymbol{a}}. \tag{5.2.27}$$

Accordingly, the Lagrangian balance of linear momentum for the system in the quasi-static range takes the form

$$\boxed{\nabla^{\boldsymbol{X}}\cdot\boldsymbol{P}+\rho_0\boldsymbol{g}=\boldsymbol{0}.} \tag{5.2.28}$$

Remark 7. The equations of balance of mass and linear momentum derived above from basic principles of the mixture theory are identical to those presented by Borja in [46] and Li et al. in [156]. In fact, Borja [46] considers the case of a three-phase mixture by taking into account the gas phase also and develops a constitutive framework, but no boundary value problems are solved. The interested reader is referred to the work in [46] where the remaining balance laws for the multi-phased system are reported.

5.3 Constitutive framework

There is the need to establish a link between the state of stress and the displacements or deformations and between the flow vector and the fluid pressure in the porous media. These links are provided by constitutive relationships that we shall explicate in this section. In particular, the stresses are assumed to be a nonlinear function of the deformations via an elastoplastic constitutive response. On the other hand, the relative flow vector is related to the fluid pressure using Darcy's law.

5.3.1 The elastoplastic model for granular media

Analogous to the case of mono-phase materials, constitutive relations in fluid saturated porous media connect the deformations in the solid matrix to a suitable measure of stress.

The relationship must connect so-called energy conjugate pairs of stress-strain measures. Consider the general definition of effective stress for saturated conditions [162, 163]

$$\boldsymbol{\sigma}' = \boldsymbol{\sigma} + \left(1 - \frac{K}{K_{\mathrm{s}}}\right) p_{\mathrm{f}} \mathbf{1}, \tag{5.3.1}$$

where K is the bulk modulus of the solid matrix and $\mathbf{1}$ is the second-order identity tensor. Borja in [163] derived expression (5.3.1) using a strong discontinuity approach for the mechanical theory of porous media, and has shown that one suitable energy conjugate pair is furnished by the effective stress $\boldsymbol{\sigma}'$ and the symmetric part of the rate of deformation tensor for the solid matrix $\boldsymbol{d} \equiv \operatorname{sym} \boldsymbol{l}$, with $\boldsymbol{l} \equiv \nabla^{\boldsymbol{x}} \boldsymbol{v}$, and where we have dropped the subscript 's' from the velocity vector as there is no room for ambiguity.

For the case of interest herein, where the solid phase is assumed to be incompressible, the above expression for the effective stress reduces to the classical form introduced by Terzaghi [164], i.e.

$$\boldsymbol{\sigma}' = \boldsymbol{\sigma} + p\mathbf{1} \qquad \Longrightarrow \qquad \boldsymbol{\tau}' = \boldsymbol{\tau} + \vartheta \mathbf{1}, \tag{5.3.2}$$

where the expression on the right-hand-side has been obtained from direct application of the relationship between the Kirchhoff and the Cauchy stress (i.e., $\boldsymbol{\tau} = J\boldsymbol{\sigma}$). Also note the subscript 'f' has been dropped from the fluid-phase pressures for simplicity of notation. For incompressible solid grains, the balance of mass for the solid phase (cf. (5.2.11a)) necessitates $\dot{\phi}^{\mathrm{s}} + \phi^{\mathrm{s}} \nabla^{\boldsymbol{x}} \cdot \boldsymbol{v} = 0$ implying $\overline{(J\dot{\phi}^{\mathrm{s}})} = 0$, and therefore

$$\phi^{\mathrm{s}} = \phi^{\mathrm{s}}_0 / J \qquad \text{and} \qquad \phi^{\mathrm{f}} = 1 - \left(1 - \phi^{\mathrm{f}}_0\right) / J, \tag{5.3.3}$$

where ϕ^{s}_0 and ϕ^{f}_0 are the reference values of ϕ^{s} and ϕ^{f} when $J = 1$. Also, the bulk modulus for the fluid phase is assumed to be constant and hence recalling its definition allows us to obtain a relationship between the intrinsic fluid pressure and the intrinsic fluid density, i.e.

$$K_{\mathrm{f}} = \rho_{\mathrm{f}} \frac{\mathrm{d}p}{\mathrm{d}\rho_{\mathrm{f}}} = \text{constant} \qquad \Longrightarrow \qquad \rho_{\mathrm{f}} = \rho_{\mathrm{f0}} \exp\left(\frac{p - p_{\mathrm{f0}}}{K_{\mathrm{f}}}\right), \tag{5.3.4}$$

where ρ_{f0} is the initial reference fluid mass density at initial pressure p_{f0}.

At this point, a constitutive framework governing the *effective* stress as a function of the solid matrix deformation can be introduced. Herein we assume the effective behavior of the granular material is governed by the three-invariant hyperelastoplastic model proposed

by the authors in [122, 152]. Here, we summarize the salient features of the model.

The model is cast within the framework of nonlinear kinematics where the total deformation gradient is assumed to allow the multiplicative decomposition into elastic and plastic parts [115] i.e.,

$$\boldsymbol{F} = \boldsymbol{F}^{\mathrm{e}} \cdot \boldsymbol{F}^{\mathrm{p}}, \tag{5.3.5}$$

where $\boldsymbol{F}^{\mathrm{e}}$ and $\boldsymbol{F}^{\mathrm{p}}$ are defined as the elastic and plastic deformation gradient, respectively.

Isotropic hyperelasticity

Consider the principal elastic stretches emanating from $\boldsymbol{F}^{\mathrm{e}} \cdot \boldsymbol{N}^a = \lambda^a \boldsymbol{n}^a$ (no sum), where λ^{e}_a for $a = 1, 2, 3$ are the principal elastic stretches in the corresponding principal directions $\boldsymbol{N}^a$ and $\boldsymbol{n}^a$ in the intermediate and current configuration, respectively. Material isotropy is satisfied if the strain-energy function $\Psi = \Psi\left(\lambda^{\mathrm{e}}_1, \lambda^{\mathrm{e}}_2, \lambda^{\mathrm{e}}_3\right)$. The elastic region is assumed to be governed by the isotropic strain energy function proposed in [1] and utilized in modeling of granular bodies in [66, 125],

$$\Psi\left(\varepsilon^{\mathrm{e}}_{\mathrm{v}}, \varepsilon^{\mathrm{e}}_{\mathrm{s}}\right) = \tilde{\Psi}\left(\varepsilon^{\mathrm{e}}_{\mathrm{v}}\right) + \frac{3}{2}\mu^{\mathrm{e}} \varepsilon^{\mathrm{e}\,2}_{\mathrm{s}}, \tag{5.3.6}$$

where

$$\tilde{\Psi}\left(\varepsilon^{\mathrm{e}}_{\mathrm{v}}\right) = -p_0 \hat{\kappa} \exp \omega, \qquad \omega = -\frac{\varepsilon^{\mathrm{e}}_{\mathrm{v}} - \varepsilon^{\mathrm{e}}_{\mathrm{v}\,0}}{\hat{\kappa}}, \qquad \mu^{\mathrm{e}} = \mu_0 + \frac{\alpha_0}{\hat{\kappa}} \tilde{\Psi}\left(\varepsilon^{\mathrm{e}}_{\mathrm{v}}\right). \tag{5.3.7}$$

The independent variables are the volumetric and deviatoric invariants of the elastic logarithmic stretch tensor, respectively,

$$\varepsilon^{\mathrm{e}}_{\mathrm{v}} = \varepsilon^{\mathrm{e}}_1 + \varepsilon^{\mathrm{e}}_2 + \varepsilon^{\mathrm{e}}_3 \qquad \text{and} \qquad \varepsilon^{\mathrm{e}}_{\mathrm{s}} = \frac{1}{3}\sqrt{2\left[\left(\varepsilon^{\mathrm{e}}_1 - \varepsilon^{\mathrm{e}}_2\right)^2 + \left(\varepsilon^{\mathrm{e}}_2 - \varepsilon^{\mathrm{e}}_3\right)^2 + \left(\varepsilon^{\mathrm{e}}_3 - \varepsilon^{\mathrm{e}}_1\right)^2\right]}, \tag{5.3.8}$$

where $\varepsilon^{\mathrm{e}}_a \equiv \ln \lambda^{\mathrm{e}}_a$. The strain energy function is an invariant function of the elastic deformations only. The Kirchhoff effective stress tensor $\boldsymbol{\tau}'$ is coaxial with the left elastic Cauchy-Green deformation tensor $\boldsymbol{b}^{\mathrm{e}} \equiv \boldsymbol{F}^{\mathrm{e}} \cdot \boldsymbol{F}^{\mathrm{e}\,\mathrm{t}}$ and defined such that

$$\boldsymbol{\tau}' = 2\frac{\partial \Psi}{\partial \boldsymbol{b}^{\mathrm{e}}} \cdot \boldsymbol{b}^{\mathrm{e}}. \tag{5.3.9}$$

The above hyperelastic model produces pressure-dependent elastic bulk and shear moduli, a feature commonly observed in the laboratory. The elastic constants necessary for a full

description of the elasticity are the reference strain $\varepsilon^{\mathrm{e}}_{\mathrm{v}\,0}$ and the reference pressure p_0 of the elastic compression curve, as well as the compressibility index $\hat{\kappa}$. The model produces coupled volumetric and deviatoric responses in the case $\alpha_0 \neq 0$ for which μ^{e} is a nonlinear function of the volumetric deformations. Otherwise, for $\alpha_0 = 0$ the responses are decoupled and the shear modulus $\mu^{\mathrm{e}} \equiv \mu_0$ is constant.

Plasticity for sands

We define the three invariants of the effective Kirchhoff stress tensor as

$$p' = \frac{1}{3}\operatorname{tr}\boldsymbol{\tau}', \qquad q = \sqrt{\frac{3}{2}}\|\boldsymbol{\xi}'\|, \qquad \frac{1}{\sqrt{6}}\cos 3\theta = \frac{\operatorname{tr}\boldsymbol{\xi}'^3}{\chi^3} \equiv y, \tag{5.3.10}$$

where $\boldsymbol{\xi}' = \boldsymbol{\tau}' - p'\mathbf{1}$ is the deviatoric component of the effective stress tensor $\boldsymbol{\tau}'$, and $\chi = \sqrt{\operatorname{tr}\boldsymbol{\xi}'^2}$. The quantity p' is called the mean normal effective stress and is assumed negative throughout. Further, θ is the Lode's angle whose values range from $0 \leq \theta \leq \pi/3$; it defines an angle on a deviatoric plane emanating from a tension corner.

From these three stress invariants we construct a yield surface of the form

$$F\left(\boldsymbol{\tau}', \pi_{\mathrm{i}}\right) = F\left(p', q, \theta, \pi_{\mathrm{i}}\right) = \zeta\left(\theta\right) q + p\eta\left(p', \pi_{\mathrm{i}}\right) \tag{5.3.11}$$

where

$$\eta = \begin{cases} M\left[1 + \ln\left(\pi_{\mathrm{i}}/p'\right)\right] & \text{if} \quad N = 0 \\ M/N\left[1 - (1-N)\left(p'/\pi_{\mathrm{i}}\right)^{N/(1-N)}\right] & \text{if} \quad N > 0. \end{cases} \tag{5.3.12}$$

The image stress $\pi_{\mathrm{i}} < 0$ controls the size of the yield surface; it is defined such that the stress ratio $\eta = -\zeta q/p = M$ when $p' = \pi_{\mathrm{i}}$. The parameter $N \geq 0$ determines the curvature of the yield surface on a meridian plane and it typically has a value less than or equal to 0.4 for sands [2]. Lode's angle θ plays the role of the third stress invariant modifying the shape of the yield and plastic potential surfaces on a deviatoric plane through the function $\zeta = \zeta\left(\theta\right)$. Here we adopt the form proposed by Gudehus in [127] and Argyris et al. in [128], namely,

$$\zeta\left(\theta\right) = \frac{(1+\varrho) + (1-\varrho)\cos 3\theta}{2\varrho} \tag{5.3.13}$$

where ϱ is a constant parameter called ellipticity. The above function is only convex for $7/9 \leq \varrho \leq 1$ [129] and satisfies the boundary conditions: (a) $\zeta = 1/\varrho$ when $\theta = 0$ i.e., tension corner; and (b) $\zeta = 1$ when $\theta = \pi/3$ i.e., compression corner. The third invariant allows to

account for the fact that soils have less yield strength in tension than in compression.

Remark 8. We note in passing that in the present work we do not make use of the shape function proposed by Willam and Warnke [130] as it has been shown recently in [165] (and experienced first hand by the authors) that such shape function, shown in equation (12) in [152], leads to convergence problems in the material subroutine when ϱ gets small. Hence, to avoid loss of robustness in our numerical simulations, we only make use of the simple shape function presented above.

Similar to the yield surface, we can postulate a plastic potential function of the form

$$G\left(\boldsymbol{\tau}', \overline{\pi}_{\mathrm{i}}\right) = G\left(p', q, \theta, \overline{\pi}_{\mathrm{i}}\right) = \zeta\left(\theta\right) q + p\overline{\eta}\left(p', \overline{\pi}_{\mathrm{i}}\right) \tag{5.3.14}$$

with

$$\overline{\eta} = \begin{cases} M\left[1 + \ln\left(\overline{\pi}_{\mathrm{i}}/p'\right)\right] & \text{if} \quad \overline{N} = 0 \\ M/\overline{N}\left[1 - \left(1 - \overline{N}\right)\left(p'/\overline{\pi}_{\mathrm{i}}\right)^{\overline{N}/\left(1-\overline{N}\right)}\right] & \text{if} \quad \overline{N} > 0. \end{cases} \tag{5.3.15}$$

When $\overline{\pi}_{\mathrm{i}} = \pi_{\mathrm{i}}$ and $\overline{N} = N$, plastic flow is associative; otherwise, it is nonassociative in the volumetric sense. Additionally, from the multiplicative decomposition of the deformation gradient, the additive decomposition of the velocity gradient $\boldsymbol{l}$ follows,

$$\boldsymbol{l} = \boldsymbol{l}^{\mathrm{e}} + \boldsymbol{l}^{\mathrm{p}} \qquad \Rightarrow \qquad \boldsymbol{d} = \boldsymbol{d}^{\mathrm{e}} + \boldsymbol{d}^{\mathrm{p}}, \tag{5.3.16}$$

where $\boldsymbol{d}^{\mathrm{e}} \equiv \operatorname{sym} \boldsymbol{l}^{\mathrm{e}}$, and $\boldsymbol{d}^{\mathrm{p}} \equiv \operatorname{sym} \boldsymbol{l}^{\mathrm{p}}$. Neglecting the plastic spin $\boldsymbol{\omega}^{\mathrm{p}}$ (see [118] for significance and consequences), we write the flow rule as

$$\boldsymbol{d}^{\mathrm{p}} = \dot{\lambda} \frac{\partial G}{\partial \boldsymbol{\tau}'}, \tag{5.3.17}$$

where $\dot{\lambda}$ is the so-called consistency parameter.

Finally, recall the definitions for the volumetric and deviatoric plastic strain rate invariants, respectively,

$$\dot{\varepsilon}_{\mathrm{v}}^{\mathrm{p}} = \operatorname{tr} \boldsymbol{d}^{\mathrm{p}} \qquad \text{and} \qquad \dot{\varepsilon}_{\mathrm{s}}^{\mathrm{p}} = \sqrt{\frac{2}{3}} \left\| \boldsymbol{d}^{\mathrm{p}} - 1/3 \dot{\varepsilon}_{\mathrm{v}}^{\mathrm{p}} \mathbf{1} \right\|. \tag{5.3.18}$$

Also, consider the state parameter ψ_{i}, which is the distance between the specific volume of

the sample and the specific volume at critical at the image pressure,

$$\psi_{\mathrm{i}} = v - v_{c0} + \widetilde{\lambda} \ln\left(-\pi_{\mathrm{i}}\right), \tag{5.3.19}$$

where v is the specific volume, v_{c0} is the reference specific volume at unit pressure, and $\widetilde{\lambda}$ is the plastic compressibility index. The state parameter ψ_{i} furnishes a link to the meso-scale by providing information about the relative density at a point in the sample. If $\psi_{\mathrm{i}} < 0$ the sample is denser than critical and if $\psi_{\mathrm{i}} > 0$ the sample is said to be looser than critical. In the case when $\psi_{\mathrm{i}} = 0$ the sample is at critical state. All of these parameters emanate from the critical state theory which postulates the existence of the critical state line [6, 153].

The hardening law, which relates the image pressure with the state of stress, the state parameter ψ_{i}, and the *deviatoric* component of plastic flow, reads

$$\dot{\pi}_{\mathrm{i}} = h\left(\pi_{\mathrm{i}}^{*} - \pi_{\mathrm{i}}\right) \dot{\varepsilon}_{\mathrm{s}}^{\mathrm{p}}, \tag{5.3.20}$$

where $\pi_{\mathrm{i}}^{*} = \pi_{\mathrm{i}}^{*}\left(p', \psi_{\mathrm{i}}\right)$, and h is a constant material property, to be calibrated in the finite deformation regime. We note in passing that the above hardening law allows for correct qualitative capture of key features in both loose and dense sands by allowing hardening and softening plastic response. More details regarding the elastoplastic model for sands presented herein and its numerical implementation can be found in [122, 131, 152].

5.3.2 Darcy's law

The relative flow vector $\boldsymbol{q}$ is related to the Cauchy pore pressure via the Eularian form of the classical Darcy's law [158, 161, 166]

$$\boldsymbol{q} = -\frac{1}{g}\boldsymbol{k} \cdot \left[\nabla^{\boldsymbol{x}} p - \boldsymbol{\gamma}_{\mathrm{f}}\right], \tag{5.3.21}$$

where $\boldsymbol{k} \equiv k\gamma_{\mathrm{f}}/\mu\mathbf{1}$ is the isotropic hydraulic conductivity tensor, the scalar k is the intrinsic permeability of the porous media, μ is the dynamic viscosity of the fluid, g is the gravitational acceleration constant, and $\gamma_{\mathrm{f}} \equiv \rho_{\mathrm{f}} g$ is the scalar specific weight of the fluid and $\boldsymbol{\gamma}_{\mathrm{f}} \equiv \rho_{\mathrm{f}}\boldsymbol{g}$ is its tensorial counterpart.

It is well documented throughout the literature that the intrinsic permeability can take the general form [158]

$$k = f_1(s)\, f_2\left(\phi^{\mathrm{f}}\right) d^2, \tag{5.3.22}$$

where s is a dimensionless parameter that expresses the effect of the shape of the solid grains, $f_1(s)$ is called shape factor, $f_2\left(\phi^{\mathrm{f}}\right)$ is called the porosity factor and d is the effective diameter of the grains. One of the most widely used relationships for the permeability is the Kozeny-Carman permeability equation proposed by Kozeny [167] and Carman [168] namely (see [158]),

$$k\left(\phi^{\mathrm{f}}\right) = \frac{1}{180}\frac{\phi^{\mathrm{f}\,3}}{\left(1-\phi^{\mathrm{f}}\right)^2}d^2, \tag{5.3.23}$$

which we will use herein to account for the effect of porosity and changes thereof in the Eulerian permeability tensor $\boldsymbol{k}$.

For completeness of presentation, we obtain the Lagrangian expression for Darcy's law by recalling the Piola transform of the relative flow vector,

$$\boldsymbol{Q} = J\boldsymbol{F}^{-1}\cdot\boldsymbol{q} = -\frac{1}{g}J\boldsymbol{F}^{-1}\cdot\boldsymbol{k}\cdot\left[\nabla^{\boldsymbol{x}}p - \boldsymbol{\gamma}_{\mathrm{f}}\right]. \tag{5.3.24}$$

By the same token, the expression can be further reduced by using the well-known relationship $\nabla^{\boldsymbol{X}}(\square) = \nabla^{\boldsymbol{x}}(\square)\cdot\boldsymbol{F}$ to obtain the fully Lagrangian form

$$\boldsymbol{Q} = -\frac{1}{g}\boldsymbol{K}\cdot\left[\nabla^{\boldsymbol{X}}p - \boldsymbol{F}^{\mathrm{t}}\cdot\boldsymbol{\gamma}_{\mathrm{f}}\right], \tag{5.3.25}$$

where $\boldsymbol{K} = J\boldsymbol{F}^{-1}\cdot\boldsymbol{k}\cdot\boldsymbol{F}^{-\mathrm{t}}$ is the pull-back hydraulic conductivity tensor.

Remark 9. Note that the intrinsic permeability is treated as a function of the *current* value of porosity ϕ^{f} and hence will need to be linearized accordingly (see equation 5.4.45). Figure 5.2 shows the variation of the intrinsic permeability with specific volume. For samples of globally undrained sand (as considered herein in the numerical simulations section), the variation in specific volume is not significant enough as to affect the results. However, in other boundary-value problems where compaction/dilation bands are allowed to form at large strains, changes in porosity can lead to changes in permeability of a few orders of magnitude [12].

5.4 Finite element implementation

In this section, the balance laws developed in Section 5.2 provide a complete set of governing equations, which allow for the solution of quasi-static deformation-diffusion boundary-value problems. We depart from the strong form of the problem, and develop the variational

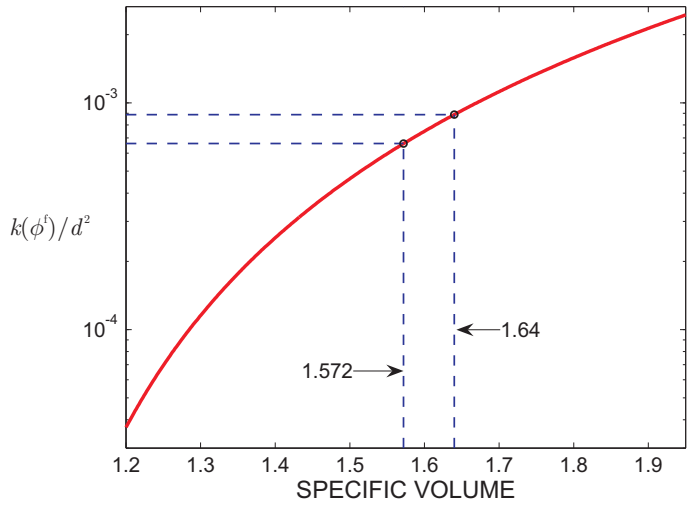

Figure 5.2: Nondimensional values of intrinsic permeability (i.e. k/d^2) as a function of specific volume v.

form and its linearized version which allows for optimal convergence of Newton-Raphson schemes, and finally present the classic matrix form known as the $\boldsymbol{u} - p$ formulation. The problem results in a parabolic system where the displacements of the solid phase and the pore-pressures are the basic unknowns in an updated Lagrangian finite element scheme [133].

5.4.1 The strong form

Consider the Lagrangian version of the strong form. Let Ω_0 be a simple body with boundary Γ_0 defined by the solid matrix in the reference configuration. Let $\boldsymbol{N}$ be the unit normal vector to the boundary Γ_0. We assume the boundary Γ_0 admits the decomposition [119]

$$\begin{array}{rclcl} \Gamma_0 & = & \overline{\Gamma_0^d \cup \Gamma_0^t} & = & \overline{\Gamma_0^p \cup \Gamma_0^q}, \\ \emptyset & = & \Gamma_0^d \cap \Gamma_0^t & = & \Gamma_0^p \cap \Gamma_0^q, \end{array} \tag{5.4.1}$$

where Γ_0^d, Γ_0^t, Γ_0^p, and Γ_0^q are open sets and $\emptyset$ is the empty set. Figure 5.3 shows the region Ω_0 and its boundary Γ_0 decomposed as described above.

The Lagrangian strong form for the quasi-static case and incompressible solid grains reads: find the displacements $\boldsymbol{u} \equiv \boldsymbol{x} - \boldsymbol{X} : \overline{\Omega}_0 \rightarrow \mathbb{R}^{n_{sd}}$ and the Cauchy pore-pressures

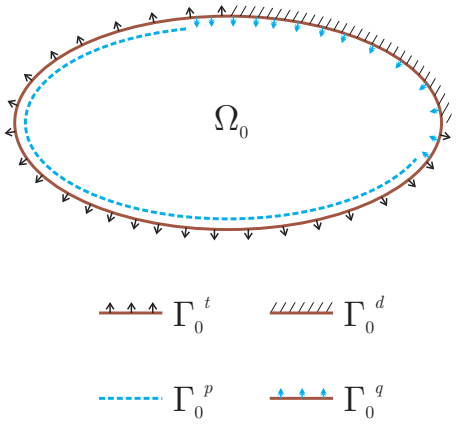

Figure 5.3: Reference domain Ω_0 with decomposed boundary Γ_0

$p : \overline{\Omega}_0 \to \mathbb{R}$ such that

$$\nabla^{\boldsymbol{X}} \cdot \boldsymbol{P} + \rho_0 \boldsymbol{g} = \boldsymbol{0} \quad \text{in} \quad \Omega_0 \tag{5.4.2}$$

$$\dot{\rho}_0 + \nabla^{\boldsymbol{X}} \cdot \boldsymbol{Q} = 0 \quad \text{in} \quad \Omega_0 \tag{5.4.3}$$

$$\boldsymbol{u} = \overline{\boldsymbol{u}} \quad \text{on} \quad \Gamma_0^d \tag{5.4.4}$$

$$\boldsymbol{P} \cdot \boldsymbol{N} = \boldsymbol{t} \quad \text{on} \quad \Gamma_0^t \tag{5.4.5}$$

$$p = \overline{p} \quad \text{on} \quad \Gamma_0^p \tag{5.4.6}$$

$$\boldsymbol{Q} \cdot \boldsymbol{N} = -Q \quad \text{on} \quad \Gamma_0^q \tag{5.4.7}$$

where n_{sd} is the number of spatial dimensions to be considered, $\overline{\boldsymbol{u}}$ and $\overline{p}$ are the prescribed displacements and pressure on the Dirichlet boundaries Γ_0^d and Γ_0^p, respectively. By the same token, $\boldsymbol{t}$ and Q are the prescribed traction vector and influx with respect to the Neumann boundaries Γ_0^t and Γ_0^q, respectively. Finally, it is necessary to specify the initial conditions

$$\boldsymbol{u}(\boldsymbol{X}, t = 0) = \boldsymbol{u}_0(\boldsymbol{X}), \qquad p(\boldsymbol{X}, t = 0) = p_0(\boldsymbol{X}), \tag{5.4.8}$$

where $\boldsymbol{X}$ is a point in Ω_0.

5.4.2 The variational form

To define the weak or variational form, two classes of functions need to be characterized [119]. The first class is composed of trial solutions, which are required to satisfy the Dirichlet

boundary conditions. The spaces of trial solutions for the displacement and pressure fields are, respectively [169]

$$\mathcal{S}_u = \{\boldsymbol{u} : \Omega_0 \to \mathbb{R}^{n_{sd}} |\ u_i \in H^1,\ \boldsymbol{u} = \overline{\boldsymbol{u}} \ \text{ on } \ \Gamma_0^d\}, \tag{5.4.9}$$

$$\mathcal{S}_p = \{p : \Omega_0 \to \mathbb{R} |\ p \in H^1,\ p = \overline{p} \quad \text{on } \ \Gamma_0^p\}, \tag{5.4.10}$$

where H^1 is the space of Sobolev functions of first degree. The second class of functions are the weighting functions or variations. We require the weighting functions to vanish on Dirichlet boundaries. Thus, let the spaces of weighting functions associated with the displacement and pressure field be, respectively

$$\mathcal{V}_u = \{\boldsymbol{\eta} : \Omega_0 \to \mathbb{R}^{n_{sd}} |\ \eta_i \in H^1,\ \boldsymbol{\eta} = \boldsymbol{0} \ \text{ on } \ \Gamma_0^d\}, \tag{5.4.11}$$

$$\mathcal{V}_p = \{\psi : \Omega_0 \to \mathbb{R} |\ \psi \in H^1,\ \psi = 0 \quad \text{on } \ \Gamma_0^p\}. \tag{5.4.12}$$

Let $G : \mathcal{S}_u \times \mathcal{S}_p \times \mathcal{V}_u \to \mathbb{R}$ be given by

$$G(\boldsymbol{u}, p, \boldsymbol{\eta}) = \int_{\Omega_0} \left(\nabla^{\boldsymbol{X}} \boldsymbol{\eta} : \boldsymbol{P} - \rho_0 \boldsymbol{\eta} \cdot \boldsymbol{g}\right) \mathrm{d}\Omega_0 - \int_{\Gamma_0^t} \boldsymbol{\eta} \cdot \boldsymbol{t} \, \mathrm{d}\Gamma_0. \tag{5.4.13}$$

Under suitable smoothness conditions, $G(\boldsymbol{u}, p, \boldsymbol{\eta}) = 0$ can be shown to be equivalent to balance of linear momentum in the strong form, i.e., equations (5.4.2), (5.4.4) and (5.4.5). Similarly, let $H : \mathcal{S}_u \times \mathcal{S}_p \times \mathcal{V}_p \to \mathbb{R}$ take the form

$$H(\boldsymbol{u}, p, \psi) = \int_{\Omega_0} \left[\psi \dot{\rho}_0 - \nabla^{\boldsymbol{X}} \psi \cdot \boldsymbol{Q}\right] \mathrm{d}\Omega_0 - \int_{\Gamma_0^q} \psi Q \, \mathrm{d}\Gamma_0. \tag{5.4.14}$$

Once again, under suitable smoothness conditions, $H(\boldsymbol{u}, p, \psi) = 0$ can be shown to be equivalent to balance of mass in the strong form, i.e., equations (5.4.3), (5.4.6) and (5.4.7). Consequently, the Lagrangian weak form of the problem reads: find $\boldsymbol{u} \in \mathcal{S}_u$ and $p \in \mathcal{S}_p$ such that for all $\boldsymbol{\eta} \in \mathcal{V}_u$ and $\psi \in \mathcal{V}_p$

$$G(\boldsymbol{u}, p, \boldsymbol{\eta}) = H(\boldsymbol{u}, p, \psi) = 0. \tag{5.4.15}$$

It is our objective to develop an updated Lagrangian scheme and hence, we need to express the Lagrangian integrand of the above weak form in Eulerian form. We accomplish this by

recalling the identities

$$\int_{\Omega_0} \nabla^{\boldsymbol{X}} \boldsymbol{\eta} : \boldsymbol{P}\, \mathrm{d}\Omega_0 = \int_{\Omega_0} \nabla^{\boldsymbol{x}} \boldsymbol{\eta} : \boldsymbol{\tau}\, \mathrm{d}\Omega_0, \qquad \int_{\Omega_0} \nabla^{\boldsymbol{X}} \psi \cdot \boldsymbol{Q}\, \mathrm{d}\Omega_0 = \int_{\Omega_0} J\, \nabla^{\boldsymbol{x}} \psi \cdot \boldsymbol{q}\, \mathrm{d}\Omega_0, \quad (5.4.16)$$

which we can insert into equations (5.4.13) and (5.4.14) above to get

$$G(\boldsymbol{u}, p, \boldsymbol{\eta}) = \int_{\Omega_0} (\nabla^{\boldsymbol{x}} \boldsymbol{\eta} : \boldsymbol{\tau} - J\rho \boldsymbol{\eta} \cdot \boldsymbol{g})\, \mathrm{d}\Omega_0 - \int_{\Gamma_0^t} \boldsymbol{\eta} \cdot \boldsymbol{t}\, \mathrm{d}\Gamma_0, \quad (5.4.17)$$

and

$$H(\boldsymbol{u}, p, \psi) = \int_{\Omega_0} [\psi \dot{\rho}_0 - J\, \nabla^{\boldsymbol{x}} \psi \cdot \boldsymbol{q}]\, \mathrm{d}\Omega_0 - \int_{\Gamma_0^q} \psi Q\, \mathrm{d}\Gamma_0. \quad (5.4.18)$$

Finally, for the sake of compactness of presentation, we introduce the following notations,

$$g_1(\boldsymbol{u}, p) = \int_{\Omega_0} \nabla^{\boldsymbol{x}} \boldsymbol{\eta} : \left(\boldsymbol{\tau}' - Jp\mathbf{1}\right) \mathrm{d}\Omega_0, \quad (5.4.19a)$$

$$g_2(\boldsymbol{u}, p) = -\int_{\Omega_0} J\rho \boldsymbol{\eta} \cdot \boldsymbol{g}\, \mathrm{d}\Omega_0, \quad (5.4.19b)$$

$$g_{\mathrm{ext}}(t) = \int_{\Gamma_0^t} \boldsymbol{\eta} \cdot \boldsymbol{t}\, \mathrm{d}\Gamma_0, \quad (5.4.19c)$$

and similarly

$$h_1(\boldsymbol{u}, p) = \int_{\Omega_0} \psi \dot{\rho}_0 \mathrm{d}\Omega_0, \quad (5.4.20a)$$

$$h_2(\boldsymbol{u}, p) = \int_{\Omega_0} \frac{J}{g}\, \nabla^{\boldsymbol{x}} \psi \cdot \boldsymbol{k} \cdot [\nabla^{\boldsymbol{x}} p - \boldsymbol{\gamma}_{\mathrm{f}}]\, \mathrm{d}\Omega_0, \quad (5.4.20b)$$

$$h_{\mathrm{ext}}(t) = \int_{\Gamma_0^q} \psi Q\, \mathrm{d}\Gamma_0, \quad (5.4.20c)$$

so that equation (5.4.15) implies

$$G(\boldsymbol{u}, p, \boldsymbol{\eta}) = g_{\mathrm{ext}}(t) - g_1(\boldsymbol{u}, p) - g_2(\boldsymbol{u}, p), \quad (5.4.21)$$

$$H(\boldsymbol{u}, p, \psi) = h_{\mathrm{ext}}(t) - h_1(\boldsymbol{u}, p) - h_2(\boldsymbol{u}, p). \quad (5.4.22)$$

Time integration and linearization of the variational form

Satisfaction of the weak form will entail solving a coupled nonlinear system of equations where the primary variables are the displacements $\boldsymbol{u}$ and the pore pressure p, hence the

name $\boldsymbol{u}-p$ formulation. At the same time, the $\boldsymbol{u}-p$ formulation is resolved using an iterative Newton-Raphson procedure, which necessitates the system Jacobians or consistent tangents in closed form for optimal asymptotic convergence rates. For the particular model proposed herein, it is possible to calculate such consistent tangents and thus attain optimal convergence rates. This is furnished by the fact that the elastoplastic model proposed is integrated within the return mapping algorithm framework [117], which allows for a closed form expression for the elastoplastic consistent tangent operator (see [122, 131, 152] for more details).

Consider the generalized trapezoidal family of methods [119] utilized in the solution of parabolic problems. The one-step scheme relies on the advancement of the solution at time station t_{n+1} from converged values at t_n, i.e.

$$\left\{ \begin{array}{c} \boldsymbol{u} \\ p \end{array} \right\}_{n+1} = \left\{ \begin{array}{c} \boldsymbol{u} \\ p \end{array} \right\}_{n} + \Delta t \left(1-\alpha\right) \left\{ \begin{array}{c} \dot{\boldsymbol{u}} \\ \dot{p} \end{array} \right\}_{n} + \Delta t \alpha \left\{ \begin{array}{c} \dot{\boldsymbol{u}} \\ \dot{p} \end{array} \right\}_{n+1}, \tag{5.4.23}$$

where α is the integration parameter and $\Delta t \equiv t_{n+1} - t_n$ is the time step. Several classical schemes emanate for suitable choices of the integration parameter. For $\alpha = 0$ the scheme reduces to the explicit Euler algorithm, $\alpha = 1/2$ captures the Crank-Nicolson scheme, and $\alpha = 1$ reduces to the implicit backward Euler. For a detailed discussion about the stability and accuracy of the above-mentioned family please see [119]. With the purpose of obtaining a numerical scheme purely dependent on displacements $\boldsymbol{u}$ and pressure p, we integrate equation (5.4.22) using the trapezoidal family and obtain

$$\begin{aligned} H_{\Delta t}\left(\boldsymbol{u}, p, \psi\right) = \int_{\Omega_0} \psi \Delta\rho_0 \, \mathrm{d}\Omega_0 \quad &- \quad \Delta t \int_{\Omega_0} \underbrace{\left[\alpha J \nabla^{\boldsymbol{x}} \psi \cdot \boldsymbol{q} + \left(1-\alpha\right)\left(J \nabla^{\boldsymbol{x}} \psi \cdot \boldsymbol{q}\right)_n\right]}_{\left(J \nabla^{\boldsymbol{x}} \psi \cdot \boldsymbol{q}\right)_{n+\alpha}} \mathrm{d}\Omega_0 \\ &- \quad \Delta t \int_{\Gamma_0^q} \psi \underbrace{\left(\alpha Q + \left(1-\alpha\right) Q_n\right)}_{Q_{n+\alpha}} \mathrm{d}\Gamma_0, \end{aligned} \tag{5.4.24}$$

where $\Delta\rho_0 \equiv \rho_0 - \rho_{0\,n}$ and where we have omitted the '$n+1$' subscript for simplicity of notation. Similar to the results obtained above, the variational form implies

$$H_{\Delta t}\left(\boldsymbol{u}, p, \psi\right) = h_{\mathrm{ext}}^{\Delta t}\left(t\right) - h_1^{\Delta t}\left(\boldsymbol{u}, p\right) - h_2^{\Delta t}\left(\boldsymbol{u}, p\right), \tag{5.4.25}$$

where

$$\begin{aligned} h_{\text{ext}}^{\Delta t}(t) &= \Delta t \int_{\Gamma_0^q} \psi Q_{n+\alpha} \mathrm{d}\Gamma_0 \\ h_1^{\Delta t}(\boldsymbol{u}, p) &= \int_{\Omega_0} \psi \Delta\rho_0 \, \mathrm{d}\Omega_0 \\ h_2^{\Delta t}(\boldsymbol{u}, p) &= -\Delta t \int_{\Omega_0} \left(J \nabla^{\boldsymbol{x}} \psi \cdot \boldsymbol{q}\right)_{n+\alpha} \mathrm{d}\Omega_0. \end{aligned} \tag{5.4.26}$$

The Newton-Raphson approach follows the standard procedure in which the governing equations from the weak form are expanded about a configuration $\left(\boldsymbol{u}^k, p^k\right)$ and only linear terms are kept i.e.,

$$0 = G(\boldsymbol{u}, p, \boldsymbol{\eta}) \approx G\left(\boldsymbol{u}^k, p^k, \boldsymbol{\eta}\right) + \delta G\left(\boldsymbol{u}^k, p^k, \boldsymbol{\eta}\right), \tag{5.4.27}$$

$$0 = H_{\Delta t}(\boldsymbol{u}, p, \psi) \approx H_{\Delta t}\left(\boldsymbol{u}^k, p^k, \psi\right) + \delta H_{\Delta t}\left(\boldsymbol{u}^k, p^k, \psi\right), \tag{5.4.28}$$

hence, implying

$$-G\left(\boldsymbol{u}^k, p^k, \boldsymbol{\eta}\right) = \delta G\left(\boldsymbol{u}^k, p^k, \boldsymbol{\eta}\right), \tag{5.4.29}$$

$$-H_{\Delta t}\left(\boldsymbol{u}^k, p^k, \psi\right) = \delta H_{\Delta t}\left(\boldsymbol{u}^k, p^k, \psi\right). \tag{5.4.30}$$

Therefore, the iterative strategy necessitates evaluation of the variations $\delta G\left(\boldsymbol{u}^k, p^k, \boldsymbol{\eta}\right)$ and $\delta H_{\Delta t}\left(\boldsymbol{u}^k, p^k, \psi\right)$. Note that equation (5.4.27) is solved at time t_{n+1} as implied by our notation.

The variation of $\delta G(\boldsymbol{u}, p, \boldsymbol{\eta})$ implies

$$\delta G(\boldsymbol{u}, p, \boldsymbol{\eta}) = \delta g_{\text{ext}}(t) - \delta g_1(\boldsymbol{u}, p) - \delta g_2(\boldsymbol{u}, p), \tag{5.4.31}$$

where $\delta g_{\text{ext}}(t) = 0$ for deformation-independent tractions. Application of the chain rule then yields

$$\delta g_1(\boldsymbol{u}, p) = \int_{\Omega_0} \left[\delta \nabla^{\boldsymbol{x}} \boldsymbol{\eta} : \left(\boldsymbol{\tau}' - Jp\mathbf{1}\right) + \nabla^{\boldsymbol{x}} \boldsymbol{\eta} : \delta\left(\boldsymbol{\tau}' - Jp\mathbf{1}\right)\right] \mathrm{d}\Omega_0, \tag{5.4.32}$$

where

$$\delta\,\nabla^{\boldsymbol{x}}\,\boldsymbol{\eta} = -\nabla^{\boldsymbol{x}}\,\boldsymbol{\eta}\cdot\nabla^{\boldsymbol{x}}\,\delta\boldsymbol{u}, \tag{5.4.33}$$

$$\delta\left(\boldsymbol{\tau}' - Jp\mathbf{1}\right) = \left(\boldsymbol{c}^{\mathrm{ep}} + \boldsymbol{\tau}'\oplus\mathbf{1} + \boldsymbol{\tau}'\ominus\mathbf{1} - Jp\mathbf{1}\otimes\mathbf{1}\right) : \nabla^{\boldsymbol{x}}\,\delta\boldsymbol{u} - J\delta p\mathbf{1} \tag{5.4.34}$$

$$\delta J = J\,\nabla^{\boldsymbol{x}}\cdot\delta\boldsymbol{u}. \tag{5.4.35}$$

The fourth-order tensor $\boldsymbol{c}^{\mathrm{ep}}$ is the elastoplastic consistent tangent operator emanating from the constitutive model described in Section 4.2. We get

$$\delta g_1\left(\boldsymbol{u},p\right) = \int_{\Omega_0}\left[\nabla^{\boldsymbol{x}}\,\boldsymbol{\eta} : \left(\boldsymbol{a}^{\mathrm{ep}} + Jp\left(\mathbf{1}\ominus\mathbf{1} - \mathbf{1}\otimes\mathbf{1}\right)\right) : \nabla^{\boldsymbol{x}}\,\delta\boldsymbol{u} - \nabla^{\boldsymbol{x}}\cdot\boldsymbol{\eta}J\delta p\right]\mathrm{d}\Omega_0, \tag{5.4.36}$$

where

$$\boldsymbol{a}^{\mathrm{ep}} \equiv \boldsymbol{c}^{\mathrm{ep}} + \boldsymbol{\tau}'\oplus\mathbf{1} \tag{5.4.37}$$

is the total elastoplastic tangent operator and $\mathcal{L}_{\boldsymbol{v}}\boldsymbol{\tau}' = \boldsymbol{c}^{\mathrm{ep}} : \boldsymbol{d}$ where $\mathcal{L}_{\boldsymbol{v}}\boldsymbol{\tau}'$ is the Lie derivative of the effective stress tensor $\boldsymbol{\tau}'$ (see Andrade and Borja [152] for notations). By the same token,

$$\begin{aligned}\delta g_2\left(\boldsymbol{u},p\right) &= -\int_{\Omega_0}\delta\rho_0\boldsymbol{\eta}\cdot\boldsymbol{g}\,\mathrm{d}\Omega_0,\\ &= -\int_{\Omega_0} J\left(\nabla^{\boldsymbol{x}}\cdot\delta\boldsymbol{u} + \frac{\phi^{\mathrm{f}}}{K_{\mathrm{f}}}\delta p\right)\boldsymbol{\eta}\cdot\boldsymbol{\gamma}_{\mathrm{f}}\,\mathrm{d}\Omega_0,\end{aligned} \tag{5.4.38}$$

where we have used equation (5.3.3), $\delta\rho_{\mathrm{s}} = 0$, and the following key results

$$\delta\phi^{\mathrm{f}} = \left(1-\phi^{\mathrm{f}}\right)\nabla^{\boldsymbol{x}}\cdot\delta\boldsymbol{u}, \tag{5.4.39}$$

$$\delta\rho_{\mathrm{f}} = \frac{\rho_{\mathrm{f}}}{K_{\mathrm{f}}}\delta p. \tag{5.4.40}$$

Similarly,

$$\delta H_{\Delta t}\left(\boldsymbol{u},p,\psi\right) = \delta h_{\mathrm{ext}}^{\Delta t}\left(t\right) - \delta h_1^{\Delta t}\left(\boldsymbol{u},p\right) - \delta h_2^{\Delta t}\left(\boldsymbol{u},p\right), \tag{5.4.41}$$

where $\delta h_{\mathrm{ext}}^{\Delta t}\left(t\right) = 0$ for configuration- and pressure-independent mass flux. Thus,

$$\delta h_1^{\Delta t}\left(\boldsymbol{u},p\right) = \int_{\Omega_0}\psi\delta\rho_0\mathrm{d}\Omega_0 = \int_{\Omega_0}\psi\rho_{\mathrm{f}}J\left(\nabla^{\boldsymbol{x}}\cdot\delta\boldsymbol{u} + \frac{\phi^{\mathrm{f}}}{K_{\mathrm{f}}}\delta p\right)\mathrm{d}\Omega_0. \tag{5.4.42}$$

Now, we compute

$$\begin{aligned}\delta h_2^{\Delta t}(\boldsymbol{u},p) &= \alpha\Delta t\int_{\Omega_0}\frac{1}{g}\delta\left(J\,\nabla^{\boldsymbol{x}}\psi\cdot\boldsymbol{k}\right)\cdot\left(\nabla^{\boldsymbol{x}}p-\boldsymbol{\gamma}_{\mathrm{f}}\right)\mathrm{d}\Omega_0\\ &+ \alpha\Delta t\int_{\Omega_0}\frac{1}{g}J\,\nabla^{\boldsymbol{x}}\psi\cdot\boldsymbol{k}\cdot\delta\left(\nabla^{\boldsymbol{x}}p-\boldsymbol{\gamma}_{\mathrm{f}}\right)\mathrm{d}\Omega_0,\end{aligned}\tag{5.4.43}$$

where

$$\delta\,\nabla^{\boldsymbol{x}}\psi = -\nabla^{\boldsymbol{x}}\psi\cdot\nabla^{\boldsymbol{x}}\delta\boldsymbol{u}\tag{5.4.44}$$

$$\delta\boldsymbol{k} = \frac{1}{\mu}\left(k'\gamma_{\mathrm{f}}\delta\phi^{\mathrm{f}}+k\delta\rho_{\mathrm{f}}g\right)\mathbf{1}\tag{5.4.45}$$

$$\delta\,\nabla^{\boldsymbol{x}}p = \nabla^{\boldsymbol{x}}\delta p-\nabla^{\boldsymbol{x}}p\cdot\nabla^{\boldsymbol{x}}\delta\boldsymbol{u}\tag{5.4.46}$$

$$\delta\boldsymbol{\gamma}_{\mathrm{f}} = \delta\rho_{\mathrm{f}}\boldsymbol{g}.\tag{5.4.47}$$

5.4.3 The matrix form

The spatial discretization is furnished by the classical Galerkin method whereby the displacement and the pressure fields are approximated by [119]

$$\boldsymbol{u} \approx \boldsymbol{N}\boldsymbol{d}+\boldsymbol{N}^{\xi}\boldsymbol{\xi},\tag{5.4.48}$$

$$p \approx \overline{\boldsymbol{N}}\boldsymbol{p}+\boldsymbol{N}^{\zeta}\boldsymbol{\zeta},\tag{5.4.49}$$

where $\boldsymbol{N}$ is the array of displacement shape functions, $\boldsymbol{d}$ is the vector of unknown displacements, $\boldsymbol{N}^{\xi}$ is the array of shape functions approximating the displacement boundary conditions, $\boldsymbol{\xi}$ is the vector of prescribed nodal displacements, $\overline{\boldsymbol{N}}$ is the array of pressure shape functions, $\boldsymbol{p}$ is the vector of unknown pore-pressures, $\boldsymbol{N}^{\zeta}$ is the array of shape functions approximating the pressure boundary conditions, and $\boldsymbol{\zeta}$ is the vector of prescribed nodal pore-pressures. Then, following the Galerkin recipe, the weighting functions are approximated by

$$\boldsymbol{\eta} \approx \boldsymbol{N}\boldsymbol{c},\tag{5.4.50}$$

$$\psi \approx \overline{\boldsymbol{N}}\overline{\boldsymbol{c}},\tag{5.4.51}$$

where $\boldsymbol{c}$ and $\overline{\boldsymbol{c}}$ are arbitrary constant vectors. The spatial and temporal discretization leads to the matrix form of the problem, which reads: find the vectors $\boldsymbol{d}$ and $\boldsymbol{p}$ such that

$$\left\{ \begin{array}{c} \boldsymbol{G}_{\text{ext}} \\ \boldsymbol{H}_{\text{ext}} \end{array} \right\} - \left\{ \begin{array}{c} \boldsymbol{G}_{\text{int}} \\ \boldsymbol{H}_{\text{int}} \end{array} \right\} \equiv \left\{ \begin{array}{c} \boldsymbol{R}_g \\ \boldsymbol{R}_h \end{array} \right\}, \tag{5.4.52}$$

where

$$\boldsymbol{G}_{\text{ext}}(t) \equiv \int_{\Gamma_0^t} \boldsymbol{N}^t \boldsymbol{t} \, \mathrm{d}\Gamma_0, \tag{5.4.53}$$

$$\boldsymbol{G}_{\text{int}}(\boldsymbol{d}, \boldsymbol{p}) \equiv \int_{\Omega_0} \left[\boldsymbol{B}^t \left(\boldsymbol{\tau}' - Jp\boldsymbol{\delta} \right) - \rho_0 \boldsymbol{N}^t \boldsymbol{g} \right] \mathrm{d}\Omega_0, \tag{5.4.54}$$

and

$$\boldsymbol{H}_{\text{ext}}(t) \equiv \Delta t \int_{\Gamma_0^q} \overline{\boldsymbol{N}}^t Q_{n+\alpha} \, \mathrm{d}\Gamma_0, \tag{5.4.55}$$

$$\boldsymbol{H}_{\text{int}}(\boldsymbol{d}, \boldsymbol{p}) \equiv \int_{\Omega_0} \left[\overline{\boldsymbol{N}}^t \Delta\rho_0 - \Delta t \left(J\boldsymbol{\Gamma}^t \boldsymbol{q} \right)_{n+\alpha} \right] \mathrm{d}\Omega_0. \tag{5.4.56}$$

After algebraic manipulations, the Newton-Raphson incremental solution at the $k+1$ iteration is updated using

$$\left[\begin{array}{cc} \boldsymbol{K}_g & \boldsymbol{\Phi}_g \\ \boldsymbol{K}_h + \alpha\Delta t \overline{\boldsymbol{K}}_h & \boldsymbol{\Phi}_h + \alpha\Delta t \overline{\boldsymbol{\Phi}}_h \end{array} \right]_k \left\{ \begin{array}{c} \delta\boldsymbol{d} \\ \delta\boldsymbol{p} \end{array} \right\}_{k+1} = \left\{ \begin{array}{c} \boldsymbol{R}_g \\ \boldsymbol{R}_h \end{array} \right\}_k. \tag{5.4.57}$$

The reader is referred to Appendix A where a detailed presentation of the matrix form of the problem is given.

Remark 10. Some authors have pointed out the existence of numerical instabilities at the onset of the deformation-diffusion problem when considering the case of incompressible fluid phase [170, 171]. In fact, Murad and Loula [170, 172] showed, in the context of linear elasticity, that at the onset of deformation the system is form-identical to the classical problem of incompressible elasticity or Stoke's flow in fluid mechanics. This is also true in the context of poroplasticity at large strains. The system can be shown to reduce to

$$\left[\begin{array}{cc} \hat{\boldsymbol{A}} & \hat{\boldsymbol{B}} \\ \hat{\boldsymbol{C}} & \boldsymbol{0} \end{array} \right] \left\{ \begin{array}{c} \delta\boldsymbol{u} \\ \delta\boldsymbol{p} \end{array} \right\} = \left\{ \begin{array}{c} \boldsymbol{F}_1 \\ \boldsymbol{F}_2 \end{array} \right\}, \tag{5.4.58}$$

and thus,

$$\hat{\boldsymbol{C}}\hat{\boldsymbol{A}}^{-1}\hat{\boldsymbol{B}}\delta\boldsymbol{p} = \hat{\boldsymbol{C}}\hat{\boldsymbol{A}}^{-1}\boldsymbol{F}_1 - \boldsymbol{F}_2, \tag{5.4.59}$$

where $\hat{\boldsymbol{A}}$ is a $nu \times nu$ square matrix, $\hat{\boldsymbol{B}}$ is a $nu \times nq$ rectangular matrix, and $\hat{\boldsymbol{C}}$ is a $nq \times nu$ matrix, with nu and nq representing the number of displacement and pore pressure unknowns, respectively. Hence, for $\hat{\boldsymbol{C}}\hat{\boldsymbol{A}}^{-1}\hat{\boldsymbol{B}}$ to have full rank, we must have $nu \geq np$. One way to avoid stability problems associated with this constraint is to satisfy the so-called Babuška-Brezzi condition (see [119, 159]). On the other hand, for the deformation-diffusion problem at hand, investigators have used stabilization techniques available to solve mixed problems. Wan in [171] used the Petrov-Galerkin technique proposed by Hughes et al. in [173] for solution of Stokes flow. Similarly, Mira et al [174] used Simo-Rifai elements [175] to obtain stable solutions for the deformation-diffusion problem. In this particular work, we only use mixed finite elements satisfying the Babuška-Brezzi stability condition.

5.5 Localization of saturated granular media

In this section, we will derive expressions for the Eulerian acoustic tensors corresponding to the locally (fully) drained and locally undrained conditions. These expressions are useful as they signal the loss of strong ellipticity of the corresponding drained and undrained global tangent operator. As in the classical case of mono-phase bodies, the onset of localization, as measured by the loss of positive definiteness in the acoustic tensor, can be used to define the local direction of a shear band and maybe even as a switch for a change in the material behavior inside the band. Here, two extreme cases are considered. Firstly, we look at the case of a fully drained porous medium, which basically reduces back to the classical mono-phase theory. Secondly, we investigate the case of locally undrained behavior, where the global tangent is influenced by the bulk compressibility of the fluid phase, but relative flow is not present anywhere in the sample. In a way, this latter case is analogous to the drained case, but with a different underlying constitutive relation (one in which the fluid phase plays a role, but there is no diffusion). The global tangent $\boldsymbol{a}^{\mathrm{ep}}$ obtained in the previous section is used to obtain the drained and undrained localization criteria.

It is important to note that in general, saturated media behave somewhere in between locally drained and locally undrained conditions. For either extreme case, it is possible to write down an expression relating the total stress rate and the rate of deformation for the granular matrix i.e., $\delta\boldsymbol{P} = \mathbf{A} : \delta\boldsymbol{F}$, where $\mathbf{A}$ is the suitable (drained or undrained) first

tangent operator with components $\mathrm{A}_{iJkL} := \partial P_{iJ}/\partial F_{kL}$ [30, 64]. Consequently, we require continuity of total tractions across the band and hence (cf., equation (2.35) in [64]),

$$[\![\mathbf{A} : \delta\boldsymbol{F}]\!] \cdot \boldsymbol{N} = \mathbf{0} \tag{5.5.1}$$

where $[\![\square]\!]$ is the jump operator across the band and $\boldsymbol{N}$ is the normal to an impending shear band in the reference configuration. Furthermore, by assuming the first tangent operator is continuous across the band we can write $[\![\mathbf{A} : \delta\boldsymbol{F}]\!] = \mathbf{A} : [\![\delta\boldsymbol{F}]\!]$. From [64] we get $[\![\dot{\boldsymbol{F}}]\!] = [\![\boldsymbol{V}]\!] \otimes \boldsymbol{N}/h_0$, where $[\![\boldsymbol{V}]\!]$ is the material velocity jump and h_0 is the (finite) thickness of the planar band in the reference configuration. Continuity of tractions requires

$$\frac{1}{h_0}\boldsymbol{\mathcal{A}} \cdot [\![\boldsymbol{V}]\!] = \mathbf{0}, \qquad \mathcal{A}_{ik} = N_J \mathrm{A}_{iJkL} N_L \tag{5.5.2}$$

For $h_0 \neq 0$, the necessary condition for localization is

$$\det \boldsymbol{\mathcal{A}} = 0 \tag{5.5.3}$$

with $\boldsymbol{\mathcal{A}}$ as the Lagrangian acoustic tensor. Finally, pushing the Lagrangian acoustic tensor forward, we obtain the Eulerian acoustic tensor, i.e.

$$A_{ik} = n_j a_{ijkl} n_l \tag{5.5.4}$$

with $a_{ijkl} := F_{jJ} F_{lL} \mathrm{A}_{iJkL}$ as the total spatial tangent operator and $\boldsymbol{n}$ as the normal to the deformation band in the current configuration. A standard argument then yields the Eulerian necessary condition for localization,

$$\det \boldsymbol{A} = 0. \tag{5.5.5}$$

Recall the relationship between the total First Piola Kirchhoff stress and the Kirchhoff stress, i.e. $\boldsymbol{P} = \boldsymbol{\tau} \cdot \boldsymbol{F}^{-t}$, which together with equation (5.3.1) yields

$$\boldsymbol{P} = \boldsymbol{P}' - \theta \boldsymbol{F}^{-t}. \tag{5.5.6}$$

For the case of locally drained conditions, we have $\delta\boldsymbol{P} = \delta\boldsymbol{P}'$ and thus, it is straight forward

to show that the Eulerian acoustic tensor takes the classical form [64, 152]

$$A_{ik} \equiv A^d_{ik} = n_j a^{\text{ep}}_{ijkl} n_l \tag{5.5.7}$$

where a^{ep}_{ijkl} are the components of the total tangent operator defined in equation (5.4.37). Similarly, for the locally undrained case, we have $\boldsymbol{q} = \boldsymbol{0}$ point-wise, and consequently the equation of balance of mass (5.2.14) reduces to

$$\dot{\vartheta} = -\left(J\frac{K_{\text{f}}}{\phi^{\text{f}}} - \vartheta \right) \nabla^{\boldsymbol{x}}\cdot \boldsymbol{v}. \tag{5.5.8}$$

Taking the time derivative of $\boldsymbol{P}$ and utilizing equation (5.5.6), results in the undrained rate equation

$$\delta\boldsymbol{P} = \underbrace{\left[\mathbf{A}^{\text{ep}} + \left(J\frac{K_{\text{f}}}{\phi^{\text{f}}} - \theta \right) \boldsymbol{F}^{-t} \otimes \boldsymbol{F}^{-t} + \theta \boldsymbol{F}^{-t} \ominus \boldsymbol{F}^{-1} \right]}_{\overline{\mathbf{A}}^{\text{ep}}} : \delta\boldsymbol{F}, \tag{5.5.9}$$

where $\mathbf{A}^{\text{ep}}$ and $\overline{\mathbf{A}}^{\text{ep}}$ are the drained and undrained first elastoplastic tangent operators, respectively. Therefore, in this case we have

$$\boldsymbol{A} = \boldsymbol{A}^d + J\frac{K_{\text{f}}}{\phi^{\text{f}}} \boldsymbol{n} \otimes \boldsymbol{n}. \tag{5.5.10}$$

We note that the undrained acoustic tensor consists of the drained acoustic tensor plus a volumetric contribution emanating from the compressibility of the fluid phase. The expression for the acoustic tensor derived above is very similar to that obtained by Borja in [46] for the case of infinitesimal deformations.

Remark 11. The spectral search algorithm proposed by the authors in [152] is utilized in the next section to search for the onset of strain localization under both locally drained and locally undrained conditions utilizing suitable expressions for the acoustic tensor as obtained above.

5.6 Numerical simulations

In this section, several globally undrained plane strain compression test are performed. Macroscopically dense and loose samples of sand with and without inhomogeneities at the meso-scale are sheared to failure, whenever possible. The objective of these boundary-value

problems is to study the effect of meso-scale inhomogeneities in the porosity on the stability and flow characteristics of sand specimens. It will be shown that the inhomogeneities, even though small, have a profound impact on the macroscopic behavior of the samples. Furthermore, it is shown that the constitutive model used to describe the effective stress for the underlying sand specimens captures some of the main features observed in sand specimens tested in the laboratory.

The material parameters utilized in the simulations are summarized in Tables 5.1 and 5.2. We refer the reader to Section 5.3 for details regarding the material parameters and their significance.

Symbol	Value	Parameter
$\widetilde{\kappa}$	0.03	compressibility
α_0	0	coupling coefficient
μ_0	2000 kPa	shear modulus
p_0	-99 kPa	reference pressure
$\epsilon^{\mathrm{e}}_{\mathrm{v}0}$	0	reference strain

Table 5.1: Summary of hyperelastic material parameters for plane strain compression problems.

Symbol	Value	Parameter
$\widetilde{\lambda}$	0.04	compressibility
M	1.2	critical state parameter
v_{c0}	1.8	reference specific volume
N	0.4	for yield function
$\overline{N}$	0.2	for plastic potential
ϱ	0.78	ellipticity
h	280/70	hardening coefficient for dense/loose samples

Table 5.2: Summary of plastic material parameters for plane strain compression problems.

5.6.1 Plane strain compression in globally undrained dense sands

In this subsection, we present the results obtained from performing globally undrained plane strain compression simulations on both inhomogeneous and homogeneous samples of dense sand. The inhomogeneous sample is constructed by prescribing a randomly generated specific volume field, which displays a higher horizontal than vertical correlation. The inhomogeneous sample is shown in Figure 5.4 where the initial specific volume field is

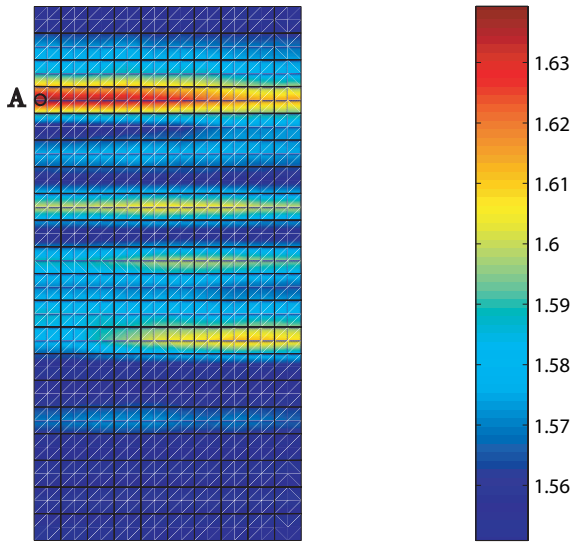

Figure 5.4: Initial specific volume for dense sand specimen superimposed on undeformed finite element mesh.

superimposed on the undeformed finite element mesh. The sample is 5 cm wide and 10 cm tall and has been discretized using a mesh composed of 200 $Q9P4$ isoparametric elements [nine displacement nodes plus four (continuous) pressure nodes]. This kind of finite element has been shown to satisfy the Babuška-Brezzi stability condition and hence avoid stability problems associated with consolidation of porous media (see end of Section 5.4 for discussion on stability). The mean specific volume for the sample is 1.572, making the sample dense macroscopically. However, some pockets are relatively loose with specific volume as high as 1.64. The range in the specific volume for the dense sample is 1.54–1.64.

The boundary conditions for the numerical experiments are as follows. The top and bottom faces of the sample are supported on rollers (Dirichlet BCs) with the bottom left corner fixed with a pin for stability. The bottom face is constrained from displacing in the vertical direction, whereas the top face is given a vertical displacement responsible for compacting the sample in the axial direction. At the same time, the lateral faces are confined with an initial pressure of 100 kPa (Newman BCs) to simulate the confining pressure in a plane strain device. As for the boundary conditions associated with the flow equations, all faces of the sample are no-flow boundaries (Dirichlet BCs), provoking a globally undrained condition (although the permeability is finite locally and so there is a locally drained condition). This condition is equivalent to having an impermeable

membrane surrounding the specimen, which is typically used in undrained compression tests in the laboratory. The testing conditions favor homogeneous deformations in the absence of material inhomogeneities and gravity effects.

The inhomogeneous sample of dense sand is loaded monotonically until failure. Figure 5.5(a) shows a plot of the determinant for the *drained* acoustic tensor at a deformed state after 5% nominal axial deformation. Also, the figure shows the contour of deviatoric strains at 5% axial strain with superimposed relative fluid flow vectors $\boldsymbol{q}$ in subfigure (b). The instant in time is selected so as to show a fully developed deformation band and to underscore the need for a finite deformation formulation. The developed deformation band allows for several interesting observations. It can be seen that the vanishing of the determinant for the drained acoustic tensor $\boldsymbol{A}^d$ correlates very well with areas of intense localized deviatoric strains. Furthermore, the flow vectors $\boldsymbol{q}$ superimposed on both the contour for the determinant function and the contour for the deviatoric strain clearly show a strong influence of the deformation band on the flow characteristics in the sample. In fact, in this particular case, the deformation pattern appears to be 'attracting' the flow into the deformation band and away from the rest of the sample. This suggests a mostly dilative behavior of the sand within the deformation band, which will certainly tend to attract fluid flow.

The dilative behavior of the sand specimen can be clearly observed in Figure 5.6(a) where the contour for the volumetric strains is plotted against the deformed finite element mesh at an axial strain of 5%. Distinct areas of dilative (positive) volumetric response can be identified along the developed deformation band. This behavior is consistent with the signature behavior of relatively dense sands in the laboratory, which mostly tend to dilate during shear deformation [74, 153]. This dilative response has been also reproduced by plasticity models such as Drucker-Prager, which account for plastic dilation [143, 144] . This important feature is captured by the model developed herein by including meso-scale information about the porosity (and hence relative density) in the hardening law via the state parameter ψ_{i}. Because of the coupling effect between the response of the porous medium and the fluid flow, Figure 5.6(b) shows distinct areas of low Cauchy fluid pressures corresponding to those where the volumetric response is dilative. In fact, it is obvious from the figure that strong gradients in the fluid pressure are generated and are consistent with the deformation pattern of the sample and are responsible for the amount and direction of fluid flow. It should be noted at this point that because of the small dimensions of the sample, gravitational effects do not play a major role and hence there is not much meaning

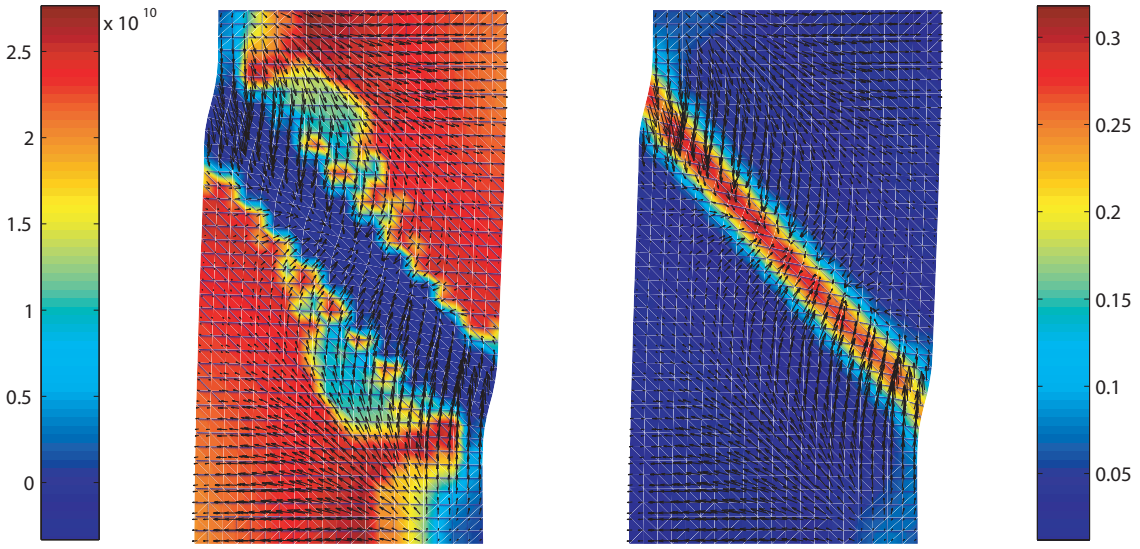

Figure 5.5: (a) Contour of the determinant function for the drained acoustic tensor at a nominal axial strain of 5% and (b) deviatoric strains in contour with superimposed relative flow vectors $\boldsymbol{q}$ at 5% axial strain for dense sand sample.

in distinguishing 'excess' pore fluid pressure from total pore fluid pressure.

At this point, it is clear that the deformation pattern is strongly coupled with the fluid flow, but it is not clear what the role of the meso-scale is in the overall stability of the undrained sample. To shed some light into this question, we compare the response of the inhomogeneous sand sample against its homogeneous counterpart. This type of analyses has been performed before in the context of *drained* or effective material response (e.g., see [122, 152] for analyses on 'dry' samples of dense sand). In these previous studies, it was found that the meso-scale is responsible for triggering instabilities at the specimen scale, reducing the load carrying capacity of the sample of dense sand. The same type of analysis is performed here with very similar results. The force-displacement curves for both inhomogeneous and homogeneous samples of dense sand are plotted in Figure 5.7. In this figure, the reactive stresses at the top face of the samples are plotted against the nominal axial strain. The homogeneous sample is constructed by imposing a constant value of initial specific volume at 1.572 (the mean value of the distribution shown in Figure 5.4). The load-displacement responses are superimposed on each other for the first 2% axial strain, at which point the inhomogeneous sample bifurcates (both drained and undrained acoustic

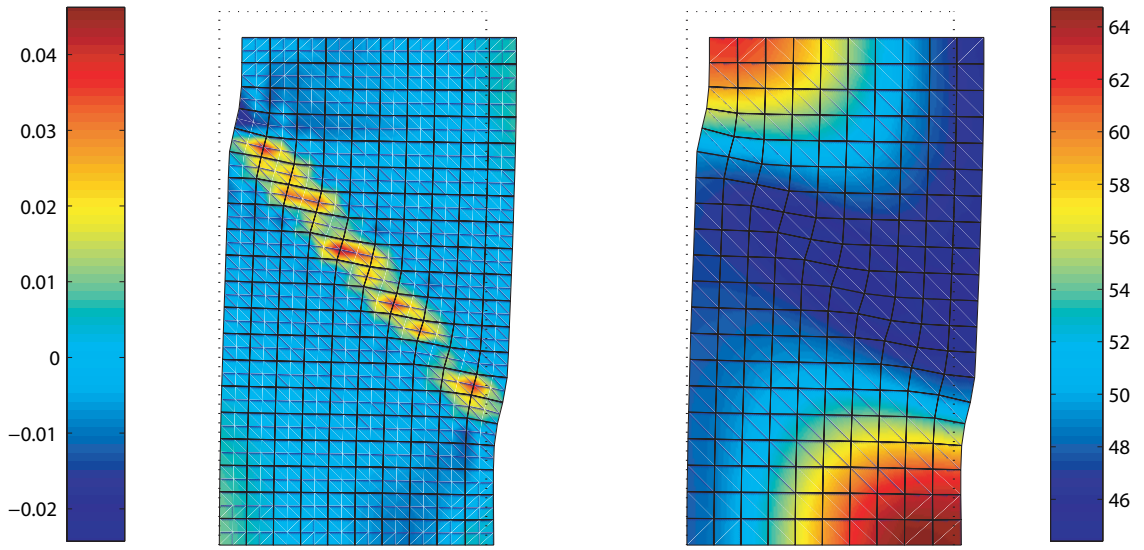

(a) (b)

Figure 5.6: (a) Volumetric strain contour superimposed on deformed finite element mesh at 5% axial strain and (b) contour of Cauchy fluid pressure p on deformed sample at 5% axial strain (in kPa) for dense sand sample. Dotted lines delineate undeformed configuration.

tensors loose positive definiteness at about 1.9% axial strain). The homogeneous sample does not localize and in fact continues to harden until the end of the simulation at 4% axial strain. On the other hand, after localization is detected in the inhomogeneous sample, the response is characterized by softening and the sample does not recover its load carrying capacity.

Localization above is defined as the first time either the drained or undrained acoustic tensor loses positive definiteness at any (Gauss) point in the sample. The point where the sample localized for the first time is shown in Figure 5.4 and referred to as point A. The determinant functions for both drained and locally undrained acoustic tensors at point A are plotted in Figure 5.8. Localization occurred around 1.9% nominal axial strain when both determinants for the drained and undrained acoustic tensor went negative for the first time. In this particular case, both localization criteria coincided, but in cases when the point in question was below the critical state line, the drained localization criterion superseded the undrained criterion. In this particular simulation, we never observed the determinant of the undrained acoustic tensor vanishing before that of the drained acoustic tensor.

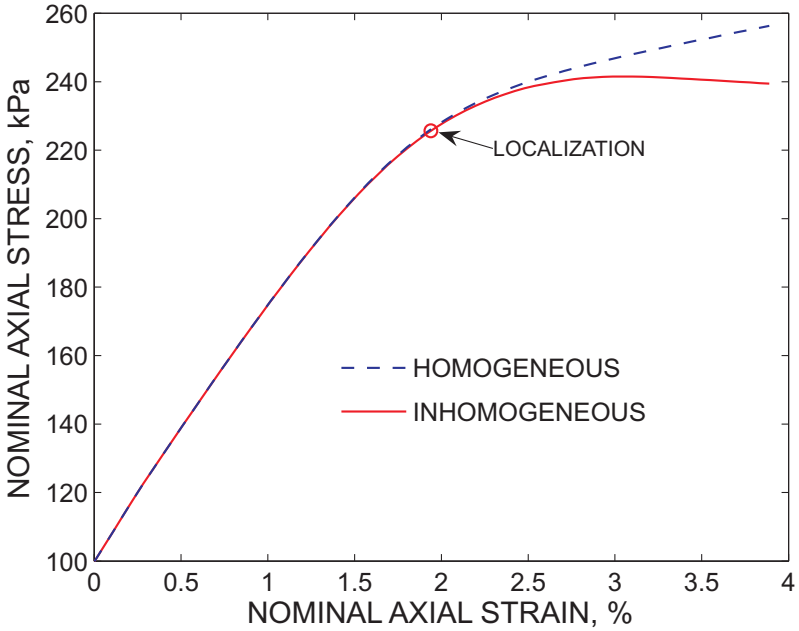

Figure 5.7: Force-displacement curve for inhomogeneous and homogeneous samples of dense sand.

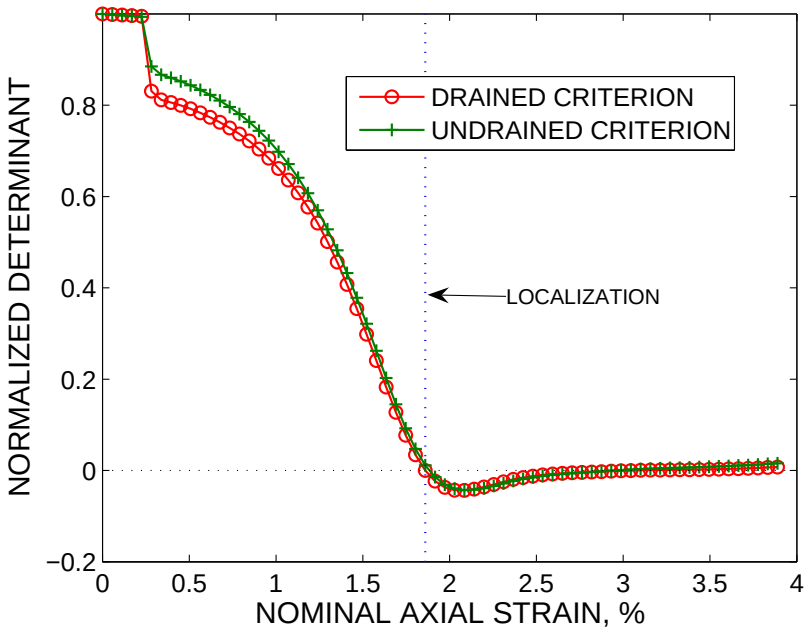

Figure 5.8: Normalized determinant functions at point A for dense sand sample.

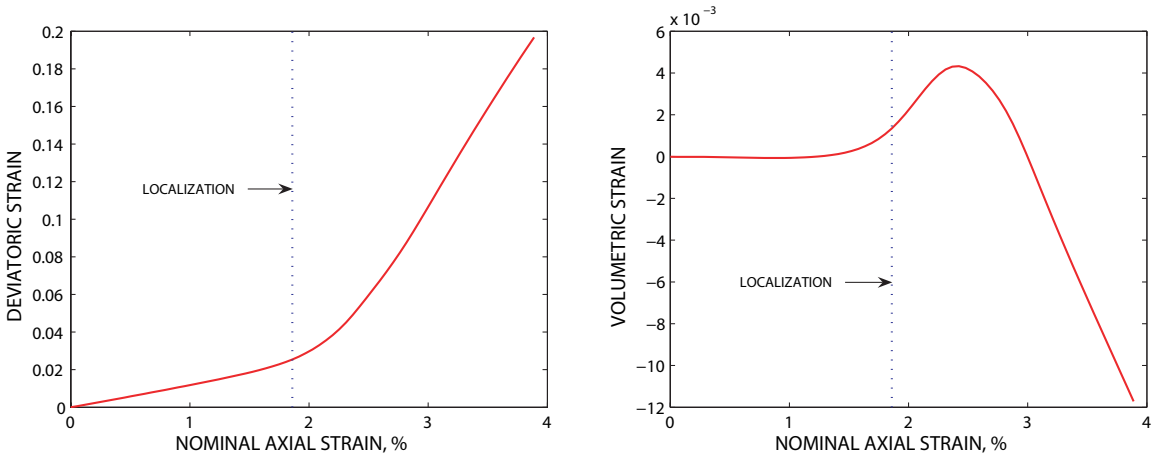

Figure 5.9: (a) Deviatoric strain invariant at Gauss point A for sample of dense sand (b) volumetric strain invariant at Gauss point A for sample of dense sand.

Once localization occurs at point A, the modes of deformation tend to change considerably at that location. As expected, deviatoric deformations are magnified once localization is detected. The volumetric and deviatoric strain invariants are plotted in Figure 5.9 where it is easily seen that after 1.9% axial strain, the slope of the deviatoric strain curve is about five times steeper than before localization is detected. Also, the point in question seems to compact very little initially, followed by significant dilation, which is consistent with the macroscopic behavior of dense sands. The volumetric behavior of point A can be further observed from Figure 5.10 where the specific volume at that point is plotted against the effective pressure and the CSL for the material is plotted for reference. It is interesting to note that even though point A lies above the critical state line, its volumetric behavior is closer to that of a drained point below the CSL. This is because the rest of the sample is behaving macroscopically as a dense sand and the coupling between the solid matrix and the fluid flow is really what governs deformation. The matrix at point A may 'want' to contract, but the fact that point A is more permeable that some other parts of the sample makes it easier for the fluid to flow into point A and hence force it to dilate. This last observation shows that the saturated behavior of a globally undrained sample could be sharply distinct to that of a perfectly drained one.

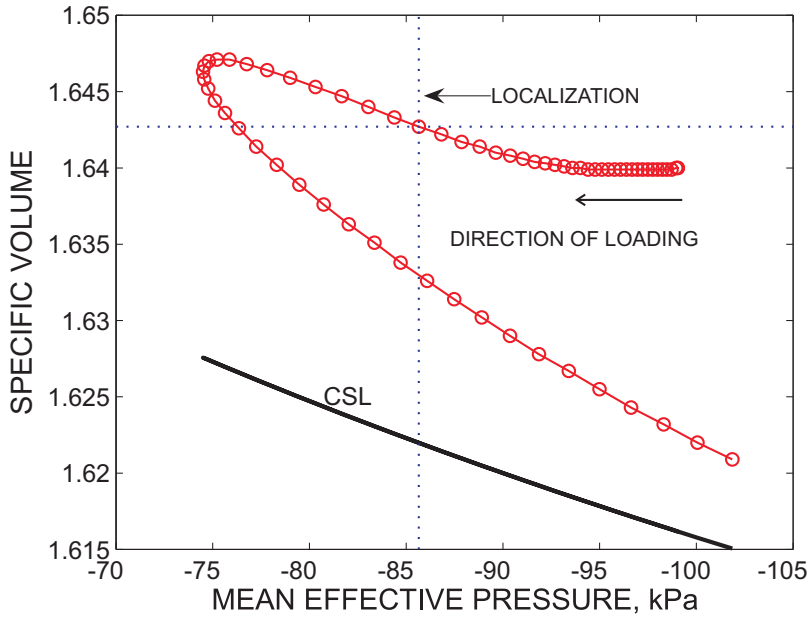

Figure 5.10: Specific volume plot as a function of effective pressure at point A for dense sand sample

5.6.2 Plane strain compression in globally undrained loose sands

To obtain a somewhat complete picture of the behavior of saturated granular materials under shear deformations, globally undrained compression tests are performed on samples of macroscopically loose sands. In this set of tests, we compare the response of an inhomogeneous sample of sand against its homogeneous counterpart. As in the previous subsection, the initial inhomogeneity is furnished by the initial distribution of specific volume, which follows a pattern identical to that shown in Figure 5.4 above. The only difference here is the range and mean of the distribution in order to reflect a macroscopically loose sample of sand. The initial range of specific volume for the loose sample is depicted in Figure 5.11 and goes from 1.62 to 1.66. This particular range is much narrower than that chosen in the previous set of simulations, the sample appears to be more homogeneous than the dense sand sample. The average specific volume for the sample of loose sand is 1.62 (cf. with that for the dense sand sample at 1.572). This average value of specific volume puts the sample above the CSL on average and hence we expect the behavior of the structure to be macroscopically similar to a homogeneous sample of loose sand. As for the rest of the

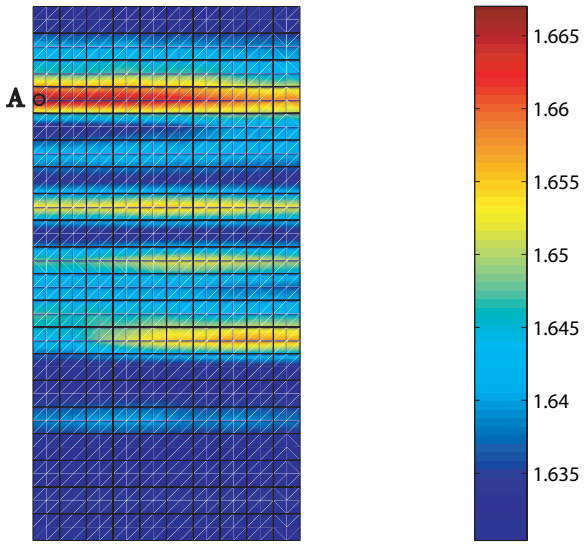

Figure 5.11: Initial specific volume for loose sand specimen superimposed on undeformed finite element mesh.

material parameters, they are almost identical to those in the previous subsection and are summarized in Tables 5.1 and 5.2. The only difference in the material parameters between the dense sand samples and the loose ones is the hardening coefficient h, which is 280 in the case of the dense sands and 70 for the loose sands. This reflects the fact that relatively loose sands show 'flatter' force-displacement curves.

The 5×10 cm sample is discretized using the same mesh as the dense sand samples and the imposed boundary conditions are also identical. Hence, any difference in the behavior of the structure is due to the different phenomenological behavior implied by the underlying effective stress constitutive model and triggered by the difference in relative densities. This is due to the fact that the phenomenological model can realistically capture the difference in behavior of sand samples at different relative densities.

Similar to the dense sand sample, the inhomogeneous sample of loose sand is loaded monotonically by prescribing a uniform vertical displacement at the top face of the sample. Figure 5.12 shows a plot of the determinant of the *undrained* acoustic tensor and the deviatoric strain invariant for the loose sand sample at 5% axial strain. The relative flow vectors $\boldsymbol{q}$ are superimposed on the aforementioned contours to give a relative sense of the interaction between the deformation and flow patterns. Once again, the instant in time is chosen such that the deformation band is fully developed. As in the case of the dense

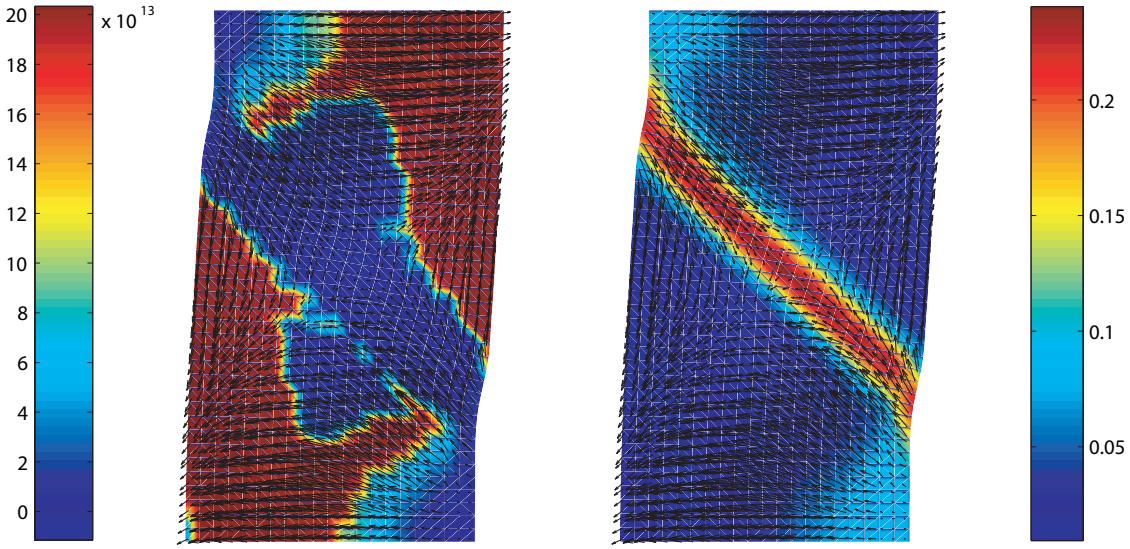

(a) (b)

Figure 5.12: (a) Contour of the determinant function for the undrained acoustic tensor at a nominal axial strain of 5% and (b) deviatoric strains in contour with superimposed relative flow vectors $\boldsymbol{q}$ at 5% axial strain for loose sand sample.

sand sample, the localization criterion for the undrained acoustic tensor $\boldsymbol{A}$ correlates very well with high concentrations of deviatoric strains in the sample. In fact, the profile for the determinant of the drained acoustic tensor $\boldsymbol{A}^d$ looks similar with a different order of magnitude throughout. The deformation pattern again influences the flow characteristics in the sample but with an opposite effect to that observed in the dense sample. For the case of loose sand deforming under globally undrained conditions, the incipient shear band appears to be 'repelling' fluid flow. This deformation-diffusion behavior suggests a compactive behavior within the shear band compared to a relatively less compressive and perhaps even dilative deformation pattern elsewhere in the sample. Another contrasting feature is the fact that the deformation band is initially (at lower values of axial strain) less pronounced and less localized and looks more diffuse than that for the dense sample, which is again consistent with the behavior of relatively loose sands which tend to fail in a more diffuse mode in the laboratory. These seem to be a novel results since, as far as we know, no results showing compactive shear bands repelling fluid flow have been reported in the literature (e.g. see works by Armero [143] and Larsson and Larsson [144] who only report *dilative* shear bands).

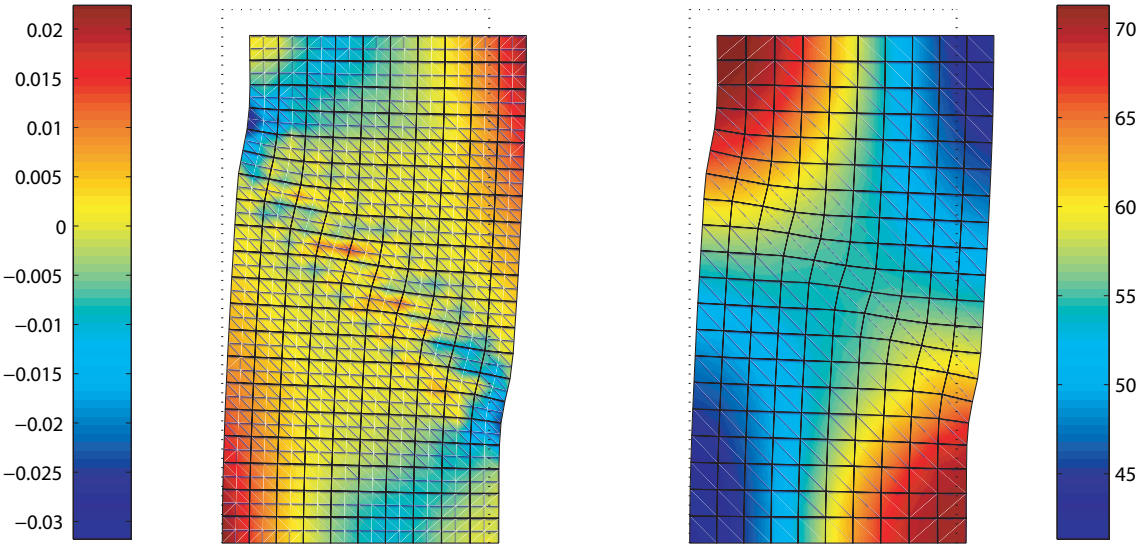

(a) (b)

Figure 5.13: (a) Volumetric strain contour superimposed on deformed finite element mesh at 5% axial strain and (b) contour of Cauchy fluid pressure p on deformed sample at 5% axial strain (in kPa) for loose sand sample. Dotted lines delineate undeformed configuration.

The suggested compactive behavior within the deformation band is truly appreciated when one plots the volumetric strain invariant at 5% axial strain. Figure 5.13(a) shows such deformation contour superimposed on the deformed finite element mesh. There are well-defined pockets of compactive behavior on what can be defined as the ends of the deformation band. The rest of the band is not as compactive (in fact the center is slightly dilating) as the ends, but the upper-right and lower-left corners are much more dilative in comparison to the band. This is the reason why the fluid pressure contour shown in 5.13(b) looks like a saddle. There is a relative low at the center of the band (and the specimen) but there are maxima at the ends of the deformation band. The dilative pockets described above constitute regions where the Cauchy fluid pressure p is at a minimum in the sample. This explains the direction of the relative flow, which tends to go away from the ends of the deformation band, towards the center of the band and in general away from the band (see Figure 5.12 above). This pressure and flow pattern is clearly different from that observed in the sample of dense sand and is consistent with the behavior of an undrained sample of relatively loose sand.

The effect of the inhomogeneities in the porosity field at the meso-scale can be seen by

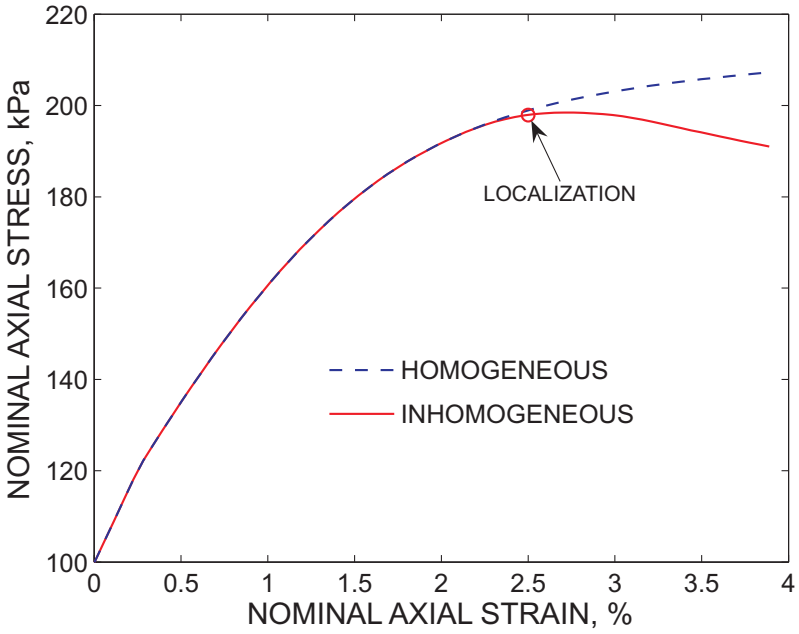

Figure 5.14: Force-displacement curve for inhomogeneous and homogeneous samples of loose sand.

comparing the force-displacement curve for the inhomogeneous sample against that of the homogeneous sample. Figure 5.14 shows a plot of the nominal axial stress at the top face for both inhomogeneous and homogeneous samples of loose sand. The curves are clearly identical up to about 2.4% axial strain point at which the inhomogeneous sample localizes and subsequently softens. The homogeneous sample did not localize by any criterion and did not show any signs of softening up to 4% axial strain. The fact that the curves coincide up to the point of bifurcation suggests that the effect of the meso-scale inhomogeneity is minimal early in the deformation-diffusion process. However, it is clear that the inhomogeneities ultimately alter the load-carrying capacity of the inhomogeneous sample, which is macroscopically softer than its homogeneous counterpart. Also note the flatter slope in the force-displacement curves obtained for the loose sample than those for the dense sample; a direct effect of the relative density and hardening coefficient.

The localization point at 2.4% axial strain is defined by the vanishing of the determinant of both drained and undrained acoustic tensors at point A, which is depicted in Figure 5.11. Both localization criteria are met at the same time at point A and hence there is no room for ambiguity when one speaks of loss of positive definiteness of the acoustic tensor. It is

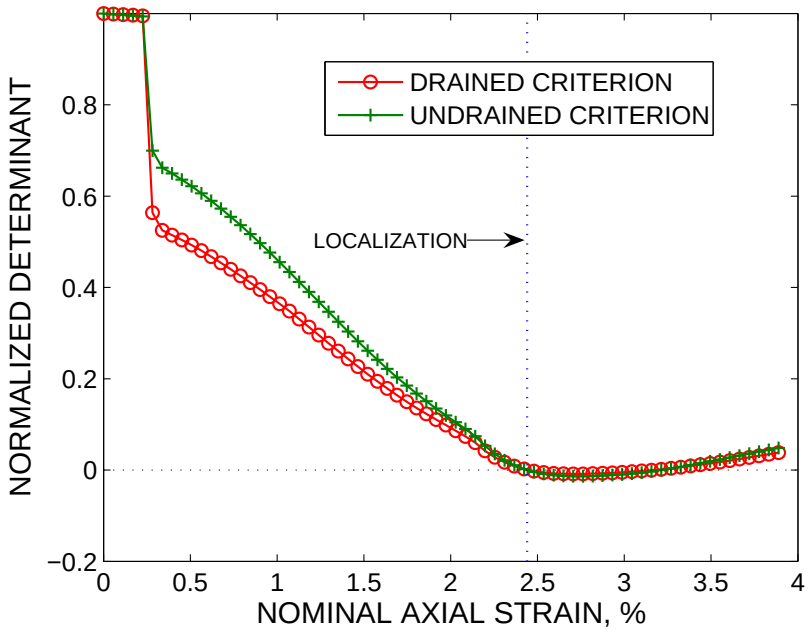

Figure 5.15: Normalized determinant functions at point A for loose sand sample.

interesting to note that localization occurs first at the same point in both dense and loose samples. This might be due to the fact that this point is relatively looser in both specimens and hence tends to fail first in both instances. Figure 5.15 shows a plot of the normalized determinant for both the drained and locally undrained acoustic tensors. It is observed that both determinants vanish at around 2.4% axial strain. In this simulation, all points that lost positive definiteness of the acoustic tensor did so for the drained and undrained acoustic tensors at the same time. Comparison with the dense sand simulation shows that localization was attained at a later time, which suggests a more ductile behavior associated with the loose sand sample.

It is interesting to observe the modes of deformations at point A in the sample before and after localization is attained. As in the dense sand sample, point A exhibits a steepening in the slope of the deviatoric strain after localization, which is shown in Figure 5.16(a). In fact, the sample exhibits three times more deviatoric deformation in the last 1.6% axial strain than in the first 2.4% axial strain. Also, point A remains basically incompressible up to the onset of localization. Figure 5.16(b) shows the volumetric strain invariant versus axial strain, where it is observed that point A did not change in volume until it reached

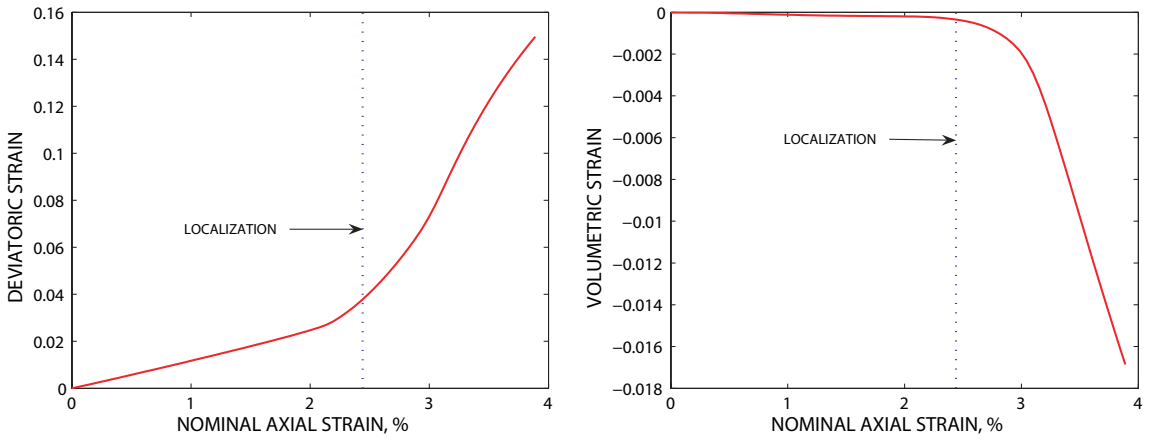

(a) (b)

Figure 5.16: (a) Deviatoric strain invariant at Gauss point A for sample of loose sand (b) volumetric strain invariant at Gauss point A for sample of loose sand.

localization, after which point it compacted quite a bit. In this case, which can be contrasted to the case of the dense sample of sand, point A behaves more as a typical 'drained' point after localization: experiencing volume loss, which leads to an area of high pressure because the fluid cannot escape fast enough. Figure 5.17 shows the relation between specific volume and the mean Kirchhoff effective pressure. The specific volume is pretty much constant up to the onset of localization and subsequently the state is attracted towards the CSL. Once again, the behavior at point A is of course affected by the surrounding area in the sample and also, and perhaps more importantly, by the coupling imposed by the balance laws.

Finally, Figure 5.18 shows the convergence profile at various stages in the loading protocol for the plane strain compression test on the inhomogeneous sample of loose sand. Consistent linearization performed in the proposed finite element procedure, combined with the fact that the effective stress constitutive model features a consistent tangent operator available in closed form [152], leads to an overall rate of convergence that enjoys the optimal quadratic rate associated with the full Newton-Raphson scheme. Furthermore, the fact that finite elements satisfying the Babuška-Brezzi stability condition are utilized, translates into solutions free of spurious oscillations in the fluid pressure associated with instabilities near initial time when the sample behaves as an undrained incompressible solid [170, 172].

Remark 12. It is important to note that the finite element solutions presented above do suffer from mild pathological mesh dependence once the onset of localization has been

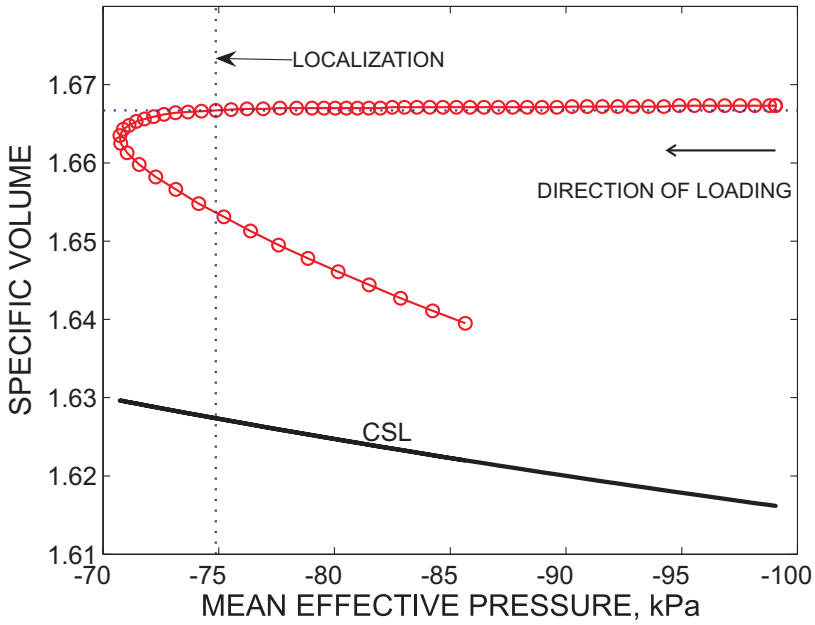

Figure 5.17: Specific volume plot as a function of effective pressure at point A for loose sand sample

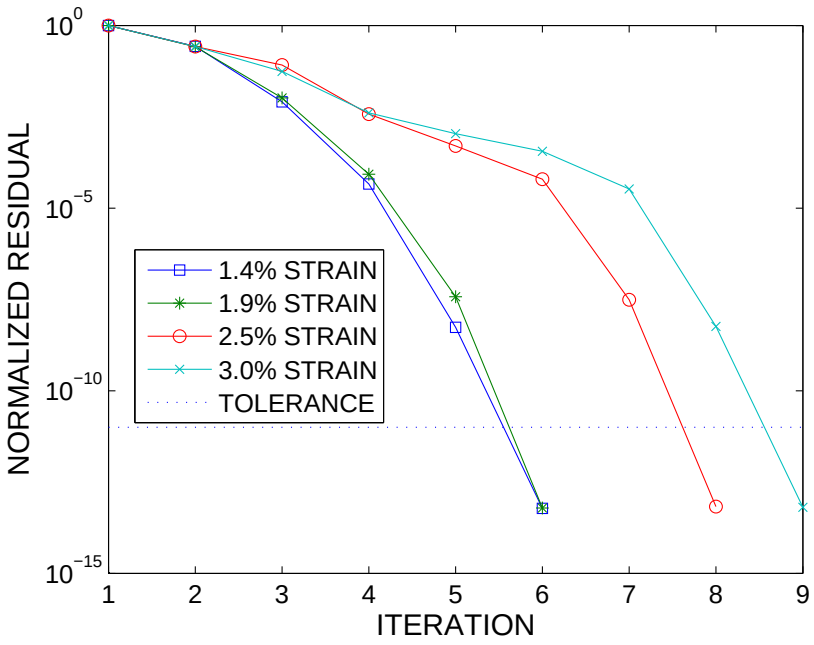

Figure 5.18: Convergence profile at various values of axial strain for plane strain compression test on sample of loose sand.

detected. It has been show by Zhang and Schrefler [176] that even though the fluid flow equation introduces a length scale via the permeability coefficient, it might not be enough if the effective stress equations are not further regularized by, say, adding a viscous term. However, the conclusions reached above are qualitative and should not be affected by this detail.

To illustrate this 'mild' dependence, we perform a simple mesh sensitivity study. For simplicity, we solve same boundary value problem presented above in Section 5.6.1. Consider the same homogeneous sample with specific volume $v = 1.572$ but with an arbitrary 'weak' region (i.e., $v = 1.6$) in the specimen as illustrated in Figure 5.19. Two meshes are analyzed: one consisting of 50 $Q9P4$ elements and another one consisting of 200 such elements. The results of the undrained compression tests are summarized in Figures 5.20 and 5.21. Figure 5.20 shows the force displacement curves for the 50 and 200 element mesh compared against the perfectly homogeneous response (i.e., $v = 1.572$ throughout). It is shown that the perturbed samples are less stiff than the homogeneous sample and that the responses of the two inhomogeneous samples are identical up to 3% axial strain, corresponding to a level

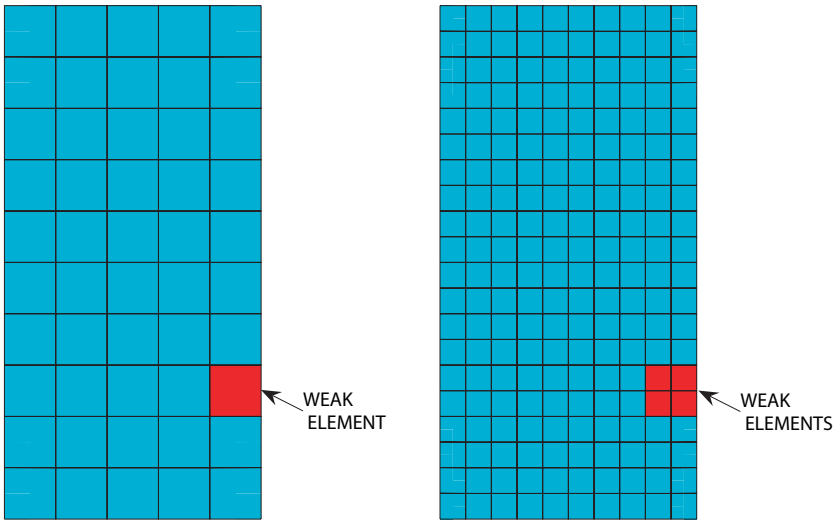

Figure 5.19: Perturbed samples of dense sand with otherwise homogeneous specific volume $v = 1.572$. (a) Mesh composed of 50 $Q9P4$ elements and (b) mesh composed of 200 $Q9P4$.

of strain passed the drained localization criterion. In fact both inhomogeneous samples detect the onset of drained localization simultaniously, as expected. By the time undrained localization is detected in the fine mesh sample, the force displacement curves are starting to diverge.

Figure 5.21 shows the deviatoric strains with superimposed relative flow vectors on both finite element meshes. It is clear that the apparent width of the shear band is a function of the element size; the width of the shear band decreases proportional to the element size. However, the pattern of deformation and the direction of flow is identical in both samples. Both samples develop dilative shear bands that tend to attract fluid flow. Hence, we say mesh dependence is 'mild' as both meshes display the same overall mechanical behavior: both predict softer responses, identical onset of drained localization, and appearance of dilative shear bands.

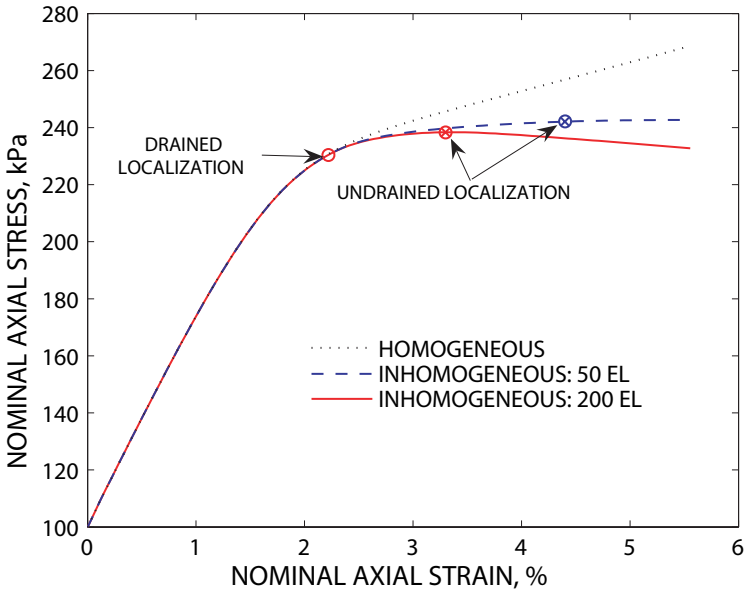

Figure 5.20: Force displacement curves comparing perfectly homogeneous response to that of perturbed samples

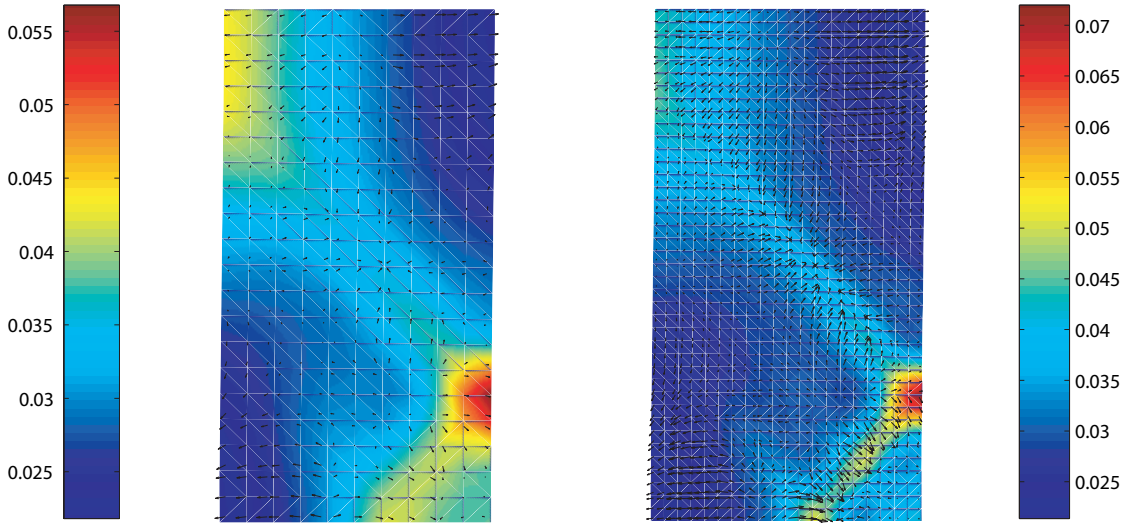

(a) (b)

Figure 5.21: Deviatoric strains in contours with superimposed relative flow vectors $\boldsymbol{q}$ at 3% axial strain for (a) 50 element mesh and (b) 200 element mesh

5.7 Conclusion

We have presented a finite element model for the simulation of saturated porous media exhibiting meso-scale inhomogeneities in the porosity field. The continuum balance laws have been derived and utilized within a finite element framework from which the basic unknowns: solid displacements and Cauchy pore fluid pressures have been resolved in a $\boldsymbol{u} - p$ mixed finite element scheme. The scheme features stable solutions with optimum rates of convergence. Representative numerical examples dealing with plane strain compression of undrained samples of dense and loose sands have been presented to underscore the importance of meso-scale inhomogeneities on the stability and flow characteristics through a deforming sand specimen. We have shown that behavior of saturated granular media is more complex than that inferred from macroscopic observations and that even small imperfections at a scale smaller than specimen size can trigger global failure and influence the amount and direction of flow. Furthermore, the behavior of relatively dense and loose samples differ substantially as the volumetric behavior of the solid matrix is coupled with the fluid flow, hence affecting the effective pressures, which govern strength in geomaterials. These last observations are unique to this study in which porosity has been coupled with the hydraulic conductivity and effective stress behavior of the underlying granular media, thereby capturing both compactive and dilative modes of deformation banding.

Chapter 6

Conclusion and future work

We have proposed a meso-scale numerical model for predicting the location and direction of deformation banding in saturated sands. A novel constitutive model for sands was developed with the objective of capturing the most important features of sand behavior: nonlinearity and irrecoverable deformations, pressure dependence, different strength under triaxial compression/extension, relative density dependence, and nonassociative plastic flow. The elastoplastic constitutive model developed herein uniquely captures all of these features and is capable of accounting for spatial fluctuations in the porosity field, as measured, for example, by X-Ray Computed Tomography. For sands, the meso-scale resolution of the porosity field is in the millimeter scale. Motivated by the fact that CT technology can capture meso-scale defects in samples of sand, we have demonstrated that these imperfections—though small—must be taken into account when analyzing the behavior of sand specimens.

The meso-scale constitutive model was implemented in a nonlinear continuum mechanics framework by designing a return mapping algorithm along the principal directions of deformation. From the return mapping algorithm, the consistent tangent operator was obtained in closed form and utilized in the finite element implementation of the model to guarantee asymptotic quadratic rate of convergence. Numerical simulations at large strains were performed for drained samples of dense sands under plane strain and triaxial conditions. Both structured and unstructured porosity fields were used in the simulations. It was concluded that the meso-scale inhomogeneities in the porosity consistently triggered instabilities in the form of deformation bands. Localization was detected using a search algorithm designed to exploit the spectral directions of the stress tensor, making the 3D search very efficient.

Comparisons between inhomogeneous samples and their homogeneous counterparts showed that, after some axial deformation, the meso-scale inhomogeneities triggered instabilities that were unique to the inhomogeneous samples. Consistently, homogeneous and inhomogeneous samples predicted initially identical force-displacement curves, with homogeneous samples becoming stiffer after the inhomogeneities triggered softening and/or strain localization in the perturbed samples. This last observation is critical as it shows that, since the inhomogeneities do not influence the mechanical behavior of samples from the onset, it is possible to calibrate the meso-scale model based on data from laboratory tests on 'homogeneous' specimens during the phase when the responses are identical. We plan to exploit this nice feature in a subsequent calibration phase, where we will couple the model with experimental results obtained in the laboratory.

The question of soil-fluid interaction and the effect of drainage has also been analyzed in this dissertation against the backdrop of the proposed meso-scale constitutive model. The mixture theory and nonlinear continuum mechanics have been invoked to derive the balance laws governing the deformation-diffusion process in saturated bodies. A mixed $\boldsymbol{u} - p$ formulation was developed to solve the balance laws in time and space. Numerical simulations of plane strain compression under globally undrained conditions in samples of loose and dense sands were conducted. Results were consistent with the findings under drained conditions: meso-scale inhomogeneities (even small ones) trigger instabilities that lead to the development of shear bands. These bands influence the flow characteristics in the sample as they tend to attract flow in the case of dense sands but rather repel flow in the case of loose sands. This is a direct consequence of the fact that dense sands behavior is mostly dilative, whereas that of loose sands is mostly contractive. To the knowledge of the author, all results reported in the literature show dilative shear bands attracting fluid flow. This is the only work showing the effect of compactive shear bands repelling fluid flow. This model is capable of capturing these effects because it accounts for the influence of relative density explicitly as well as plastic dilation/compaction.

It is concluded that meso-scale inhomogeneities, which are inevitably present in 'homogeneous' samples of sand, play a crucial role in the mechanical behavior of specimens under drained and undrained conditions at finite strains.

Possible improvements of this work include implementing the theory developed in Chapter 5 in three dimensions. Even though the framework is fully three-dimensional, the numerical examples are all in plane strain. It is necessary to implement the model utilizing brick

elements equipped with the mixed formulation. One has to be careful, however, as satisfaction of the Babuška-Brezzi condition in 3D is not straight-forward. Therefore, development of stabilized nonlinear finite elements may become necessary to avoid stability problems associated with the deformation-diffusion problem near time $t = 0^+$. Another possible (and necessary) improvement of this work, is the use of enhanced elements to circumvent the mesh dependence associated with the onset of strain localization. This improvement would allow for a more robust post-localization simulation. Also, it is necessary to develop and implement post-bifurcation constitutive models for sands to be able to simulate post-localization behavior more realistically.

Development of meso-scale models based on particulate mechanics is also possible but outside the scope of this dissertation. The approach here has been to develop a purely continuum formulation including information at the meso-scale. One can imagine that a multi-scale approach looking at the inter-particle behavior, and then transferring stress-strain responses to the macro-scale or for calibrating the already existing meso-scale model at the gauss points, is quite plausible. The effects of boundary conditions need also be investigated. It is well know that the end platens in compression tests—even well lubricated ones—introduce friction at the boundaries that makes the deformation inhomogeneous. It is therefore necessary to incorporate these end constrains by using, for example, contact elements to simulate the effect of friction from the platens.

The aspect of diffuse instabilities has been explicitly avoided in this dissertation but should be studied in the near future as it could open doors to the understanding and simulation of important instabilities mostly associated with loose sands. Diffuse instabilities such as liquefaction must be studied in order to predict the catastrophic effects associated with this phenomenon under fully dynamic excitations.

Appendix A

Finite element $\boldsymbol{u}-p$ formulation

Equation (5.4.42) can be rewritten in indicial notation as

$$\delta g_1 = c_{iA}\int_{\Omega_0}\left[N_{A,j}\left(a^{\mathrm{ep}}_{ijkl}+Jp\left(\delta_{il}\delta_{jk}-\delta_{ij}\delta_{kl}\right)\right)N_{B,l}\delta d_{Bk}-JN_{A,i}\overline{N}_B\delta p_B\right]\mathrm{d}\Omega_0, \quad \text{(A.0.1)}$$

following the notations in [119] (cf. equations (5.4.49) and (5.4.51)),

$$u_i \approx \sum_{A\in\eta-\eta_d} N_A d_{iA}+\sum_{A\in\eta_d} N^{\xi}_A\xi_A \quad \text{(A.0.2)}$$

$$p \approx \sum_{A\in\overline{\eta}-\eta_p} \overline{N}_A p_A+\sum_{A\in\eta_p} N^{\zeta}_A\zeta_A \quad \text{(A.0.3)}$$

$$\eta_i \approx \sum_{A\in\eta-\eta_d} N_A c_{iA} \quad \text{(A.0.4)}$$

$$\psi \approx \sum_{A\in\overline{\eta}-\eta_p} \overline{N}_A\overline{c}_A \quad \text{(A.0.5)}$$

where η and $\overline{\eta}$ denote the set of global node numbers for the displacement and pressure, respectively. Similarly, we let η_d and η_p be the nodes at which the displacements and pressures are prescribed, hence $\eta-\eta_d$ and $\overline{\eta}-\eta_p$ represent the active sets for the displacement and pressure, respectively. By the same token,

$$\delta g_2 = -c_{iA}\int_{\Omega_0} JN_A\gamma_{\mathrm{f}i}\left[N_{B,j}\delta d_{jB}+\frac{\phi^{\mathrm{f}}}{K_{\mathrm{f}}}\overline{N}_B\delta p_B\right]\mathrm{d}\Omega_0. \quad \text{(A.0.6)}$$

The linearized equations pertaining to the balance of mass equations can also be rewritten in indicial notation i.e.,

$$\delta h_1^{\Delta t} = \overline{c}_A \int_{\Omega_0} J\overline{N}_A \rho_{\mathrm{f}} \left[N_{B,j}\delta d_{jB} + \frac{\phi^{\mathrm{f}}}{K_{\mathrm{f}}}\overline{N}_B \delta p_B \right] \mathrm{d}\Omega_0, \tag{A.0.7}$$

and

$$\begin{aligned}
\delta h_2^{\Delta t} &= \frac{\alpha\Delta t}{g}\overline{c}_A \int_{\Omega_0} J k_{ij} \left[\overline{N}_{A,i} N_{B,k}\delta d_{kB} - \overline{N}_{A,k} N_{B,i}\delta d_{kB} \right] (p_{,j} - \gamma_{\mathrm{f}j})\, \mathrm{d}\Omega_0 \\
&+ \frac{\alpha\Delta t}{g}\overline{c}_A \int_{\Omega_0} \frac{J}{\mu}\overline{N}_{A,i}\delta_{ij} k' \gamma_{\mathrm{f}} \left(1 - \phi^{\mathrm{f}}\right) N_{B,k}\delta d_{kB}\, (p_{,j} - \gamma_{\mathrm{f}j})\, \mathrm{d}\Omega_0 \\
&+ \frac{\alpha\Delta t}{g}\overline{c}_A \int_{\Omega_0} J\overline{N}_{A,i} \frac{k_{ij}}{K_{\mathrm{f}}}\overline{N}_B \delta p_B\, (p_{,j} - \gamma_{\mathrm{f}j})\, \mathrm{d}\Omega_0 \\
&+ \frac{\alpha\Delta t}{g}\overline{c}_A \int_{\Omega_0} J\overline{N}_{A,i} k_{ij} \left[\overline{N}_{B,j}\delta p_B - \frac{\gamma_{\mathrm{f}j}}{K_{\mathrm{f}}}\overline{N}_B \delta p_B - p_{,k} N_{B,j}\delta d_{kB} \right] \mathrm{d}\Omega_0.
\end{aligned} \tag{A.0.8}$$

From this point forward we adopt Voigt notation and hence, a fourth-order tensor $\boldsymbol{\alpha}$ is mapped into a 9×9 array i.e.,

$$\boldsymbol{\alpha} = \begin{bmatrix} [\alpha_{iikk}] & [\alpha_{ii(kl)}] & [\alpha_{ii[kl]}] \\ [\alpha_{(ij)kk}] & [\alpha_{(ij)(kl)}] & [\alpha_{(ij)[kl]}] \\ [\alpha_{[ij]kk}] & [\alpha_{[ij](kl)}] & [\alpha_{[ij][kl]}] \end{bmatrix} \qquad \text{(no sum)} \tag{A.0.9}$$

where $i, j, k, l = 1, 2, 3$, and $i \neq j$ and $k \neq l$. Also, each submatrix in square brackets represents a 3×3 array. For example,

$$[\alpha_{(ij)[kl]}] = \begin{bmatrix} \alpha_{(12)[12]} & \alpha_{(12)[23]} & \alpha_{(12)[31]} \\ \alpha_{(23)[12]} & \alpha_{(23)[23]} & \alpha_{(23)[31]} \\ \alpha_{(31)[12]} & \alpha_{(31)[23]} & \alpha_{(31)[31]} \end{bmatrix}, \tag{A.0.10}$$

where the parentheses signify a symmetric operator, whereas the square brackets signify a skew-symmetric operator. For example,

$$\alpha_{(12)[23]} = \frac{1}{4}\left(\alpha_{1223} - \alpha_{1232} + \alpha_{2123} - \alpha_{2132}\right). \tag{A.0.11}$$

Similarly, a second-order tensor $\nabla^{\boldsymbol{x}}\boldsymbol{\eta}$ is mapped into a 9×1 vector i.e.,

$$\nabla^{\boldsymbol{x}}\boldsymbol{\eta} = \left\{\eta_{1,1},\eta_{2,2},\eta_{3,3},2\eta_{(1,2)},2\eta_{(2,3)},2\eta_{(3,1)},2\eta_{[1,2]},2\eta_{[2,3]},2\eta_{[3,1]}\right\}^t \tag{A.0.12}$$

such that the scalar product $\eta_{i,j}\alpha_{ijkl}\eta_{k,l} \equiv \nabla^{\boldsymbol{x}}\boldsymbol{\eta}^t\boldsymbol{\alpha}\,\nabla^{\boldsymbol{x}}\boldsymbol{\eta}$ is recovered. Also, given the finite element approximations in $(5.4.51)_{1,2}$ we have

$$\nabla^{\boldsymbol{x}}\boldsymbol{\eta} = \boldsymbol{B}\boldsymbol{c} \tag{A.0.13}$$

$$\nabla^{\boldsymbol{x}}\psi = \boldsymbol{\Gamma}\overline{\boldsymbol{c}}, \tag{A.0.14}$$

where $\boldsymbol{B}$ is the usual strain-displacement matrix i.e., $\boldsymbol{B} = [\boldsymbol{B}_1,\boldsymbol{B}_2,\ldots,\boldsymbol{B}_{nu}]$, and

$$\boldsymbol{B}_A = \begin{bmatrix} N_{A,1} & 0 & 0 \\ 0 & N_{A,2} & 0 \\ 0 & 0 & N_{A,3} \\ N_{A,2} & N_{A,1} & 0 \\ 0 & N_{A,3} & N_{A,2} \\ N_{A,3} & 0 & N_{A,1} \\ N_{A,2} & -N_{A,1} & 0 \\ 0 & N_{A,3} & -N_{A,2} \\ -N_{A,3} & 0 & N_{A,1} \end{bmatrix}. \tag{A.0.15}$$

By the same token, the matrix $\boldsymbol{\Gamma} = [\boldsymbol{\Gamma}_1,\boldsymbol{\Gamma}_2,\ldots,\boldsymbol{\Gamma}_{np}]$. The components of $\boldsymbol{\Gamma}$ read

$$\boldsymbol{\Gamma}_A = \left\{\overline{N}_{A,1},\overline{N}_{A,2},\overline{N}_{A,3}\right\}^t. \tag{A.0.16}$$

It is convenient at this point to introduce the following operators. Let $\boldsymbol{a}$ be a vector or first-order tensor with components a_i with $i=1,2,3$, then let

$$\epsilon(\boldsymbol{a}) = \begin{bmatrix} a_1 & 0 & 0 & \frac{1}{2}a_2 & 0 & \frac{1}{2}a_3 & \frac{1}{2}a_2 & 0 & -\frac{1}{2}a_3 \\ 0 & a_2 & 0 & \frac{1}{2}a_1 & \frac{1}{2}a_3 & 0 & -\frac{1}{2}a_1 & \frac{1}{2}a_3 & 0 \\ 0 & 0 & a_3 & 0 & \frac{1}{2}a_2 & \frac{1}{2}a_1 & 0 & -\frac{1}{2}a_2 & \frac{1}{2}a_1 \end{bmatrix}. \tag{A.0.17}$$

Similarly, let $\boldsymbol{\beta}$ be a third-order tensor with components β_{ijk} where $i, j, k = 1, 2, 3$, then

$$\boldsymbol{r}\left(\beta_{ijk}\right) = \left[\begin{array}{ccc} \left[\beta_{ikk}\right] & \left[\beta_{i(jk)}\right] & \left[\beta_{i[jk]}\right] \end{array}\right] \qquad \text{(no sum)} \tag{A.0.18}$$

where $j \neq k$ within the 3×9 array. Each submatrix in square brackets represents a 3×3 array, for instance,

$$\left[\beta_{ikk}\right] = \left[\begin{array}{ccc} \beta_{111} & \beta_{122} & \beta_{133} \\ \beta_{211} & \beta_{222} & \beta_{233} \\ \beta_{311} & \beta_{322} & \beta_{333} \end{array}\right] \tag{A.0.19}$$

Using the arrays and mappings presented above, we can write the matrix equation for the iterative Newton-Raphson scheme. The variational form for the equation of linear momentum implies

$$\boldsymbol{R}_g^k = \left[\begin{array}{cc} \boldsymbol{K}_g & \boldsymbol{\Phi}_g \end{array}\right]_k \left\{\begin{array}{c} \delta\boldsymbol{d} \\ \delta\boldsymbol{p} \end{array}\right\}_{k+1}, \tag{A.0.20}$$

where

$$\boldsymbol{K}_g = \int_{\Omega_0} \left[\boldsymbol{B}^t \left(\boldsymbol{a}^{\mathrm{ep}} + Jp\left(\mathbf{1} \ominus \mathbf{1} - \mathbf{1} \otimes \mathbf{1}\right)\right) \boldsymbol{B} - \boldsymbol{N}^t \boldsymbol{\gamma}_{\mathrm{f}} J \boldsymbol{\delta}^t \boldsymbol{B}\right] \mathrm{d}\Omega_0 \tag{A.0.21}$$

$$\boldsymbol{\Phi}_g = -\int_{\Omega_0} J \left[\boldsymbol{B}^t \boldsymbol{\delta} \overline{\boldsymbol{N}} + \boldsymbol{N}^t \boldsymbol{\gamma}_{\mathrm{f}} \frac{\phi^{\mathrm{f}}}{K_{\mathrm{f}}} \overline{\boldsymbol{N}}\right] \mathrm{d}\Omega_0, \tag{A.0.22}$$

with $\boldsymbol{\delta} = \{1, 1, 1, 0, 0, 0, 0, 0, 0\}^t$. Similarly, the variational form for the integrated (in time) equation of balance of mass implies

$$\boldsymbol{R}_h^k = \left[\begin{array}{cc} \boldsymbol{K}_h + \alpha \Delta t \overline{\boldsymbol{K}}_h & \boldsymbol{\Phi}_h + \alpha \Delta t \overline{\boldsymbol{\Phi}}_h \end{array}\right]_k \left\{\begin{array}{c} \delta\boldsymbol{d} \\ \delta\boldsymbol{p} \end{array}\right\}_{k+1}, \tag{A.0.23}$$

where

$$\boldsymbol{K}_h = \int_{\Omega_0} \overline{\boldsymbol{N}}^t J \rho_{\mathrm{f}} \boldsymbol{\delta}^t \boldsymbol{B} \, \mathrm{d}\Omega_0 \tag{A.0.24}$$

$$\boldsymbol{\Phi}_h = \int_{\Omega_0} \overline{\boldsymbol{N}}^t J \rho_{\mathrm{f}} \frac{\phi^{\mathrm{f}}}{K_{\mathrm{f}}} \overline{\boldsymbol{N}} \, \mathrm{d}\Omega_0 \tag{A.0.25}$$

$$\begin{aligned} \overline{\boldsymbol{K}}_h &= \int_{\Omega_0} \frac{J}{g} \boldsymbol{\Gamma}^t \left[\left(\boldsymbol{k} + \frac{k'}{\mu} \gamma_{\mathrm{f}} \left(1 - \phi^{\mathrm{f}} \right) \mathbf{1} \right) \cdot \left(\nabla^{\boldsymbol{x}} p_{\mathrm{f}} - \boldsymbol{\gamma}_{\mathrm{f}} \right) \right] \boldsymbol{\delta}^t \boldsymbol{B} \, \mathrm{d}\Omega_0 \\ &- \int_{\Omega_0} \frac{J}{g} \boldsymbol{\Gamma}^t \left[\boldsymbol{\epsilon} \left(\boldsymbol{k} \cdot \left(\nabla^{\boldsymbol{x}} p - \boldsymbol{\gamma}_{\mathrm{f}} \right) \right) + \boldsymbol{r} \left(k_{ik} p_{,j} \right) \right] \boldsymbol{B} \mathrm{d}\Omega_0 \end{aligned} \tag{A.0.26}$$

$$\overline{\boldsymbol{\Phi}}_h = \int_{\Omega_0} \frac{J}{g} \boldsymbol{\Gamma}^t \boldsymbol{k} \left[\frac{1}{K_{\mathrm{f}}} \left(\nabla^{\boldsymbol{x}} p - \boldsymbol{\gamma}_{\mathrm{f}} \right) \overline{\boldsymbol{N}} + \boldsymbol{\Gamma} \right] \mathrm{d}\Omega_0, \tag{A.0.27}$$

and hence the incremental solution in equation (5.4.57).

Bibliography

[1] G. T. Houlsby. The use of a variable shear modulus in elasto-plastic models for clays. *Computers and Geotechnics*, 1:3–13, 1985.

[2] M. G. Jefferies. Nor-Sand: a simple critical state model for sand. *Géotechnique*, 43:91–103, 1993.

[3] S. L. Kramer. *Geotechnical Earthquake Engineering*. Prentice-Hall, New Jersey, 1996.

[4] K. A. Alshibli, S. N. Batiste, and S. Sture. Strain localization in sand: plane strain versus triaxial compression. *Journal of Geotechnical and Geoenvironmental Engineering, ASCE*, 129:483–494, 2003.

[5] A. J. Durrani, A. S. Elnashai, Y. M. A. Hashash, S. J. Kim, and A. Masud. The Kashmir earthquake of October 8, 2005. A quick look report. Technical Report 05-04, Mid-America Earthquake Center, 2005.

[6] A. Schofield and P. Wroth. *Critical State Soil Mechanics*. McGraw-Hill, New York, 1968.

[7] J. Graham, J. H. A. Crooks, and A. L. Bell. Yield states and stress–strain behaviour of natural soft clays. *Canadian Geotechnical Journal*, 20:502–516, 1983.

[8] P. V. Lade and J. M. Duncan. Elastoplastic stress-strain theory for cohesionless soil. *Journal of the Geotechnical Engineering Division, ASCE*, 101:1037–1053, 1975.

[9] D. H. Cornforth. Some experiments on the influence of strain conditions on the strength of sand. *Géotechnique*, 14:143–167, 1964.

[10] H. B. Poorooshasb, I. Holubec, and A. N. Sherbourne. Yielding and flow of sand in triaxial compression: Part I. *Canadian Geotechnical Journal*, 3:179–190, 1966.

[11] H. B. Poorooshasb, I. Holubec, and A. N. Sherbourne. Yielding and flow of sand in triaxial compression: Parts II and III. *Canadian Geotechnical Journal*, 4:376–397, 1967.

[12] A. Aydin. Fractures, faults, and hydrocarbon entrapment, migration and flow. *Marine and Petroleum Geology*, 17:797–814, 2000.

[13] G. Castro. Liquefaction of sands. *Harvard University, Harvard Soil Mechanics Series 81*, Jan 1969.

[14] K. Ishihara. Liquefaction and flow failure during earthquakes. *Géotechnique*, 43:351–415, 1993.

[15] J. Desrues, R. Chambon, M. Mokni, and F. Mazerolle. Void ratio evolution inside shear bands in triaxial sand specimens studied by computed tomography. *Géotechnique*, 46:527–546, 1996.

[16] L. B. Wang, J. D. Frost, and J. S. Lai. Three-dimensional digital representation of granular material microstructure from X-Ray tomography imaging. *Journal of Computing in Civil Engineering, ASCE*, 18:28–35, 2004.

[17] P. Wriggers and S. O. Moftah. Mesoscale models for concrete: Homogenisation and damage behaviour. *Finite Elements in Analysis and Design*, 42:623–636, 2006.

[18] S. Häfner, S. Eckardt, T. Luther, and C. Könke. Mesoscale modeling of concrete: Geometry and numerics. *Computers & Structures*, 84:450–461, 2006.

[19] K. Nübel and W. Huang. A study of localized deformation pattern in granular media. *Computer Methods in Applied Mechanics and Engineering*, 193:2719–2743, 2004.

[20] M. Mokni and J. Desrues. Strain localization measurements in undrained plane-strain biaxial tests on hostun rf sand. *Mechanics of Cohesive-Frictional Materials*, 4:419–441, 1998.

[21] C. Han and G. Vardoulakis. Plane-strain compression experiments on water-saturated fine-grained sand. *Géotechnique*, 41:49–78, 1991.

[22] R. J. Finno, W. W. Harris, M. A. Mooney, and G. Viggiani. Shear bands in plane strain compression of loose sand. *Géotechnique*, 47:149–165, 1997.

[23] R. J. Finno, D. K. Atmatzidis, and S. B. Perkins. Observed performance of deep a excavation in clay. *Journal of Geotechnical Engineering, ASCE*, 115:1045–1064, 1989.

[24] R. J. Finno and S. M. Nerby. Saturated clay response during braced cut construction. *Journal of Geotechnical Engineering, ASCE*, 115:1065–1084, 1989.

[25] J. Hadamard. *Leçons sur la propagation des ondes et les équations de l'hydrodynamique*. Librarie Scientifique A, Paris, 1903.

[26] R. Hill. A general theory of uniqueness and stability in elastic-plastic solids. *Journal of the Mechanics and Physics of Solids*, 6:236–249, 1958.

[27] T. Thomas. *Plastic Flow and Fracture in Solids*. Academic Press, New York, NY, 1961.

[28] J. Mandel. Conditions de stabilité et postulat de Druker. In J. Kravtchenko and P. M. Sirieys, editors, *Rheology and Soil Mechanics*. Springer, 1966.

[29] J. W. Rudnicki and J. R. Rice. Conditions for localization of deformation in pressure-sensitive dilatant materials. *Journal of the Mechanics and Physics of Solids*, 23:371–394, 1975.

[30] J. E. Marsden and T. J. R. Hughes. *Mathematical Theory of Elasticity*. Prentice-Hall, Englewood Cliffs, NJ, 1983.

[31] J. C. Simo, J. Oliver, and F. Armero. An analysis of strong discontinuities induced by strain-softening in rate-independent inelastic solids. *Computational Mechanics*, 12:277–296, 1993.

[32] M. Ortiz. An analytical study of the localized failure modes of concrete. *Mechanics of Materials*, 6:159–174, 1987.

[33] D. Bigoni and T. Hueckel. Uniqueness and localization—i. Associative and non-associative elastoplasticity. *International Journal for Solids and Structures*, 28:197–213, 1991.

[34] K. Runesson, N. S. Ottosen, and D. Peric. Discontinuous bifurcations of elastic-plastic solutions at plane stress and plane strain. *International Journal of Plasticity*, 7:99–121, 1991.

[35] N. S. Ottosen and K. Runesson. Properties of discontinuous bifurcation solutions in elasto-plasticity. *International Journal of Solids and Structures*, 27:401–421, 1991.

[36] M. K. Neilsen and H. L. Schreyer. Bifurcations in elastic-plastic materials. *International Journal for Solids and Structures*, 30:521–544, 1993.

[37] D. Bigoni and D. Zaccaria. On strain localization analysis of elastoplastic materials at finite strains. *International Journal of Plasticity*, 9:21–33, 1993.

[38] L. Szabó. Shear band formulations in finite strain elastoplasticity. *International Journal for Solids and Structures*, 31:1291–1308, 1994.

[39] J. Desrues R. Chambon, S. Crochepeyre. Localization criteria for non-linear constitutive equations of geomaterials. *Mechanics of Cohesive-Frictional Materials*, 5:61–82, 2000.

[40] W. A. Olsoon and D. J. Holcomb. Compaction localization in porous rock. *Geophysical Research Letters*, 27:3537–3540, 2000.

[41] K. A. Issen and J. W. Rudnicki. Conditions for compaction bands in porous rock. *Journal of Geophysical Research*, 105:21529–21536, 2000.

[42] J. W. Rudnicki. Shear and compaction band formation on an elliptic yield cap. *Journal of Geophysical Research*, 109:1–10, 2004.

[43] R. I. Borja and A. Aydin. Computational modeling of deformation bands in granular media. I. Geological and mathematical framework. *Computer Methods in Applied Mechanics and Engineering*, 193:2667–2698, 2004.

[44] J. W. Rudnicki. Formulation for studying coupled deformation pore fluid diffusion effects on localization of deformation. *AMD (Symposia Series) (American Society of Mechanical Engineers, Applied Mechanics Division)*, 57:35–44, 1983.

[45] R. Larsson, K. Runesson, and S. Sture. Embedded localization band in undrained soil based on regularized strong discontinuity—theory and fe-analysis. *International Journal of Solids and Structures*, 33:3081–3101, 1996.

[46] R. I. Borja. Cam-Clay plasticity, Part V: A mathematical framework for three-phase deformation and strain localization analyses of partially saturated porous media. *Computer Methods in Applied Mechanics and Engineering*, 193:5301–5338, 2004.

[47] C. Callari and F. Armero. Analysis and numerical simulation of strong discontinuities in finite strain poroplasticity. *Computer Methods in Applied Mechanics and Engineering*, 193:2941–2986, 2004.

[48] I. Vardoulakis. Deformation of water-saturated sand: I. uniform undrained deformation and shear banding. *Géotechnique*, 46:441–456, 1996.

[49] I. Vardoulakis. Deformation of water-saturated sand: II. effect of pore water flow and shear banding. *Géotechnique*, 46:457–472, 1996.

[50] J. H. Prevost. Localization of deformations in elastic-plastic solids. *International Journal for Numerical and Analytical Methods in Geomechanics*, 8:187–196, 1984.

[51] M. Ortiz, Y. Leroy, and A. Needleman. A finite element method for localized failure analysis. *Computer Methods in Applied Mechanics and Engineering*, 61:189–214, 1987.

[52] Y. Leroy and M. Ortiz. Finite element analysis of strain localization in frictional materials. *International Journal for Numerical and Analytical Methods in Geomechanics*, 13:53–74, 1989.

[53] Z. Bažant, T. Belytschko, and T. P. Chang. Continuum theory for strain-softening. *Journal of Engineering Mechanics, ASCE*, 110:1666–1692, 1984.

[54] J. H. Prevost and B. Loret. Dynamic strain localization in elasto-(visco-)plastic solids, part 1. General formulation and one-dimensional examples. *Computer Methods in Applied Mechanics and Engineering*, 83:275–294, 1990.

[55] J. H. Prevost and B. Loret. Dynamic strain localization in elasto-(visco-)plastic solids, part 2. Plane strain examples. *Computer Methods in Applied Mechanics and Engineering*, 83:275–294, 1990.

[56] H. B. Muhlhaus and I. Vardoulakis. The thickness of shear bands in granular materials. *Géotechnique*, 37:271–283, 1987.

[57] X. Li and H. Tang. A consistent return mapping algorithm for pressure-dependent elastoplastic Cosserat continua and modelling of strain localization. *Computers & Structures*, 83:1–10, 2005.

[58] F. Armero and K. Garikipati. An analysis of strong discontinuities in multiplicative finite strain plasticity and their relation with the numerical simulation of strain localization in solids. *International Journal for Solids and Structures*, 33:2863–2885, 1996.

[59] R. Larsson and K. Runesson. Element-embedded localization band based on regularized displacement discontinuity. *Journal of Engineering Mechanics, ASCE*, 122:402–411, 1996.

[60] R. A. Regueiro and R. I. Borja. A finite element model of localized deformation in frictional materials taking a strong discontinuity approach. *Finite Elements in Analysis and Design*, 33:283–315, 1999.

[61] R. I. Borja. A finite element model for strain localization analysis of strongly discontinuous fields based on standard Galerkin approximation. *Computer Methods in Applied Mechanics and Engineering*, 190:1529–49, 2000.

[62] R. I. Borja and R. A. Regueiro. Strain localization in frictional materials exhibiting displacement jumps. *Computer Methods in Applied Mechanics and Engineering*, 190:2555–2580, 2001.

[63] R. A. Regueiro and R. I. Borja. Plane strain finite element analysis of pressure sensitive plasticity with strong discontinuity. *International Journal of Solids and Structures*, 38:3647–3672, 2001.

[64] R. I. Borja. Bifurcation of elastoplastic solids to shear band mode at finite strains. *Computer Methods in Applied Mechanics and Engineering*, 191:5287–5314, 2002.

[65] K. H. Roscoe and J. H. Burland. On the generalized stress–strain behavior of 'wet' clay. In J. Heyman and F. A. Leckie, editors, *Engineering Plasticity*, pages 535–609. Cambridge University Press, 1968.

[66] R. I. Borja and C. Tamagnini. Cam-Clay plasticity, Part III: Extension of the infinitesimal model to include finite strains. *Computer Methods in Applied Mechanics and Engineering*, 155:73–95, 1998.

[67] R. Nova and D. M. Wood. A constitutive model for sand in triaxial compression.

International Journal for Numerical and Analytical Methods in Geomechanics, 3:255–278, 1979.

[68] M. Pastor, O. C. Zienkiewicz, and A. H. C. Chan. Generalized plasticity and the modeling of soil behaviour. *International Journal for Numerical and Analytical Methods in Geomechanics*, 14:151–190, 1990.

[69] J. M. Pestana and A. J. Whittle. Formulation of a unified constitutive model for clays and sands. *International Journal for Numerical and Analytical Methods in Geomechanics*, 23:1215–1243, 1999.

[70] H. Matsuoka and T. Nakai. A new failure criterion for soils in three-dimensional stresses. In *Conference on Deformation and Failure of Granular Materials*, pages 253–263. IUTAM, 1982.

[71] P. V. Lade and M. K. Kim. Sigle hardening constitutive model for frictional materials II. Yield criterion and plastic work contours. *Computers and Geotechnics*, 6:13–29, 1988.

[72] D. Perić and M.A. Ayari. Influence of Lode's angle on the pore pressure generation in soils. *International Journal of Plasticity*, 18:1039–1059, 2002.

[73] D. Perić and M.A. Ayari. On the analytical solutions for the three-invariant Cam clay model. *International Journal of Plasticity*, 18:1061–1082, 2002.

[74] R. D. Holtz and W. D. Kovacs. *An Introduction to Geotechnical Engineering*. Prentice-Hall, Inc., Englewood Cliffs, NJ, 1981.

[75] M. T. Manzari and Y. F. Dafalias. A critical state two-surface plasticity model for sands. *Géotechnique*, 43:255–272, 1997.

[76] N. Khalili, M. A. Habte, and S. Valliappan. A bounding surface plasticity model for cyclic loading of granular soils. *International Journal for Numerical Methods in Engineering*, 63:1939–1960, 2005.

[77] R. Nova. The role of non-normality in soil mechanics and some of its mathematical consequences. *Computers and Geotechnics*, 31:185–191, 2004.

[78] K. A. Alshibli, S. Sture, N. C. Costes, M. L. Frank, F. R. Lankton, S. N. Batiste, and R. A. Swanson. Assessment of localized deformations in sand using x-ray computed tomography. *Geotechnical Testing Journal, ASCE*, 23:274–299, 2000.

[79] K. A. Alshibli and S. Sture. Shear band formation in plane strain compression. *Journal of Geotechnical and Geoenvironmental Engineering, ASCE*, 126:495–503, 2000.

[80] J. Desrues and G. Viggiani. Strain localization in sand: an overview of the experimental results obtained in grenoble using stereophotogrammetry. *International Journal for Numerical and Analytical Methods in Geomechanics*, 28:279–321, 2004.

[81] R. J. Finno, W. W. Harris, and M. A. Mooney. Strain localization and undrained steady state of sands. *Journal of Geotechnical Engineering, ASCE*, 122:462–473, 1996.

[82] G. Gudehus and K. Nübel. Evolution of shear bands in sand. *Géotechnique*, 54:187–201, 2004.

[83] A. L. Rechenmacher and R. J. Finno. Digital image correlation to evaluate shear banding in dilative sands. *Geotechnical Testing Jounal, ASCE*, 27:1–10, 2004.

[84] A. L. Rechenmacher and R. J. Finno. Shear band displacements and void ratio evolution to critical state in dilative sands. In J. F. Labuz and A. Drescher, editors, *Bifurcation and Instabilities in Geomaterials*, pages 13–22. A. A. Blakema Publishers, 2003.

[85] I. Vardoulakis, M. Goldscheider, and G. Gudehus. Formation of shear bands in sand bodies as a bifurcation problem. *International Journal for Numerical and Analytical Methods Geomechanics*, 2:99–128, 1978.

[86] I. Vardoulakis and B. Graf. Calibration of constitutive models for granular materials using data from biaxial experiments. *Géotechnique*, 35:299–317, 1985.

[87] E. Bauer, W. Wu, and W. Huang. Influence of an initially transverse isotropy on shear banding in granular materials. In J. F. Labuz and A. Drescher, editors, *Bifurcation and Instabilities in Geomaterials*, pages 161–172. A. A. Blakema Publishers, 2003.

[88] R. I. Borja and T. Y. Lai. Propagation of localization instability under active and passive loading. *Journal of Geotechnical and Geoenvironmental Engineering, ASCE*, 128:64–75, 2002.

[89] R. Chambon and J. C. Moullet. Uniqueness studies in boundary value problems involving some second gradient models. *Computer Methods in Applied Mechanics and Engineering*, 193:2771–2796, 2004.

[90] R. Chambon, D. Caillerie, and C. Tamagnini. A strain space gradient plasticity theory for finite strain. *Computer Methods in Applied Mechanics and Engineering*, 193:2797–2826, 2004.

[91] F. Darve, G. Servant, F. Laouafa, and H. D. V. Khoa. Failure in geomaterials: continuous and discrete analyses. *Computer Methods in Applied Mechanics and Engineering*, 193:3057–3085, 2004.

[92] R. de Borst and H. B. Mühlhaus. Gradient-dependent plasticity: Formulation and algorithmic aspects. *International Journal for Numerical Methods in Engineering*, 35:521–539, 1992.

[93] A. Gajo, D. Bigoni, and D. M. Wood. Stress induced elastic anisotropy and strain localisation in sand. In H. B. Mühlhaus, A. Dyskin, and E. Pasternak, editors, *Bifurcation and Localisation Theory in Geomechanics*, pages 37–44. A. A. Blakema Publishers, 2001.

[94] S. Kimoto, F. Oka, and Y. Higo. Strain localization analysis of elasto-viscoplastic soil considering structural degradation. *Computer Methods in Applied Mechanics and Engineering*, 193:2845–2866, 2004.

[95] P. A. Klerck, E. J. Sellers, and D. R. J. Owen. Discrete fracture in quasi-brittle materials under compressive and tensile stress states. *Computer Methods in Applied Mechanics and Engineering*, 193:3035–3056, 2004.

[96] B. Muhunthan, O. Alhattamleh, and H. M. Zbib. Modeling of localization in granular materials: effect of porosity and particle size. In J. F. Labuz and A. Drescher, editors, *Bifurcation and Instabilities in Geomaterials*, pages 121–131. A. A. Blakema Publishers, 2003.

[97] E. Oñate and J. Rojek. Combination of discrete element and finite element methods for dynamic analysis of geomechanics problems. *Computer Methods in Applied Mechanics and Engineering*, 193:3087–3128, 2004.

[98] M. Ortiz and A. Pandolfi. A variational cam-clay theory of plasticity. *Computer Methods in Applied Mechanics and Engineering*, 193:2645–2666, 2004.

[99] M. R. Salari, S. Saeb, K. J. Willam, S. J. Patchet, and R. C. Carrasco. A coupled elastoplastic damage model for geomaterials. *Computer Methods in Applied Mechanics and Engineering*, 193:2625–2643, 2004.

[100] J. Tejchman and G. Gudehus. Shearing of a narrow granular layer with polar quantities. *International Journal for Numerical and Analytical Methods in Geomechanics*, 25:1–28, 2001.

[101] I. Vardoulakis, E. Vairaktaris, and E. Papamichos. Subsidence diffusion-convection: I. the direct problem. *Computer Methods in Applied Mechanics and Engineering*, 193:2745–2760, 2004.

[102] R. G. Wan and P. J. Guo. Constitutive modelling of granular materials with focus to microstructure and its effect on strain localization. In J. F. Labuz and A. Drescher, editors, *Bifurcation and Instabilities in Geomaterials*, pages 149–160. A. A. Blakema Publishers, 2003.

[103] Z. Q. Yue, S. Chen, and L. G. Tham. Finite element modeling of geomaterials using digital image processing. *Computers and Geotechnics*, 30:375–397, 2003.

[104] R. I. Borja and S. R. Lee. Cam-Clay plasticity, Part I: Implicit integration of elastoplastic constitutive relations. *Computer Methods in Applied Mechanics and Engineering*, 78:49–72, 1990.

[105] R. I. Borja. Cam-Clay plasticity, Part II: Implicit integration of constitutive equation based on nonlinear elastic stress predictor. *Computer Methods in Applied Mechanics and Engineering*, 88:225–240, 1991.

[106] K. Been and M. G. Jefferies. A state parameter for sands. *Géotechnique*, 35:99–112, 1985.

[107] K. Ishihara, F. Tatsuoka, and S. Yasuda. Undrained deformation and liquefaction of sand under cyclic stresses. *Soils and Foundations*, 15:29–44, 1975.

[108] A. Gens and D.M. Potts. Critical state models in computational geomechanics. *Engineering Computations*, 5:178–197, 1988.

[109] R. J. Jardine, D. M. Potts, A. B. Fourie, and J. B. Burland. Studies of the influence of non-linear stress-strain characteristics in soil-structure interaction. *Géotechnique*, 36:377–396, 1986.

[110] P. V. Lade. Static instability and liquefaction of loose fine sandy slopes. *Journal of Geotechnical Engineering, ASCE*, 118:51–71, 1992.

[111] R. I. Borja, K. M. Sama, and P. F. Sanz. On the numerical integration of three-invariant elastoplastic constitutive models. *Computer Methods in Applied Mechanics and Engineering*, 192:1227–1258, 2003.

[112] J. C. Simo and T. J. R. Hughes. *Computational Inelasticity*. Prentice-Hall, New York, 1998.

[113] J. Sulem, I. Vardoulakis, E. Papamichos, A. Oulahna, and J. Tronvoll. Elasto-plastic modelling of red wildmoor sandstone. *Mechanics of Cohesive-Frictional Materials*, 4:215–245, 1999.

[114] R. I. Borja. Computational modeling of deformation bands in granular media. II. Numerical simulations. *Computer Methods in Applied Mechanics and Engineering*, 193:2699–2718, 2004.

[115] E. H. Lee. Elastic-plastic deformation at finite strain. *Journal of Applied Mechanics*, 36:1–6, 1969.

[116] L. E. Malvern. *Introduction to the Mechanics of a Continuous Medium*. Prentice-Hall, Inc., Englewood Cliffs, NJ, 1969.

[117] J. C. Simo. Algorithms for static and dynamic multiplicative plasticity that preserve the classical return mapping schemes of the infinitesimal theory. *Computer Methods in Applied Mechanics and Engineering*, 99:61–112, 1992.

[118] Y. F. Dafalias. Plastic spin: necessity or redundancy? *International Journal of Plasticity*, 14:909–931, 1998.

[119] T. J. R. Hughes. *The Finite Element Method*. Prentice-Hall, Englewood Cliffs, NJ, 1987.

[120] J. C. Nagtegaal, D. M. Parks, and J. R. Rice. On numerically accurate finite element solutions in the fully plastic regime. *Computer Methods in Applied Mechanics and Engineering*, 4:153–177, 1974.

[121] J. C. Simo, R. L. Taylor, and K. S. Pister. Variational and projection methods for the volume constraint in finite deformation elasto-plasticity. *Computer Methods in Applied Mechanics and Engineering*, 51:177–208, 1985.

[122] R. I. Borja and J. E. Andrade. Critical state plasticity, Part VI: Meso-scale finite element simulation of strain localization in discrete granular materials. *Computer Methods in Applied Mechanics and Engineering*, 2006. In press for the John Argyris Memorial Special Issue.

[123] W. Lode. Versuche ueber den einfluss der mitt leren Hauptspannung auf das Fliessen der Metalle Eisen Kupfer und Nickel. *Zeitschrift fuer Physik*, 36:913–939, 1926.

[124] G. A. Holzapfel. *Nonlinear Solid Mechanics*. John Wiley & Sons Ltd, West Sussex, UK, 2000.

[125] R. I. Borja, C. Tamagnini, and A. Amorosi. Coupling plasticity and energy-conserving elasticity models for clays. *Journal of Geotechnical and Geoenvironmental Engineering, ASCE*, 123:948–957, 1997.

[126] R. I. Borja. Plasticity modeling and computation. Lecture Notes, Stanford University, California, 2005.

[127] G. Gudehus. Elastoplastische stoffgleichungen fur trockenen sand. *Ingenieur-Archiv*, 42:151–169, 1973.

[128] J. H. Argyris, G. Faust, J. Szimmat, E. P. Warnke, and K. J. Willam. Recent developments in the finite element analysis of prestressed concrete reactor vessels. *Nuclear Engineering and Design*, 28:42–75, 1974.

[129] J. Jiang and Pietruszczak. Convexity of yield loci for pressure sensitive materials. *Computers and Geotechnics*, 5:51–63, 1988.

[130] K. J. Willam and E. P. Warnke. Constitutive model for the triaxial behaviour of concrete. In *Concrete Structures Subjected to Triaxial Stresses*, Bergamo, Italy, May 1974. ISMES.

[131] J. E. Andrade and R. I. Borja. Fully implicit numerical integration of a hyperelastoplastic model for sands based on critical state plasticity. In K. J. Bathe, editor, *Computational Fluid and Solid Mechanics 2005*, pages 52–54. Elsevier Science Ltd., 2005.

[132] J. Bonet and R. D. Wood. *Nonlinear Continuum Mechanics for for Finite Element Analysis*. Cambridge University Press, Cambridge, UK, 1997.

[133] T. Belytschko, W. K. Liu, and B. Moran. *Nonlinear Finite Elements for Continua and Structures*. John Wiley & Sons Ltd., West Sussex, UK, 2000.

[134] M. Ortiz and J. B. Martin. Symmetry-preserving return mapping algorithms and incrementally extremal paths - a unification of concepts. *International Journal for Numerical Methods in Engineering*, 8:1839–1853, 1989.

[135] K. Willam. Constitutive models for engineering materials. In *Encyclopedia of Physical Science and Technology*, volume 3. Academic Press, third edition, 2002.

[136] J. Oliver and A. E. Huespe. Theoretical and computational issues in modeling material failure in strong discontinuity scenarios. *Computer Methods in Applied Mechanics and Engineering*, 193:2987–3014, 2004.

[137] J. Mosler. Numerical analyses of discontinuous material bifurcation: strong and weak discontinuities. *Computer Methods in Applied Mechanics and Engineering*, 194:979–1000, 2005.

[138] M. Shahinpoor. Statistical mechanical considerations on the random packing of granular materials. *Powder Technology*, 25:163–176, 1980.

[139] J. R. Benjamin and C. A. Cornell. *Probability, Statistics, and Decision for Civil Engineers*. McGraw-Hill, Inc., New York, 1970.

[140] T. Y. Lai, R. I. Borja, B. G. Duvernay, and R. L. Meehan. Capturing strain localization behind a geosynthetic-reinforced soil wall. *International Journal for Numerical and Analytical Methods in Geomechanics*, 27:425–451, 2003.

[141] J. R. Rice. On the stability of dilatant hardening for saturated rock masses. *Journal of Geophysical Research*, 80:1531–1536, 1975.

[142] J. W. Rudnicki. Effects of dilatant hardening on the development of concentrated shear deformation in fissured rock masses. *Journal of Geophysical Research*, 89:9259–9270, 1984.

[143] F. Armero. Formulation and finite element implementation of multiplicative model of coupled poro-plasticity at finite strains under fully saturated conditions. *Computer Methods in Applied Mechanics and Engineering*, 171:205–241, 1999.

[144] J. Larsson and R. Larsson. Non-linear analysis of nearly saturated porous media: theoretical and numerical formulation. *Computer Methods in Applied Mechanics and Engineering*, 191:3885–3907, 2002.

[145] B. A. Schrefler, H. W. Zhang, M. Pastor, and O. C. Zienkiewicz. Strain localisation modeling and pore pressure in saturated sand samples. *Computational Mechanics*, 22:266–280, 1998.

[146] W. Ehlers, T. Graf, and M. Ammann. Deformation and localization analysis of partially saturated soil. *Computer Methods in Applied Mechanics and Engineering*, 193:2885–2910, 2004.

[147] B. Loret and J. H. Prevost. Dynamic strain localization in fuid-saturated porous media. *Journal of Engineering Mechanics, ASCE*, 117:907–922, 1991.

[148] B. A. Schrefler, L. Sanavia, and C. E. Majorana. A multiphase medium model for localisation and postlocalisation simulation in geomaterials. *Mechanics of Cohesive-Frictional Materials*, 1:95–114, 1996.

[149] H. W. Zhang, L. Sanavia, and B. A. Schrefler. An internal lenght scale in dynamic strain localization of multiphase porous media. *Mechanics of Cohesive-Frictional Materials*, 4:443–460, 1999.

[150] P. Steinmann. A finite element formulation for strong discontinuities in fluid-saturated porous media. *Mechanics of Cohesive-Frictional Materials*, 4:133–152, 1999.

[151] A. L. Rechenmacher. Grain-scale processes governing shear band initiation and evolution in sands. *Journal of the Mechanics and Physics of Solids*, 54:22–45, 2006.

[152] J. E. Andrade and R. I. Borja. Capturing strain localization in dense sands with random density. International Journal for Numerical Methods in Engineering, in press, 2006.

[153] D. M. Wood. *Soil Behaviour and Critical State Soil Mechanics*. Cambridge University Press, Cambridge, UK, 1990.

[154] R. M. Bowen. Theory of mixtures. In A. C. Eringen, editor, *Continuum Physics*, volume III—Mixtures and EM Field Theories, New York, NY, 1976. Academic Press.

[155] R. J. Atkin and R. E. Craine. Continuum theories of mixture: basic theory and historical development. *Quarterly Journal of Mechanics and Applied Mathematics*, 29:209–244, 1976.

[156] C. Li, R. I. Borja, and R. A. Regueiro. Dynamics of porous media at finite strain. *Computer Methods in Applied Mechanics and Engineering*, 193:3837–3870, 2004.

[157] F. Armero and C. Callari. An analysis of strong discontinuities in a saturated poro-plastic solid. *International Journal for Numerical Methods in Engineering*, 46:1673–1698, 1999.

[158] J. Bear. *Dynamics of Fluids in Porous Media*. American Elsevier Publishing Company, Inc., New York, NY, 1972.

[159] O. C. Zienkiewicz and R. L. Taylor. *The Finite Element Method*, volume 1. Butterworth-Heinemann, Oxford, UK, fifth edition, 2000.

[160] J. H. Prevost. Mechanics of continuous porous media. *International Journal of Engineering Science*, 18:787–800, 1980.

[161] O. Coussy. *Mechanics of Porous Continua*. John Wiley & Sons Ltd, West Sussex, UK, 1995.

[162] A. Nur and J. D. Byerlee. An exact effective stress law for elastic deformation of rock with fluids. *Journal of Geophysical Research*, 76:6414–6419, 1971.

[163] R. I. Borja. On the mechanical energy and effective stress in saturated and unsaturated porous continua. *International Journal of Solids and Structures*, 43:1764–1786, 2006.

[164] K. Terzaghi. *Theoretical Soil Mechanics*. John Wiley & Sons Ltd, New York, NY, 1943.

[165] P. Pivonka and K. Willam. The effect of the third invariant in computational plasticity. *Engineering Computations*, 20:741–753, 2003.

[166] O. C. Zienkiewicz, A. H. C. Chan, M. Pastor, B. A. Schrefler, and T. Shiomi. *Computational Geomechanics*. John Wiley & Sons Ltd, New York, NY, 1999.

[167] J. Kozeny. Über kapillare Leitung des Wassers im Boden. *Sitzungsberichte der Kaiserlichen Akademie der Wissenschaften in Wien*, 136:271–306, 1927.

[168] P. C. Carman. Fuid flow through a granular bed. *Transactions of the Institution of Chemical Engineers of London*, 15:150–156, 1937.

[169] R. I. Borja and E. Alarcon. A mathematical framework for finite strain elastoplastic consolidation Part 1: Balance laws, variational formulation, and linearization. *Computer Methods in Applied Mechanics and Engineering*, 122:145–171, 1995.

[170] M. A. Murad and A. F. D. Loula. Improved accuracy in finite element analysis of Biot's consolidation problem. *Computer Methods in Applied Mechanics and Engineering*, 95:359–382, 1992.

[171] J. Wan. *Stabilized Finite Element Methods for Coupled Geomechanics and Multiphase Flow*. PhD thesis, Stanford University, Stanford, CA, 2002.

[172] M. A. Murad and A. F. D. Loula. On stability and convergence of finite element approximations of Biot's consolidation problem. *International Journal for Numerical Methods in Engineering*, 37:645–667, 1994.

[173] T. J. R. Hughes, L. P. Franca, and M. Balestra. A new finite element formulation for computational fluid dynamics: V. Circumvemting the Babuška-Brezzi condition. *Computer Methods in Applied Mechanics and Engineering*, 59:85–99, 1986.

[174] P. Mira, M. Pastor, T. Li, and X. Liu. A new stabilized enhanced strain element with equal order of interpolation for soil consolidation problems. *Computer Methods in Applied Mechanics and Engineering*, 192:4257–4277, 2003.

[175] J. C. Simo and M. S. Rifai. A class of mixed assumed strain methods and the method of incompatible modes. *International Journal for Numerical Methods in Engineering*, 29:1595–1638, 1990.

[176] H. W. Zhang and B. A. Schrefler. Particular aspects of internal lenght scales in strain localization analysis of multiphase porous materials. *Computer Methods in Applied Mechanics and Engineering*, 193:2867–2884, 2004.